

Design and Analysis of Propeller Blade Geometry using the PDE Method

Christopher Wojciech Dekanski

Submitted in accordance with the requirements of
Doctor of Philosophy

The University of Leeds
Department of Applied Mathematical Studies

August 1993

The candidate confirms that the work submitted is his own and that appropriate credit
has been given where reference has been made to the work of others.

Abstract

This thesis aims to incorporate geometric and functional design of surfaces using a method known as the PDE method. In particular, it will be demonstrated how the PDE method can be extended to represent an existing marine propeller geometry. Conventionally a propeller surface representation is generated by fitting a B-spline surface through a collection of given propeller blade sections. The PDE method is applied as a boundary-valued problem and consequently it will be demonstrated how a single patch of surface can be used to represent each propeller blade. This is achieved through the parametrisation of the base section of the blade, which can then be altered along the span of the blade. The advantages gained from this technique are firstly that a fair surface is automatically generated, due to the nature of the PDE method. This would not be automatically achieved using a B-spline representation and hence manipulation of the surface would be required. Secondly, the emphasis is on the fact that we can produce a surface representation which is controlled by a small parameter set. This will be fundamental to the final stage of the thesis.

In the second part it will be shown that the PDE generated surface is of a form which makes the hydrodynamic analysis of the propeller feasible using methods referred to as panel methods. In this section the pressure distribution over the propeller surface will be calculated, along with the performance of the propeller, which can be compared with the predicted performance from other techniques.

The compatibility between the panel method and the PDE generated surface, along with the small parameter set lays the foundations for the final part of the thesis in which the propeller performance will be improved by searching through various parameter subspaces. The emphasis will be on improvement of efficiency. However, to maintain feasible geometries, constraints will be included based on the cavitation numbers of propellers, which will ensure that the final propeller design is non-cavitating.

Acknowledgements

I would like to express my gratitude to my supervisors at the University of Leeds, Professor M. I. G. Bloor and Dr M. J. Wilson of the Department of Applied Mathematics for their unlimited help and encouragement during the writing of this thesis. I wish them every success with future projects. I would also like to thank Professor H. Nowacki for useful discussions, and for providing me with the opportunity to use the facilities of the Technische Universitat, Berlin and for further advice at subsequent meetings.

Most importantly, I would like to dedicate this thesis to my mum and dad, Norma and Jim Dekanski for a lifetime of love, support and understanding, and to Jue, for being so special. Thanks also to family and friends for their encouragement and friendship.

I am also grateful to the S.E.R.C. for financial support during my research, and to the British Council for support for the British German Academic Research Collaboration Program. Thanks also to Dr. T. David for introducing me to the DataVisualiser package, on which the pressure distributions over the propeller blades' surfaces are displayed.

Last, but not least, thanks to 'Doc' Chris Graddon for making maths so interesting!

Contents

1	Introduction	1
1.1	Overview of thesis	1
1.2	Overview of CAD/CAM	2
1.3	Computer Aided Design	3
1.4	Surface generation techniques	5
1.4.1	Parametric curve and surface representation	6
1.4.2	Ferguson cubic surface	8
1.4.3	Bézier surfaces	9
1.4.4	B-spline surfaces	10
1.4.5	PDE generated surfaces	11
1.5	Geometric propeller design and manufacture	12
1.5.1	Propeller geometry	12
1.5.2	Fillet design	15
1.5.3	NC machining of propeller blades	16
1.5.4	Blade surface fairness	17
1.6	Approach to hydrodynamic design of propellers	18
1.6.1	Inverse methods	18
1.6.2	Propeller analysis	20
1.6.3	Assumptions made in propeller design	21
1.7	Design of PDE generated blades	22
1.7.1	Applicability to propeller manufacture	23
1.7.2	Accurate propeller representation	25
1.8	Analysis of propeller performance	25
1.9	Improvement of propeller design	26
1.9.1	Shape optimisation	27

1.9.2	Constraints and penalty functions	28
2	The PDE method of design	30
2.1	Introduction	30
2.1.1	Curvilinear coordinates on a parametric surface	30
2.2	The PDE method	31
2.3	Example:A surface blend	33
2.3.1	Tangency conditions	35
2.3.2	Analytic solutions	36
2.4	Effect of parameters	38
2.4.1	Observations	41
2.5	Free form surface design	41
2.5.1	A wine glass	42
2.5.2	Curvature derivatives	43
3	Generic design of propellers	47
3.1	Introduction	47
3.2	Propeller generation	48
3.2.1	Section curve	49
3.2.2	Boundary conditions	52
3.2.3	Parameter control	53
3.2.4	The projected view of the propeller	56
3.3	Numerical solutions to elliptic PDEs	57
3.3.1	Finite difference approximations to derivatives	57
3.3.2	Derivative boundary conditions	60
3.3.3	Solutions of linear equations	61
3.3.4	Successive over relaxation iteration	61
3.3.5	The generated propeller	62
3.4	Fillet design	64
3.4.1	Boundary conditions	65
3.4.2	Results	66
3.5	The functionality of PDE surfaces	68
3.6	Prandtl lifting line theory	68
3.6.1	Results	71

4 Propeller blade representation	74
4.1 Introduction	74
4.1.1 Airfoil sections	74
4.1.2 The mean line	76
4.2 NACA sections	78
4.3 Approximating NACA sections	79
4.3.1 NACA 4-digit wing sections	81
4.3.2 Comparison of 4-digit section with 6-series section	82
4.3.3 Improvement of fit for thickness distribution	84
4.3.4 Results	86
4.4 Fourier analysis of blade section	88
4.5 Generation of blade	90
4.5.1 Skew and rake	91
4.5.2 Derivative conditions	92
4.6 Comparison between propeller geometries	94
4.7 Tip geometry	98
5 Panel method implementation	103
5.1 Introduction	103
5.2 Potential flow theory	104
5.2.1 Green's method of solution	107
5.3 Potential solution using panel methods	107
5.3.1 Panel generation	108
5.3.2 Panel source and doublet distribution	109
5.3.3 Calculation of induced velocities	110
5.3.4 Kutta condition	112
5.3.5 Application of boundary conditions	113
5.3.6 Solution of simultaneous equations	114
5.3.7 The influence of the vortex sheet	115
5.4 Propeller model	115
5.4.1 Number of blades	116
5.4.2 Steady state rotation	116
5.4.3 The trailing wake geometry	117
5.5 Flow calculation for Eckhardt and Morgen propeller	121

5.5.1	Performance of a propeller	122
5.6	Results	124
5.6.1	Loss and gain of performance.	129
6	Automatic optimisation of propeller shape	134
6.1	Introduction	134
6.1.1	Areas of improvement	135
6.2	Cavitation considerations	135
6.2.1	Why reduce cavitation?	136
6.2.2	Cavitation numbers in propeller design	136
6.2.3	Design limitations for non-cavitating propellers	137
6.3	Verification of Eckhardt and Morgen propeller design	139
6.4	Improvement of design	139
6.4.1	Powell's Quadratically Convergent Method	141
6.4.2	Golden Section search	141
6.4.3	Penalty functions	143
6.5	Results	144
6.5.1	Case 1	145
6.5.2	Case 2	149
6.5.3	Case 3	152
6.6	Discussion	153
6.6.1	Case 4	155
6.6.2	Results	155
6.6.3	Case 5	156
7	Conclusion	162
A	The analytic solution for the 6th order PDE	166
A.1	Method of solution	166
B	The induced velocity at a point due to a source and doublet distribution on a plane quadrilateral	168
B.1	Source distribution	168
B.2	The doublet distribution	172
B.3	The vortex sheet	172

C	The derivation of PDE boundary conditions	174
C.1	Introduction	174
C.2	Example 2.3: A surface blend	174
C.3	The Wine Glass	177
C.4	Boundary conditions for the generic blade	179
C.5	The projected view of the propeller	181
C.6	Fillet design	181
C.7	The NACA propeller blade	184

List of Figures

1.1	An example of an ambiguous model designed using wire frame sculpturing.	4
1.2	Two types of surface generated from a non-parametric explicit equation. .	5
1.3	The tangent vector to the parametric curve $\alpha(t)$	6
1.4	The representation and manipulation of a Bézier curve in CAD.	7
1.5	A bicubic surface patch.	8
1.6	A Bézier surface patch and control mesh.	10
1.7	The propeller surface and blade section.	13
1.8	The complete blade geometry of the propeller.	14
1.9	Clamping of the blade fillet onto the hub.	15
1.10	A compound radius fillet.	16
1.11	A PDE generated blade which has been NC-machined.	24
2.1	The surface patch in E^3 mapped to from R^2	31
2.2	The trimlines governing the blend between the cone and sphere.	34
2.3	The surface blend between a sphere and cone.	37
2.4	Smoothing parameter $a = 0.02$	39
2.5	Smoothing parameter $a = 8.0$	39
2.6	Tangent magnitudes increased: $S_{top} = 4.0, S_{bot} = 2.05$	40
2.7	Tangent magnitude has change in sign: $S_{top} = -4.0$	40
2.8	The original wine glass produced using no second derivatives.	45
2.9	The inclusion of curvature derivatives.	45
2.10	The produced wine glass using curvature parameters.	46
2.11	An example of extreme curvature conditions on the surface.	46
3.1	The expanded and projected view of the propeller.	49
3.2	The vortex issued round a sharp corner.	50
3.3	The starting vortex from the Kutta condition.	51

3.4	The profile used for the propeller blade section at the root.	53
3.5	The airscrew blade.	55
3.6	The marine propeller blade.	55
3.7	The boundary value problem.	56
3.8	The finite difference mesh and points.	58
3.9	The finite difference grid.	60
3.10	The generated propeller surface.	63
3.11	The propeller surface mesh.	63
3.12	The variety of hub designs of a propeller.	64
3.13	The fillet geometry.	65
3.14	The generated fillet.	67
3.15	The propeller and fillet.	67
3.16	The representation of a lifting line.	69
3.17	The 'elliptic' wing.	72
3.18	The circulation about the wing.	72
3.19	The 'rectangular' wing.	73
3.20	The circulation about the wing.	73
4.1	The velocity components of the wing section.	76
4.2	The $a=0.8$ mean line and loading.	77
4.3	The NACA wing section.	79
4.4	Comparison of the 4-digit mean line distribution and $a=0.8$ meanline. . .	83
4.5	Comparison of the 4-digit thickness and modified NACA 66 thickness. . .	83
4.6	Comparison of the 4-digit section and NACA section.	84
4.7	The approximation to the modified 66 section.	87
4.8	The new wing section.	87
4.9	Comparison between Fourier series and NACA 4-section.	90
4.10	Illustration of skew.	91
4.11	The distributions for the given data and the PDE generated blade. . . .	95
4.12	The generated propeller.	96
4.13	The assembled blade sections.	97
4.14	Comparison of section profiles.	97
4.15	Curve fitting through maximum thickness at tip.	98
4.16	The discontinuity at the tip between $r = 0.995R$ and $r = R$	100

4.17	The continuous tip profile between $r = 0.995R$ and $r = R$ for $S_{top} = 0$	100
4.18	Approximations to the distributions for a smooth tip geometry.	101
4.19	The PDE generated propeller with continuity imposed at the tip.	102
4.20	An example of a skew propeller generated from the PDE method.	102
5.1	Distribution of panels over wing.	111
5.2	Trailing wake geometry.	113
5.3	Velocity components represented by lifting lines.	118
5.4	The propeller and trailing wake.	120
5.5	Forces on an Airfoil Section	122
5.6	Comparison of coefficients of lift across the span of the blades.	125
5.7	Pressure distribution around blade at approximately $x=0.7$	126
5.8	Velocity distribution around blade at approximately $r=0.7$	127
5.9	The pressure distribution over the surface of the propeller.	128
5.10	Pitch angle curves of Eckhardt and Morgen design procedure.	129
5.11	Comparison of coefficients of lift across the blade.	131
5.12	Pressure distribution on blade at approximately $r = 0.7$	132
5.13	The pressure distribution over the surface of the original propeller.	132
6.1	The bracketting of a function $f(x)$	141
6.2	A bracket produced by the penalty function p_1	144
6.3	Geometric distributions for optimisation case 1	147
6.4	Coefficients of lift for case 1.	148
6.5	Pressure distribution at $r = 0.7$ for case 1.	148
6.6	Coefficients of lift for case 2.	150
6.7	Geometric distributions for optimisation case 2	151
6.8	Pressure distribution at $r = 0.7$ for case 2.	152
6.9	Geometric distributions for optimisation case 3	154
6.10	Coefficients of lift for case 5.	157
6.11	Pressure distribution at $r = 0.7$ for case 5.	157
6.12	Geometric distributions for optimisation case 5	158
6.13	Surface pressure distribution for case 1.	160
6.14	Surface pressure distribution for case 2.	160
6.15	Surface pressure distribution for case 3.	161
6.16	Surface pressure distribution for case 5.	161

B.1	A planar panel lying in the element coordinate system	169
B.2	The contribution from a line vortex	172
B.3	Evaluation of the vortex sheet velocity component	173
C.1	The trimline on the hub	182
C.2	The isolines on the hub	183

List of Tables

2.1	Effect of parameters on surface blend.	38
2.2	Parameter values for the original and modified wine glass.	44
2.3	Parameter values for the final wine glass and 'standard lamp'.	44
3.1	Parameter values for the two propeller blades.	54
3.2	Residuals for the SOR iteration.	62
3.3	Parameters of the fillet.	66
3.4	Residuals for the SOR process for the PDE generated fillet.	66
4.1	x_l/l =non-dimensional distance along section from nose, y =ordinate of section measured perpendicular to mean line, m_x =maximum ordinate of mean line, m =ordinate of mean line t_x =maximum thickness of Section.	80
4.2	Values of the variables for the NACA 4-series thickness distribution.	86
4.3	Parameter values for the PDE generated surface.	96
4.4	Parameter values for the PDE generated surface.	99
5.1	Comparison between lifting method of Eckhardt and Morgen and panel method	124
5.2	Output for propeller operating with alternative pitch distribution.	130
5.3	Propeller performance for a variety of parameter changes.	133
6.1	Complete data for the Eckhardt and Morgen propeller	140
6.2	Parameter values for case 1	145
6.3	Output for optimised propeller	146
6.4	Parameter values for case 2	149
6.5	Output for optimised propeller	149
6.6	Parameter values for case 3	152
6.7	Output for optimised propeller	153

6.8 Performance of altered propeller.	156
6.9 Parameter values for case 5	156
6.10 Output for optimised propeller	159

Nomenclature

Chapter 1

$y = f(x)$	-	explicit equation of curve
$\underline{\alpha}(t) = (\alpha_1, \alpha_2, \alpha_3)$	-	parametric equation of curve
t	-	scalar parameter of curve
$\alpha_1, \alpha_2, \alpha_3$	-	coordinates of curve in E^3
$\underline{\alpha}'(t)$	-	tangent vector to curve
Δt	-	small increment along curve $\underline{\alpha}(t)$
$\underline{\alpha}''(t)$	-	curvature vector of curve
$\underline{a}_i \quad i = 0, \dots, n$	-	control points of curve
$g_k(t) \quad k = 0, 1, 2, 3$	-	Bernstein basis function
$f(x, y, z) = 0$	-	implicit equation of surface patch
x, y, z	-	coordinates of surface in E^3
$\underline{X}(u, v) = (x(u, v), y(u, v), z(u, v))$	-	parametric surface patch
u, v	-	independent variables of surface
$x(u, v), y(u, v), z(u, v)$	-	dependent variables of surface
$\underline{X}_u, \underline{X}_v$	-	first derivatives on surface
$\underline{X}_{uu}, \underline{X}_{vv}$	-	second derivatives on surface
\underline{a}_{ij}	-	control points of surface
i, j	-	subscripts
C^0, C^1, C^2	-	degree of continuity between surface patches
$\underline{T}_0 = (t_0, t_1, \dots, t_m)$	-	knot vector of B-spline curve
$N_{i,p}(t)$	-	normalised B-spline of degree p
$D_{u,v}^m ()$	-	partial differential operator of degree m
$\underline{f}(u, v)$	-	forcing term of surface
D	-	diameter of propeller
$R = D/2$	-	radius of propeller
P_S	-	shaft horse power
n	-	revs per second
r	-	radius at specific blade section

Nomenclature

r_h	-	radius of hub
$x = r/R$	-	non-dimensional marker along blade span
c	-	chord length of blade section
x	-	non-dimensional marker along chord section
m_x	-	maximum camber of blade section
p	-	position of maximum camber along chord
t_x	-	maximum thickness of blade section
ϕ	-	pitch angle of section
P	-	pitch of blade section
κ	-	Gaussian curvature
$\kappa_{min}, \kappa_{max}$	-	principal curvatures of surface

Chapter 2

Ω	-	domain of surface patch in R^2
u_0, v_0	-	isolines on surface
$\delta\Omega$	-	boundary of domain
$\partial/\partial n$	-	partial derivative in direction of normal
G	-	Green's identity
a	-	smoothing parameter for PDE surface
$u = u_0, u = u_1$	-	trimlines of blend surface
$\underline{X}_u(u, v), \underline{X}_v(u, v)$	-	coordinate vectors for surface
\underline{N}	-	unit normal to surface patch
\underline{t}	-	tangent to surface
$\underline{A}_0(u), \underline{A}_n(u), \underline{B}_n(u)$	-	Fourier polynomials for analytic PDE surface
$\underline{a}_{00}, \dots, \underline{a}_{05},$ $\underline{a}_{n1}, \dots, \underline{a}_{n6}$	-	vector-valued coefficients for PDE surface

Nomenclature

Design parameters for surface blend

R_s	-	radius of sphere
R_c	-	base radius of cone
h_c	-	height of cone
R_{top}	-	radius of trimline on sphere
R_{bot}	-	radius of trimline on cone
d_1	-	height of trimline on sphere
d_2	-	height of trimline on cone
h	-	$d_1 - d_2$
S_{top}	-	derivative parameter on sphere
S_{bot}	-	derivative parameter on cone
a	-	smoothing parameter

Design parameters for wine glass

R_{top}	-	radius of rim
R_{bot}	-	radius of base
d	-	height of glass
S_t	-	radial first derivative at rim
S_b	-	radial first derivative at base
S_{top}	-	z first derivative at rim
S_{bot}	-	z first derivative at base
C_t	-	radial second derivative at rim
C_b	-	radial second derivative at base
C_{top}	-	z second derivative at rim
C_{bot}	-	z second derivative at base

Nomenclature

Chapter 3

h, k	-	discretised length in u, v direction of Ω
p, q	-	number of mesh points in u, v directions
\underline{X}_p	-	value of surface at $X(ih, jk)$
$\tau = ah/k$	-	parameter of finite difference scheme
A, b	-	matrices associated with finite difference scheme
\underline{x}	-	matrix of unknowns (surface coords)
$a_{i,j}$	-	i, j^{th} position of matrix A
$P_{i,j}$	-	mesh points
$x_i^{(n)}$	-	n^{th} approximation to x_i in iterative scheme
$g(v)$	-	derivative condition on $\delta\Omega$
g_i	-	discretised form of $g(v)$
ω	-	relaxation factor/acceleration parameter
R_i	-	residual of difference scheme
y	-	span station of wing
$\alpha_e(y)$	-	effective incidence of wing
ϵ	-	downwash angle of wing
$\omega(y)$	-	downwash velocity of wing
$\Gamma(y)$	-	bound vorticity
$\alpha(y)$	-	geometric angle of wing section
C_l	-	coefficient of lift
a_∞	-	lift curve slope
V	-	forward speed of wing
θ	-	parameter along wing
d	-	span of wing
ρ	-	density of air
$\mu = a_\infty c/8d$	-	parameter of monoplane equation

Nomenclature

Design parameters for generic blade

f	-	position of tip
d	-	length of blade
c	-	length of section
t_x	-	maximum thickness of section
β	-	twist of blade
r_h	-	radius of central hub
m_x	-	maximum camber of section
S_x, E_x	-	x first derivatives
S_y, E_y	-	y first derivatives
S_{top}, S_{bot}	-	z first derivatives

Design parameters for fillet

R_{bot}	-	radius of trimline on hub
R_C	-	radius of hub
S_{cyl}	-	parameter governing radial rate of change of u isolines
g	-	length of fillet
$c, \beta, t_x, m_x, E_x, E_y$	-	as in generic blade

Chapter 4

C_P	-	coefficient of pressure
v/V_∞	-	velocity component of section thickness
$\Delta v/V_\infty$	-	velocity component of mean line
$\Delta v_a/V_\infty$	-	velocity of thickness at attack angle
V_r/V_∞	-	resultant velocity
P_R	-	local load coefficient
a	-	non-dimensional loading coefficient
C_{Li}	-	ideal lift coefficient
α_i	-	angle of ideal lift

Nomenclature

y_c	-	camber distribution
$\tan \theta$	-	slope of mean line
y_t	-	thickness distribution
X_U, Y_U	-	ordinates of upper side of section
X_L, Y_L	-	ordinates of lower side of section

Design parameters for actual propeller

$X_f(v)$	-	fourier series for chordwise marker x
$Y_{cf}(v)$	-	fourier series for camber y_c
$Y_{stf}(v)$	-	fourier series for $y_t \sin \theta$
$Y_{ctf}(v)$	-	fourier series for $y_t \cos \theta$
ϵ_x, ϵ_y	-	scaling factor at tip
f	-	skew parameter
g	-	rake parameter
D	-	diameter
c	-	chordlength of base section
m_x	-	maximum camber of base section
t_x	-	maximum thickness of base section
S_{top}	-	1 st derivative in z at tip
S_{bot}	-	1 st derivative in z at base
S_{xu}, S_{xl}	-	1 st derivative for chordlength
S_{tu}, S_{tl}	-	1 st derivative for thickness
S_{cu}, S_{cl}	-	1 st derivative for camber
C_{xu}, C_{xl}	-	2 nd derivative for chordlength
C_{tu}, C_{tl}	-	2 nd derivative for thickness
C_{cu}, C_{cl}	-	2 nd derivative for camber

Nomenclature

Chapter 5

$\underline{\omega}$	-	vorticity
\underline{V}	-	fluid velocity
p	-	pressure
\underline{v}	-	disturbance velocity
ϕ	-	scalar potential
\underline{V}_∞	-	onset flow
V_∞	-	ship advance speed
\underline{V}_{in}	-	incoming flow
ω	-	angular velocity
ρ	-	density of water
σ_j	-	source strength on panel j
μ_j	-	doublet strength on panel j
$r(P, q)$	-	distance between point P and point q
\underline{n}_i	-	normal to surface on panel i
\underline{c}_i	-	centroid of panel i
\underline{V}_i	-	velocity at point i
\underline{V}_{sij}	-	induced velocity on panel i from panel j source distribution
\underline{V}_{dij}	-	induced velocity on panel i from panel j doublet distribution
\underline{V}_u	-	velocity on upper surface
\underline{V}_l	-	velocity on lower surface
\underline{V}_m	-	average velocity at trailing edge
A, B	-	influence matrices
A_{ij}, B_{ij}	-	components of influence matrices
N	-	number of panels
Z	-	number of blades
\underline{V}_l	-	velocity component from vortex sheet
\underline{v}_r	-	angular velocity
\underline{N}_0	-	origin of pivot

Nomenclature

r_{ci}	-	vector from pivot to centroid i
u	-	induced velocity of section
u_a	-	axial velocity of section
u_t	-	tangential velocity of section
β	-	advance angle of section
β_i	-	hydrodynamic pitch angle
ϕ	-	pitch of section
P_i	-	pitch of moderately loaded propeller
λ	-	advance coefficient
C_{Pu}	-	pressure on upper side of blade
C_{Pl}	-	pressure on lower side of blade
C_D	-	coefficient of drag
L	-	lift of section
T	-	thrust of propeller
C_T	-	coefficient of thrust
Q	-	torque of propeller
C_Q	-	coefficient of torque
P	-	power of propeller
C_P	-	coefficient of power
η	-	efficiency of propeller
A_0	-	propeller disc area

Chapter 6

p_{min}	-	minimum pressure on blade surface
$\frac{\Delta p_{max}}{q}$	-	point of minimum pressure
q	-	dynamic pressure
p_0	-	atmospheric pressure
p_v	-	vapour pressure
σ_0	-	propeller cavitation number
σ_x	-	local section cavitation number

Nomenclature

g	-	acceleration due to gravity
h	-	depth of immersion of centreline of propeller
A_e/A_0	-	blade area ratio
C_1, C_2	-	wing section coefficients
S	-	safety margin against cavitation
$f(x_1, \dots, x_n)$	-	function to be optimised
(a, b)	-	interval for bracketting a function $f(x)$
u_1, \dots, u_n	-	basis functions
P_0, \dots, P_n	-	vector of optimised functions
p_1, \dots, p_n	-	penalty functions
c_1, \dots, c_n	-	cost functions
h_1, \dots, h_n	-	difference functions
t	-	maximum dimension of panel
I_{00}, I_{20}	-	moments of panel
$\underline{x}_1, \underline{x}_2, \underline{x}_3, \underline{x}_4$	-	corners of panel in ref coords
$\zeta_1, \zeta_2, \zeta_3, \zeta_4$	-	corners of panels in local coords
$\eta_1, \eta_2, \eta_3, \eta_4$	-	corners of panels in local coords

Chapter 1

Introduction

1.1 Overview of thesis

The aim of this thesis is to incorporate geometric and functional design using a method devised by Bloor and Wilson [1], known as the PDE method. By this it is meant that the geometry of a particular surface is generated. Then, using this PDE surface we are able to evaluate some objective function, such as the thrust of a propeller, and alter the surface by manipulation of the control parameters of the PDE method such that the objective function adheres to some given requirement. The particular example under consideration in this thesis is that of applying the PDE method to the generation of a marine propeller. Using a conventional CAD system, a marine propeller can be represented as a set of section curves along each blade. A surface is formed by generating a B-spline or Bézier surface [2] which approximates these sections at all points; these in turn can be manipulated by a control mesh [2] to alter the blade geometry. In the first section of this thesis, the aim is to show that the PDE method can also be applied to the generation of a marine propeller, and that the generated surface can be manipulated so as to represent existing propeller geometries, which will be used in the second part of the thesis as the starting point for functional design.

The PDE method generates the propeller by manipulation of the boundary conditions of a surface patch, which implies that a much smaller parameter set is needed to produce a blade than that required to generate the B-spline control mesh. This, as will be shown in the second part of the thesis, is an important property where the hydrodynamic design and evaluation of the propeller performance are considered.

If a computer representation of an object's geometry is generated, then its physical

properties can be simulated using some physical model on the computer - in this case the performance and flow properties of the propeller. There are a variety of techniques which can be used for this purpose such as lifting surface methods [3], and boundary element methods which are commonly referred to as panel methods [4]. In the second part of this thesis it will be demonstrated that the PDE generated surface is in a form from which the flow characteristics of the propeller can conveniently be determined using a panel method. These characteristics will include the pressure distributions over the surface and the generated thrust and efficiency of the complete propeller. The evaluation of these characteristics is a necessary task where propeller blade geometries are initially represented as computer models, since water basin testing [5] cannot be carried out without expensive model building, implying that a mathematical formulation must be implemented if the characteristics of the propeller are to be determined cheaply.

In the last section of the thesis it will be demonstrated how the design of the propeller can be altered to improve the efficiency of the generated propeller. This will be done whilst adhering to specific constraints on the surface - the main one being that cavitation does not occur on the blade's surface. This is necessary as cavitation is a phenomenon which frequently causes problems on propellers [6]. For instance, it can produce vibrations around the propeller which cause noise and a loss in efficiency, or even cause structural damage to the blades due to the pressure build up on their surfaces [6].

Therefore, by optimisation of the PDE control parameter set, an improved propeller geometry will be determined which has a greater efficiency while keeping within the restrictions caused by cavitation. Thus, if we wish to produce realistic results it is necessary for us to have an appropriate starting geometry for the optimisation, and it is the PDE generated propeller which we will use in this instance.

Firstly, a brief overview of various aspects of computer aided design and how they relate to the problem in hand will be given.

1.2 Overview of CAD/CAM

In what follows we will discuss various aspects of Computer Aided Design (CAD) and Computer Aided Manufacture (CAM). In particular we will deal broadly with the variety of techniques which have been developed for surface representation to illustrate how they differ from the design approach of the PDE method. The areas considered will be specifically within the confines of the design and representation of propeller blades,

and will include topics such as surface blade representation, fillet design [7] and automatic manufacture [8].

Secondly, we will discuss the different computer models used to evaluate the physical properties of the propeller, and used to design a propeller with given requirements. It will further be demonstrated how the surface generation method used throughout this thesis is applicable to all of the above aspects of propeller design.

1.3 Computer Aided Design

CAD can be used to assist designers to create and visualise models. The assistance provided can range from providing a draughting system for producing scale diagrams of machinery, to obtaining the solutions of problems such as how to make the best use of a given floor space in order to meet known specifications, such as the size and number of machines intended to occupy the area.

Over the last 30 years the influence of computers on all aspects of geometric design has developed to a great extent. With the knowledge accumulated, many facets of geometric modelling have been much enhanced, thus benefiting a designer in regard of savings in time, labour, materials and cost. As a result of this, a greater reliance has been placed on computers for the manipulation and visualisation of models, which previously would have had to be built in order to consider their feasibility.

Prior to the introduction of the CAD environment the draughtsman would provide the link between the design of an object and its production. Measurements would be taken from a 2 dimensional surface (the paper) so that a prototype could be manufactured. Any deficiencies in the performance of the component would only come to light when the complete object were tested. Then, if alterations were needed on the object, a new design would have to be produced. For an example of exactly how objects were manufactured prior to the advent of surface representation, specifically the development of the Bézier curve and surface, the reader is referred to the article of Bézier [9], in which the process used to manufacture car bodies at Renault is described.

Of course, as designers became more experienced in their particular field, their intuitive estimates as to the likely correctness of a new design could be incorporated and many problems could be avoided from an early stage; however as no two problems ever have exactly the same difficulties, modifications were still required.

With the introduction of geometric modelling and design many of the problems of

having to redraw models ceased. The initial design could be described with the likes of 'turnkey' (packaged hardware-software) [8] design systems, such as CAM-X, DUCT which evolved throughout the 1970s. Many of the advantages of computerised draughting systems over old techniques lay in the speed of preparing a drawing; for although a completely new design took almost the same time to prepare, complicated regions could be drawn more easily by enlarging regions of the screen and, secondly, where identical components or small variations are required, there is a great advantage in time and speed using these systems.

Much of the designer's activities then consisted of manipulation to inspect the design and alterations to add new information, or to correct discrepancies between plans and actuality. Draughting systems were improved with the inclusion of simultaneous orthogonal views on-screen; however, for the design of car panels and ship hulls, geometric modelling was needed to view the object in perspective, rather than as a line drawing representation on the screen.

Some of the early visualisation representations proved far from infallible, as ambiguity often occurred in some perspective views, as can be seen from figure (1.1), in which it is difficult to decide in which direction the model is facing. This is due to there being no obvious way to represent depth in the figure.

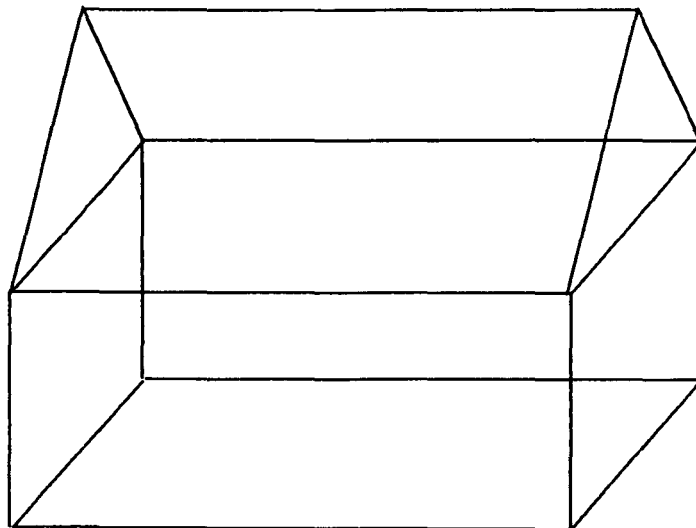


Figure 1.1: An example of an ambiguous model designed using wire frame sculpturing.

However, with the inclusion of hidden line removal, the models could be viewed unambiguously, while research and development of surface polygon rendering enabled the complete visualisation of objects to be realised, with features such as light sources giving a real feel to the object. This leads to the present in which complex surface models can

readily be manipulated and visualised on powerful workstations.

1.4 Surface generation techniques

In general, a surface in 3 dimensions can be thought of as being a patch with boundaries defined by a set of curves. Such surface patches can be thought of as the simplest ‘building blocks’ from which more elaborate surfaces can be constructed by the union of these patches, with requirements such as geometric continuity between adjacent patches [10].

There are many examples of mathematical equations which represent surfaces. These include the equation

$$f(x, y, z) = 0 \quad (1.1)$$

which is the implicit equation of a surface. If linear, such as $ax + by + cz = 0$, this defines a plane, whereas when of second order a quadric surface will be defined, such as $x^2 + y^2 + z^2 - r^2 = 0$ which describes the surface of a sphere. Alternatively, the equation

$$y = f(x) \quad (1.2)$$

is an explicit non-parametric function which defines a curve in R^2 . From curves such as this surfaces can be derived, either by sweeping out the curve as in figure (1.2a) where the curve $y = f(x)$ is swept out along the z -axis, or by rotating the curve to give a surface of revolution [11], as in figure (1.2b) which illustrates the equation $y = f(x)$ rotated about the y axis.

Thus many surfaces can be represented by implicit or explicit functions. However, there are limitations to their ability to represent an easily deformable surface, which is

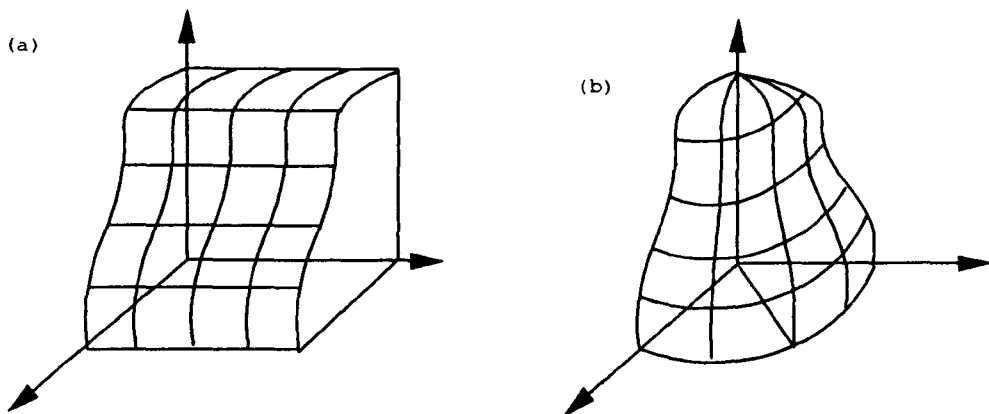


Figure 1.2: Two types of surface generated from a non-parametric explicit equation.

our prime aim when working within a modelling environment. If we wished to model a car body for instance, could an implicit equation be easily found to describe such a surface?

This is where parametric surface representation becomes very important as most surfaces generated from this class of technique are easy to manipulate.

1.4.1 Parametric curve and surface representation

A familiar way of representing a curve in CAD is in terms of a single scalar parameter. If the curve given by $\underline{\alpha}(t) = (\alpha_1(t), \alpha_2(t), \alpha_3(t))$ is considered, then for different values of the scalar parameter t , $\underline{\alpha}(t)$ will represent different points lying on the curve. Furthermore, once a parameterisation for a curve has been found, geometrical properties of the curve can be evaluated, such as its smoothness, which is of prime importance in areas such as hull form design for large ships, where a ‘fair’ set of curves are one of the most important requirements [12].

For a curve to be smooth, the parameterisation must be such that at all points, the derivatives $d\alpha_1/dt$, $d\alpha_2/dt$ and $d\alpha_3/dt$ exist. If the curve is smooth, other geometric properties of the curve can be determined, such as its velocity vector, or tangent vector and the curvature [11]. The velocity vector is given by

$$\underline{\alpha}'(t) = \left(\frac{d\alpha_1}{dt}, \frac{d\alpha_2}{dt}, \frac{d\alpha_3}{dt} \right) \quad (1.3)$$

and can be interpreted geometrically as

$$\underline{\alpha}'(t) = \frac{d\underline{\alpha}}{dt} = \lim_{\Delta t \rightarrow 0} \left(\frac{\underline{\alpha}(t + \Delta t) - \underline{\alpha}(t)}{\Delta t} \right) \quad (1.4)$$

which implies that as $\Delta t \rightarrow 0$ the vector $\underline{\alpha}(t + \Delta t) - \underline{\alpha}(t)$ becomes tangent to the curve at the point $\underline{\alpha}(t)$, as in figure (1.3).

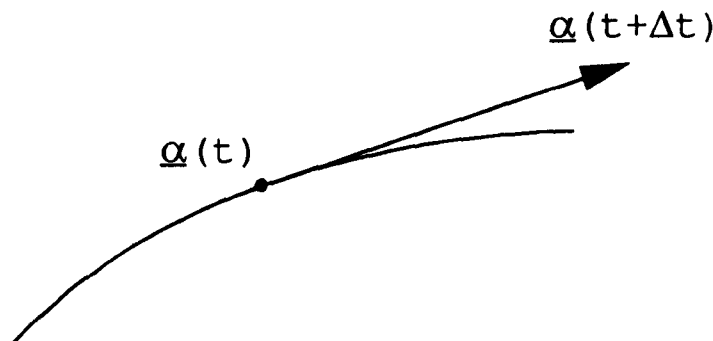


Figure 1.3: The tangent vector to the parametric curve $\underline{\alpha}(t)$.

The concept of a tangent vector is often used to ensure continuity is maintained between adjacent patches of surface.

The vector $\underline{\alpha}''(t)$ gives a measure of how rapidly the curve pulls away from the tangent line at $\underline{\alpha}(t)$. This is also an important property of curves, since this can be used to give a measure of the fairness [12]. Thus, by observing the curvature distribution, the curve (or surface) can be manipulated to be as smooth as possible.

In CAD the functions most often used to define parametric curves are polynomials such as

$$\underline{\alpha}(t) = (1-t)^3 \underline{a}_0 + 3t(1-t)^2 \underline{a}_1 + 3t^2(1-t) \underline{a}_2 + t^3 \underline{a}_3 \quad (1.5)$$

where the parameter range is conventionally $0 \leq t \leq 1$ and where $\underline{a}_0, \underline{a}_1, \underline{a}_2, \underline{a}_3$ are vector constants commonly referred to as the control points of the curve [13]. The above equation is in fact the definition of a Bézier cubic curve, which was introduced into the field of curve and surface design by Pierre Bézier in the late 1960s [14]. The functions $(1-t)^3$ etc are given more generally by

$$g_k(t) = \frac{3!}{k!(3-k)!} t^k (1-t)^{3-k} \quad k = 0, 1, 2, 3 \quad (1.6)$$

and are cubic Bernstein basis functions [15]. By taking t over the range $0 \leq t \leq 1$ it can be seen that the Bézier curve produced is an approximation to the control polygon as illustrated in figure (1.4a). This follows from the work of Weierstrass [16] who proved that any continuous univariate function can be approximated by polynomials up to any given tolerance.



Figure 1.4: The representation and manipulation of a Bézier curve in CAD.

Furthermore, the velocity vector of this curve is given by

$$\underline{\alpha}'(t) = 3(1-t)^2(\underline{a}_1 - \underline{a}_0) + 6t(1-t)(\underline{a}_2 - \underline{a}_1) + 3t^2(\underline{a}_3 - \underline{a}_2) \quad (1.7)$$

from which it can be seen that at $t = 0$, $\underline{\alpha}'(t) = 3(\underline{a}_1 - \underline{a}_0)$, which is parallel to $(\underline{a}_1 - \underline{a}_0)$, and at $t = 1$, $\underline{\alpha}'(t) = 3(\underline{a}_3 - \underline{a}_2)$ which is parallel to $(\underline{a}_3 - \underline{a}_2)$.

Therefore, it can be seen that by moving the control points \underline{a}_1 and \underline{a}_2 the shape of the curve is altered, as the tangent direction at the end points are changed as in figure (1.4b).

By extending the concept of curve parameterisation, a surface can be defined. The most common form of a parametric surface patch is the four sided patch [17]. This is generated by taking polynomial functions similar to the form given in equation (1.5) in two independent variables u and v , which are defined over some real valued domain. The surface patch is then defined by the vector-valued function $\underline{X}(u, v) = (x(u, v), y(u, v), z(u, v))$.

1.4.2 Ferguson cubic surface

One of the earliest examples of a polynomial surface patch was given by the Ferguson cubic surface patch [17]

$$\underline{X}(u, v) = \sum_{i=0}^3 \sum_{j=0}^3 \underline{a}_{ij} u^i v^j \quad (1.8)$$

for $0 \leq u, v \leq 1$ and where \underline{a}_{ij} represent the control points of the surface. The surface patch is defined by imposing the positional $\underline{X}(u, v)$ and tangential vectors $(\underline{X}_u, \underline{X}_v)$ at the corners of the patch as in figure (1.5). From this the values of the control points

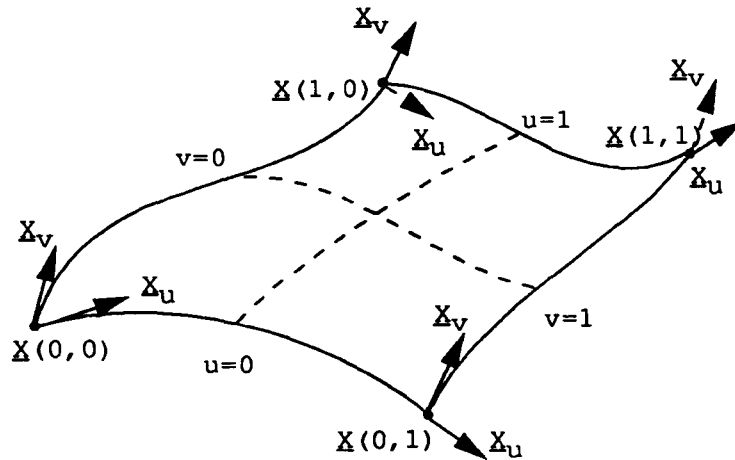


Figure 1.5: A bicubic surface patch.

\underline{a}_{ij} can be determined. The Ferguson patch also has the property that there is sufficient flexibility to ensure C^1 (or tangent) continuity across its boundary. This means that when connected to other similar patches, not only will there be C^0 continuity, i.e. the curves at the boundaries of adjacent patches will be coincident, but there will be tangent plane continuity between the two patches which is necessary to ensure that a smooth surfaces is generated.

The Ferguson (F-) patch is one example of a set of bicubic patches defined as above in equation (1.8). As can be seen above, 16 sets of control vectors \underline{a}_{ij} need to be evaluated to define the surface - 12 of these are obtained from the positional and tangential conditions at the corners of the patch, with the F-patch having the additional property that at the corners of the patch, the vectors $\underline{X}_{uv}, \underline{X}_{vu}$ are set to zero. By some authors, these are referred to as the 'twist vectors' of the patch and can be thought of as how the patch twists from one corner to the next [18]. The F-patch is a special case of the generated bicubic patch as it has these twist vectors set to zero, whereas the more general bicubic patch can have these vectors set to non-zero values.

1.4.3 Bézier surfaces

Some of the next work implemented in surface design was provided by Pierre Bézier [14] in conjunction with the Renault car company. To design a car prior to the advent of computer modelling, a stylist would look at a sketch to see whether a full scale representation would be satisfactory, and would redraw it by hand if not adequate. Then, when satisfactory, a master template would be produced as the standard for the production of the car with which to compare machined parts. The machined part would then be compared to the master template and kept if it looked satisfactory, otherwise it would be discarded [9]. With the Bézier surface a three dimensional model of the car could be generated. This could be manipulated using the control points of the surface in the same manner as the Bézier curve to produce a satisfactory design. When completed, this could easily be split into separate surface patches, which correspond to the panels of the car body. It is then straightforward to determine the machine path for these patches which could in turn be machined.

The surface patches devised by Bézier were defined by

$$\underline{X}(u, v) = \sum_{i=0}^3 \sum_{j=0}^3 \underline{a}_{ij} g_i(u) g_j(v) \quad (1.9)$$

where $g_i(u), g_j(v)$ are as given by equation (1.6) and the Bézier surface is manipulated by a control net in much the same manner as the Bézier curves in section (1.4.1).

The Bézier surface patch is closely related to the Ferguson surface as illustrated by Faux and Pratt [17], since the Bézier curves which define the surface are simply a reformulation of the Ferguson curves. However, the reformulation means that no tangent vectors need to be specified as with the Ferguson patch. Figure (1.6) illustrates how the Bézier curves are combined to generate a control net and produce one such surface patch.

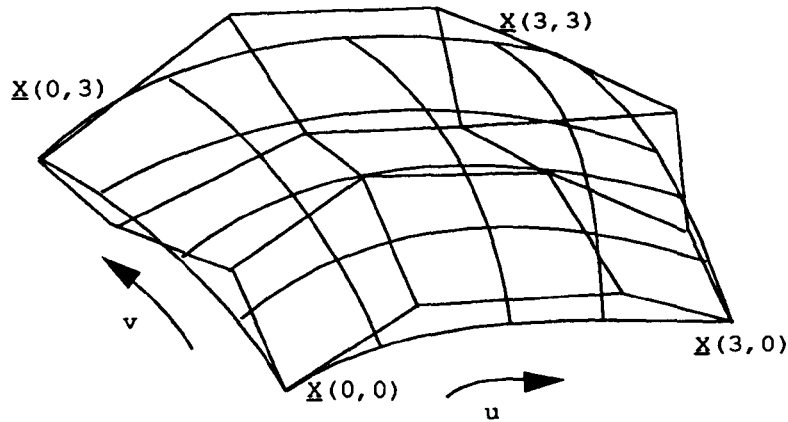


Figure 1.6: A Bézier surface patch and control mesh.

To allow more control of the surface, and to permit higher orders of continuity across the patch boundary (such as C^2 curvature continuity) than just tangential continuity, it is possible to increase the number of control points. However this means that a higher order Bernstein function is required as described in [17].

With the Bézier surface, the designer has an intuitive feel of the way in which the surface can be altered by simply creating the control polygon and, by manipulation of the net, can alter the approximating surface. This provides some explanation as to why the Bézier surfaces are successfully used in the car industry [19].

1.4.4 B-spline surfaces

Among the most recent of curve and surface representations to be devised are those of B-spline curves and surfaces, which were introduced into curve and surface design in the 1970s by W. Gordon and R. Riesenfeld [20].

To define the B-splines, we proceed as follows. If $t_i \leq t_{i+1}$ are real numbers and

$$N_{i,0}(t) = \begin{cases} 1 & \text{if } t_i \leq t < t_{i+1}, t_i < t_{i+1} \\ 0 & \text{otherwise} \end{cases} \quad (1.10)$$

$$N_{i,p}(t) = \frac{t - t_i}{t_{i+p} - t_i} N_{i,p-1}(t) + \frac{t_{i+p+1} - t}{t_{i+p+1} - t_{i+1}} N_{i+1,p-1}(t) \quad (1.11)$$

is called a normalised B-spline of degree p [13], with the knot vector being defined as $\underline{T} = (t_0, t_1, \dots, t_m)$. In CAD two main types of knots are used; uniform (with equally spaced knots) and non-uniform [13]. Furthermore, if the first and last knots are repeated $p + 1$ times then the knot vector is non-uniform and non-periodic [13].

Bézier curves and surfaces can be viewed as a special case of the B-spline curves and surfaces [13]. These B-splines are geometrically similar to the splines originally used by draughtsmen which were used to approximate a set of points by a curve which had the minimum energy in it [10].

The B-spline surface is defined by

$$\underline{X}(u, v) = \sum_{i=0}^m \sum_{j=0}^n \underline{a}_{ij} N_{i,p}(u) N_{j,q}(v) \quad (1.12)$$

where the main difference between B-spline and Bézier surfaces is that for the case of Bézier surfaces the control polygon uniquely defines the surface, whereas B-spline surfaces require the knot vector in addition to the control net. B-spline surfaces also have the important property of knot insertion [21]. By including more knots the control polygon will converge to the curve and so the approximation to the curve is improved. Additionally, since the basis functions are non-zero over only finite regions, local control of the surface is available to the designer. Therefore, by adding more knots, the designer can easily limit the region of the surface affected by a control point modification.

1.4.5 PDE generated surfaces

The method for surface generation used in this thesis is described as the PDE method and was devised by Bloor and Wilson originally as a means of producing C^1 continuous bridging surfaces or surface blends between two or more primary surfaces [22]. The method is based on the idea that the surface can be generated by regarding it as the solution to a suitably posed boundary value problem in some (u, v) parameter space; in particular, as the solution to a suitably chosen elliptic partial differential equation

$$D_{u,v}^m(\underline{X}) = \underline{f}(u, v), \quad (1.13)$$

where the boundary conditions are such that the surface blend has edges coincident with some arbitrary curves on the primary surface. These edges are commonly known as the trimlines of the blend, and for a blend the surface is tangent plane continuous across these trimlines.

Extending the method from the design of blend surfaces, it was illustrated how, by relaxing the continuity conditions on the boundaries, the design of free-form surfaces could be achieved. Examples of such surfaces include those of a yacht hull and a telephone handset [23]. The method has the virtue of describing a complex surface in terms of a relatively small set of parameters which are derived from the boundary conditions.

Secondly, a global manipulation of the surface is possible within the approach, which is useful when dealing with geometries on a large scale, such as those of marine propellers and ship hulls. Surface manipulation on a large scale is easier than with B-spline surfaces where movement of many control points is required to facilitate changes on the surface.

Finally, due to the fact that B-splines are part of the data exchange standards within many packages, work has been carried out by Brown [24] on the aspects of B-spline representation of PDE surfaces, and conversely of PDE representation of given B-spline surfaces. This is achieved by methods such as collocation [25] and in particular, weighted residual methods, such as that described by Galerkin's method [25]. This enables a local manipulation of surfaces originally generated by a PDE by consideration of their B-spline representation and is an added feature of the PDE method.

1.5 Geometric propeller design and manufacture

In this section we discuss the existing ways in which propeller blades are created, from the initial design of the geometry to the final manufacture of the realised blade.

1.5.1 Propeller geometry

Marine propellers comprise several parts - the propeller blades, the central hub through which the blades are attached to the vessel, and the fillet which attaches the blades to the hub [26]. The propeller blade has two main hydrodynamic surfaces. The surface of the blade which faces aft and is referred to as the face or suction side, and the surface which faces forward which is referred to as the back or pressure side. The tip of the blade joins the leading edge of the propeller to the trailing edge where the face and back intersect, which occurs at the maximum radius from the centre of the hub to which the blade is attached. If the radius of the propeller blade is given by R , then the propeller diameter will be defined as $D = 2R$.

Frequently, one of the first criterion in designing a propeller is the determination of the optimum diameter [27]. This should either be designed to give a tip clearance alongside the hull of the vessel, or be determined from an estimation of the power and characteristics of the propelling machinery, according to Saunders [28]. The optimum diameter can be decided upon by a calculation based on a Troost series [29], by taking

$$D = \frac{15.24(P_s)^{0.2}}{(n)^{0.6}} \quad (1.14)$$

where D is the diameter in metres, P_s the shaft horse power, and n the number of revolutions per second. This is then reduced by 3% to obtain the optimum behind diameter with clearance, as described in Eckhardt and Morgen [27]. A non-dimensionalised constant x is defined along the length, or span of the blade such that $r_h/R \leq x \leq 1$ where $x = r/R$, r is the radius at some blade section along the span, and r_h is the radius of the hub. From this the radius of the hub is taken to lie within the range $0.15R \leq r_h \leq 0.25R$.

Propeller blade geometry is most often supplied as two dimensional data in the form of wing (or blade) sections located at evenly spaced intervals along the blade span [26]. These wing sections are chosen to give the required hydrodynamic performance of the propeller, and are typically one of the families of NACA sections [30]. In many propeller designs the wing section is chosen to have the same basic shape along the span of the blade, and the variation in geometry comes from the length of the wing section, known as the chord length, c , the maximum thickness of the section, t_x and the maximum camber of the wing section, m_x . These properties are illustrated in figure (1.7), where a marine propeller blade section is shown. For a complete geometric description of the constructed blade the reader is referred to Chapter 4.

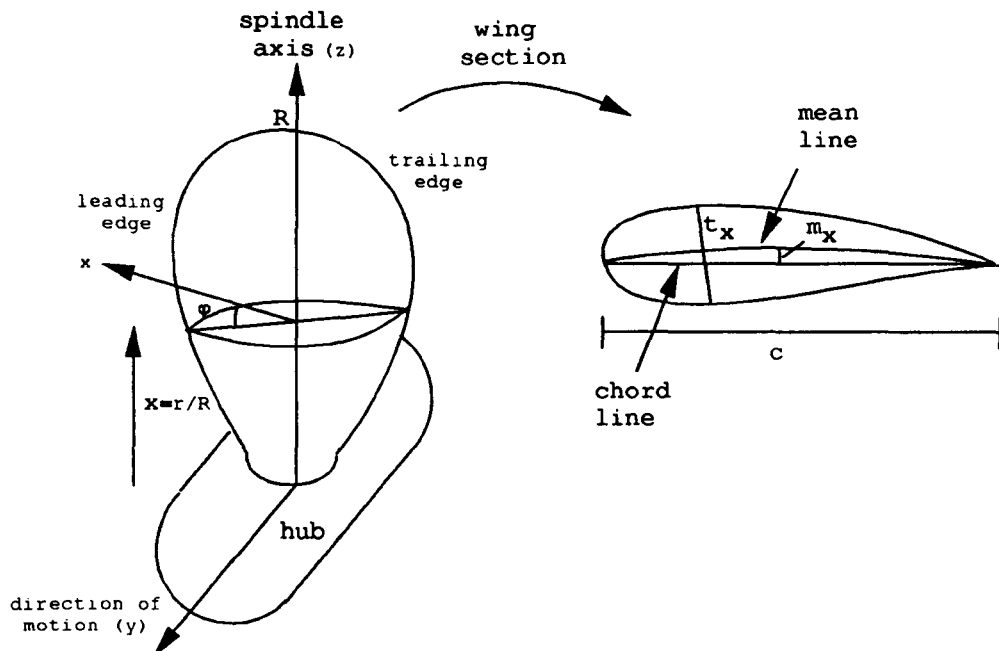


Figure 1.7: The propeller surface and blade section.

Once the two dimensional section geometry at each span is determined, the three dimensional blade can be generated. This is achieved by firstly rotating each of the sections about either its midchord point, or point of maximum thickness, about the (z)

(or spindle axis [26]), through an angle ϕ which is determined for each section. The angle ϕ is chosen so that each of the sections are appropriately aligned to the incoming flow to generate the desired lift on the propeller blade surface, and is referred to as the advance angle of the section. If we consider the blade section to be attached to a screw thread, then the corresponding advance of the blade for one given revolution is called the pitch [26] of the blade section. In one revolution, the blade will move along a helix, the circumferential distance given by $2\pi r$, where r is the particular radius of the section. Thus, the pitch P will be given by

$$P = 2\pi r \tan \phi. \quad (1.15)$$

Finally, the blade section is projected onto an imaginary cylinder, whose radius coincides with the radius at which the section is situated. Thus, in figure (1.8), we see that the two dimensional blade section is rotated about the spindle axis, and projected to form the wrapped section. This is repeated for each defined blade section.

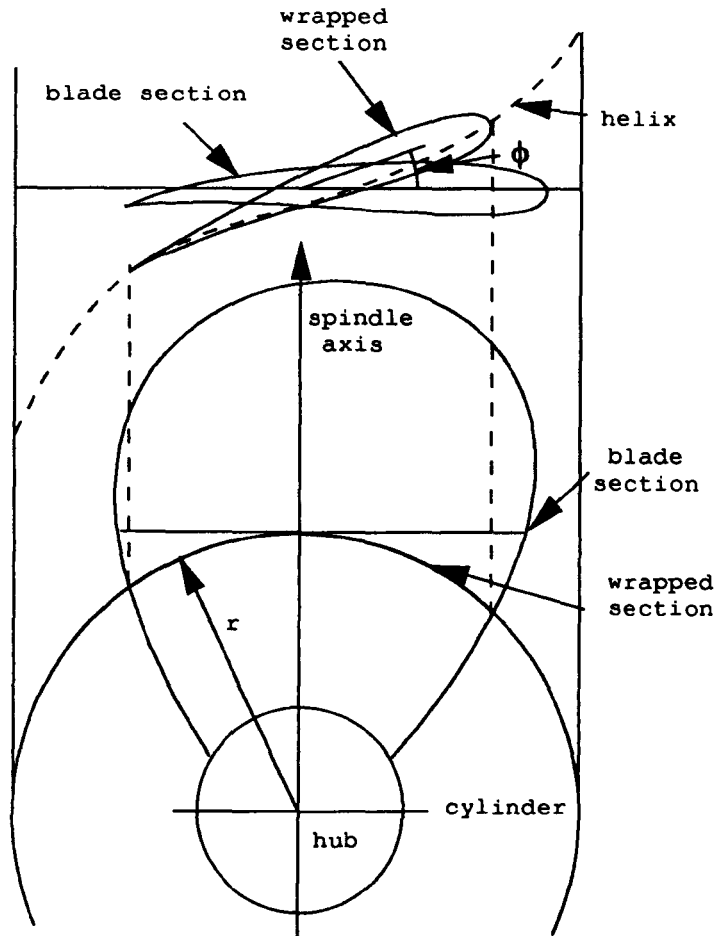


Figure 1.8: The complete blade geometry of the propeller.

It can be seen from figure (1.8) that the chord line of the section thus forms part of a

helix on the cylinder in the same manner as a screw thread.

These section curves can thus be thought of as representing the frame, or 'skeleton' of the propeller. One particular way to generate the complete surface to fit these sections, is by taking a B-spline surface which interpolates them. The B-spline surface can be thought to create a 'skin' over the frame, and it is from this idea that this method is sometimes referred to as a 'skinning method' [31].

1.5.2 Fillet design

In order to ensure that the blade can be attached to the hub of the propeller a fillet often needs to be generated [26]. This produces a smooth transition from the blade to the hub, and is generated as a continuation of the blade, from some section near to its base, so that the blade can easily be clamped onto the hub as illustrated in figure (1.9).

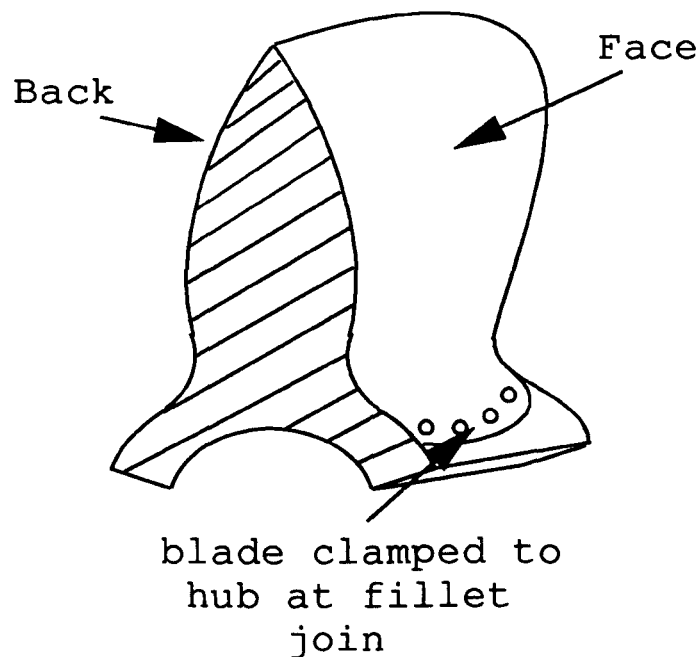


Figure 1.9: Clamping of the blade fillet onto the hub.

It should also be noted that a fillet is essentially the same as a blending surface; where the term blend originates from a mathematical background while the term fillet is from an engineering discipline. The fillet as illustrated above generally has the property that it adds strength to the join between the hub and the blade.

It is often advantageous for the fillet to have a constant stress in order to minimise the chances of the blade snapping. One standard way for producing a constant stress fillet is by using a compound radius fillet as illustrated in figure (1.10). The fillet is produced by

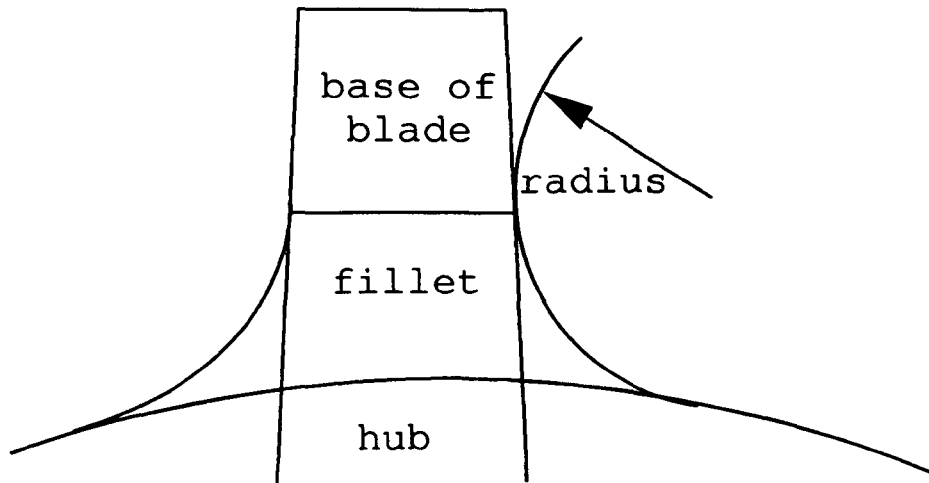


Figure 1.10: A compound radius fillet.

a rolling-ball method [7], where the imaginary surface swept out by a ball rolling around the joint is used as the fillet, as described by Rossignac and Requicha. The production of the fillet by this method produces a smooth, continuous surface from the blade to the hub, which means that this surface can be cut out by an NC (numerically controlled) machine [32].

For NC milling the fillet can be mathematically represented by a continuous function which can be used to describe the machine tool paths. One method where these paths are generated is in the work of Choi and Ju [33], in which explicit blend surfaces between parametric surfaces are constructed by simulating the action of the rolling ball. The restrictions they impose on the blend surface is that it is smooth, and without singularities or self intersections [33]. The ability to be able to NC machine a propeller blade is an important factor in manufacture, as will be described.

1.5.3 NC machining of propeller blades

At present, surfaces such as propeller blades are machined either by tracing out plaster templates, or by tracing along a machine path generated from the computer model of the surface. The problem with tracing out the plaster template is that the templates are expensive and time-consuming to produce. Therefore, it is advantageous to be able to generate machine paths from a computer representation.

NC machining of propeller blades offers production efficiency, accuracy and repeatability [32]. One of the reasons for this is that when producing a blade by hand there is bound to be a variable human factor concerned with reproducing the same blade for a

multi-bladed propeller which can have an effect on performance and damage to structure. However, once machined, hand finishing of the blades is often undertaken to smooth the surface to a specified degree.

Secondly, when considering production costs of the propeller, even for a ship propeller the cost will be lower for automatic machining due to the time taking less than half that of a hand produced blade. This consideration even includes the initial cost of the outlay for the machine and so the generation of automatic machine paths is one area worth pursuing.

1.5.4 Blade surface fairness

A smooth surface is essential to keep power requirements down on a propeller blade [34]. Attempts have been made for many years to estimate the penalty in power incurred by increased propeller roughness. Grigson, for example [35], conducted his studies into the power loss incurred by propeller roughness by increasing the drag coefficients of the propeller blade to approximate the surface roughness, and demonstrated that a considerable power loss occurs when a surface becomes rougher.

Patience [34] also states that the blade surface wastage caused by impingement or corrosion leads to turbulence which increases the drag, resulting in loss of efficiency. This development of roughness can be accelerated if the propeller has coarse regions, usually concentrated on small areas (such as the leading edge). These can cause accelerated cavitation and so damage the blade in this way. Other ways in which rough surfaces lead to damage are from the fact that when the propeller is stationary, a rough surface is easier for marine growth than a smooth surface and so experiences a greater build up of barnacles and other marine life.

In turn maintenance can be costly: estimated by Patience at about \$170 per square metre of blade surface, which proves expensive when regrinding a $20m^2$ blade. In relation to the cost of the propeller, this is obviously not expensive. However, it is the rate at which the blades become rough which is important. It proves to be a difficult task to regrind the blades; often needing to be undertaken when the vessel is in dry dock. Thus, if the blade surface becomes so bad as to be ineffectual while in service, the whole ship may have to be taken out of service while repairs are undertaken or the propeller replaced.

Thus, it is required that the blades are fair [12], or smooth. If automatic milling is to occur, then a fair surface will be necessary to provide the machine path. Any model with

surface fluctuations will have these accentuated when produced by an NC machine.

The fairness of a surface cannot very easily be mathematically defined. Unlike curve fairing, which can be undertaken by examining the curvature along the curve, surface fairing is a vague concept. There are many measures of a surface fairness; one of these being to consider the light reflected off a surface. For instance, if we examine the panel of a new car door, we would expect to see the light reflected uniformly off it, and observe no dents, unlike an older door.

One important geometric measure of a surface's curvature is given by the Gaussian curvature κ , which describes the local shape of a surface and is obtained by taking the product of the maximum and minimum principal curvatures κ_{max} and κ_{min} at a point [36]. These quantities are easy to calculate on a parametrically described surface as can be seen in [36]. A standard fairness measure can then be defined by the function

$$\int_S (\kappa_{min}^2 + \kappa_{max}^2) ds \quad (1.16)$$

as demonstrated by Nowacki and Reese [12]. This represents a simplified analogy of the strain energy of flexure and torsion in a thin rectangular elastic plate of small deflection. Thus, by minimisation of the above expression, the surface can be made as fair as possible.

1.6 Approach to hydrodynamic design of propellers

In this section we deal with the ways in which the hydrodynamic design, analysis and improvement of propellers is commonly undertaken. The design of propellers can be approached from two directions, given by de Campos et al [37] as the following

- Inverse methods for propulsor design
- Direct methods for propulsor analysis

1.6.1 Inverse methods

The term 'inverse methods' signifies that the required performance of a propeller is specified at the start of the design. This is obtained by establishing a circulation distribution over the blades which will produce the desired total thrust, usually subject to considerations of efficiency and cavitation [37]; the basic assumptions are that the thrust should be maximised whilst keeping the power input low, since the ratio of the power input to power output gives a measure of the efficiency of the propeller.

The ongoing research into propeller design has been to look at ways to improve the efficiency produced. This has always been important but was no more so than during the 1970s when the oil crisis occurred. At this time the simplest and most wide-spread methods to improve efficiency were to slow the propeller down and make them produce more thrust. However, now emphasis is placed on changing the geometry of the propellers, for instance by the introduction of blade sections which are cupped at the trailing edge [38]. Other emphasis has been placed on the introduction of various combinations of propellers, such as counter-rotating propellers of different sizes, ducted propellers and appendages which enable the flow field coming off the ship hull to be rotating counter to the propeller at a steady rate so that an improvement of the onset flow into the propeller can be obtained [39].

In the second stage a blade configuration that will produce this prescribed distribution of circulation for a given set of design requirements is determined. These will include the number of blades, (optimum) propeller diameter, propeller rate of revolution and speed of advance.

The basis for determining the radial distribution of circulation that would result in optimum efficiency for a propeller in a uniform flow was first determined by Betz [40]. He found that the optimum propeller developed a trailing vortex system that formed a rigid helicoidal surface.

The first technique used to attain the geometry was implemented by Prandtl from his lifting line concept [41]. The propeller could be designed by concentrating the circulation around the blades on individual lifting lines, and the flow at each section could be regarded as two dimensional.

This approach was extremely successful for airscrews, which had high-aspect-ratio blades and operated in front of the aircraft in relatively uniform inflow. However, since marine propellers have low-aspect-ratio blades as their lift coefficient needs to be limited to prevent cavitation, the lifting line theory was not satisfactory.

By introducing a correction to the camber of the section, the theory could be made applicable, and it was Lerbs [42] who produced one of the first, and most comprehensive, design methods for marine propellers with arbitrary circulation distributions. This method is still, in fact, used today as a basis for determining propeller efficiencies. Around the same time another notable design method was published by Eckhardt and Morgen [27]. This includes aspects of both design and analysis by using corrections to pitch and

camber to take into account the curvature of the flow. Morgen et al [43] later published more extensive correction factors to the lifting line method to determine the distributions of pitch and camber.

As computers appeared, it was seen that the use of empirical charts and data to obtain these designs was a time consuming process and so, new, more accurate methods were evolved. The main ones were based on a propeller-lifting surface theory [44], and are known as vortex lattice lifting surface methods. In the design process the blade surface is partially known, with the pitch and camber to be determined. The surface is assumed thin and is discretised into a sheet of unknown source terms and either normal dipoles or vortices. This is because the propeller is assumed to be operating in an unbounded, incompressible fluid, from which the velocity potential at a point on the surface can be obtained using Green's formula. The source and vortex distributions are obtained by satisfying a boundary condition of zero velocity normal to the surface, and the process is continued until the appropriate pitch and camber are found for the operating conditions, as has been illustrated by Kerwin and Greeley [44].

1.6.2 Propeller analysis

Propeller analysis is more concerned with obtaining the performance of the propeller for a given geometry. It can also be used to determine other features of the propeller, such as whether the propeller will be any good when trying to limit cavitation, or for reasons of strength considerations.

Again lifting line methods can be used to analyse the propeller (using the Eckhardt and Morgen method for instance). This would give a rough estimate of the thrust produced by the propeller using 2 dimensional estimations for circulation, velocity etc. However, when other requirements need to be considered then the lifting line method is inadequate. The propeller may have to ensure that physical criteria are upheld, such as being non-cavitating, and so a better analysis method needs to be employed which will accurately give a complete pressure distribution over the surface, from which cavitation can be considered.

Lifting surface methods have been used successfully to obtain propeller performance by Kerwin and Lee [3], and unsteady cavitation has also been considered by Szantyr and Glover [45]. However the principle shortcoming of the lifting surface representation is given by the local errors near the leading edge where pressure suction can occur [6].

These errors have been overcome to some extent by Lighthill [46] in which the flow around the leading edge of a parabolic body is matched to the 3 dimensional flow. This is mostly applicable to thin sections, and so not all marine propellers can be considered.

The most applicable approach which treats the geometry exactly as it is defined is given by the panel method [4]. This is an extension of lifting surface models, in which the geometry is discretised into many panels and a potential flow is assumed around the geometry. The major difference between lifting surface and panel methods is that whereas lifting surface methods generate panels over a surface which goes through the mean lines of each section, panel methods generate panels over the actual surface of the propeller blade. The panels then have associated with them some distributions of sources and doublets [47], which produce the potential flow. The first implementation of the panel method was undertaken by Hess and Smith [48], for the case of non-lifting flow and has continually been used and upgraded to suit a variety of needs (the primary extension being to lifting flows [4]).

The vast improvement of the panel method over lifting line or surface methods, is in the exact representation of virtually any geometry. The propeller can be modelled easily and any problems, such as those associated around the leading edge, can be alleviated by discretising the panels more closely together in such regions to pick up these features. Thus, the flow in areas such as these, where pressure peaks may occur, can easily be determined.

From the determination of the pressure and velocity fields (which are assumed to be potential flows) cavitation problems can also be considered, such as has been demonstrated by Kinnas [49] in his analysis and design of supercavitating foils using a boundary element method.

1.6.3 Assumptions made in propeller design

The complexity of the particular mathematical model for the flow about the blade will influence the results obtained. A marine propeller is located behind the ship's hull and so the onset flow in front of the propeller must be allowed for, if not exactly calculated. In the majority of cases the model used to design the propeller simulates the propeller flow by considering it to be an incompressible flow which is aligned with a uniform flow field. However, this is an approximation which is used to make modelling simpler. In reality a propeller will never operate in a uniform flow field as it is not sufficiently far from the

ship's hull for the problem of the interaction of the hull wake to be separated from the propeller inflow, and so accurate predictions need to be obtained for the wake field.

One analysis done by Cheng and Hadler [50] on the series of Victory ships produced values of the circumferential distribution of the wake velocity. This was completed at the Netherlands Ship Model Basin as it was necessary to determine the results for a scale model, as a towing tank is the only practical means to determine the wake field of the ship since full scale measurements are difficult to obtain due to unidentified influences [51]. However caution must be exercised when interpreting the results of model testing since different Reynolds numbers will cause problems when scaling the results. Ligtelijn [51] states that a scale factor of not more than 30 should be used to provide reasonable results from towing tanks.

Therefore model testing can provide results from which more complex mathematical models can eventually be derived. These can then be used to verify whether close approximations to observed results are being obtained. As a result of this, work has been carried out with models of non-uniform flows. The analysis of the unsteady flow around extreme propeller shapes has been done by Kinnas and Hsin [52] by including harmonics in the inflow to the propeller. Other methods include analysis of the complete propeller with the ship hull by Larsson [53]. The ship hull is modelled using a potential based panel method with a thin skin covering it to represent the boundary layer and the region surrounding the propeller is modelled using a Navier Stokes flow.

Depending upon the type and accuracy of calculations required, either a uniform or non-uniform potential flow can be used. It will be discussed in the next section which particular features of the propeller design are to be studied, and in particular, how the PDE method can be applied to produce certain advantages of design and analysis over other existing methods.

1.7 Design of PDE generated blades

The initial aim of this thesis is to illustrate how the PDE surface design method can be applied to the representation and manipulation of propeller blade geometries as described in section (1.5.1). Chapter 2 will deal exclusively with the mechanism adopted by the PDE method for blend and surface design. It will illustrate many of the method's qualities by consideration of a few examples and will illustrate the ease with which generated surfaces may be manipulated via the parameter set.

In section (1.5.1) it was illustrated how a conventional propeller blade is described. The PDE approach can also be applied to this task, due to the nature of the propeller blade being described by geometrically similar airfoil sections located at constant radii along the blade span. Dekanski, Bloor and Wilson [54] demonstrated that by producing a generic airfoil section, the complete propeller blade could be generated with similar sections repeated through the span. Thus, in the initial stages of the propeller representation, this model will be reproduced in Chapter 3 to illustrate the fact that this blade can be generated with a small parameter set. Due to the airfoil sections being generic, the produced blade will not represent any existing geometries, but will be used to give a feel of the way in which the parameters control the geometry of the blade. This is of particular interest in Chapter 4 where existing propeller blade geometries will be approximated using a single patch of surface, while still maintaining a small parameter set.

It should be noted that the actual boundary conditions used throughout this thesis (in particular in Chapters 2, 3 and 4) are simply stated at the appropriate places. For complete explanations of the derivation and justification of the choice of boundary conditions and parameters the reader is referred to Appendix C at the end of this thesis.

1.7.1 Applicability to propeller manufacture

The PDE generated propeller is actually more closely applicable to the generation and manufacture of propellers than might at first be imagined. Consider the way in which propellers are conventionally manufactured and their requirements for smooth surfaces and fillet generation, as described in section (1.5).

Once a mathematical representation of the blade surface has been created, then the actual blade is cut out to be fixed onto the hub. To ensure the blade can be fixed, a fillet must be generated, as described in section (1.5.2), which is, as has been stated, in fact a surface blend. Since the PDE method originated from the notion of blend design [1], it is straight-forward to demonstrate how the PDE method is applicable to the generation of fillets. Chapter 3 will demonstrate how a generic fillet (the stress requirements will not be considered) can be created to attach the propeller blade to the hub of the propeller.

Furthermore, since the fillet and blade surface are represented parametrically it is possible to generate NC paths for the milling of such models. Work has been carried out by Houghton and Mullane in the Department of Mechanical Engineering at Leeds University [55]. They successfully demonstrated that machine paths could be created

from PDE blade representations, from which they produced both wax and aluminium models of the blade surfaces, with the inclusion of a constant radius fillet at the base.

Also, A.E. Turbines of Bradford [56] produced a scale foam representation of an actual propeller blade data set generated using the PDE method as described in chapter 4. Figure (1.11) shows the blade, which has only had one side machined due to the fact that the actual blade geometry is nearly 4 metres long, and so the scaled version is too thin to machine in a foam block. It will be seen that the PDE method can be used to generate a fast, explicit representation of the blade surface, from which NC machine instructions can be generated.

The PDE generated surfaces will naturally be smooth due to their origin as the solutions of elliptic equations. What then of B-spline surfaces? Brown, [24] has illustrated that surfaces derived from the PDE method prove to be fair, since plots of the surface curvature do not show any disturbances (or ‘wiggles’ as described by Munchmeyer [57]). In the case of the same B-spline approximations to the same surfaces, it was found that wiggles occurred, which could be suppressed with the techniques described earlier of knot insertion and degree elevation.

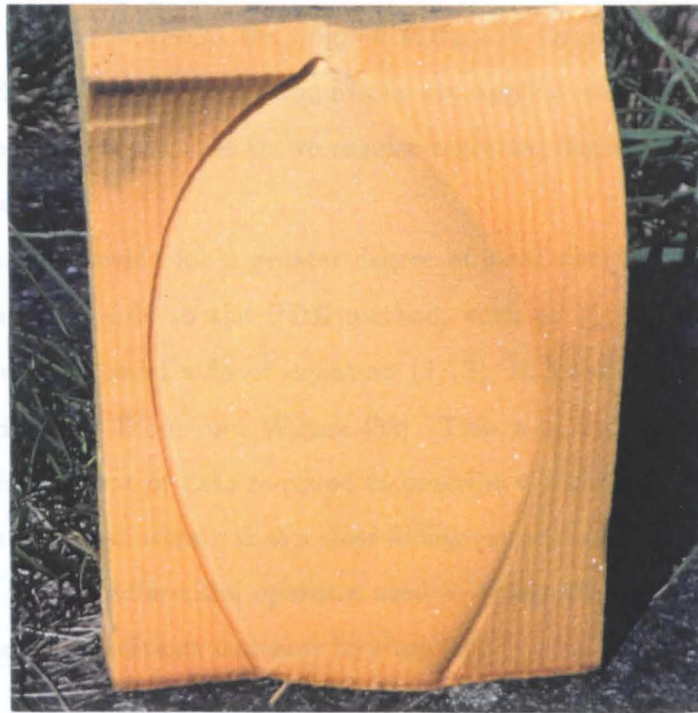


Figure 1.11: A PDE generated blade which has been NC-machined.

1.7.2 Accurate propeller representation

As opposed to Chapter 3 which is concerned with producing a generic blade geometry, Chapter 4 deals with the more difficult task of propeller blade representation by considering the problem of generating a propeller whose various distributions are given in the results of the paper of Eckhardt and Morgen [27].

This is undertaken since one of the aims of this thesis is to illustrate the potential of the PDE method with reference to the functionality of generated surfaces. In particular this will involve the implementation of a panel method to predict the propeller performance of a given geometry, and so as an accurate prediction is being attained, the geometry of the propeller surface needs to be realistic in order to test the accuracy of the panel method.

The main problem for the PDE method in the approximation of existing surfaces is that it is not obvious how positional and tangential boundary conditions can be used to represent accurately the existing geometry of the propeller, if at all. One way of overcoming this is by B-spline representation. However, the aim of the latter part of the thesis is to illustrate the flexibility of the PDE method with regard to the improvement of the propeller design using a small parameter set; and so from this point of view it would be a retrograde step to represent the original surface in terms of B-splines. Once it has been determined how the boundary conditions are applied we need to approximate the distributions along the blade, and so we require a greater degree of local control for this particular problem.

Various ideas to provide for a greater degree of local control have been successfully demonstrated with regards to the PDE method, such as by the inclusion of 'forcing' functions on the right hand side of equation (1.13), to produce local areas of surface change as described by Bloor and Wilson [58]. This is of little benefit in this case, as these increase the amount of data required to describe the surface.

In this thesis we will illustrate that a close fitting surface can be obtained by increasing the order of the partial differential operator used to obtain the surface. This implies that additional boundary conditions can now be supplied.

1.8 Analysis of propeller performance

As already stated, it is the functionality of surfaces generated using the PDE method which is under consideration, in particular the surfaces of marine propellers. In this respect we aim to illustrate how the performance of the generated propeller model can be

obtained. Consideration will be given to the thrust, efficiency and also to the cavitating properties of the propeller. Once the performance has been predicted, then the next task will be to improve the design of the propeller geometry.

As an illustration of the process, a simple example will be given in Chapter 3. This considers a wing shape, which is of a similar geometry to the airscrew blade, and thus enables Prandtl's lifting line method to be used to determine its circulation (and hence lift) in a uniform flow field. Then, by altering a bare minimum of parameters that control the geometry, it will be seen that, not only will the geometry be affected, but the circulation and lift will alter too. This is of course obvious, but what is not obvious is how the maximum lift can be determined by altering the geometric parameters.

The solution to this problem of improving the efficiency of a propeller, by alteration of the surface design parameters will then be discussed, and implemented in Chapter 6; not, however, using the lifting line method which was used as a mere demonstration of the underlying principles, but by determining the efficiency through the more accurate panel method described in Chapter 5.

Thus, in Chapter 5, a panel method will be implemented to determine the pressure distributions over the propeller's surface. From this the thrust, power and efficiency can be determined along with areas where pressure peaks occur, which are critical to cavitation considerations. It should be emphasised that the aim is not to implement the most sophisticated of methods - those which include wake realignment, non-uniform inflows [52], etc. - but to illustrate the potential of the PDE method for improving the generated surface. The panel method to be implemented in this thesis is based on the SPARV panel method [59]. However, changes are needed as this panel method was designed for aircraft wing geometries in uniform flight, and hence modifications are required for trailing wake geometries and other effects. It should be noted that the PDE generated surface is automatically in a form compatible with panel methods, and so this is one advantage over other surface generation techniques in which discretisation of the surface is firstly required.

1.9 Improvement of propeller design

The final topic under consideration is the improvement that can be made to the initial propeller design. Using the panel method described above the thrust and efficiency of the propeller designed in Chapter 4 are evaluated. This is the propeller described by Eckhardt

and Morgen and so comparisons can be made between the thrust they determine and that determined by the panel method to verify its accuracy. In this part of the thesis we aim to show that by optimising the parameter set to improve the efficiency, a new design of propeller can be obtained. Therefore, since the geometry of Chapter 4 is used as the starting design, it is not required that an exact interpolation of the propeller geometry is sought; just that an approximation of an actual propeller geometry can be determined. Nonetheless the geometry attained in Chapter 4 is pretty close to the design data.

Since the parameters introduced through the boundary conditions of the PDE method are the unknowns being optimised, some sort of constraints need to be put on the surface so that the geometry remains a feasible design. This is done by considering the cavitating properties of the propeller with the requirements that the final design be non-cavitating.

This method of propeller design is different to that described by the inverse methods in section (1.6.1) in that the initial geometry is prescribed, and a better performance is sought. In other words, this technique falls into the category of shape optimisation.

1.9.1 Shape optimisation

The example of optimising the thrust (or efficiency if power limitations are included) by manipulation of the propeller surface is just one particular example in the field of shape optimisation [60]. This involves the idea of optimising some property which is dependent on the shape while satisfying other criteria, either physical, geometrical or a combination of the two.

One method of obtaining optimum designs is that of Kinnas [39] where the full design of a ducted propeller is obtained by using a non-linear optimisation to obtain the circulation of the propeller.

In shape optimisation the optimum function is searched for by altering the surface. Imam [61] states that an appropriate selection of shape representation is necessary for effective optimisation. If we have many control parameters to alter the shape then a long search will be required to find the optimum of the function on the surface. This is due to the fact that the method of optimisation takes one control parameter at a time and searches the parameter space for an optimum value of the function. Once this is found, the next parameter is varied until a new optimum is found and so forth until all parameters have been determined and a level of convergence in value of the optimum function has been reached. To demonstrate the difference between the applicability of the

PDE method and other techniques, two methods for optimisation are described below.

The first example of an optimisation technique is by Larsson [53] where the minimum wave resistance around a Ro-Ro ship is sought. The geometry of the hull is defined by a set of points on the surface, associated with each of these is a design variable which represents the location of the point along a line in which it is constrained to move. This presents a non-linear optimisation problem which can be solved for each of the design variables by linearisation. Larsson et al attached constraints to the volume of the ship and by optimising over the surface with 21 variables they obtained an optimum design which slightly increased the volume of the ship.

On the other hand Lowe [62] illustrates how PDE generated surfaces can be used to produce optimum designs; in particular he uses the PDE method to generate boat hulls, from which a search over a small parameter set gives him designs for boat hulls of minimum wave resistance. The search Lowe carries out is over a parameter set which has just 7 variables to define the shape, and is subject to constraints on the draught, displacement and stability of the vessel. His results appear to give similar findings to those achieved by Larsson, and so illustrate the value of a smaller set of defining parameters for the surface.

Further complexities are met in the method used for the optimisation. As described, this searches around the parameter space looking for an optimum value of each parameter in turn. The conjugate gradient method of Fletcher Powell [63] needs to evaluate gradient directions to obtain a direction for the search. For complicated surfaces this proves to be time consuming. Coupled with the need to implement the full panel method every time a new value is chosen to determine the value of the thrust, time is of the essence in the procedure. Fortunately, Powell [64] has implemented a more basic optimisation procedure in which no derivatives are needed, and it is this which will be utilised in chapter 6.

1.9.2 Constraints and penalty functions

We could quite easily go searching around the parameter space until an optimum value of the function is found. However, this may produce a design which is impractical to manufacture - it may be so highly cambered that separation is inevitable. Therefore, it is necessary that constraints can be imposed on the optimisation process to keep the design realistic. This is done by penalty functions which affect the function value if a constraint is broken so that the circumstance cannot exist.

In Chapter 6 we are dealing with the notion of improving the efficiency of the propeller

design. The geometry of the propeller is contained within the workings of the PDE method. The physics, on the other hand, will be controlled by including a set of bounds on the cavitating properties of the blade [65]. This is due to the fact that cavitation plays a major role in the performance of the propeller, from the onset of noise and vibration to propeller blade erosion [6]. Thus, most of the constraints used in the optimisation process are derived from cavitation constraints to ensure that the best possible performance is obtained.

Finally, the conclusion will discuss the work included in this thesis and the PDE method's applicability to a design system for marine propellers with reference to the areas described throughout this introduction and the results obtained in this thesis.

Chapter 2

The PDE method of design

2.1 Introduction

In this chapter it will be illustrated how the PDE method can be used for the generation of blending surfaces and free-form surfaces, as discussed in Chapter 1. It will further be shown how the PDE method can be extended from earlier work [23], so that a greater degree of control over the surface can be exercised, which will be a necessity for the propeller blade representation discussed in Chapter 4.

2.1.1 Curvilinear coordinates on a parametric surface

The PDE method has been devised for generating surfaces by regarding them as solutions to partial differential equations [1]. Mathematically the surface is given by the function $\underline{X}(u, v)$ such that

$$\underline{X}(u, v) = (x(u, v), y(u, v), z(u, v)) \quad (2.1)$$

where u and v are independent variables defined over some real valued domain Ω , and the Cartesian coordinates x , y and z of points on the surface are given as functions of u and v .

It can be seen from equation (2.1) above that the surface may be regarded as a mapping from a region of R^2 , given by the domain in u and v parameter space, into E^3 (Euclidean 3-space) as illustrated in figure (2.1).

The parameters u and v can be regarded as defining a curvilinear coordinate system on the surface $\underline{X}(u, v)$. If the value of one of the variables, u say is fixed at u_0 , then the function $\underline{X}(u_0, v)$ will now be a function of the other scalar parameter only. This results

in a curve which lies on the surface $\underline{X}(u, v)$. By continuing this process for one variable and then the other over arbitrarily spaced values in the u, v interval, a parametric net of two one-parameter families of curves is formed on the surface, which has been mapped from a regular grid in R^2 where the grid lines are parallel to the coordinate axes in the (u, v) plane. These curves over the surface may be referred to as the isoparametric lines since one of the variables is constant along them.

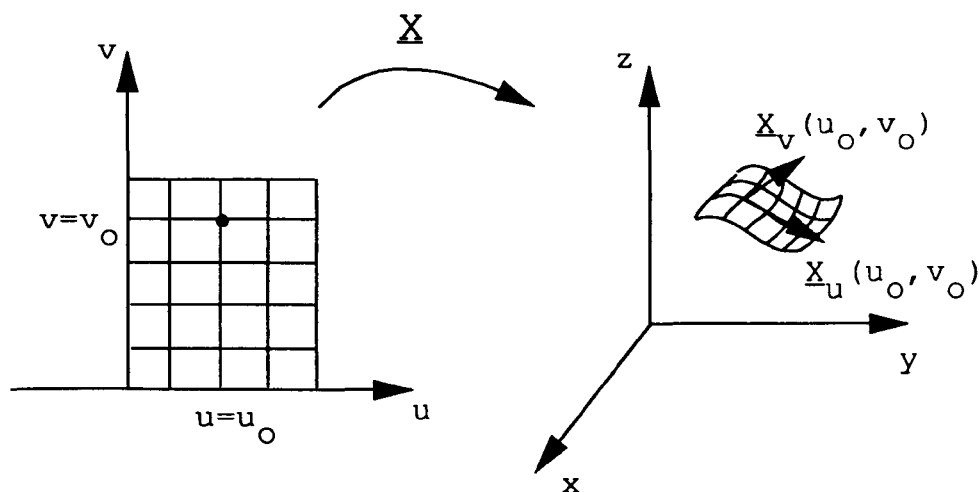


Figure 2.1: The surface patch in E^3 mapped to from R^2 .

2.2 The PDE method

The surface patch $\underline{X}(u, v)$ is obtained by posing suitable conditions along the boundary of the domain $\delta\Omega$. From this it is natural to obtain the surface $\underline{X}(u, v)$ by regarding it as the solution of a partial differential equation of the general form

$$D_{u,v}^m(\underline{X}) = \underline{f}(u, v) \quad (2.2)$$

where $D_{u,v}^m(\)$ is a partial differential operator of order m in the independent variables u and v . The solution of equation (2.2) gives the surface in the parametric form (2.1). The choice of partial differential operator is taken to be elliptic since this ensures that the solution $\underline{X}(u, v)$ can be found by posing conditions on the boundary of the domain $\delta\Omega$. The boundary conditions are posed in terms of the parameters u and v in the (u, v) parameter space.

The degree of the partial differential operator will determine the required amount of boundary data. If m is taken to be 2 then only boundary conditions representing the

position of the curve need to be imposed. When m is taken to be 4 then the normal derivatives in the (u, v) plane also need to be imposed around the boundary edges. The first derivatives can be used to control the direction of the surface normal at the edges of the patch, and hence can be used to give tangent plane continuity between adjacent surface patches when considered in the context of blend design.

The particular equation that has been used throughout the work of Bloor and Wilson is

$$\left(\frac{\partial^2}{\partial u^2} + a^2 \frac{\partial^2}{\partial v^2} \right)^2 X = 0. \quad (2.3)$$

This is a biharmonic operator modified by the inclusion of the term a which has been designated the smoothing parameter [1]. This operator has many applications within the field of continuum mechanics. One of its applications is to thin plate theory where the unknown function represents the transverse displacement of a flexible thin plate bent by a load [12].

It should be noted at this stage that the smoothing parameter can take a constant value or can be a function of u and v . For the case where a is constant then a simple rescaling between the directions has been achieved (this can be seen by replacing v with v/a [66], [23]).

The elliptic partial differential operator in equation (2.3) represents a smoothing process in which the value of the function at any point on the surface is, in a certain sense, an average of the surrounding values. In this way a surface is obtained as a smooth transition between the boundary conditions imposed on both the function and its first derivative.

The solution of each of the dependent variables (x, y, z) can be written using Green's second identity, and will be of the form

$$x = \frac{1}{2\pi} \int_{\delta\Omega} x_c \frac{\partial(\Delta G)}{\partial n} - \Delta G \left(\frac{\partial x}{\partial n} \right)_c ds \quad (2.4)$$

for the variable x , say, where Δ is the partial differential operator in u and v , the subscript c denotes values on the boundary $\delta\Omega$, and $\partial/\partial n$ denotes the partial derivative in the direction of the outward normal to the contour $\delta\Omega$. The integral on the right hand side of equation (2.4) represents the smoothing of the function and its normal derivative specified on the boundary. That is, at any point P in Ω , x is a weighted average of its value and the value of its normal derivative over the bounding contour, and it can be deduced therefore that solving a fourth order PDE, such as that given by (2.3) ensures that a smooth surface

can be generated for given boundary conditions. This proves particularly advantageous when working in the field of blends and fillet generation, as has been seen earlier.

To obtain an appropriate surface the boundary value problem must be correctly set up and the solution sought. There are two different types of boundary value problem which will be solved. The first of these is the case in which both sets of trimlines in the u and v directions are non-periodic, and in the case of blend generation the position and normal derivative continuity conditions must be satisfied over the boundaries of the domain. In the second case the trimlines $u = u_0$ and $u = u_1$ are periodic in v , and thus a closed loop of surface results. In this instance boundary conditions are applied solely on $u = u_0$ and $u = u_1$. This type of surface occurs frequently in blend problems where the primary surfaces are primitives such as spheres, cylinders etc. Periodicity is also the case for many applications in free-form surface design, as will be illustrated later. The method of blend generation will now be demonstrated by way of an example.

2.3 Example:A surface blend

In this example a blend is considered between a cone and a sphere. The example is contrived purely to illustrate the mechanics and control of the PDE method. The requirements are that the generated blend will form a smooth and continuous bridging surface between two primary objects.

Firstly, the cone and the sphere (which are considered as the primary surfaces) must both be parametrised. The equation of the sphere is given by

$$x = R_s \sin \phi \cos v_s \quad (2.5)$$

$$y = R_s \sin \phi \sin v_s \quad (2.6)$$

$$z = R_s \cos \phi + d_1 \quad (2.7)$$

over the range $0 \leq v_s \leq 2\pi$, $0 \leq \phi \leq \pi$ and where R_s is the radius of the sphere.

The equation of the cone is given by

$$x = \zeta R_c \cos v_c \quad (2.8)$$

$$y = \zeta R_c \sin v_c \quad (2.9)$$

$$z = h_c(1 - \zeta) \quad (2.10)$$

for $0 \leq \zeta \leq 1$ and $0 \leq v_c \leq 2\pi$ and where R_c is the base radius of the cone and h_c is the height of the cone.

To produce a blend between the two primary surfaces, trimlines must be imposed on the cone and sphere. By making the (u, v) domain over which the blend will be produced $0 \leq u \leq 1, 0 \leq v \leq 2\pi$, then periodic trimlines can be produced as in figure (2.2). Here it is advantageous to take v such that $v = v_c = v_s$.

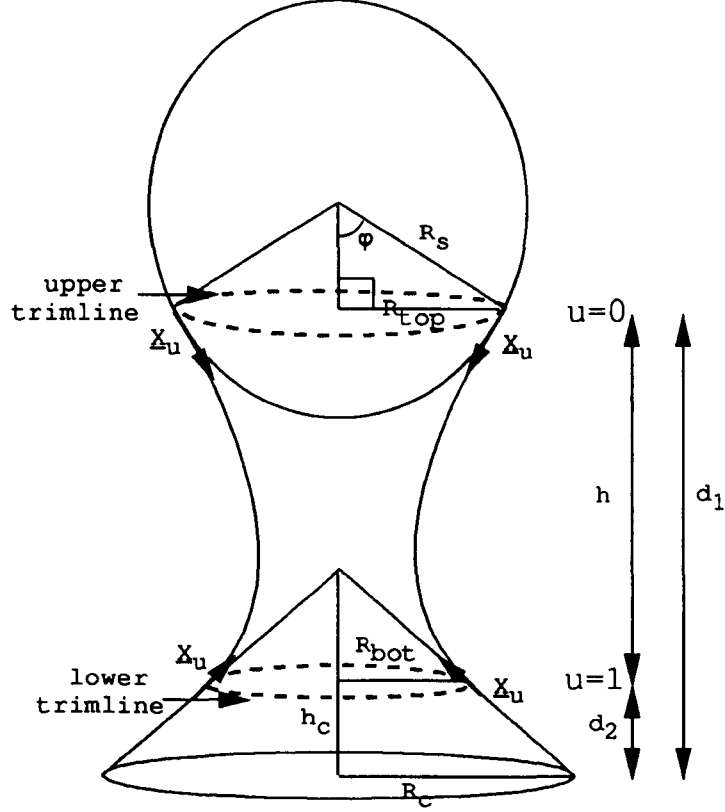


Figure 2.2: The trimlines governing the blend between the cone and sphere.

By imposing the trimline on the sphere to be the isoparametric line $u = 0$ on the blend, and the trimline on the cone to be the isoparametric line $u = 1$, the positional boundary conditions for the blend are defined as

$$x(0, v) = R_{top} \cos v \quad (2.11)$$

$$y(0, v) = R_{top} \sin v \quad (2.12)$$

$$z(0, v) = d_1 \quad (2.13)$$

and

$$x(1, v) = R_{bot} \cos v \quad (2.14)$$

$$y(1, v) = R_{bot} \sin v \quad (2.15)$$

$$z(1, v) = d_2 \quad (2.16)$$

where $d_2 < d_1$ and $h = d_1 - d_2$ is the distance between the trimlines.

Again it should be noted that in this example due to the range over which v varies and the sinusoidal nature of the boundary conditions, a periodic surface will be formed, and boundary conditions need only be applied on $u = 0$ and $u = 1$

2.3.1 Tangency conditions

Since the equation being solved is fourth order it is necessary to calculate the first derivatives of x, y and z on the trimlines.

The standard procedure is to define the vectors

$$\underline{X}_u = \frac{\partial X}{\partial u} \quad \underline{X}_v = \frac{\partial X}{\partial v} \quad (2.17)$$

to be the coordinate vectors for the surface parameterisation, as is illustrated in figure (2.1). These are assumed to be linearly independent, i.e. non parallel, which implies that $\underline{X}_u \times \underline{X}_v \neq 0$. The unit normal at any point on the parametric surface can now be easily obtained and is defined by

$$\underline{N} = \frac{\underline{X}_u \times \underline{X}_v}{|\underline{X}_u \times \underline{X}_v|}. \quad (2.18)$$

If \underline{X}_u and \underline{X}_v are perpendicular to each other, then $\underline{X}_u \cdot \underline{X}_v = 0$ and $\underline{X}_u, \underline{X}_v$ and \underline{N} will form a local orthogonal set at the point. The normal at the point of a surface is perpendicular to both the coordinate vectors at that point (in fact the normal is perpendicular to the tangent of all curves which pass through that point [36]). Now, if the vector product is taken between the normal and a vector tangent to the trimline, this will give a vector tangent to the surface at the trimline, which is suitable for the definition of the tangency conditions. Thus, the first order tangency conditions can be obtained from

$$\underline{t} = \frac{\underline{X}_u \times \underline{X}_v}{|\underline{X}_u \times \underline{X}_v|} \times \underline{X}_v \quad (2.19)$$

at each of the primary surfaces.

Now on the trimline on the sphere the conditions

$$R_s \sin \phi = R_{top} \quad R_s \cos \phi = (R_s^2 - R_{top}^2)^{1/2} \quad (2.20)$$

hold. Therefore, on the sphere around the trimline the normal to the surface is given by

$$\underline{N} = (\sin \phi \cos v, \sin \phi \sin v, \cos \phi) \quad (2.21)$$

and the tangency boundary conditions are obtained from equation (2.19), that is

$$x_u(0, v) = -S_1 \left(\frac{R_s^2 - R_{top}^2}{R_{top}^2} \right)^{1/2} \cos v \quad (2.22)$$

$$y_u(0, v) = -S_1 \left(\frac{R_s^2 - R_{top}^2}{R_{top}^2} \right)^{1/2} \sin v \quad (2.23)$$

$$z_u(0, v) = S_1 \quad (2.24)$$

where $S_1 = S_{top} \cdot R_{top}/R_s$ with S_{top} being a tangent parameter.

Similarly, on the cone the tangency boundary conditions on the trimline $u = 1$ can be obtained, and are defined as

$$x_u(1, v) = -S_2 \frac{R_c}{h_c} \cos v \quad (2.25)$$

$$y_u(1, v) = -S_2 \frac{R_c}{h_c} \sin v \quad (2.26)$$

$$z_u(1, v) = S_2 \quad (2.27)$$

where S_2 is defined in Appendix C. The parameters S_{top} and S_{bot} control the speed of the isoparametric u -lines as they approach the trimlines through their magnitude, while their sign determines the direction from which the blend approaches the primary surface. Care needs to be paid in some instances, as increasing the tangent magnitude too much may result in a self-intersecting surface being generated. It should further be noted that the choice of derivative conditions is not unique.

The boundary value problem has been set up and so the elliptic PDE can be solved. This can sometimes be done analytically or more generally by using numerical methods such as the Successive Over Relaxation method [67] to obtain an approximate solution. In many cases where periodicity is present, from the form of the boundary conditions, an analytic solution can be sought from the method of separation of variables [68], in a similar manner to that described in Appendix A.

2.3.2 Analytic solutions

An analytic solution to equation (2.3) can be obtained for examples in which the boundary conditions are similar to those described above. In the example where a closed loop of surface is considered, by inspection of the boundary conditions, a solution can be sought of the form

$$\underline{X}(u, v) = \underline{A}_0(u) + \sum_{n=1}^{\infty} (\underline{A}_n(u) \cos nv + \underline{B}_n(u) \sin nv) \quad (2.28)$$

where

$$\underline{A}_0(u) = \underline{a}_{00} + \underline{a}_{01}u + \underline{a}_{02}u^2 + \underline{a}_{03}u^3 \quad (2.29)$$

$$\underline{A}_n(u) = \underline{a}_{n1}e^{anu} + \underline{a}_{n2}ue^{anu} + \underline{a}_{n3}e^{-anu} + \underline{a}_{n4}ue^{-anu} \quad (2.30)$$

$$\underline{B}_n(u) = \underline{b}_{n1}e^{anu} + \underline{b}_{n2}ue^{anu} + \underline{b}_{n3}e^{-anu} + \underline{b}_{n4}ue^{-anu} \quad (2.31)$$

and $\underline{a}_{n1}, \dots, \underline{b}_{n4}$ are vector-valued constants which are determined by the positional and tangential boundary conditions imposed on the trimlines $u = 0$ and $u = 1$.

The surface $\underline{X}(u, v)$ is then obtained, and is given in the form

$$x(u, v) = X1(u) \cos v \quad (2.32)$$

$$y(u, v) = Y1(u) \sin v \quad (2.33)$$

$$z(u, v) = d_1 + S_{top}u + (3d_2 - 3d_1 - 2S_{top} - S_{bot})u^2 + (S_{bot} + S_{top} + 2d_1 - 2d_2)u^3. \quad (2.34)$$

where $X1(u), Y1(u)$ are of the form of equation (2.30). The analytic surface is illustrated in figure (2.3). The parameters are given by $h = 1.14, R_{top} = 0.5, R_{bot} = 0.5, S_{top} = 2.0, S_{bot} = 0.5$ and $a = 4.0$.



Figure 2.3: The surface blend between a sphere and cone.

2.4 Effect of parameters

In the previous example there are three main parameters which are used to control the blend, those being the tangent parameters S_{top} , S_{bot} and the smoothing parameter a .

The parameter a has been termed the smoothing parameter by Bloor and Wilson, and can have three independent values, one for each of the dependent (x, y, z) distributions. It can be interpreted in this way due to the fact that it controls the relative smoothing of the variables in the u and v directions. Since a changes the length scale in the v direction, it can be shown [66] that a boundary layer exists near $u = 0$ and $u = 1$ which is of thickness $O(1/a)$ in u , which means that changes in the u direction occur over a relatively short length scale for large a and over a large scale for small a . Therefore by altering the smoothing parameter the degree to which the boundary conditions propagate into the blend can be varied.

Cheng further discusses the smoothing parameter a [69]. He maintains that the smoothing parameter can be thought of as a ‘thumbweight’. Thus, for small values of a , a fuller surface is generated while for larger values a blend is generated which has a thinner waistline. The smoothing parameter need not be constant-valued; it can be a function of u and v . Cheng, for instance, tackles the problem of generating a bossing on a ship by considering the smoothing parameter to be variable throughout the surface [69].

For tangent continuity at the trimlines it is required that $\underline{X}_u \times \underline{X}_v$ is parallel to the normal of the primary surface. It has been seen that \underline{X}_v will be determined by the parameterisation of the trimline on the primary surface. However, within the constraints of tangent continuity there is still scope for modification of the surface through the choice of \underline{X}_u at the boundary, i.e. by altering the parameters S_{top} and S_{bot} in this example.

To illustrate these features and the ease with which a blending surface can be manipulated, a few examples will be considered by modifying the original blend between the cone and the sphere where $R_s = 1.0$, $R_c = 1.0$, $R_{top} = R_{bot} = 0.5$ and $h = 1.14$.

Parameter	Figure (2.4)	Figure (2.5)	Figure (2.6)	Figure (2.7)
S_{top}	2.0	2.0	4.0	-4.0
S_{bot}	0.5	0.5	2.05	0.5
a	0.02	8.0	3.0	3.0

Table 2.1: Effect of parameters on surface blend.

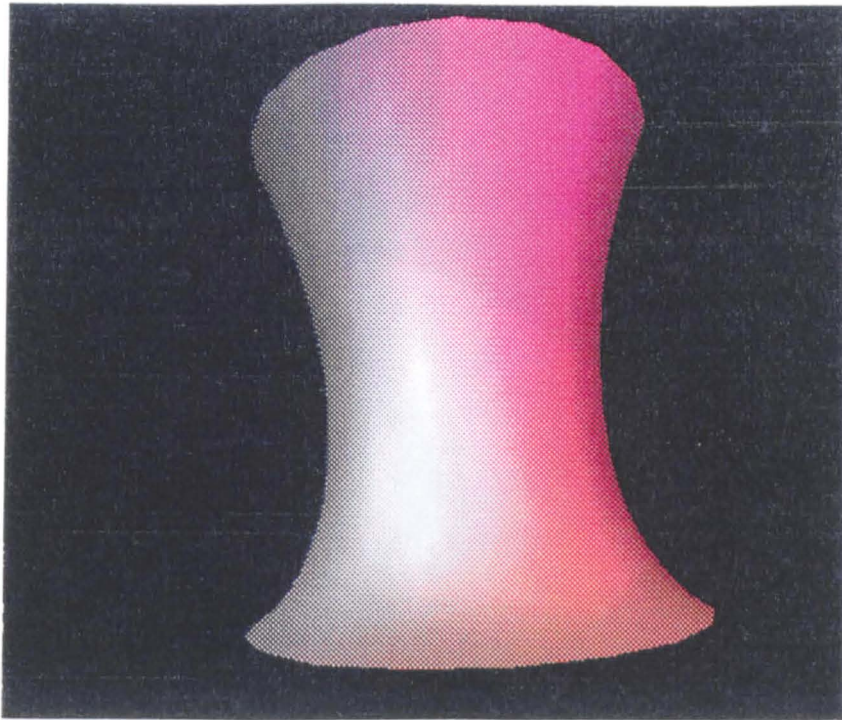


Figure 2.4: Smoothing parameter $a = 0.02$.

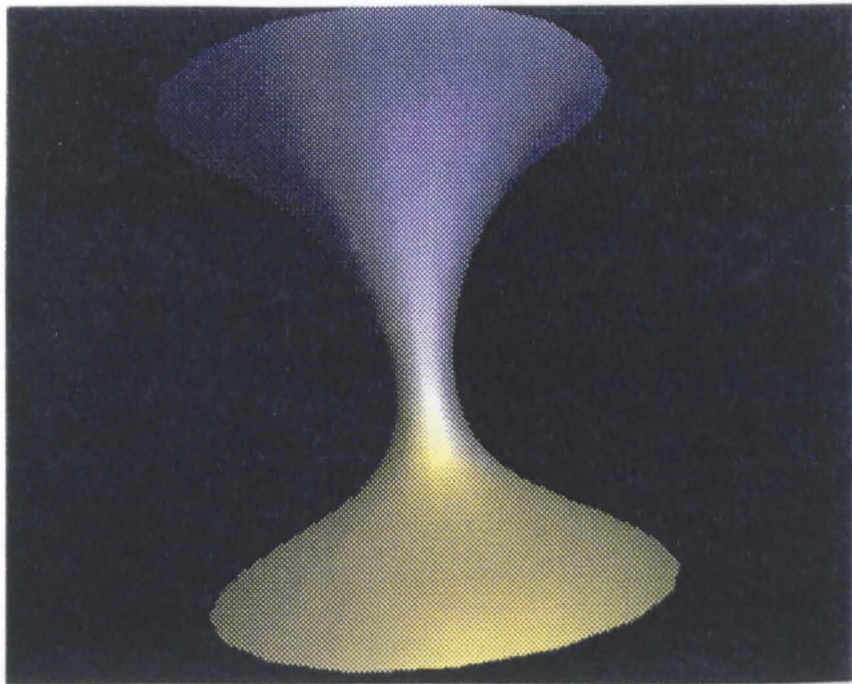


Figure 2.5: Smoothing parameter $a = 8.0$.

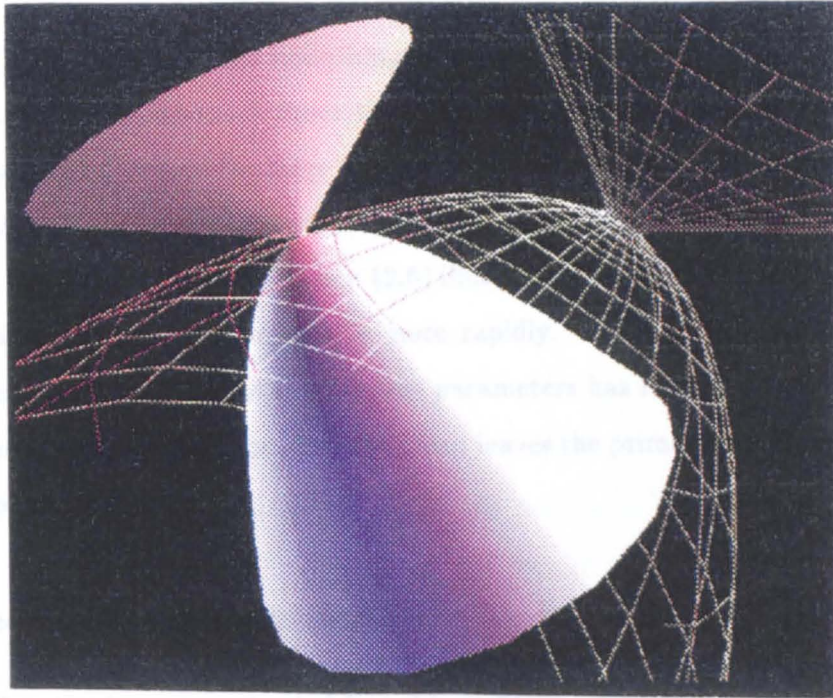


Figure 2.6: Tangent magnitudes increased: $S_{top} = 4.0, S_{bot} = 2.05$.

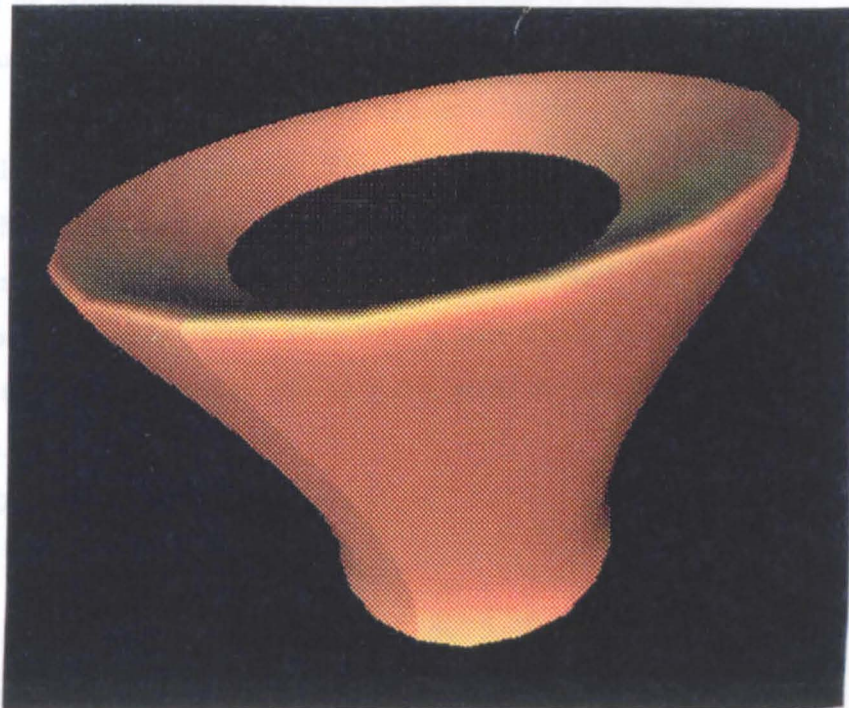


Figure 2.7: Tangent magnitude has change in sign: $S_{top} = -4.0$.

2.4.1 Observations

In figure (2.4) the value of the smoothing parameter has been reduced. This illustrates that the blend has become much fuller than in the original example. This is in marked contrast to figure (2.5) where the large value of the smoothing parameter ensures that the blend is much narrower and the analogy of Cheng, that the parameter can be used as a thumbweight, becomes apparent. Figure (2.6) illustrates that as the tangent magnitudes are increased, the iso u -lines propagate more rapidly. Finally, figure (2.7) illustrates the blend generated when one of the tangent parameters has its sign reversed; while the blend remains tangent continuous, now the blend leaves the primary surface in a direction opposite to before.

2.5 Free form surface design

The PDE method can be extended from blend design into the area of free-form design by relaxation of the continuity conditions on the boundaries [23]. Whereas in the previous example it was required that the PDE surface meet two primary surfaces, in free-form design the positional boundary curves and also the coordinate direction (or ‘tangent’) vectors can be used more freely to control the shape of the surface.

Bloor and Wilson have demonstrated free-form surface generation using 4th order equations. However, as mentioned in the introduction, in Chapter 4 an approximate propeller blade will be generated. This will necessitate the use of a 6th order equation to obtain the surface as it ensures 2nd order derivatives (termed the ‘curvature’ vectors) can be defined around the boundary curves, which adds a new dimension to the control available for the surface patch. Therefore, a brief discussion of free-form surfaces in the context of 6th order equations will be given, so as to illustrate the additional control of the surface.

The PDE being considered here is

$$\left(\frac{\partial^2}{\partial u^2} + a^2 \frac{\partial^2}{\partial v^2} \right)^3 \underline{X} = 0 \quad (2.35)$$

where the periodic analytic solution is of a similar form to equation (2.28); however the expansions for the unknowns are now given by

$$\begin{aligned} \underline{A}_0(u) &= \underline{a}_{00} + \underline{a}_{01}u + \underline{a}_{02}u^2 + \underline{a}_{03}u^3 + \underline{a}_{04}u^4 + \underline{a}_{05}u^5 \\ \underline{A}_n(u) &= \underline{a}_{n1}e^{anu} + \underline{a}_{n2}ue^{anu} + \underline{a}_{n3}e^{-anu} + \underline{a}_{n4}ue^{-anu} + \underline{a}_{n5}u^2e^{anu} + \underline{a}_{n6}u^2e^{-anu} \end{aligned}$$

$$\underline{B}_n(u) = \underline{b}_{n1}e^{anu} + \underline{b}_{n2}ue^{anu} + \underline{b}_{n3}e^{-anu} + \underline{b}_{n4}ue^{-anu} + \underline{b}_{n5}u^2e^{anu} + \underline{b}_{n6}u^2e^{-anu}$$

and $\underline{a}_{n1}, \dots, \underline{b}_{n6}$ are vector-valued constants determined by the positional, tangential and curvature boundary conditions. The expressions for $\underline{A}_0(u)$, $\underline{A}_n(u)$ and $\underline{B}_n(u)$ have been obtained by the standard procedure of separation of variables as described in Appendix A.

As an example of the versatility of the additional parameters, the generation of a simple wine glass will be considered.

2.5.1 A wine glass

To demonstrate the effect of the additional derivatives on the generated surface, it is a good idea to consider a simple design. Generating a wine glass bulb does not prove very difficult using the original 4th order elliptic equation to obtain the surface, as has been demonstrated by Lowe [62]. However, generating a wine glass which includes the bulb, the stem and the base from a single surface patch proves more difficult if a suitable shape is to be realised, since we cannot get enough variation via the surface control.

By considering the boundary conditions to be the rim and the base of the glass, the surface will simply be a surface of revolution whose cross-sectional radius varies with the height of the cross section above the base.

Thus, the positional conditions can be given by

$$x(0, v) = R_{top} \cos v \quad (2.36)$$

$$y(0, v) = R_{top} \sin v \quad (2.37)$$

$$z(0, v) = d \quad (2.38)$$

and

$$x(1, v) = R_{bot} \cos v \quad (2.39)$$

$$y(1, v) = R_{bot} \sin v \quad (2.40)$$

$$z(1, v) = 0 \quad (2.41)$$

over the domain $0 \leq u \leq 1$ and $0 \leq v \leq 2\pi$. The tangency conditions will take a similar form;

$$x_u(0, v) = S_t \cos v \quad (2.42)$$

$$y_u(0, v) = S_t \sin v \quad (2.43)$$

$$z_u(0, v) = S_{top} \quad (2.44)$$

and

$$x_u(1, v) = S_b \cos v \quad (2.45)$$

$$y_u(1, v) = S_b \sin v \quad (2.46)$$

$$z_u(1, v) = S_{bot} \quad (2.47)$$

where S_t, S_b control the rate at which the surface propagates radially, and S_{top}, S_{bot} the z derivatives. The posed boundary conditions have the analytic solution, if considered as the solution to the 4th order PDE;

$$x = [(b_1 + b_2 u) \cosh(au) + (b_3 + b_4 u) \sinh(au)] \cos v \quad (2.48)$$

$$y = [(c_1 + c_2 u) \cosh(au) + (c_3 + c_4 u) \sinh(au)] \sin v \quad (2.49)$$

$$z = d + S_{top} u + (-3d - 2S_{top} - S_{bot})u^2 + (2d + S_{bot} + S_{top})u^3 \quad (2.50)$$

where b_1, \dots, c_4 are obtained from the boundary conditions. The generated wine glass is illustrated in figure (2.8) at the end of the section.

2.5.2 Curvature derivatives

It is probable that the shape of the glass is not as desired. The shape of the glass in figure (2.8) is more of a blended shape between the bulb of the glass and the base circle. It would look more realistic if the stem were longer with the base of the bulb having a flatter appearance than that of figure (2.8). By including the second derivative terms such that

$$x_{uu}(0, v) = C_t \cos v \quad (2.51)$$

$$y_{uu}(0, v) = C_t \sin v \quad (2.52)$$

$$z_{uu}(0, v) = C_{top} \quad (2.53)$$

at the glass rim and

$$x_{uu}(1, v) = C_b \cos v \quad (2.54)$$

$$y_{uu}(1, v) = C_b \sin v \quad (2.55)$$

$$z_{uu}(1, v) = C_{bot} \quad (2.56)$$

at the base, where $C_t, C_b, C_{top}, C_{bot}$ control the rate of change of the second derivatives. This means that the regions where the surface is at its fullest can be moved around.

Figure (2.9) illustrates how the region of the bowl is contained within an area closer to the rim of the glass. Also the rate of change of the tangents can be controlled at the base, so that the stem is straighter than in figure (2.8) where the stem is quite curved. Figure (2.10) illustrates the complete design where not only is the bowl region restricted to a certain area, but the base of the bowl is made to flatten out before smoothly joining onto the fairly straight stem of the glass. These shapes would not have been achievable with only tangent control at the boundaries. Finally, it can be seen in figure (2.11) how extreme values of the curvature parameters can be used to make the surface alter direction several times throughout the surface. This example illustrates a coarse impression of a 'standard' lamp.

This discussion illustrates the extra control over the surface shape that can be exercised by using a 6th order equation. Particular emphasis is placed on the aspect of enabling the direction of the surface to twist several times. It is with this in mind that the initial surface design of a propeller blade will be considered.

Par	Fig (2.8)	Fig (2.9)	Par	Fig (2.8)	Fig (2.9)	Par	Fig (2.8)	Fig (2.9)
R_{top}	3.0	3.0	S_{top}	-10.0	-27.0	C_{top}	0.0	170.0
R_{bot}	3.0	3.0	S_{bot}	-5.0	-3.0	C_{bot}	0.0	0.0
d	10.0	10.0	S_t	5.0	10.0	C_t	0.0	3.0
a	1.8	12.0	S_b	16.0	19.0	C_b	0.0	60.0

Table 2.2: Parameter values for the original and modified wine glass.

Par	(2.10)	(2.11)	Par	(2.10)	(2.11)	Par	(2.10)	(2.11)
R_{top}	0.9	1.0	S_{top}	-27.0	-27.0	C_{top}	240.0	350.0
R_{bot}	0.7	0.8	S_{bot}	-1.0	0.01	C_{bot}	10.0	5.0
d	5.0	5.0	S_t	5.0	6.0	C_t	8.0	320.0
a	14.0	14.0	S_b	4.0	6.0	C_b	12.0	-50.0

Table 2.3: Parameter values for the final wine glass and 'standard lamp'.

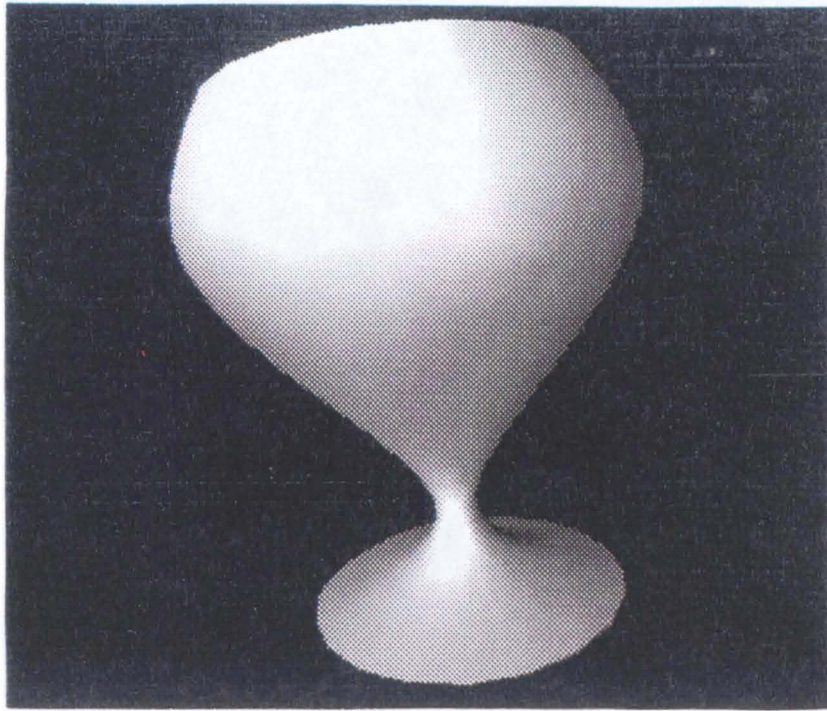


Figure 2.8: The original wine glass produced using no second derivatives.

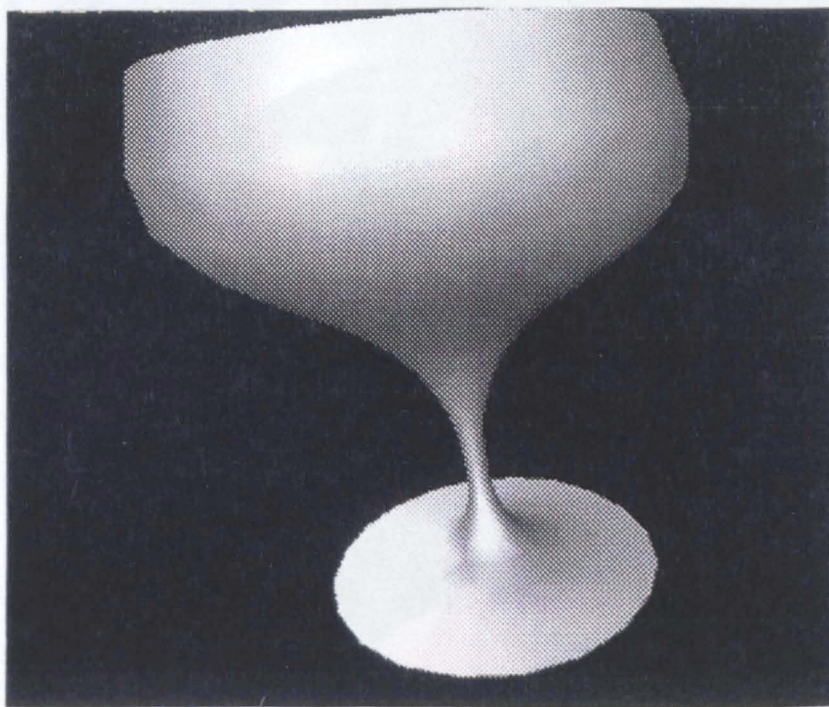


Figure 2.9: The inclusion of curvature derivatives.

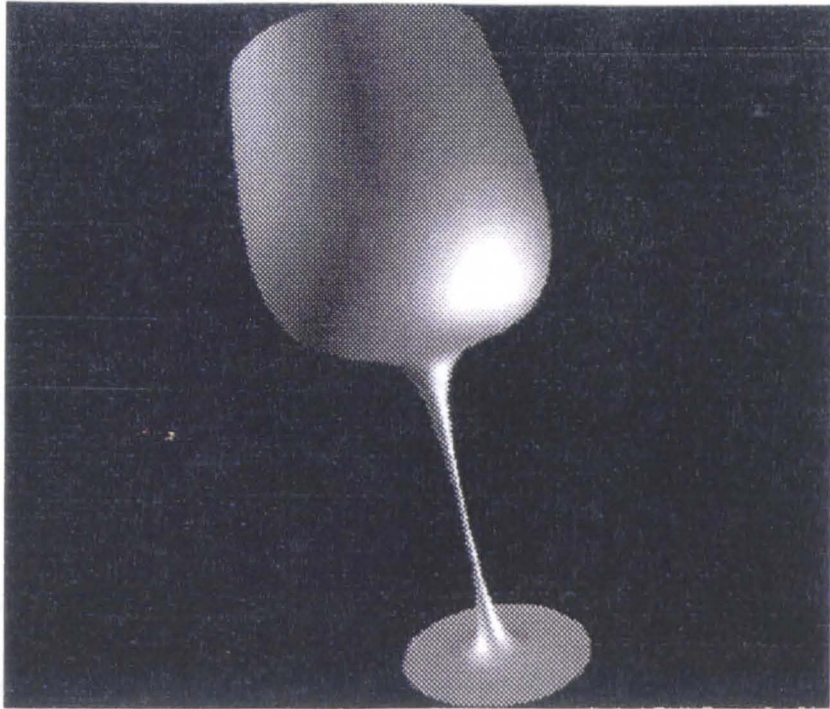


Figure 2.10: The produced wine glass using curvature parameters.

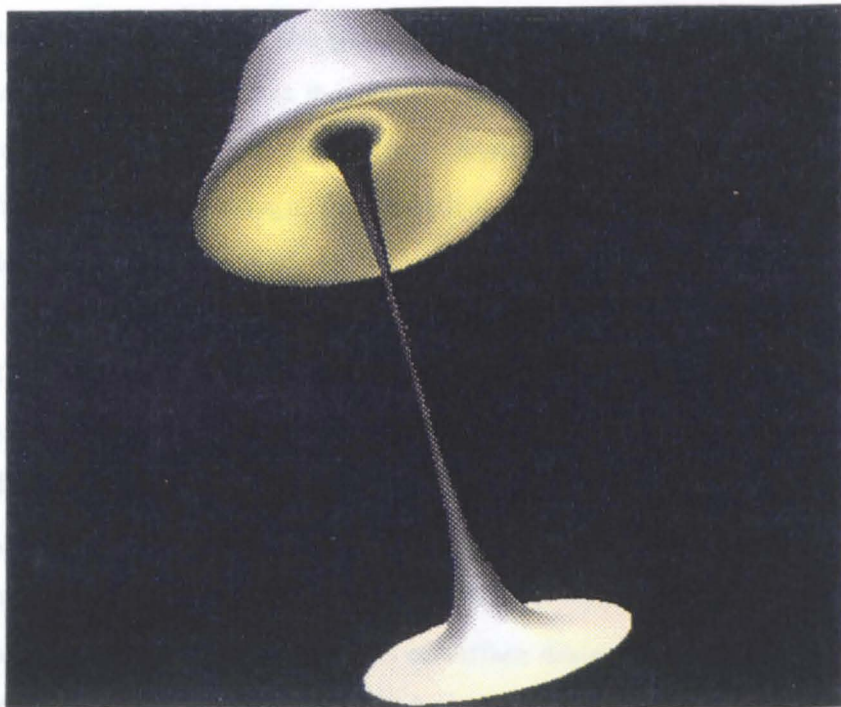


Figure 2.11: An example of extreme curvature conditions on the surface.

Chapter 3

Generic design of propellers

3.1 Introduction

In the introduction some of the requirements of generated propeller surfaces were described. These included the requirements that the surface should be unambiguous when rendered at a workstation and that the manipulation of the surface via a set of control parameters should preferably be intuitively obvious, and in the case of the PDE generated surface, that a small number of parameters govern the surface once the boundary curves are described. Furthermore, for the particular example of the propeller blade design, the blade surface should be such that it is smooth, or fair.

In the last chapter the PDE method was illustrated by consideration of blend generation and free-form surface design, from which it was seen that once an initial boundary value problem had been specified, the parameter set governing the problem completely defines the surface and facilitates control of its shape. Again it is emphasised that, compared to other surface generation techniques such as B-spline surfaces, the set of shape parameters specifying the surface is small. Although boundary curves need to be defined for the PDE surface patch, boundary curves need also to be defined for B-spline surfaces, and indeed, B-spline curves could be used as boundary conditions for PDE surfaces. Secondly, it was illustrated that the PDE method has the characteristic of producing smooth surfaces which are fair within the context of surface design [24].

In this chapter it will be demonstrated how the PDE method can be used to generate a basic propeller blade shape. Few functional characteristics of the propeller will be considered, which implies that the initial design will mainly be for its visual appearance. This is in order that a simple boundary problem can be set up, and the way in which

different parameters alter the shape of the blade demonstrated. This simple illustration will be followed in the next chapter by a complete description of how existing propeller geometries can be represented.

Additionally, in this chapter it will be demonstrated how the PDE method can be used to integrate the physical properties of the generated surface with its geometric design. By assuming the geometry of a simple airscrew to be similar to that of an aircraft wing, we will illustrate how Prandtl's lifting line theory can be used to obtain the aerodynamic characteristics of the wing. It will further be demonstrated, how, by altering certain geometric parameters which control the shape of the wing, the aerodynamic properties can be altered. The lifting line theory implemented assumes that each local section of the wing is travelling in a uniform flow that has the characteristics of the local flow.

This example is used to illustrate the first stages in a design technique which involves the idea of being able to optimise some measure of merit function over the space of the geometric and physical parameter set.

However, to arrive at this latter stage, it must first be demonstrated how the PDE method can be used to design and represent propeller blade surfaces.

3.2 Propeller generation

A propeller blade is a complex three-dimensional form, as was described in section (1.5.1); with the geometry most often defined by a designer in terms of two-dimensional data consisting of the form of blade sections, from which the three-dimensional geometry of the complete blade is generated. The two-dimensional data defines a section which is of a shape similar to that of an airfoil, and is located at intervals along the span of the blade and varies in length, maximum thickness, maximum camber at each location, given by $x = r/R$.

As described in section (1.5.1) the physical geometry of the propeller is derived by a sequence of rotations of the blade sections about the spindle axis, with each section being wrapped onto a fictitious cylinder. This is known as the projected view of the propeller [28].

The propeller can actually be represented in two forms; the projected view and the expanded view of the propeller. The expanded view is used to give an illustration of the chordwise distribution of the blade sections and may include overlaid views of other distributions, such as the maximum thickness at each section of the blade span, and the

pitch curve which shows the angle to which the expanded sections are aligned with the incoming local flow, which aids the generation of the local lift of the section.

An illustration is included below of the expanded and projected view of a propeller blade taken from the geometry given by Eckhardt and Morgen [27].

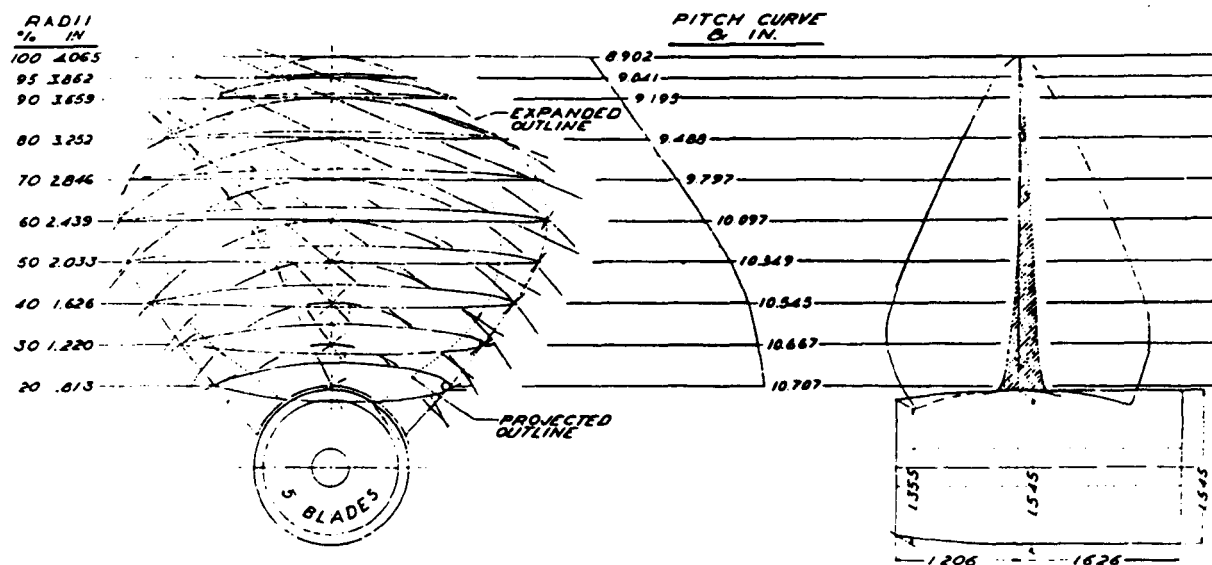


Figure 3.1: The expanded and projected view of the propeller.

3.2.1 Section curve

Since the local airfoil section throughout the propeller blade is inherently the same, with the only differences being in its chordlength, maximum thickness, and maximum camber distributions, it can be seen that to generate a propeller blade surface it is reasonable to define some airfoil section as the boundary condition at one end of the PDE surface patch. The surface can then be generated by taking the boundary conditions on the other trimline to be the tip of the propeller.

In the next chapter an actual airfoil design will be used, but at the present time, to illustrate the generic model, the simple curve

$$x = c \cos v \tag{3.1}$$

$$y = t_x \sin 2v \quad (3.2)$$

over the range $-\pi/2 \leq v \leq \pi/2$ will be used, where c and t_x are positive constants to be defined later.

It should be noted that the range over which v varies is here different from in previous examples where the range was taken from 0 to 2π . This new parameter range is chosen so that the singular nature of the surface at the trailing edge can be accounted for and the solution obtained in closed form.

That the trailing edge is sharp is important. In the case of inviscid flow around a sharp corner, the velocity at the corner becomes infinite [70]; however in the case of a real flow, the velocity remains finite and because of the large velocity gradients, the flow separates from the sharp edge resulting in a vortex as in figure (3.2).

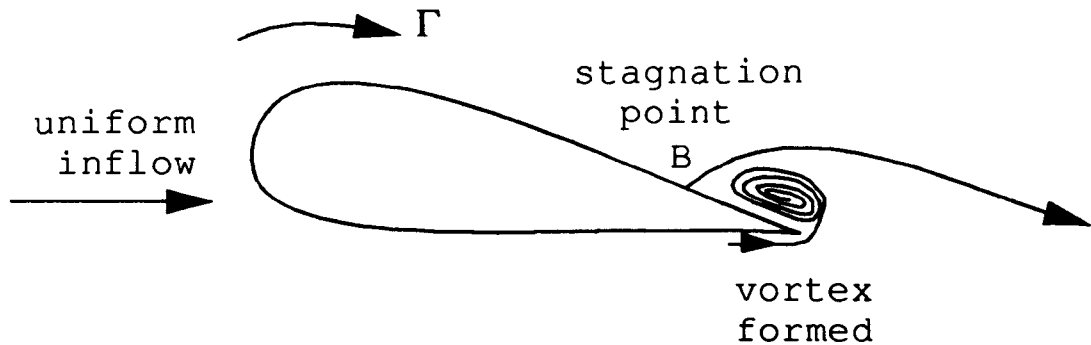


Figure 3.2: The vortex issued round a sharp corner.

In a starting flow this vortex is shed and thus induces a compensating clockwise circulation to satisfy Kelvin's circulation theorem [70]. This circulation causes the stagnation point B to move towards the trailing edge. Only when the flow leaves the trailing edge smoothly will a stable condition be achieved, and this is known as the Kutta Condition [70]. This is what occurs in a real fluid and the vorticity which is detached from the trailing edge and is left downstream is known as the starting vortex [70], as illustrated in figure (3.3).

Unless the trailing edge is sharp it is not possible for the flow to leave both the upper and lower surfaces smoothly. In reality, since the trailing edge is always slightly rounded a very thin wake is formed which extends some distance downstream. This trailing wake is important in determining the flow characteristics and will be considered more fully in Chapter 5.

In this example the trailing edge is sharp, whereas in the actual geometry considered

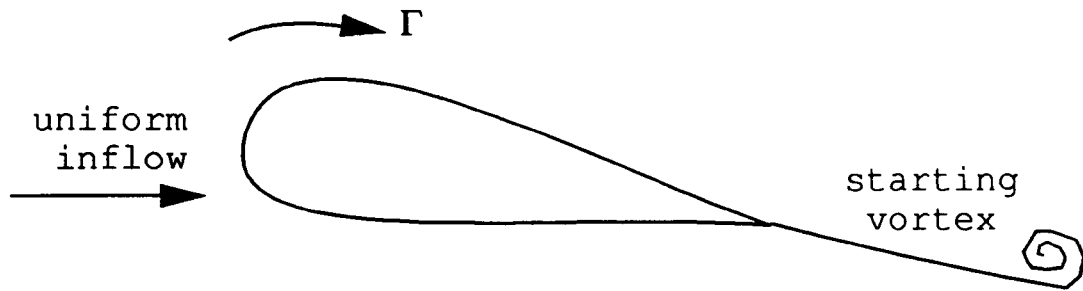


Figure 3.3: The starting vortex from the Kutta condition.

in the next chapter, the trailing edge will be slightly rounded as in the real blade.

To recap, in the PDE method, boundary conditions are defined at the root of the blade, and also at the tip, which means that a blade will be generated with the property of having airfoil like sections along its span. This method of generating the propeller blade is different in many aspects to conventional methods of propeller blade construction.

Umlauf [71], for instance, obtains the propeller blade surface from knowing the section profile at each span station. These sections are then rotated and curved to form a skeleton for the propeller blade. Then, by using a skinning method a surface is laid over these curves. This is achieved by fitting a B-spline surface to the given section curves. With this technique, Umlauf has the actual data given at certain sections, but must minimise the errors present in the fairness of the generated surface, whereas the PDE method naturally produces a fair surface, but does not fit exactly the section profiles specified. If existing propellers need to be represented then the problem the PDE method must overcome is the approximation of various airfoil properties at each section, which as we shall see in the next chapter proves possible with the control afforded by the PDE method. The fact that these distributions are continuous functions throughout the span is essential to this approach.

It must be borne in mind at this stage that we do not envisage the PDE method as a representational tool in the way that B-spline surfaces can be used. However, in order to perform some realistic optimisation, as will be seen in Chapter 6, it is necessary to have some realistic geometry as a point from which to start. The ability to alter, and improve, this generated geometry, will demonstrate the practicability of the PDE method of design, the likes of which would not be feasible for a B-spline surface.

3.2.2 Boundary conditions

In order to generate a blade shape using the PDE method we need to define boundary conditions. A simple set of boundary conditions which can be used to generate the blade shape are given below. The basic airfoil shape is of a slightly different form to that of equations (3.1-2) since twist and camber have been incorporated into the design. As a closed loop of surface is considered, the conditions are given solely on the $u = 0$ and $u = 1$ trimlines by

$$x(0, v) = f \quad (3.3)$$

$$y(0, v) = 0 \quad (3.4)$$

$$z(0, v) = d \quad (3.5)$$

at the tip of the blade, and

$$x(1, v) = (c \cos \beta + m_x \sin \beta) \cos v + t_x \sin \beta \sin 2v - \frac{m_x}{2} (\cos 2v + 1) \sin \beta \quad (3.6)$$

$$y(1, v) = t_x \cos \beta \sin 2v + (m_x \cos \beta - c \sin \beta) \cos v - \frac{m_x}{2} (\cos 2v + 1) \cos \beta \quad (3.7)$$

$$z(1, v) = r_h \quad (3.8)$$

at the root of the blade, where

- c defines the base length of the section
- t_x defines the maximum base thickness of the section
- d is the span or radius of the blade
- r_h is the radius of the central hub
- f is the position of the tip.

The parameter β is used to produce the twist or pitch distribution along the blade span so that each airfoil section is at an appropriate angle of incidence to the inflow for the given section in order to produce the required lift. The parameter m_x is used to give the basic section profile a camber distribution, which results in a different camber value at each section as it, like the twist distribution, is dependent on the span station, i.e. the value of u . The camber distribution implies that the section is not symmetrical about its centreline (unless $m_x = 0$) and so aids in the generation of lift of the section. Therefore, the complete section curve given at the root of the propeller, the character of which is maintained in type throughout the blade is shown in figure (3.4).

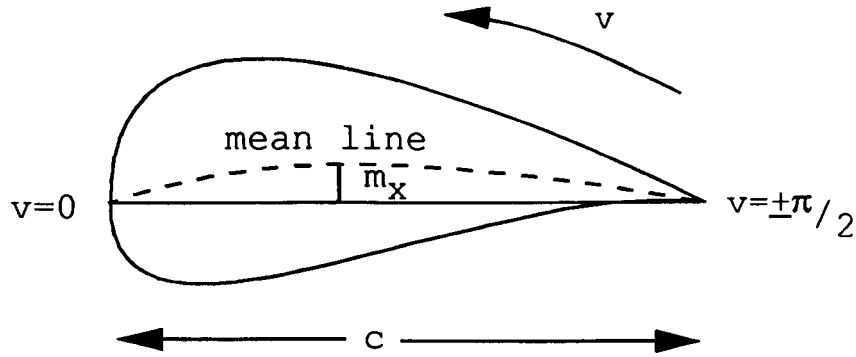


Figure 3.4: The profile used for the propeller blade section at the root.

The tangency conditions are given by

$$x_u(0, v) = S_x \cos 2v \quad (3.9)$$

$$y_u(0, v) = S_y \sin 2v \quad (3.10)$$

$$z_u(0, v) = S_{top} \quad (3.11)$$

at the tip, and

$$x_u(1, v) = E_x \cos 2v \quad (3.12)$$

$$y_u(1, v) = E_y \sin 2v \quad (3.13)$$

$$z_u(1, v) = S_{bot} \quad (3.14)$$

at the root. This produces a shape for the propeller blade which is similar in appearance to the expanded view, and which is given by the analytic solution to the PDE

$$x(u, v) = x(u) + X1 \cos v + XS2 \sin 2v + X2 \cos 2v \quad (3.15)$$

$$y(u, v) = y(u) + Y2 \sin 2v + YC1 \cos v + YC2 \cos 2v \quad (3.16)$$

$$z(u, v) = z(u) \quad (3.17)$$

where $x(u), y(u), z(u)$ are of the form of equation (2.29) and $X1, XS2$ etc. are of the form of equation (2.30). Due to the nature of the parameterisation of the boundary conditions the sharp trailing edge will be maintained throughout the span.

3.2.3 Parameter control

The complete parameter set comprises the three values of the smoothing parameter a_x, a_y and a_z and the six parameters defining the tangent magnitudes, thereby enabling

the detailed blade shape to be manipulated with only nine parameters. In addition there are of course five parameters (c, t_x, β, m_x, d) which define the geometry of the blade section and blade.

To show the ease with which the surface can be manipulated, figure (3.5) and figure (3.6) illustrate the two very different propellers; an airscrew and a marine propeller. It should further be noted, that in the case of the marine propeller many of the parameters can be held fixed, and yet a good likeness of the propeller can still be obtained e.g. the propeller can be redesigned with as little as three parameters (S_x, S_y and S_{bot}).

Of course, many of the actual features of a propeller are absent. The pitch of this PDE marine propeller does not follow any prescribed variation from the tip to the root, and this is also true for the camber distribution. In reality the camber distribution of an actual blade will be close to zero at the tip and achieve a maximum near the centre of the blade span. For an actual propeller these distributions need to be more closely controlled and, in the next chapter these distributions will be incorporated into the PDE propeller model.

Parameter	Air	Marine	Parameter	Air	Marine	Parameter	Air	Marine
a_x	1.0	0.1	E_x	3.0	0.6	d	12.0	4.0
a_y	1.0	0.1	E_y	1.6	0.2	m_x	0.3	0.2
a_z	1.0	1.0	S_{top}	3.0	0.0	c	1.5	0.75
S_x	2.0	10.0	S_{bot}	5.0	1.6	t_x	0.2	0.15
S_y	1.3	0.3	r_h	2.4	0.8	β	0.9	1.7

Table 3.1: Parameter values for the two propeller blades.

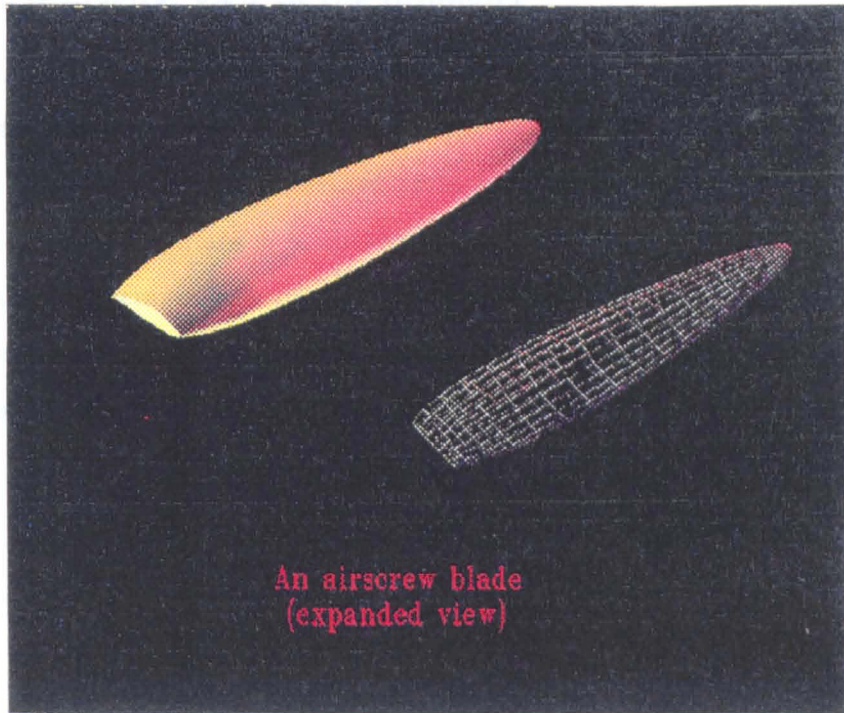


Figure 3.5: The airscrew blade.

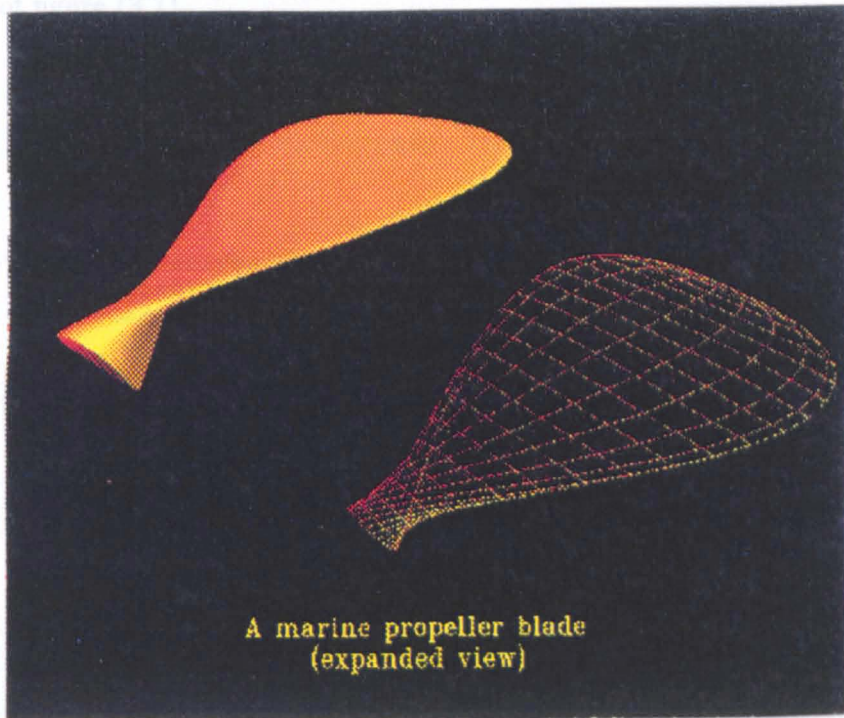


Figure 3.6: The marine propeller blade.

3.2.4 The projected view of the propeller

To generate the projected view or actual propeller geometry, each section must be curved about a fictitious cylinder. This can either be done by performing the appropriate geometric manipulation of the generated surface, given in the previous section, which will ensure the smooth surface is maintained, or the alternative way is to set up a new boundary-value problem, and to solve for the final blade geometry directly. A new set of boundary conditions can be obtained by curving the original boundary conditions (3.6-8), at the root of the blade, around the central hub (which is of radius r_h) such that if

$$r^2 = x(1, v)^2 + z(1, v)^2 \tag{3.18}$$

then

$$x'(1, v) = \frac{z(1, v) * x(1, v)}{r} \tag{3.19}$$

$$y'(1, v) = y(1, v) \tag{3.20}$$

$$z'(1, v) = \frac{z(1, v)^2}{r} \tag{3.21}$$

where x', y', z' are the new boundary conditions, and the derivative conditions are of the same form as in the previous example. The boundary value problem to be posed is now of the form of figure (3.7).

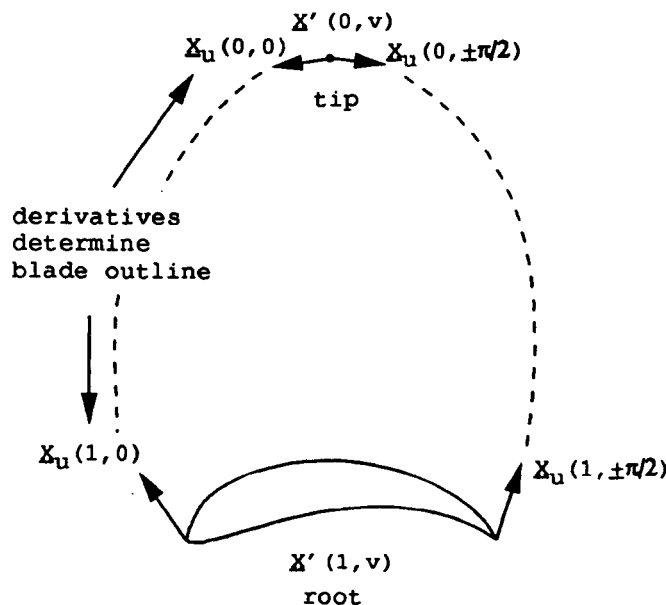


Figure 3.7: The boundary value problem.

The analytic solution to the particular PDE problem can be obtained in general when a closed loop of surface is required, and when the boundary conditions are of a sinusoidal

nature, i.e. expressed in terms of a sum of simple Fourier modes. The boundary conditions given by equations (3.19-21) are no longer of this form and so the boundary conditions must now be given as discrete data points around the curve. This now means that the solution to the elliptic PDE must be determined from numerical techniques.

3.3 Numerical solutions to elliptic PDEs

Of the numerical approximation methods available for solving differential equations, those employing finite difference schemes are among the most frequently used and easily applicable to the problem in hand [67], since the solution domain is a rectangular patch.

Finite difference methods are implemented by firstly discretising the domain over which the solution is to be obtained, by a rectangular mesh. The finite differences are approximations in the sense that the derivatives of a function at a point within the domain are approximated by differences in the function value over appropriate small intervals. Therefore, the accuracy of the solutions to the PDEs is determined by how finely the solution domain is discretised by the user, and also by the rounding-error of the computing hardware.

For the cases considered in this thesis the mesh can be formed simply from the isoparametric lines of u and v . An approximate solution to the PDE (2.4) is then found at the points of intersection, the mesh points, by solving a system of linear algebraic equations which are obtained from the approximation to the PDE at each mesh point and its neighbouring points.

The details of the solution process as it relates to the particular PDE used in this thesis is outlined in the next section.

3.3.1 Finite difference approximations to derivatives

If the solution to the PDE

$$\left(\frac{\partial^2}{\partial u^2} + a^2 \frac{\partial^2}{\partial v^2} \right) X = 0 \quad (3.22)$$

is considered over the finite domain $0 \leq u \leq 1$, $-\pi/2 \leq v \leq \pi/2$ then a mesh can be generated over the domain of the solution by considering the isoparametric lines of u and v . If the (u, v) plane is subdivided into sets of equal rectangles of sides $\delta u = h$, $\delta v = k$ then the coordinates (u, v) of the representative mesh point P will be

$$u = ih, \quad v = jk, \quad (3.23)$$

where i, j are integers, and the value of $\underline{X}(u, v)$ at the mesh point P will be given by

$$\underline{X}_P = \underline{X}(ih, jk) = (x_{i,j}, y_{i,j}, z_{i,j}) \quad (3.24)$$

as illustrated in figure (3.8).

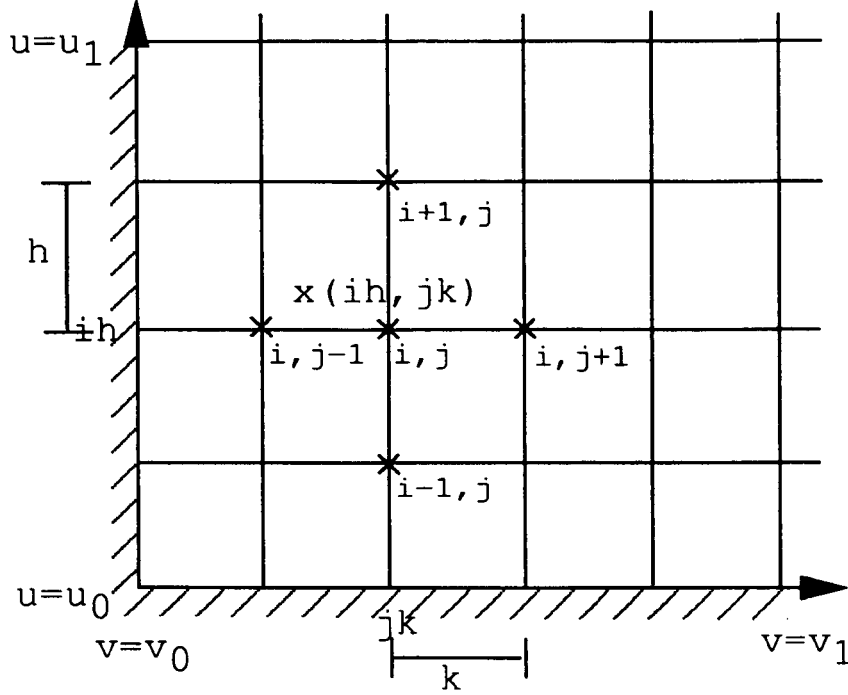


Figure 3.8: The finite difference mesh and points.

Further, if the (u, v) domain is of length $u = (u_1 - u_0)$ with $i = p$ mesh points in this direction, and $v = (v_1 - v_0)$ with $j = q$ mesh points, then

$$h = \frac{(u_1 - u_0)}{(p - 1)} \quad \text{and} \quad k = \frac{(v_1 - v_0)}{(q - 1)}, \quad (3.25)$$

and there are $(p - 2)(q - 2)$ unknown values of \underline{X} to be obtained.

If the x -component of \underline{X} is now considered to be single-valued, finite and continuous, then by applying a Taylor expansion, the equations

$$x(u + h, v) = x(u, v) + hx_u(u, v) + 1/2h^2x_{uu}(u, v) + 1/6h^3x_{uuu}(u, v) + \dots \quad (3.26)$$

$$x(u - h, v) = x(u, v) - hx_u(u, v) + 1/2h^2x_{uu}(u, v) - 1/6h^3x_{uuu}(u, v) + \dots \quad (3.27)$$

are obtained.

Addition of these expansions gives

$$x_{uu}(u, v) = \left(\frac{\partial^2 x}{\partial u^2} \right) \sim \frac{1}{h^2} \{x(u + h, v) - 2x(u, v) + x(u - h, v)\} + O(h^2) \quad (3.28)$$

where $O(h^2)$ denotes the leading order of the error in the finite difference approximation, and subtracting gives

$$x_u(u, v) = \left(\frac{\partial x}{\partial u} \right) \sim \frac{1}{2h} \{x(u+h, v) - x(u-h, v)\} + O(h^2) \quad (3.29)$$

with an error of order $O(h^2)$, and which is termed a central difference approximation.

Hence, we have a finite difference approximation to the term $\frac{\partial^2 x}{\partial u^2}$, and in a similar manner for the term $\frac{\partial^2 x}{\partial v^2}$ we can obtain the finite difference approximation

$$x_{vv}(u, v) \sim \frac{1}{k^2} \{x(u, v+k) - 2x(u, v) + x(u, v-k)\} + O(k^2). \quad (3.30)$$

These finite difference approximations can be applied at each of the mesh points, to give the modified Laplacian operator $\nabla^2 x = 0$, which can conveniently be represented by the pattern

$$\begin{bmatrix} & \frac{a^2 h^2}{k^2} & \\ 1 & -2 \left(1 + \frac{a^2 h^2}{k^2} \right) & 1 \\ & \frac{a^2 h^2}{k^2} & \end{bmatrix} x_{ij} = 0 \quad (3.31)$$

for the mesh points ($i = 1, \dots, p, j = 1, \dots, q$), and by writing

$$r^2 = \frac{a^2 h^2}{k^2} \quad (3.32)$$

the complete finite difference formula for the mesh points for equation (3.22) may be represented by

$$\begin{bmatrix} & & r^4 & & \\ & r^2 & -2r^2(1+2r^2) & r^2 & \\ 1 & -4(1+r^2) & (6+8r^2+6r^4) & -4(1+r^2) & 1 \\ & r^2 & -2r^2(1+2r^2) & r^2 & \\ & & r^4 & & \end{bmatrix} \underline{X} = 0. \quad (3.33)$$

where (3.33) is derived in Appendix C.

Note that the function value at each mesh point is related by (3.33) to the function value at surrounding mesh points, some of which are unknown, and some of which are given by discrete boundary data, and so by applying the difference formula at each mesh location, a system of linear equations of the form

$$A\underline{x} = b \quad (3.34)$$

is obtained, where A, b are the matrices obtained from the difference formulae, and \underline{x} is a vector whose components are the unknown function values at the mesh points.

3.3.2 Derivative boundary conditions

With reference to figure (3.9) in the finite difference scheme, the difference operator (3.33) at the point $P_{i,1}$ will require the function values at the surrounding points $P_{i,2}, P_{i,3}, P_{i,0}, P_{i,-1}$ in order to obtain the function value at the mesh location. The point $P_{i,-1}$ clearly lies outside the bounds of the mesh and so a way to determine it must be found.

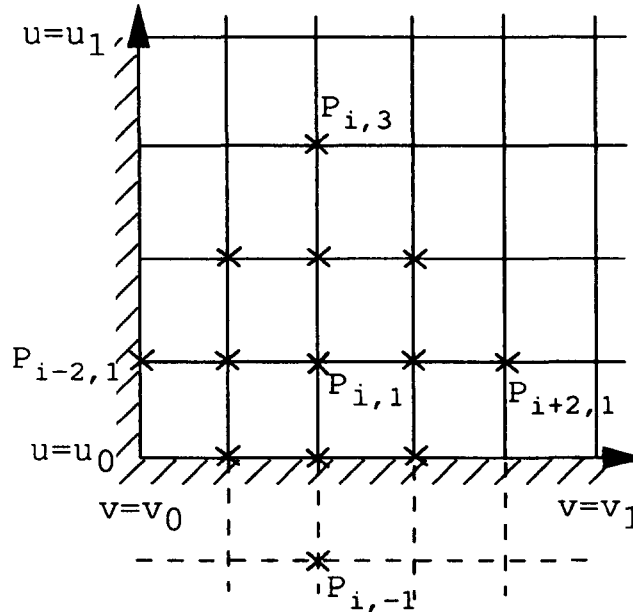


Figure 3.9: The finite difference grid.

This is achieved by consideration of a discrete approximation to the derivative conditions given at each mesh point on the boundary, which are defined by

$$\frac{\partial x}{\partial u} = g(v) \tag{3.35}$$

say. The function value at the external mesh point $P_{i,-1}$ can then be obtained, since from the central difference operator (3.29) the derivative condition on the boundary is given as

$$\frac{x_{i,1} - x_{i,-1}}{2h} = g_i, \tag{3.36}$$

where $x_{i,-1}$ is the external value at the external mesh point $P_{i,-1}$, from which we obtain the expression for the external mesh point as

$$x_{i,-1} = x_{i,1} - 2hg_i \tag{3.37}$$

Then, by substitution of equation (3.37) back into the finite difference scheme, all function values can now be expressed in terms of other surrounding function values and

known boundary and derivative conditions, and so the linear system of equations can now be solved.

3.3.3 Solutions of linear equations

For linear boundary-value problems of this type, where the average size of the surface grid is not too coarse, the solution of the simultaneous equations (3.34) will be time consuming. Methods of solution of the equations include direct and iterative methods.

Smith [67] observes that direct methods such as Gaussian elimination [72] or lower-upper decomposition solve the system in a known number of steps. However the matrix A associated with the linear equations will be sparse and banded, implying a large number of zero-valued elements. In this situation, iterative solution processes are more appropriate than direct methods. Methods such as Gaussian elimination need to fill in the zero elements with non-zero numbers which are stored for subsequent stages, whereas iterative methods ignore zero elements and so more efficiently solve this type of problem. One of the faster iterative processes is that of the Successive Over Relaxation (SOR) iteration.

3.3.4 Successive over relaxation iteration

Iterative methods use an initial approximation to obtain a second more accurate approximation to the solution, which is then in turn used, in a similar fashion to obtain a third approximation; and so on, until the current approximation satisfies the difference equation to a given tolerance and the solution has converged [72]. Thus, if the n^{th} approximation to x_i is given by $x_i^{(n)}$, then by rewriting the Gauss-Seidel equations [67], the $(n+1)^{\text{th}}$ approximation in the Successive Over Relaxation iteration can be defined as

$$x_i^{(n+1)} = x_i^{(n)} + \frac{\omega}{a_{ii}} \left[b_i - \sum_{j=1}^{i-1} a_{ij} x_j^{(n+1)} - \sum_{j=1}^m a_{ij} x_j^{(n)} \right] \quad i = 1, \dots, m \quad (3.38)$$

or in the alternative form

$$x_i^{(n+1)} = \frac{\omega}{a_{ii}} \left[b_i - \sum_{j=1}^{i-1} a_{ij} x_j^{(n+1)} - \sum_{j=i+1}^m a_{ij} x_j^{(n)} \right] - (\omega - 1)x_i^{(n)} \quad i = 1, \dots, m \quad (3.39)$$

where the factor ω is called the acceleration parameter or relaxation factor and is given by

$$1 < \omega < 2 \quad (3.40)$$

with the special case of $\omega = 1$ giving the Gauss-Seidel iteration. For the example with 45 mesh points it can be shown [72] that the error in the SOR method will decrease by a factor of 0.87 in each iteration, which is about thirty times as fast as the Gauss-Seidel method. This becomes markedly better as the number of mesh points increases.

One way of measuring the extent to which the approximate solution can be said to have converged to the actual solution is by calculating the residual of the current approximation. The residual is a measure of the amount by which the current approximation fails to satisfy the difference equations. This is obtained by substituting the iterated values x_i back into the original difference equation, to obtain the values

$$R_i \equiv b_i - Ax_i^{(n)} \quad (3.41)$$

at each of the $i = 1, \dots, p \cdot q = m$ mesh points. The root-mean-square (RMS) value is then taken as a measure of the accuracy of the approximation of the solution to the equation, over the whole domain. This is taken as

$$RMS = \sqrt{\frac{\sum R_i^2}{m}} \quad i = 1, \dots, m. \quad (3.42)$$

When this value has fallen below a given tolerance, then the solution is said to have converged.

3.3.5 The generated propeller

The boundary conditions used to generate each propeller blade were given in sections (3.2.2-4). These were applied to a mesh of size 21 by 21 and each Cartesian component (x, y, z) was solved using the SOR iteration. The number of iterations required for convergence for each component are as follows, with figures (3.10) and (3.11) illustrating the generated propeller.

Component	Residual	Number of iterations
x	$9.9934e - 06$	1078
y	$9.9563e - 06$	1124
z	$9.9599e - 06$	1476

Table 3.2: Residuals for the SOR iteration.

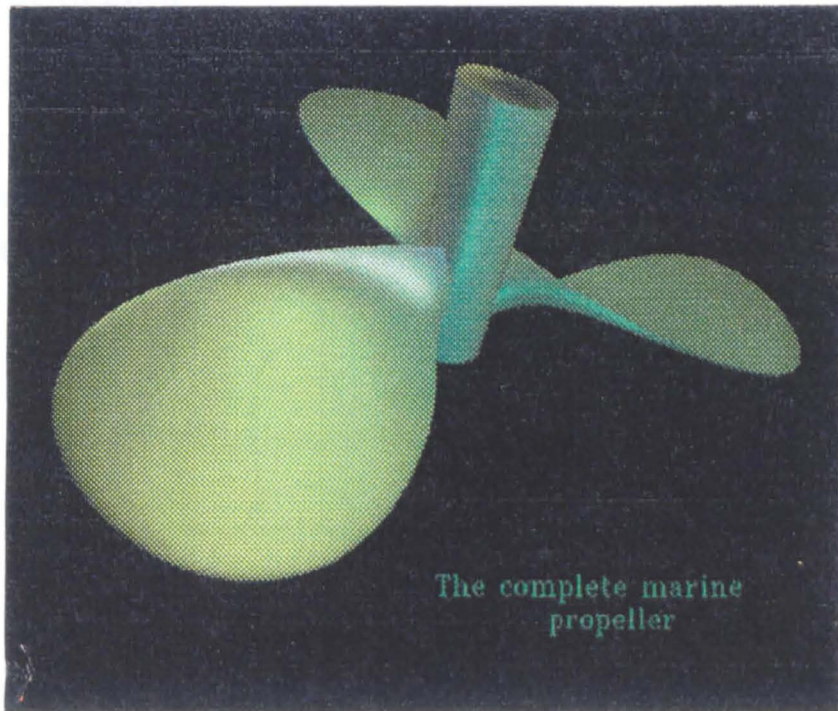


Figure 3.10: The generated propeller surface.

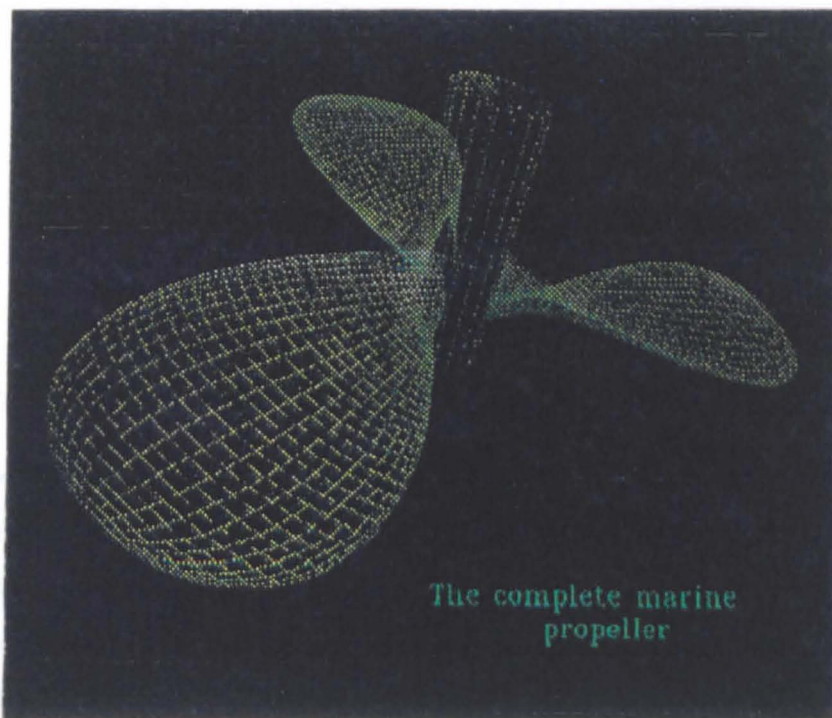


Figure 3.11: The propeller surface mesh.

There are
The variable
it makes with
in shallow
pitch propeller

For the fixed pitch propeller the forms most commonly used for the hub are cylindrical or tapered/conical [26]. Other modified forms of these shapes are bucket shaped or barrel shaped.

It has already been seen how the Pyth method can be used to generate smooth blends

3.4 Fillet design

In Chapter 1 it was commented on how the generation of a fillet between the blade and the central hub can be used to make the machining of the surface easier and how the fillet strengthens the intersection between the blade and the hub. A variety of shapes [26] can be used for the propeller hub as can be seen in figure (3.12).

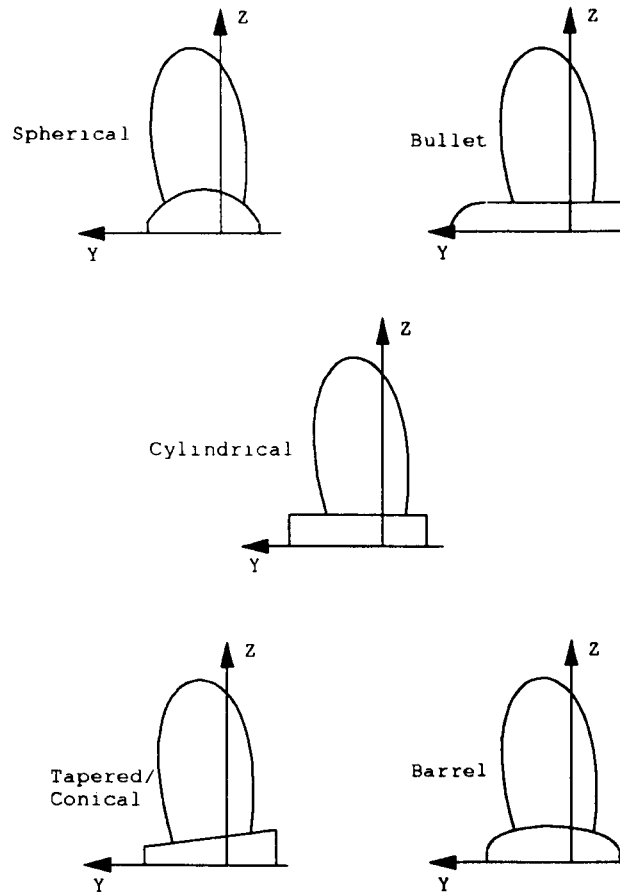


Figure 3.12: The variety of hub designs of a propeller.

There are two main types of marine propeller, the fixed and variable pitch propeller. The variable pitch propeller is one in which the blades can be moved to alter the angle it makes with the inflow, while in motion. This is particularly useful for manoeuvring in shallow or narrow channels [26], and such a propeller has a spherical hub. The fixed pitch propeller (which is to be considered throughout this thesis) is attached to the hub. For the fixed pitch propeller the forms most commonly used for the hub are cylindrical or tapered/conical [26]. Other modified forms of these shapes are bullet shaped or barrel shaped.

It has already been seen how the PDE method can be used to generate smooth blends

between two primary surfaces. In this section it will be shown how this can be extended so that the blend produced is a fillet between the central hub and the PDE generated propeller blade. The central hub will be considered to be cylindrical.

3.4.1 Boundary conditions

The boundary value problem is illustrated in figure (3.13).

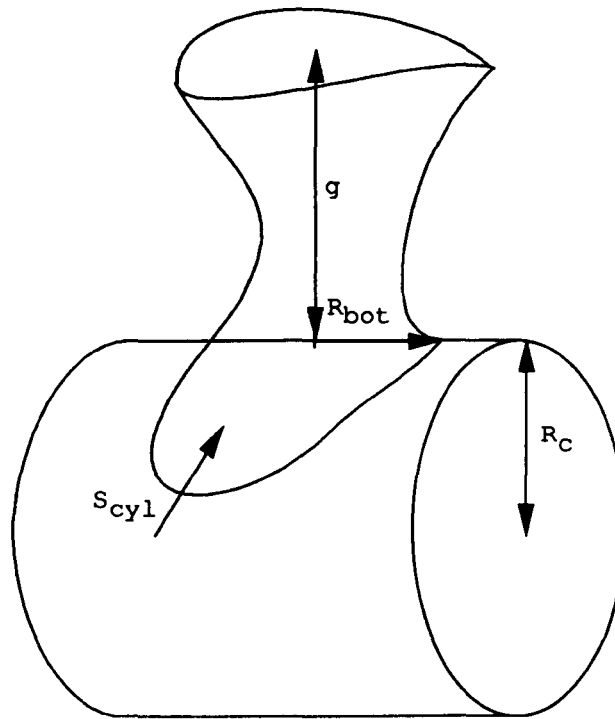


Figure 3.13: The fillet geometry.

The hub is of radius R_c , with the trimline on the hub of radius R_{bot} when projected onto the horizontal plane. The ‘height’ of the blend is given by g at the midsection of the wrapped airfoil. The parameter domain over which the blend is generated is $0 \leq u \leq 1$ and $-\pi/2 \leq v \leq \pi/2$ where a closed loop of surface is formed. The conditions on $u = 0$ are given by equations (3.19-21) as previously described for the base section of the propeller blade. On the trimline $u = 1$ the conditions imposed are that the trimline is a curve on the cylinder’s surface, whose projection onto the (x, y) plane is a circle, and is given by

$$x(1, v) = R_{bot} \cos 2v \quad (3.43)$$

$$y(1, v) = R_{bot} \sin 2v \quad (3.44)$$

$$z(1, v) = (R_c^2 - R_{bot}^2 \sin^2 2v)^{0.5} \quad (3.45)$$

with tangency conditions given by

$$x_u(1, v) = S_{cyl}(1 - t^2)^{0.5} \cos 2v \quad (3.46)$$

$$y_u(1, v) = S_{cyl}(1 - t^2)^{0.5} \sin 2v \quad (3.47)$$

$$z_u(1, v) = -S_{cyl}t \quad (3.48)$$

where

$$t = \frac{R_{bot} \sin^2 2v}{(R_c^2 - R_{bot}^2 \sin^2 2v + R_{bot}^2 \sin^4 2v)^{0.5}} \quad (3.49)$$

3.4.2 Results

The following table shows the parameters used to define the geometry.

Parameter	Value
a_x	0.1
a_y	0.1
a_z	0.1
R_{bot}	0.8
R_c	1.4
g	0.7
S_{cyl}	0.1

Table 3.3: Parameters of the fillet.

The numerical solution can now be found and below are the rates of convergence for the SOR iteration.

Component	Residual	Number of iterations
x	$9.9975e - 06$	1041
y	$9.9672e - 06$	1042
z	$9.9962e - 06$	1219

Table 3.4: Residuals for the SOR process for the PDE generated fillet.

Overleaf is the final generated blend between the hub and the propeller blade.

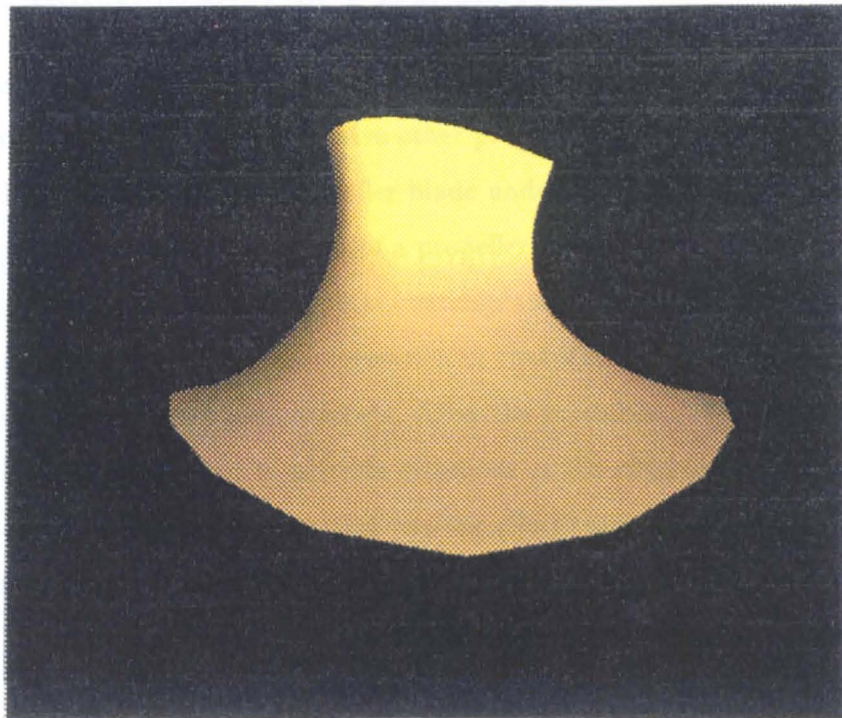


Figure 3.14: The generated fillet.

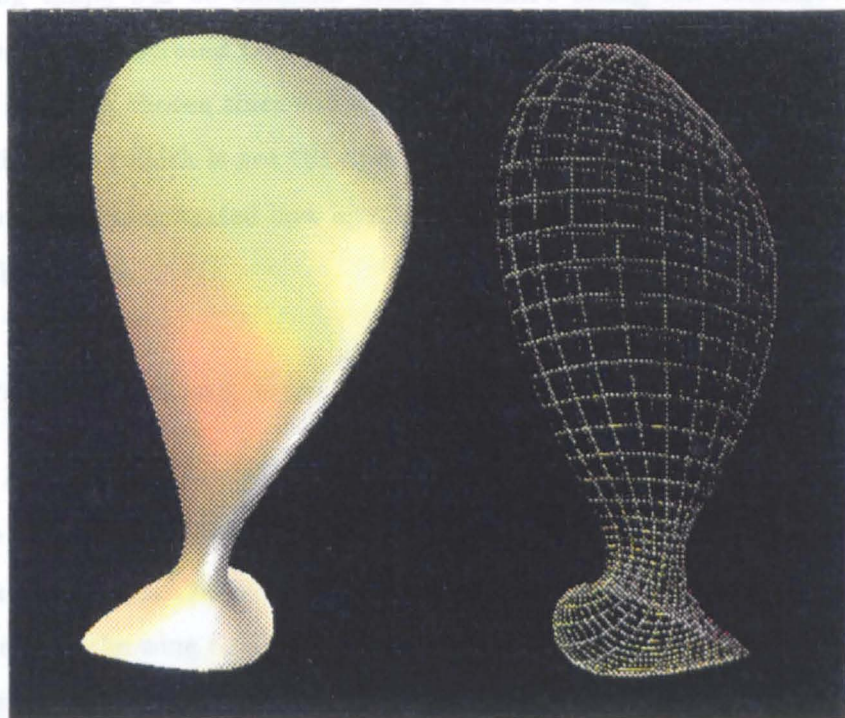


Figure 3.15: The propeller and fillet.

3.5 The functionality of PDE surfaces

Just as there is no difficulty in evaluating the surface area of a parametrically generated surface, it should also be possible to derive other properties that the surface may possess, such as the thrust generated by a propeller blade under given operating conditions.

Now, although the geometric design of a propeller blade can be straightforward, if no physical testing of the finished model were contemplated then serious consequences could arise when the propeller was put into operation in that its actual performance may fall a good deal short of its desired requirements. After the production of a new design, model tests in water tanks are needed to provide estimates of the effectiveness of the propeller. However, as described in the introduction, scaling effects and more importantly the time and cost of producing a model are factors which weigh heavily against such practices for companies.

The use of computer simulation of the physical properties of a computer generated model is therefore beneficial. Thus, in Chapter 5 it will be shown how calculations on the defined propeller geometry can be accomplished. However, by way of an introductory example to illustrate how such a surface can be analysed, in this section the circulation about a wing shape will be obtained using Prandtl's lifting line technique. The wing geometry has been generated from the approach described above for the propeller blade, and a wing has been chosen since the lifting line theory accounts for a wing travelling in a uniform direction (which is not the case for the propeller blade as it also has rotation). Finally, it will be demonstrated how alteration of the shape parameters can influence the physics of the system.

3.6 Prandtl lifting line theory

A wing of finite length d producing lift can be represented by a vortex distribution [70]. These vortices move with the wing and are known as bound vortices and extend as far as the wing tips. Vorticity is continually shed along the span of the wing if the section varies. At the wing tips these bound vorticities, if they do not have zero strength, turn through a right angle to persist as a system of vortices whose axes run parallel to the free stream direction since the vortex line cannot end within the fluid. These are known as trailing vortices [70]; the main consequence is that the air in the vicinity of the wing and behind it acquires a downward velocity component, which is known as the

induced downwash [73]. This is important since it reduces the effective incidence of the wing which alters the lift and drag characteristics.

To attempt to find a general solution for determining a vortex system to represent a finite wing is difficult. The method suggested by Prandtl assumes the bound vorticity to lie on a straight line joining the wing tips, known as the lifting line. This line is generally taken to lie along the line joining the section quarter chord points, with good results obtained provided that the aspect ratio of the wing is moderate or large; in general not less than 4.

Now consider a lifting line to be represented as follows, with the x direction signifying the direction of motion of the wing.

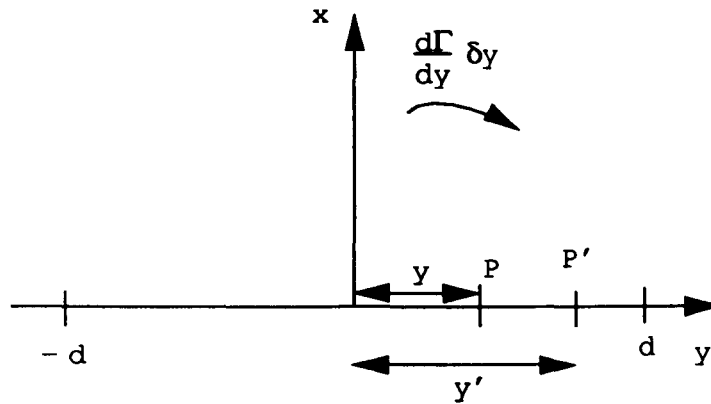


Figure 3.16: The representation of a lifting line.

At any point P on the line, the bound vorticity is $\Gamma(y)$ and there is a trailing vorticity of strength $d\Gamma/dy$ per unit length shed [73]. Now the downwash angle ϵ is small and is approximated by $\epsilon = w/V$, where w is the downwash velocity, from which the effective incidence of the wing section at some point P' will be given by

$$\alpha_\epsilon(y') = \alpha(y') - \frac{w(y')}{V} \quad (3.50)$$

where V is the forward speed of the wing.

The geometric angle of the wing section $\alpha(y')$ is known, and the downwash angle can be defined in terms of the bound vorticity [73]. Thus, some expression for the effective incidence of the wing is needed. The lift curve of a wing illustrates the way in which the coefficient of lift C_l of a two-dimensional airfoil varies with incidence. C_l is proportional to the incidence over a considerable range, until the effects of separation begin to tell,

where the slope falls away [73]. In the linear region of the curve

$$\frac{dC_l}{d\alpha} = a_\infty \quad (3.51)$$

where a_∞ is a constant, known as the lift curve slope and has a theoretical value of 2π .

Therefore, if the local lift coefficient is given by

$$C_l(y') = a_\infty \alpha_e(y') \quad (3.52)$$

and also the non-dimensional form of the coefficient of lift is given as

$$C_l = \frac{\rho V \Gamma}{1/2 \rho V^2 c} \quad (3.53)$$

Then

$$\alpha_e = \frac{2\Gamma}{cV a_\infty} \quad (3.54)$$

where c is the chord length of the section. Since the total downwash is given in terms of the bound vorticity, (3.50) is an equation in the unknown circulation $\Gamma(y)$. By introducing a parameter $y = -d \cos \theta$ so that $\theta = 0$ at the port wing tip, and $\theta = \pi$ at the starboard wing tip, the circulation may be written in the form of a Fourier series

$$\Gamma(y) = 4dV \sum_{n=1}^{\infty} A_n \sin n\theta \quad (3.55)$$

where a sine series is chosen to satisfy the requirement of zero circulation at the tips. Then this expression can be substituted into the equation representing the effective angle of incidence (3.50), which after being rearranged leads to the monoplane equation [73]

$$\sum_{n=1}^{\infty} (\mu n + \sin \theta) A_n \sin n\theta = \mu \alpha \sin \theta \quad (3.56)$$

where $\mu = a_\infty c / 8d$, which is an equation from which the Fourier coefficients may be determined as all other quantities are known at the various span positions. It is only necessary to evaluate a limited number of the coefficients; so if n are needed to give sufficient accuracy then the monoplane equation is applied at n spanwise locations and solved to find the Fourier coefficients. The Fourier coefficients are then substituted back into equation (3.56) to give the circulation along the span of the wing. It should be noted that the wing can be taken to be symmetric about the centre line and so only the circulation is obtained from $\theta = \pi/2$ to $\theta = \pi$.

3.6.1 Results

Figures (3.17) and (3.18) illustrate the example wing shape, and the circulation about the wing from the representation of the geometry by a lifting line. As can be seen the circulation falls to zero at the tip with the distribution being similar to that of an elliptic wing [70]. Figure (3.19) illustrates how a more rectangular wing can be generated from the design of figure (3.17). By increasing the value of the smoothing parameter a_x the chord length is shortened at each section, and by increasing the magnitude of the tangents x_u at the tip and reducing the value at the root, the surface appears as in figure (3.19) which is similar to that of a rectangular wing. From figure (3.20), it can be seen that the circulation about this wing shape is indeed similar to the circulation of a rectangular wing, as described in [70]. Therefore, the lifting line method appears to be applicable for these simple geometries.

If the lift

$$L = \int_{-d}^d \rho V \Gamma(y) dy \quad (3.57)$$

is considered, it can be seen that this will vary with the circulation about the wing. Thus, we can see how the lift could theoretically be obtained, and how a different value of lift would be given for the two circulation distributions in figures (3.18) and (3.20). Then, an investigation could be undertaken as to how the lift varies with the geometric properties. By implementing some optimisation routine, the maximum lift could be generated for a wing shape by alteration of the geometric parameter values. Of course, due to the lifting line representation used to determine the circulation, only a search of parameters which affect the variables c and α in the monoplane equation would be necessary, and important features such as wing thickness and camber could not be considered. However, with a different analysis model, such as the panel method to be implemented later, the complete geometry could be considered, and so an optimum value of the lift would be achieved for different sets of design parameters.

Firstly though, if these more precise methods are to be used, then an initial geometry which is a fairly good representation of an existing blade should be considered. This will be discussed in the next chapter.

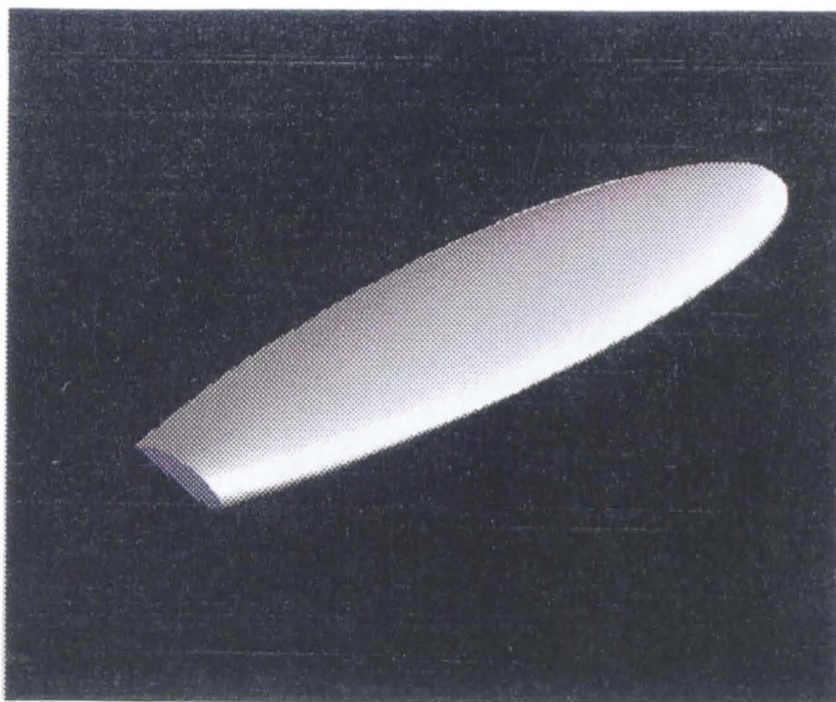


Figure 3.17: The 'elliptic' wing.

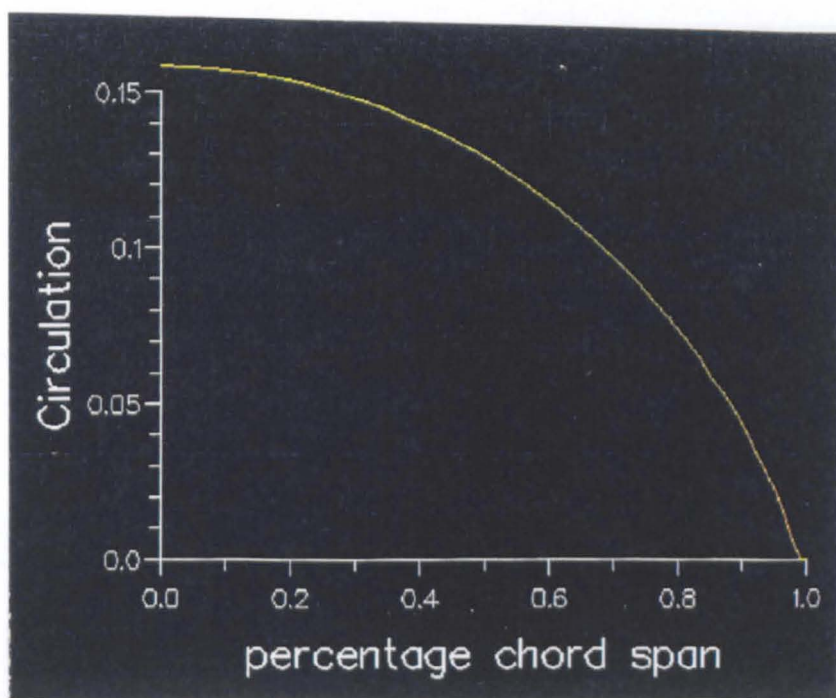


Figure 3.18: The circulation about the wing.

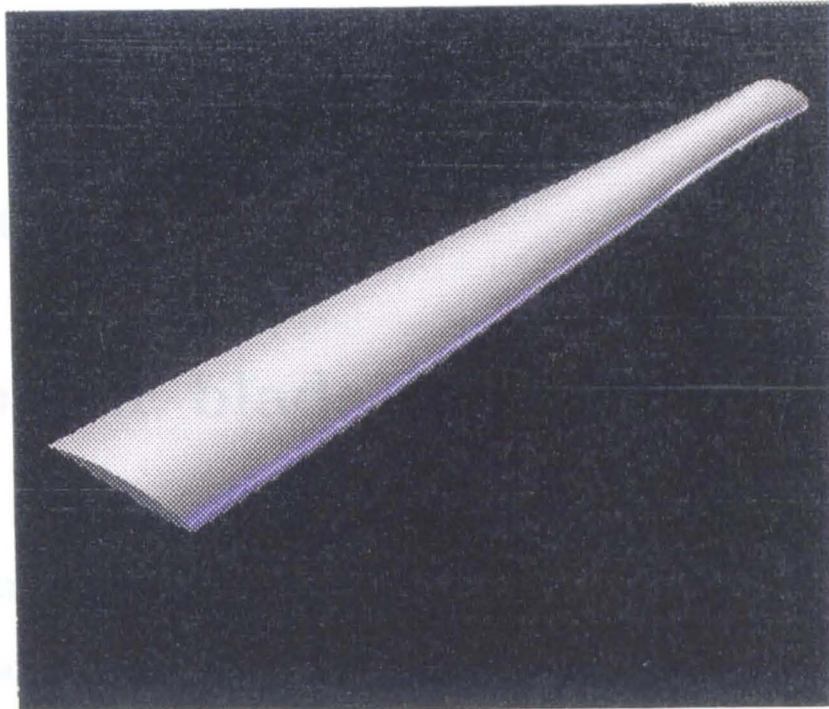


Figure 3.19: The 'rectangular' wing.

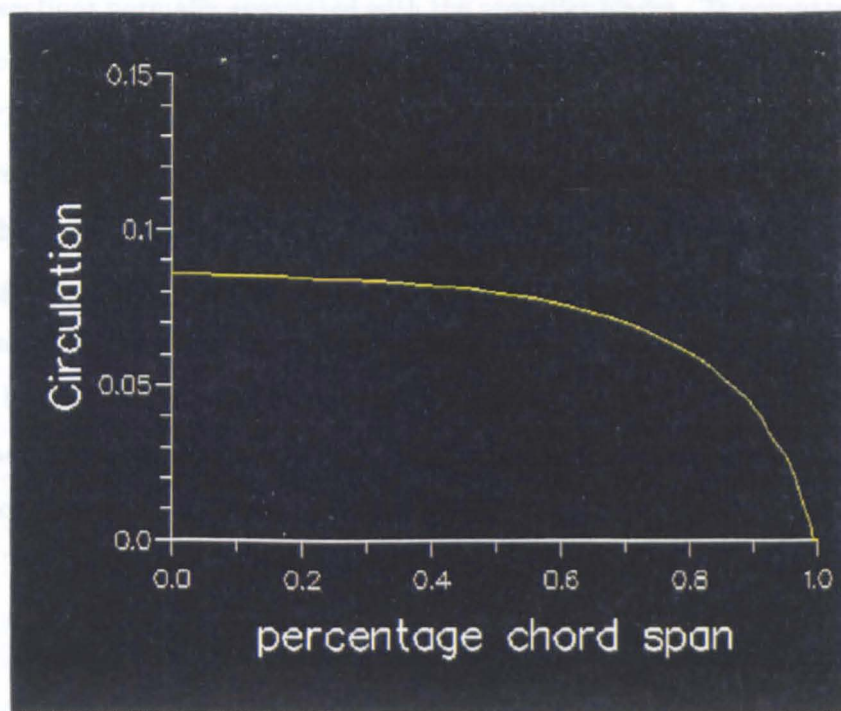


Figure 3.20: The circulation about the wing.

The conventional propeller design process begins with the selection of the blade sections as outlined in the previous chapter. These are then placed

Chapter 4

Propeller blade representation

4.1 Introduction

The model derived in the previous chapter was designed to illustrate the way in which a generic propeller surface can be defined by taking some airfoil section as a basis from which to generate the complete propeller blade. In this chapter, the model will be improved so that an accurate surface model of actual propeller geometries can be constructed, by producing a boundary curve for the PDE method which approximates the actual wing sections normally associated with the propeller blades. To compare an existing propeller geometry, the data given in the design paper of Eckhardt and Morgen [27] will be considered. This paper determines the geometry from the requirements that the propeller develops a certain performance under given operating conditions. The final geometry is defined as the coordinates of the specified airfoil section, which runs through the blade span and is given in terms of the mean line and thickness distribution, together with the maximum values of these and other distributions at each span station. A comprehensive method will be described here as to how the basic section profile can be derived so that it is suitable to be incorporated as a boundary condition into the PDE method, followed by an illustration of how accurately the spanwise distributions can be maintained throughout the blade. The generated propeller surface can then be used as a basis for the flow calculations using the panel method.

4.1.1 Airfoil sections

The conventional process for determining the geometry of a propeller begins with the selection of the blade sections as outlined in the previous chapter. These are then placed

at equally spaced stations along the span of the blade to create the expanded propeller blade. The performance of the marine propeller will depend crucially on the type of blade section used. Therefore, in order to decide whether a section may be suitable for a propeller, the pressure distribution around it must be known. Although two dimensional section data is not applied to propellers without making allowances for three dimensional flow effects, they are useful in deriving criteria upon which the selection of propeller blade sections can be based. It is then the value of minimum pressure somewhere on the surface which the designer has to look at. If this minimum pressure drops below a certain critical pressure of the fluid, cavitation may occur.

The theory of wing sections [30] permits the calculation of the pressure distribution of arbitrary sections. However, the computations required are too long to permit quick and easy calculations, and so a method of obtaining pressure distributions has been devised by regarding the velocity distribution to consist of three components, those being;

1. The velocity component resulting from the displacement effect of the thickness distribution at zero angle of attack, denoted (v/V_∞)
2. The velocity increment resulting from the mean line at its design angle of attack, denoted $(\Delta v/V_\infty)$
3. The velocity increment occurring on the thickness distribution at angles of attack, denoted $(\Delta v_a/V_\infty)$.

These velocity components are superimposed to obtain the resultant velocity at a point, from which the pressure coefficient C_P is obtained, thus

$$C_P = 1 - \left(\frac{V_r}{V_\infty} \right)^2 = 1 - \left(\frac{v}{V_\infty} \pm \frac{\Delta v}{V_\infty} \pm \frac{\Delta v_a}{V_\infty} \right)^2 \quad (4.1)$$

where the positive signs refer to the suction side and the negative signs to the pressure side, as seen from figure (4.1) overleaf. The local load is then caused by a difference of velocity between the upper and lower surfaces, which from thin wing theory the local load coefficient P_R is given by

$$P_R = 4 \frac{\Delta v_a}{V_\infty} \frac{v}{V_\infty}. \quad (4.2)$$

Therefore, when choosing a section to be used for the propeller blade, it is important to either estimate the properties of the components of the section as above, or to be able to determine the pressure distributions from some physical model. Many of these sections have their pressure distributions categorised, and are readily available in Abbott and Doenhoff [30], thus saving time.

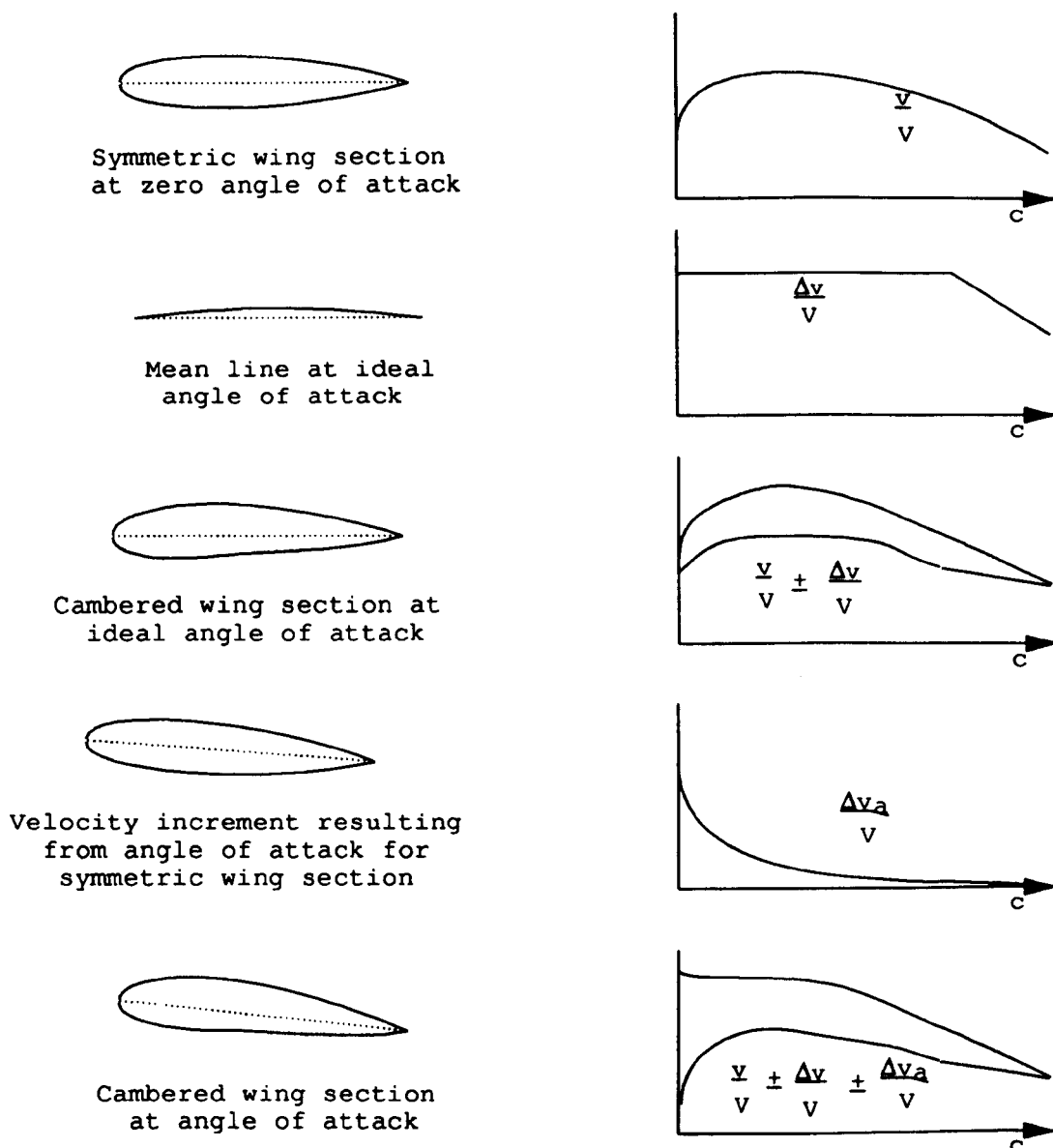


Figure 4.1: The velocity components of the wing section.

4.1.2 The mean line

Many of the properties of wing sections are primarily functions of the shape of the mean line, such as the chordwise load distribution. The mean line is considered to be the locus of points situated halfway between the upper and lower surfaces of the section, the distance being measured normal to the mean line. It is possible to design mean lines to have certain load distributions by methods derived from the theory of thin wing sections [30]. One of the most common mean line distributions in use belongs to the NACA 6-series of wing sections - more commonly referred to as NACA 'a' mean lines, which are

given by

$$\frac{y}{c} = \frac{C_{L_i}}{2\pi(a+1)} \left\{ \frac{1}{1-a} \left[\frac{1}{2} \left(a - \frac{x}{c} \right)^2 \ln \left| a - \frac{x}{c} \right| - \frac{1}{2} \left(1 - \frac{x}{c} \right)^2 \ln \left(1 - \frac{x}{c} \right) + \frac{1}{4} \left(1 - \frac{x}{c} \right)^2 - \frac{1}{4} \left(a - \frac{x}{c} \right)^2 \right] - \frac{x}{c} \ln \frac{x}{c} + g - h \frac{x}{c} \right\} \quad (4.3)$$

where

$$g = \frac{-1}{1-a} \left[a^2 \left(\frac{1}{2} \ln a - \frac{1}{4} \right) + \frac{1}{4} \right] \quad (4.4)$$

$$h = \frac{1}{1-a} \left[\frac{1}{2} (1-a)^2 \ln(1-a) - \frac{1}{4} (1-a)^2 \right] + g \quad (4.5)$$

and where y is the ordinate of the mean line measured perpendicular to the chordline, x is the chordwise marker along the section chord (of length c), and a is the non-dimensional parameter at which the loading of the mean line changes from a uniform chordwise loading to a linearly decreasing loading as can be seen in figure (4.2).

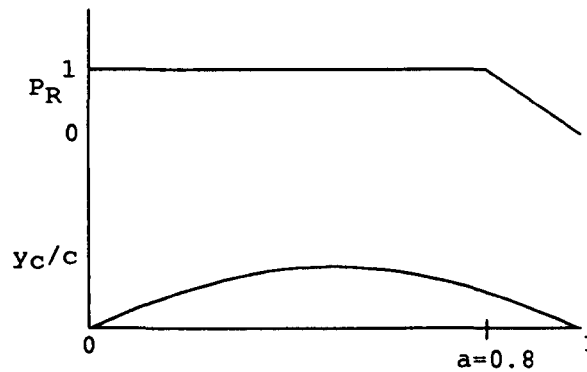


Figure 4.2: The $a=0.8$ mean line and loading.

C_{L_i} is the 'design' or 'ideal' lift coefficient. This is the lift coefficient which corresponds to the ideal angle of attack for the wing section. The ideal angle of attack was so termed by Theodorsen [74] and is such that the mean line is at an angle of lift to avoid infinite velocities at the leading edge. This angle can be obtained from thin wing theory. For angles of attack differing from the design angle of attack the velocity increments $\Delta v_a/V_\infty$ for thin sections become infinitely large at the leading edge, if the condition of smooth outflow at the trailing edge is adhered to, as described in Chapter 3.

In propeller design the NACA $a = 0.8$ and $a = 1.0$ mean lines are more frequently used than other mean line distributions since they display pressure distributions producing low drag and good cavitation characteristics.

4.2 NACA sections

Until the late 1940s the development of wing sections was entirely empirical. One of the most comprehensive investigations undertaken was by the National Advisory Committee of Aeronautics (NACA) whose wing sections are now in common use. The reason for this partly lies in the fact that the investigations were systematised by the separation of the effects of camber and thickness, and that the NACA sections form consistent families which can be combined in various ways.

The NACA 4-digit wing sections were selected to correspond to existing wing sections such as the Gottingen 398. These NACA sections were defined in terms of explicit definitions of the thickness and camber. Due to the mean line of the 4-digit section not being suitable for forward positions of the maximum camber, a new series of mean lines was developed, termed the 5-digit series. The next family of sections termed the NACA 1-series then represented the first attempt to develop sections having desired types of pressure distributions. In order to minimise the induced velocities, it was desired to locate the minimum pressure point far back, towards the trailing edge, on both surfaces. The development of these sections was hampered by the lack of adequate theory. Successive attempts to design sections by approximate theoretical methods led to the NACA 2- to 5-series; however, experience showed that none of the approximate methods tried was sufficiently accurate as to show correctly the observed changes in flow profile near the leading edge [30]. The NACA 6-series was devised by new and improved methods [30], in accordance with design criteria established with the objective of desirable drag, critical Mach number and maximum lift characteristics. These sections proved useful for propellers.

The cambered wing sections of all NACA families of wing sections are obtained by combining a mean line and a thickness distribution. The leading and trailing edges are defined as the forward and rearward extremities, respectively, of the mean line. The chord line is defined as the straight line connecting the leading and trailing edges from $x = 0.0$ to $x = 1.0$. The section is then generated by adding the thickness distribution normal to the mean line as in figure (4.3).

Thus if X_U and Y_U represent the ordinates on the upper surface of the section, and X_L and Y_L the ordinates of the lower surface, then the section will be defined by

$$X_U = x - y_t \sin \theta \quad Y_U = y_c + y_t \cos \theta \quad (4.6)$$

$$X_L = x + y_t \sin \theta \quad Y_L = y_c - y_t \cos \theta \quad (4.7)$$

where $y_c(x)$ defines the mean line, $y_t(x)$ the thickness distribution at the point x , and θ the slope of the mean line, given by

$$\tan \theta = \frac{dy_c}{dx}. \quad (4.8)$$

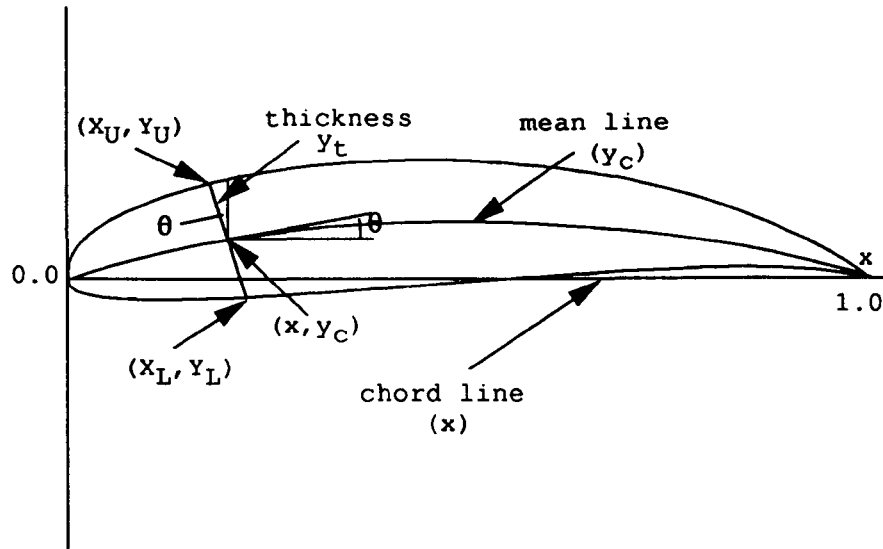


Figure 4.3: The NACA wing section.

4.3 Approximating NACA sections

The first consideration when producing a PDE generated blade which approximates the designed blade of Eckhardt and Morgen, is to approximate the actual blade section by a curve of the form applicable to the closed form solution of the PDE method. The data representing the wing section given by Eckhardt and Morgen is reproduced overleaf in table (4.1).

The particular blade to be approximated has the $a = 0.8$ mean line with a modified 66 section which belongs to the 6-series of wing sections. These two distributions (and in fact the other two distributions of table (4.1)) are among the most common combinations for a marine propeller, of thickness and camber distribution. The $a = 0.8$ mean line has, as has been mentioned in the previous section, good characteristics such as low drag. The 66 thickness distribution has a fairly blunt nose, but has too thin a tail for construction purposes. This can be remedied by making the section parabolic from the point of maximum thickness to the trailing edge. This new thickness form is termed the 'modified 66 section', where the 66 notation represents the fact that the 6-series wing

is used with the chordwise position of minimum pressure being six tenths of the chord behind the leading edge for the basic symmetrical section at zero lift.

	16 Section	Modified 66 Section	a=1. mean line	a=0.8 mean line
x_l/l	y/t_x	y/t_x	m/m_x	m/m_x
0	0	0	0	0
0.0125	0.1077	0.1155	0.097	0.091
0.025	0.1504	0.1530	0.169	0.159
0.050	0.2091	0.2095	0.287	0.271
0.075	0.2527	0.2540	0.384	0.366
0.10	0.2881	0.2920	0.469	0.448
0.20	0.3887	0.4002	0.722	0.699
0.30	0.4514	0.4637	0.881	0.863
0.40	0.4879	0.4952	0.971	0.961
0.45		0.5000	0.993	0.988
0.50	0.5000	0.4962	1.000	1.000
0.60	0.4862	0.4653	0.971	0.978
0.70	0.4391	0.4035	0.881	0.889
0.80	0.3499	0.3110	0.722	0.703
0.90	0.2098	0.1877	0.469	0.359
0.95	0.1179	0.1143	0.287	0.171
1.00	0.0100	0.0333	0	0

Table 4.1: x_l/l =non-dimensional distance along section from nose, y =ordinate of section measured perpendicular to mean line, m_x =maximum ordinate of mean line, m =ordinate of mean line t_x =maximum thickness of Section.

The complete numbering system of the 6-series is given, for example, by NACA 66,3-218 $a = 0.8$ where the 66 is as described, the 3 gives the range of lift coefficients in tenths above and below the design lift coefficient in which favourable pressure gradients exist on both surfaces, the 2 following the dash gives the design lift coefficient in tenths and the last two digits indicate the thickness of the wing section in per cent of the chord, with

$a = 0.8$ showing the type of mean line used (when the mean line designation is not given, the uniform load mean line $a = 1.0$ has been used).

The disadvantages encountered when considering the above distributions, is that they are generally given as tabulated sets of data, as in [30]. The complete section is then generated by substituting these data points into equations (4.6-7) to obtain the section. The mean line distribution can of course be given explicitly by equation (4.3), even though it is fairly complex, however the modified 66 thickness distribution has no explicit definition. Intermediate thickness ratios for data not presented in [30] can be approximated by scaling the original tabulated ordinates as required. Therefore, for the section we wish to approximate it is difficult to obtain a closed curve suitable for an analytic solution.

In order to produce a suitable closed curve, we will examine the distributions given by the NACA 4-digit series (since they are explicitly defined) to see whether they can be used to approximate the required data of table (4.1).

4.3.1 NACA 4-digit wing sections

The distributions comprising the NACA 4-digit wing sections are easy to work with since they can completely define the wing section in terms of the chord wise marker x .

The 4-digit wing section has a thickness distribution given by

$$\pm y_t = \frac{t_x}{0.2} \left(0.29690\sqrt{x} - 0.12600x - 0.35160x^2 + 0.28430x^3 - 0.10150x^4 \right) \quad (4.9)$$

where t_x is the maximum thickness expressed as a fraction of the chord. It should be noted at this stage that at the trailing edge $x = 1.0$ the thickness is given by $y_t = 0.0105t_x$ and so is finite. This is in keeping with other thickness distributions where the width at the trailing edge is finite to avoid a sharp tail (see for example columns [2], [3] for $x_l/l = 1.00$ of table (4.1)).

The mean line is given as two parabolic arcs, tangent at the position of maximum mean line ordinate p by

$$y_c = \begin{cases} \frac{m_x}{p^2} (2px - x^2) & \text{fore of } p \\ \frac{m_x}{(1-p)^2} ((1-2p) + 2px - x^2) & \text{aft of } p \end{cases} \quad (4.10)$$

where m_x is the maximum ordinate of the mean line expressed as a fraction of the chord and p is the chordwise position of m_x .

From equation (4.8) it can be seen that the slope of the mean line will be given by

$$\tan \theta = \begin{cases} \frac{2m_x}{p^2} (p - x) & \text{fore of } p \\ \frac{2m_x}{(1-p)^2} (p - x) & \text{aft of } p. \end{cases} \quad (4.11)$$

These expressions can then be substituted into equations (4.6-7) to produce the wing section. It should also be noted at this stage that the leading edge radius [30] of the section is neglected in this study.

4.3.2 Comparison of 4-digit section with 6-series section

We are now at a stage where the two sets of data can be compared. The data given in table (4.1) is as illustrated in figures (4.4), (4.5) and (4.6) for the mean line, thickness of the section and the constructed section respectively, with the data for the explicit 4-digit section of equations (4.6-11) overlaid. The $a = 0.8$ mean line is fairly symmetric and so to approximate this, a value of $p = 0.5$ is taken in equation (4.10). The value of m_x is taken to satisfy the maximum camber of the base section ($r_h/R = 0.2$) of the propeller blade in the Eckhardt and Morgen data. This is given by $m_x = 0.00474$ metres per unit chordlength. The value of t_x is taken to correspond to the maximum thickness of the base where $t_x = 0.0474$ metres per unit chordlength. It is seen from figure (4.4) that the mean line is of the order of a tenth of the thickness, and so the mean line given by the 4-digit series (4.10) with $p = 0.5$ can be considered acceptable. However, there is a pronounced difference in thickness distribution between the modified 66 section and that given by equation (4.9), as can be seen in figure (4.5). The point of maximum thickness on the modified 66 section is aft of that of the 4-digit series. Therefore, equation (4.9) representing the 4-digit series thickness, in its present form cannot be used to approximate the 66 section accurately enough for our purposes, a fact which can be verified from figure (4.6) where the complete sections are generated from the 2 different series.

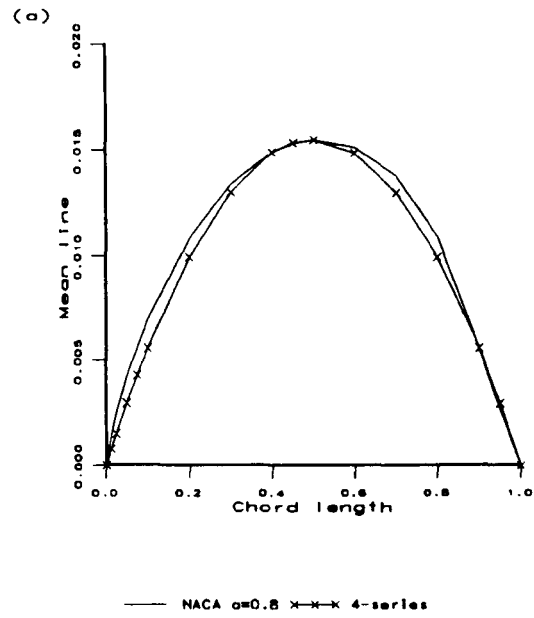


Figure 4.4: Comparison of the 4-digit mean line distribution and a=0.8 meanline.

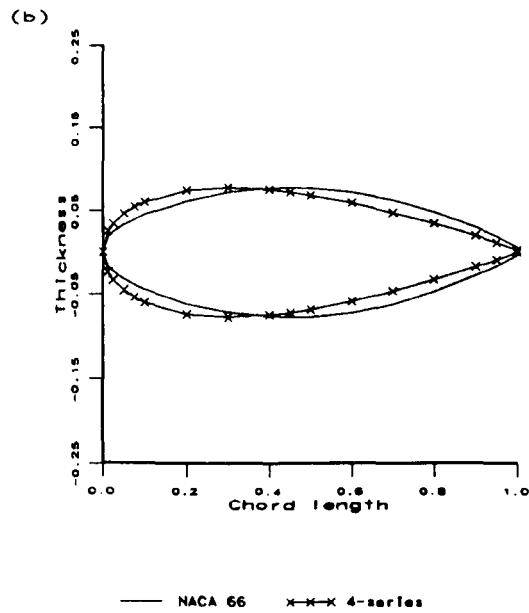


Figure 4.5: Comparison of the 4-digit thickness and modified NACA 66 thickness.

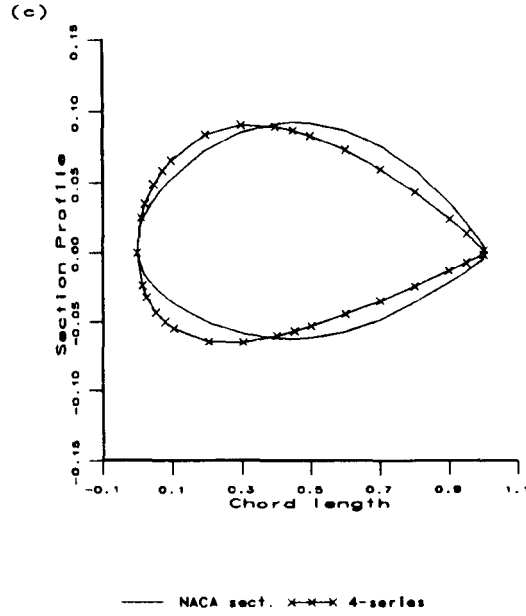


Figure 4.6: Comparison of the 4-digit section and NACA section.

4.3.3 Improvement of fit for thickness distribution

It was thought that it could be possible to obtain a better approximation of the 4-digit thickness equation (4.9) to the modified 66 section by altering the constants (0.10150, 0.12600, etc.) associated with equation (4.9). The following method was devised to do this by considering the problem of minimising the differences in thickness. To obtain the minimum of these differences, if the values of x_1/l (denoted x_0) in table (4.1) are substituted into equation (4.9), then a measure of the differences between the two distributions can be obtained. In particular, if $y_t(x_0)$ denotes the thickness of the 4-series and $y_{ss}(x_0)$ the thickness given in column [3] of table (4.1) for the corresponding values of x_0 , a measure of the thickness difference at each chord location x_0 can be defined as

$$(y_t(x_0) - y_{ss}(x_0))^2 \quad (4.12)$$

which is always positive.

Now, if we consider equation (4.9) to be a function of five variables, such that

$$y_t(a, b, c, d, e) = a\sqrt{x_0} - bx_0 - cx_0^2 + dx_0^3 - ex_0^4 \quad (4.13)$$

then a function can be defined by summing over the differences at each chord station x_0 ;

4.3.4 Results

For the example considered of the minimisation of the differences between the 4-digit thickness and the modified 66 section, the variables in equation (4.13) were determined as shown in table (4.2).

Variable	Value
a	0.1558859
b	0.041041471
c	-0.051196601
d	-0.2479716
e	-0.087263182

Table 4.2: Values of the variables for the NACA 4-series thickness distribution.

Substituting these values into equation (4.13) (paying particular attention to the signs associated with each variable), it can be seen from figure (4.7) that the approximation to the discrete data is an almost exact fit by the quartic in x . Furthermore, figure (4.8) illustrates the wing section defined explicitly in terms of the 4-digit expressions compared with the discrete data used to define the actual propeller blade section. It was, therefore, decided that the 4-digit section was a good enough approximation to be used as an alternative to the $a = 0.8$, modified 66 section.¹

Therefore, the section now needs to be converted to a form compatible with the PDE method.

¹It should be commented that this method of approximation was used for a variety of other thickness distributions, given in terms of discrete data, and produced results of the same calibre as those of figure (4.7). Therefore, it is noted that this technique is useful for obtaining approximations to sets of discrete data for the purpose of defining section curves. Also an approximation to the mean line $a = 0.8$ was derived by the same method, giving

$$y_c = a_1 x + b_1 x^2 + c_1 x^3 + d_1 x^4 \quad (4.22)$$

where a_1, b_1, c_1, d_1 are found to give an explicit approximation to the mean line of equations (4.10). The approximation to the mean line was however implemented after the remainder of the work in this thesis and so is not used throughout this work, with equations (4.10) still representing an appropriate choice of mean line distribution.

4.4 Fourier analysis of blade section

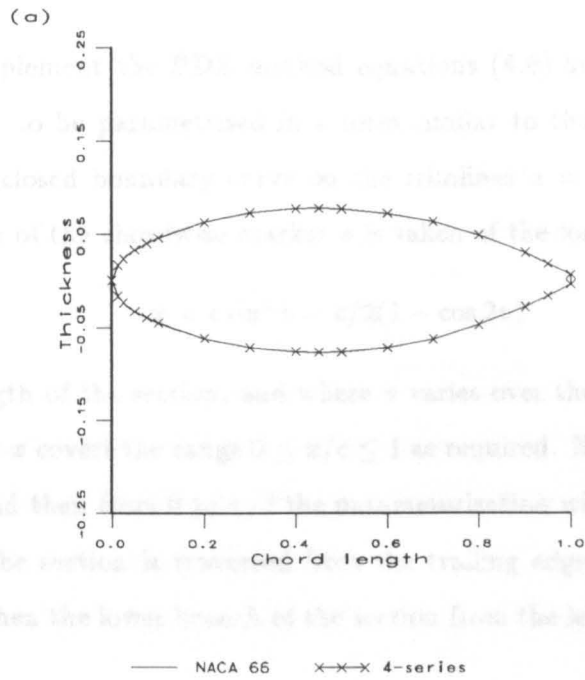


Figure 4.7: The approximation to the modified 66 section.

By making the assumption that the angle of the slope of the mean line θ will be small along the mean line (typically the maximum camber m , is much smaller than the maximum thickness t , implying that the maximum slope of the mean line will be small), the following standard assumptions hold:

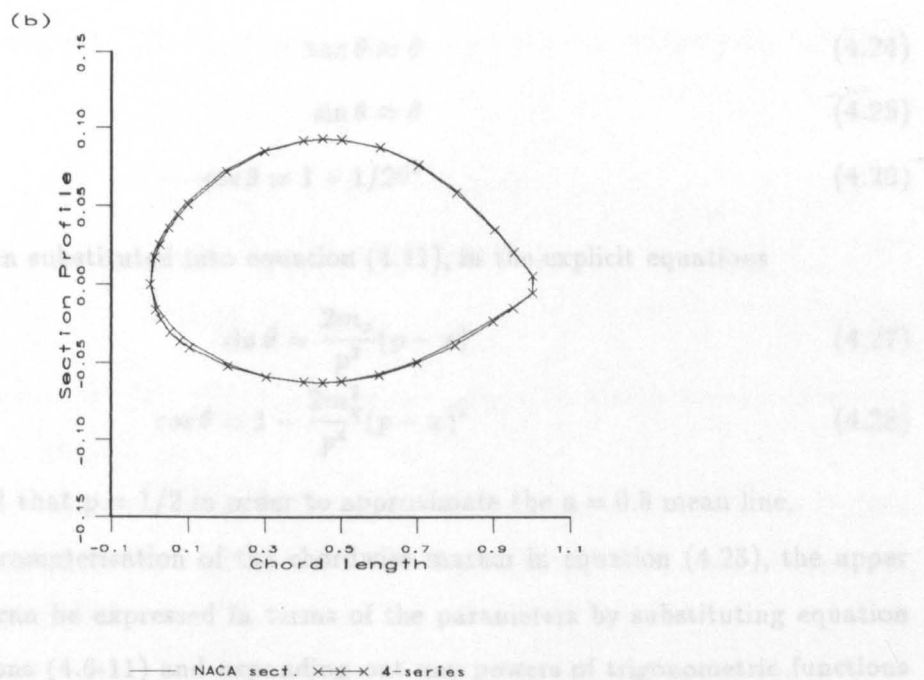


Figure 4.8: The new wing section.

From the representation of θ in equation (4.23), the upper and lower curves can be expressed in terms of the parameters by substituting equation (4.23) into equations (4.6-11). The resulting equations are powers of trigonometric functions or products which occur. In order to approximate a closed loop of surface, these are represented as a sum of Fourier terms. Thus, to obtain a solution in a closed, continuous form, each of the boundary conditions for the camber and thickness are represented as a sum of Fourier terms. The chordwise marker $g(\tau)$ and the mean line

4.4 Fourier analysis of blade section

In order to implement the PDE method equations (4.6) and (4.7) representing the blade section need to be parametrised in a form similar to those of the last chapter in order to obtain a closed boundary curve on the trimlines $u = 0$ and $u = 1$. Initially a reparameterisation of the chordwise marker x is taken of the form

$$x = c \sin^2 v = c/2(1 - \cos 2v) \quad (4.23)$$

where c is the length of the section, and where v varies over the range $-\pi/2 \leq v \leq \pi/2$, which ensures that x covers the range $0 \leq x/c \leq 1$ as required. Note that since v increases from $-\pi/2$ to 0 and then from 0 to $\pi/2$ the parameterisation will be such that firstly the upper branch of the section is traversed from the trailing edge at $x = c$ to the leading edge, $x = 0$, and then the lower branch of the section from the leading edge to the trailing edge.

By making the assumption that the angle of the slope of the mean line θ will be small along the mean line (typically the maximum camber m_x is much smaller than the maximum thickness t_x , implying that the camber, and hence the gradient of the mean line will be small), the following standard assumptions hold:-

$$\tan \theta \approx \theta \quad (4.24)$$

$$\sin \theta \approx \theta \quad (4.25)$$

$$\cos \theta \approx 1 - 1/2\theta^2 \quad (4.26)$$

which results, when substituted into equation (4.11), in the explicit equations

$$\sin \theta = \frac{2m_x}{p^2}(p - x) \quad (4.27)$$

$$\cos \theta = 1 - \frac{2m_x^2}{p^4}(p - x)^2 \quad (4.28)$$

where it is recalled that $p = 1/2$ in order to approximate the $a = 0.8$ mean line.

From the reparameterisation of the chordwise marker in equation (4.23), the upper and lower curves can be expressed in terms of the parameters by substituting equation (4.23) into equations (4.6-11) and expanding out any powers of trigonometric functions or products which occur. In order to approximate a closed loop of surface, these are represented as a sum of Fourier terms. Thus, to obtain a solution in a closed, continuous form, each of the boundary conditions involving expressions for the camber and thickness are represented as a sum of Fourier terms. The chordwise marker $x(v)$ and the mean line

distribution $y_c(v)$ are expressed to give the even Fourier expansions, denoted $X_f(v)$ and $Y_{cf}(v)$ respectively, such that (for the example of $x(v)$)

$$X_{\infty f}(v) = a_0/2 + \sum_{n=1}^{\infty} a_n \cos(2nv) \quad (4.29)$$

where

$$a_0 = \frac{2}{\pi} \int_{-\pi/2}^{\pi/2} x(v) dv, \quad (4.30)$$

$$a_n = \frac{2}{\pi} \int_{-\pi/2}^{\pi/2} x(v) \cos(2nv) dv \quad (4.31)$$

and the expansions $y_t \cos \theta$, $y_t \sin \theta$ are expressed as a sum of odd Fourier terms, denoted $Y_{ctf}(v)$ and $Y_{stf}(v)$ respectively, to accommodate the change in sign from the upper to lower surface in equations (4.6) and (4.7) with

$$Y_{\infty ctf}(v) = \sum_{n=1}^{\infty} b_n \sin(2nv) \quad (4.32)$$

where

$$b_n = \frac{2}{\pi} \int_{-\pi/2}^{\pi/2} x(v) \sin(2nv) dv. \quad (4.33)$$

The Fourier series are truncated to n terms, the value of n determined by agreement with the explicit forms of the section profile to some specified accuracy. Typically $n = 4$ was found to be sufficient. The boundary conditions for the base of the propeller blade in the form

$$x(1, v) = X_f(v) + Y_{stf}(v) \quad (4.34)$$

$$y(1, v) = Y_{cf}(v) + Y_{ctf}(v) \quad (4.35)$$

$$z(1, v) = r_h \quad (4.36)$$

where r_h is the radius of the hub, and $X_f(v)$ represents the truncated series approximation to the Eckhardt and Morgen data.

Figure (4.9) illustrates the explicit 4-digit explicit section profile with the derived boundary conditions (4.34-35) overlaid. It is observed that the differences between the two profiles are negligible.

It should finally be noted that this procedure for defining the section curve in order to obtain the boundary conditions analytically for the PDE method has been chosen, rather than a numerical solution which could use the data from Eckhardt and Morgen directly, since we can obtain a closed expression for the blade surface. By obtaining analytic approximations to the boundary conditions so that an analytic solution can be obtained,

the blade generation is almost instantaneous by comparison with a numerical solution which takes a greater time to produce a generated surface. This time difference is not only important when altering the blade's geometry, but also when altering the geometry during optimisation procedures as will be illustrated later.

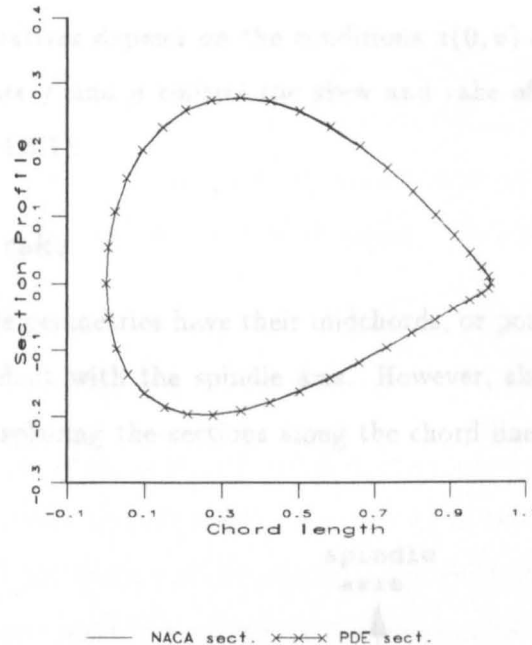


Figure 4.9: Comparison between Fourier series and NACA 4-section.

It should however be emphasised that this comprehensive (and long) procedure is not always necessary for generating boundary curves. Bloor and Wilson have devised an interactive piece of software in which the boundary curves are input by the user as discrete data points joined by a B-spline curve using a mouse and computer terminal. These curves can be manipulated by the user until desired, from which the software generates an analytic approximation of the curve for use with the PDE method.

4.5 Generation of blade

The propeller blade surface can now be generated. The boundary conditions at the base of the blade are given by equations (4.34-36) above, with the conditions on the trimline $u = 0$ at the tip being given by

$$x(0, v) = \epsilon_x x(1, v) + f \quad (4.37)$$

$$y(0, v) = \epsilon_y y(1, v) + g \quad (4.38)$$

$$z(0, v) = D/2 \quad (4.39)$$

where D is the propeller diameter. The boundary conditions at the tip are given in terms of scaled coordinates at the base, with $\epsilon_x, \epsilon_y \ll 1$ to represent the tip, from which the directions in which the tip propagates into the blade surface can be controlled, as the first and second derivatives depend on the conditions $x(0, v)$ and $y(0, v)$ as will be seen shortly. The constants f and g control the skew and rake of the blade respectively as discussed in section (4.5.1).

4.5.1 Skew and rake

Blades with simple geometries have their midchords, or points of maximum thickness in some cases, coincident with the spindle axis. However, skew can be added to more complex blades by displacing the sections along the chord lines from the axis [26], as in figure (4.10).

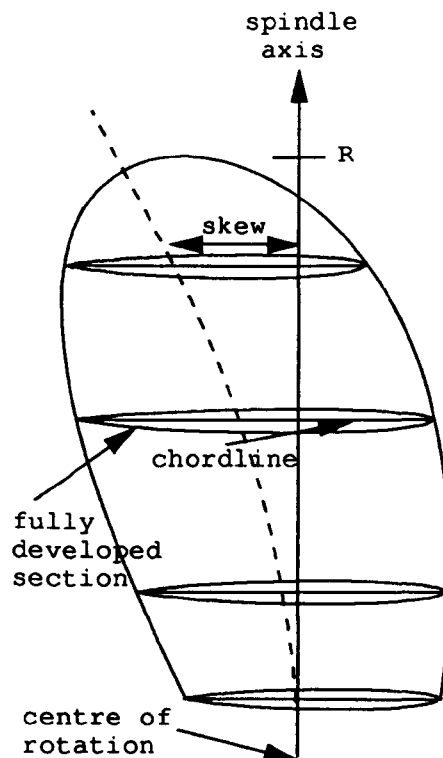


Figure 4.10: Illustration of skew.

Skew is applied to reduce the unsteady hydrodynamic loading on the blade when the propeller is operating in a highly non-uniform wake behind a ship [26]. This is presumed

to be the case as the leading edge of a skew propeller does not instantaneously pass the high wake region and so less shock is produced than for a blade passing through which has no skew.

The rake is an aft or forward displacement of the blade section perpendicular to the chordline (and the direction of skew), and is commonly used to increase the clearance between the hull and propeller

Therefore, by inclusion of the constants f and g a cubic distribution can be included for the skew and rake distributions through the blade, which is controllable through the boundary conditions. For the case considered here there is no skew or rake present, however a latter example illustrates a skew propeller. The rake is considered to be zero throughout this thesis.

4.5.2 Derivative conditions

To obtain the PDE blade geometry the derivative conditions need to be supplied. These need to be imposed in such a way that control of each of the distributions (the thickness, camber and chordlength) is maintained through the blade geometry. Therefore, a parameter is associated with each of the Fourier expansions $X_f(v)$, $Y_{stf}(v)$, Y_{ctf} , Y_{cf} to give the first derivative terms

$$x_u(1, v) = S_{xl}X_f(v) + S_{tl}Y_{stf}(v) \quad (4.40)$$

$$y_u(1, v) = S_{cl}Y_{cf}(v) + S_{tl}Y_{ctf}(v). \quad (4.41)$$

The first parameter S_{tl} affects the thickness in the y direction. This parameter also affects the x component of the section since it controls the original term $y_t \cos \theta$ (which has a Fourier series $Y_{ctf}(v)$) and the term $y_t \sin \theta$ (which has a Fourier series $Y_{stf}(v)$). Since $y_t \sin \theta$ is much smaller than $y_t \cos \theta$ the change in the x direction is much smaller than that in the y direction. The main parameter used to control the chordlength is then given by S_{xl} . This affects the term $X_f(v)$ which represents the chordwise marker. Finally the term which controls the camber is S_{cl} which is associated with the y distribution $Y_{cf}(v)$. These parameters are applied in a similar fashion at the tip of the blade to give the first derivative conditions on the boundary $u = 1$ as

$$x_u(0, v) = S_{xu}X_f(v) + S_{tu}Y_{stf}(v) \quad (4.42)$$

$$y_u(0, v) = S_{cu}Y_{cf}(v) + S_{tu}Y_{ctf}(v) \quad (4.43)$$

where the parameters at the tip will be larger than at the base due to the influence of the scaling factors ϵ_x and ϵ_y in equations (4.37-38).

Normally these boundary conditions would be sufficient to find a solution to the fourth order PDE problem. However, the solution obtained in this way does not give a sufficiently accurate representation of the Eckhardt and Morgen data. Much emphasis has been placed in this thesis on the control obtainable through the second 'curvature' derivatives and thus a 6th order PDE was introduced in order to gain the amount of control required to give an accurate representation of the actual blade geometry.

The curvature conditions are defined in exactly the same manner as the first derivatives to give the final boundary conditions for x and y , thus

$$x_{uu}(1, v) = C_{xl}X_f(v) + C_{tl}Y_{stf}(v) \quad (4.44)$$

$$y_{uu}(1, v) = C_{cl}Y_{cf}(v) + C_{tl}Y_{ctf}(v) \quad (4.45)$$

at the base of the blade, and

$$x_{uu}(0, v) = C_{xu}X_f(v) + C_{tu}Y_{stf}(v) \quad (4.46)$$

$$y_{uu}(0, v) = C_{cu}Y_{cf}(v) + C_{tu}Y_{ctf}(v) \quad (4.47)$$

at the tip to produce a solution for the x and y components of the PDE propeller blade which is of the form

$$x(u, v) = p_0(u) + \sum_{n=1}^4 A_n(u) \cos(2nv) + \sum_{n=1}^4 B_n(u) \sin(2nv) \quad (4.48)$$

$$y(u, v) = q_0(u) + \sum_{n=1}^4 C_n(u) \cos(2nv) + \sum_{n=1}^4 D_n(u) \sin(2nv) \quad (4.49)$$

where A_n, B_n, C_n and D_n are of the form

$$A_n \equiv a_1 u^2 e^{anu} + a_2 u^2 e^{-anu} + a_3 u e^{anu} + a_4 u e^{-anu} + a_5 e^{anu} + a_6 e^{-anu} \quad (4.50)$$

and

$$p_0(u) = p_0 + p_1 u + p_2 u^2 + p_3 u^3 + p_4 u^4 + p_5 u^5. \quad (4.51)$$

Due to the control achieved through the x and y conditions, the z (spanwise) coordinate need not be controlled as tightly as the others. Therefore, the z component is solved in the standard fashion for the fourth order PDE with the first derivative conditions given by

$$z_u(1, v) = S_{bot} \quad (4.52)$$

$$z_u(0, v) = S_{top} \quad (4.53)$$

which produces a solution of the form

$$z(u, v) = z_0 + z_1u + z_2u^2 + z_3u^3. \quad (4.54)$$

The constants associated with each of the solutions are obtained from the given boundary conditions as in previous examples.

The complete propeller blade is then generated by twisting each section to their associated pitch angle and curving them onto the imaginary cylinders as described previously. This is done at the final stage, and not considered as part of the initial boundary value problem, since the boundary conditions would be more complicated to set up for the initial problem.

4.6 Comparison between propeller geometries

In this section the PDE generated propeller is compared with the propeller given by Eckhardt and Morgen. Figure (4.11) displays the distributions of pitch, maximum camber, maximum thickness and chordlength for the Eckhardt and Morgen data, given by the crosses, and the PDE generated blade, illustrated by the continuous line.

It can be seen that a good fit between the two sets of data is produced. Table (4.3) illustrates the parameter values which define the blade. The number of parameters defining the PDE blade is only 23, 7 of which control the basic geometry ($m_x, t_x, D, c, f, \epsilon_x$ and ϵ_y). The other 16 are all control parameters, which is a very small set and hence practicable from the point of view of optimisation. It should also be remembered that the surface produced (as illustrated in figure (4.12)) has a smooth surface, whereas if the propeller surface were produced using a skinning method, as described in Chapter 1, then the surface would have to be checked to see if it were entirely fair. None of this verification is needed for the PDE generated propeller.

Consider now the plan view of the assembled blade sections as in figure (4.13). If one section near the centre of the blade span is highlighted, it can be read from the graphs of figure (4.11) that $m_x = 0.035$, $t_x = 0.046$, $c = 1.83$.

If these values are substituted into the original expression given by equations (4.6-11) for the NACA section, and displayed with the highlighted section, as in figure (4.14), it is seen that the section profiles match very closely and so it is deduced that the choice of derivatives ensures that the section shape is maintained along the span of the blade.

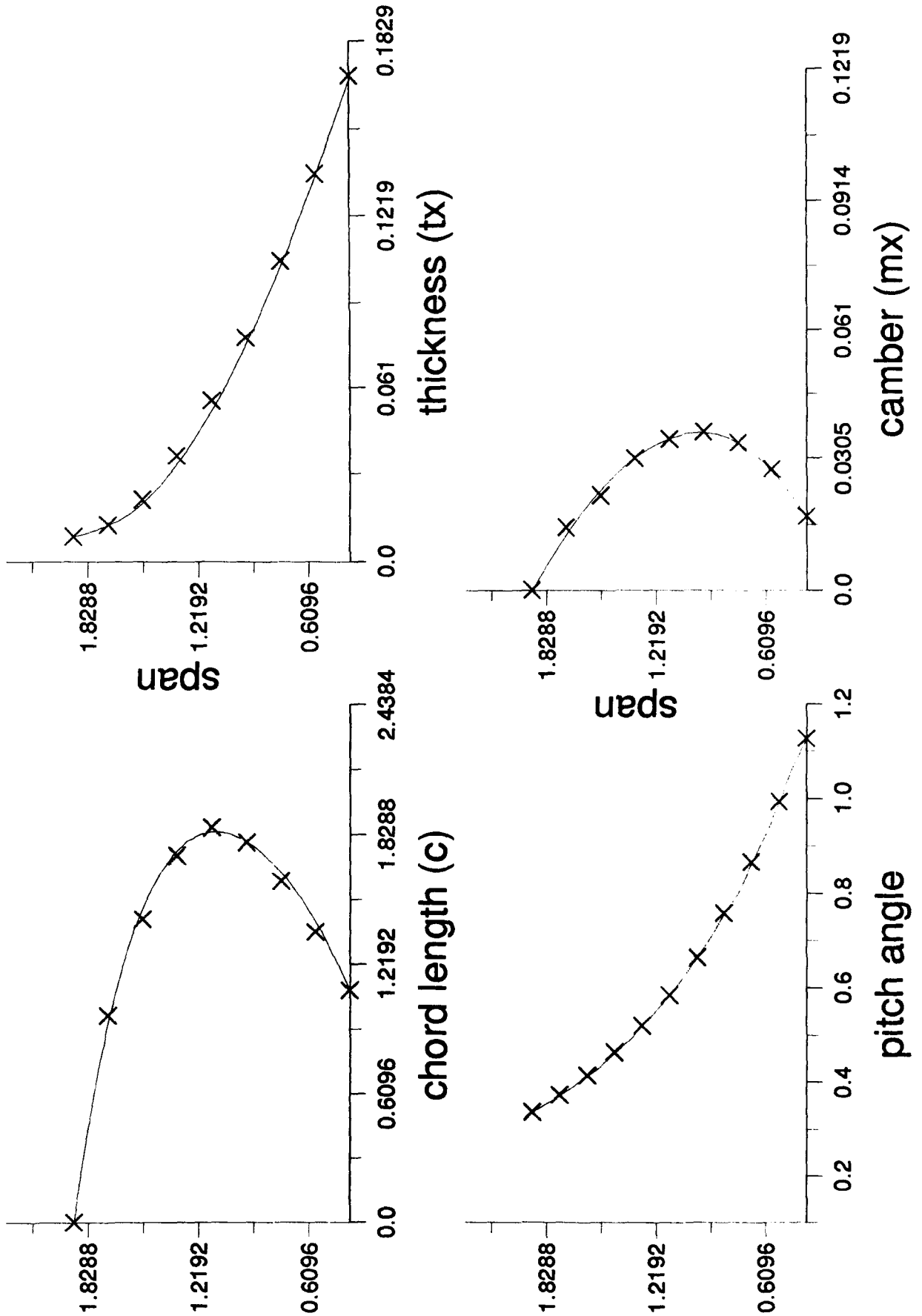


Figure 4.11: The distributions for the given data and the PDE generated blade.

Parameter Set					
Par	Fig (4.12)	Par	Fig (4.12)	Par	Fig (4.12)
m_x	0.0155	a_x	0.85	a_y	1.0
t_x	0.1555	S_{top}	4.2	S_{bot}	-1.66
D	6.25	S_{xu}	-3.8	S_{xl}	1.55
c	3.6	C_{xu}	2.1	C_{xl}	0.8
f	1.8	S_{tu}	2.0	S_{tl}	1.9
ϵ_x	0.0000	C_{tu}	1.0	C_{tl}	-1.0
ϵ_y	0.0052	S_{cu}	5.5	S_{cl}	-5.93
g	0.0	C_{cu}	2.0	C_{cl}	0.75

Table 4.3: Parameter values for the PDE generated surface.

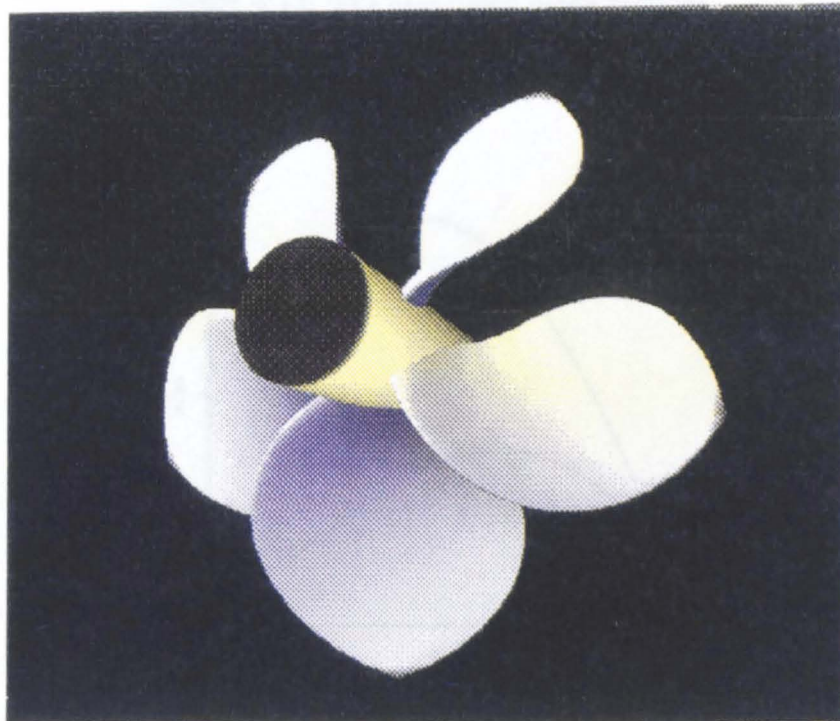


Figure 4.12: The generated propeller.

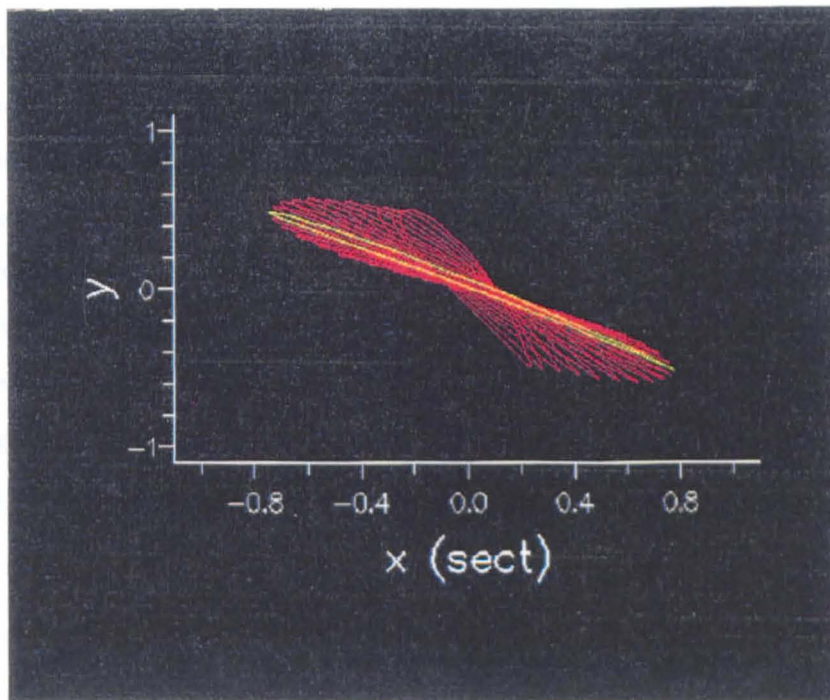


Figure 4.13: The assembled blade sections.

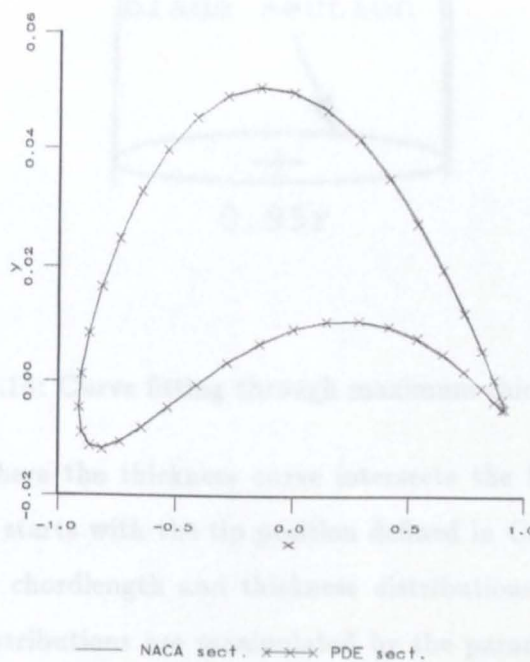


Figure 4.14: Comparison of section profiles.

4.7 Tip geometry

A frequent source of problems in the generation of a propeller blade occurs when generating the blade tip [26]. The last radius and section profile specified are often at $r = 0.95$ of the full radius of the propeller and it is therefore necessary to interpolate from this last section to produce the remainder of the surface close to the tip. This usually entails completing the blade profile in the chordwise direction, and the blade thickness to the tip. These two distributions are often produced by taking a cubic spline equation through the end points of the last known chordline to complete the blade outline curve, and by fitting an elliptic or hyperbolic profile through the last given section for the tip thickness [26], as illustrated in figure (4.15).

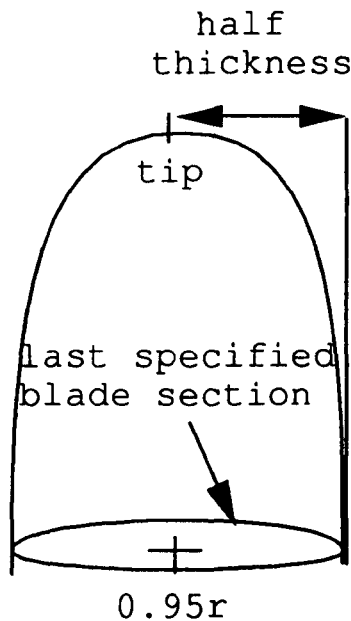


Figure 4.15: Curve fitting through maximum thickness at tip.

The tip occurs where the thickness curve intersects the blade outline curve. The PDE generated blade starts with the tip position defined in Cartesian coordinates, from which the continuous chordlength and thickness distributions are propagated into the blade span. These distributions are manipulated by the parameters at the tip and it is therefore a question of deriving the blade section distributions between the tip and the root.

In the data given by Eckhardt and Morgen, a theoretical finite value of the thickness is given, as can be seen from the graph of figure (4.11). If this is reproduced by the PDE

generated surface, as in figure (4.12) with the parameters of table (4.3) then the geometry at the tip is not represented by a point, but will be a line. Since the PDE generated surface has an analytic solution, it is possible to 'zoom in' on the surface at a close proximity to the tip. By looking at the surface close to the tip, for this finite thickness, it can be seen that a discontinuity occurs due to the parameterisation of the tip (or actual line). Figure (4.16) illustrates the discontinuity present at the tip by showing the blade from $r = R$ to $r = 0.995R$ for the finite thickness. Therefore, it is necessary to take the actual tip thickness to be zero (as would be the case in any real blade). With the aid of the control parameters S_{tu}, C_{tu} we can influence the thickness in such a way that the continuous maximum thickness distribution is zero at the tip, while rapidly moving out to approximate the finite thickness given at the tip. Again, it should be noted that for the surface to be manipulated in this way, as in the case of the wine glass in Chapter 2, a sixth order PDE is essential. For the surface to be continuous across the tip, it is also required that the upper z derivative S_{top} be set to zero. This can clearly be seen in figure (4.17). Although this implies the loss of one control parameter S_{top} it can be seen from figure (4.18) that the distributions can still be approximated. Table (4.4) illustrates the parameter values used to generate this propeller (as illustrated in figure (4.19)). The other parameter set demonstrates the ease of manipulation of the surface, as it describes the geometry of a skew propeller, which is shown in figure (4.20).

Parameter Set								
Par	(4.19)	(4.20)	Par	(4.19)	(4.20)	Par	(4.19)	(4.20)
m_x	0.016	0.016	a_x	0.85	0.9	a_y	1.0	1.1
t_x	0.156	0.156	S_{top}	0.0	0.0	S_{bot}	-2.3	-1.5
D	6.25	6.25	S_{xu}	-2.2	-3.0	S_{xl}	0.3	1.8
c	3.6	3.0	C_{xu}	28.0	1.0	C_{xl}	25.0	0.5
f	1.8	0.5	S_{tu}	640.	5.0	S_{tl}	1.0	1.0
ϵ_x	0.000	0.000	C_{tu}	-8000.	2.0	C_{tl}	-5.	-0.6
ϵ_y	0.001	0.000	S_{cu}	0.2	3.0	S_{cl}	-3.3	-2.0
g	0.0	0.0	C_{cu}	65.0	3.0	C_{cl}	35.0	1.0

Table 4.4: Parameter values for the PDE generated surface.

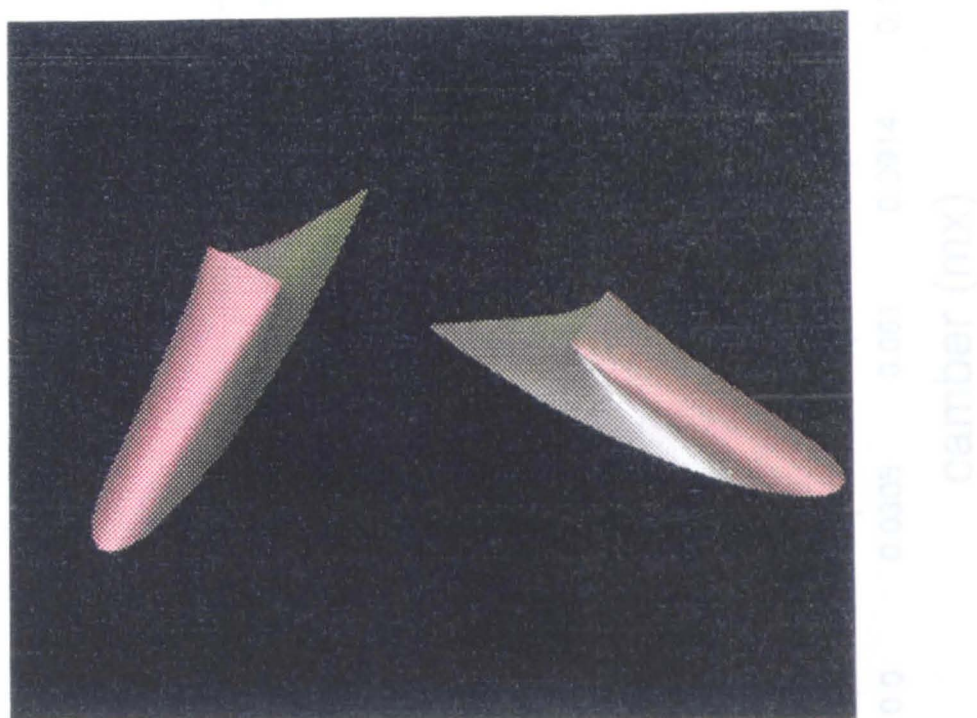


Figure 4.16: The discontinuity at the tip between $r = 0.995R$ and $r = R$.

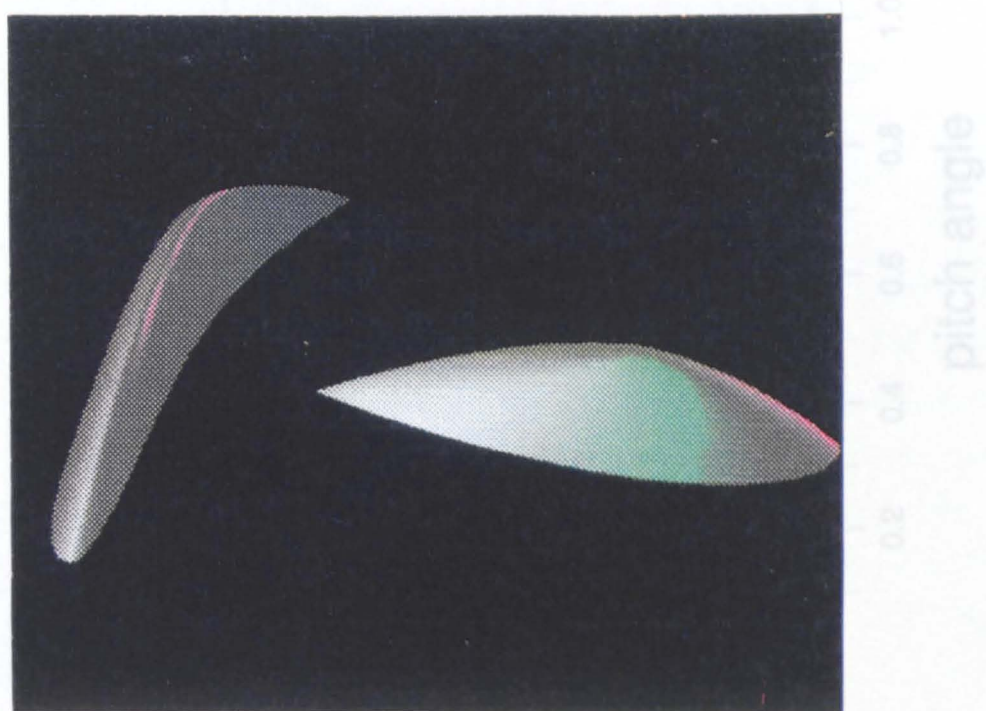


Figure 4.17: The continuous tip profile between $r = 0.995R$ and $r = R$ for $S_{top} = 0$.

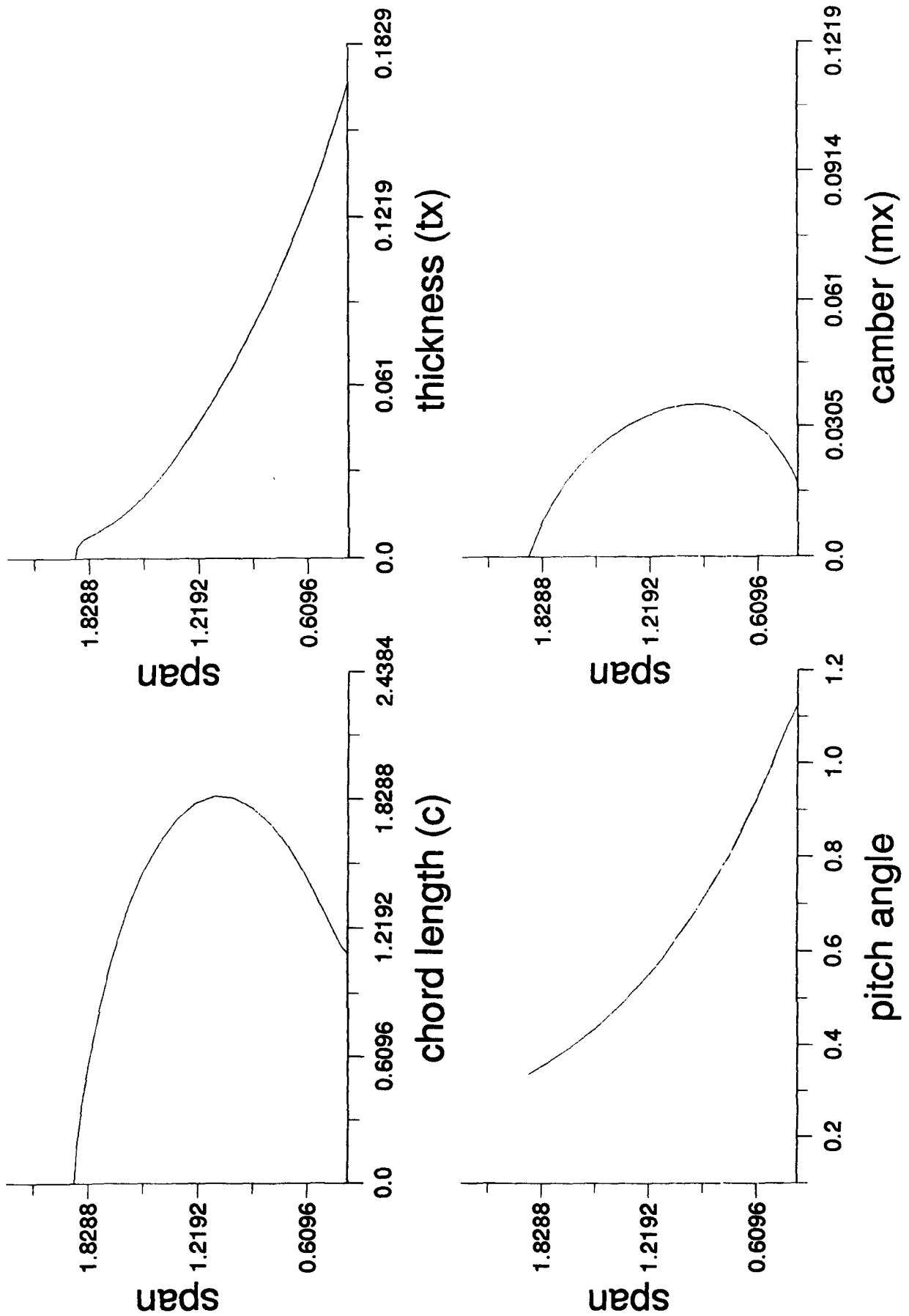


Figure 4.18: Approximations to the distributions for a smooth tip geometry.

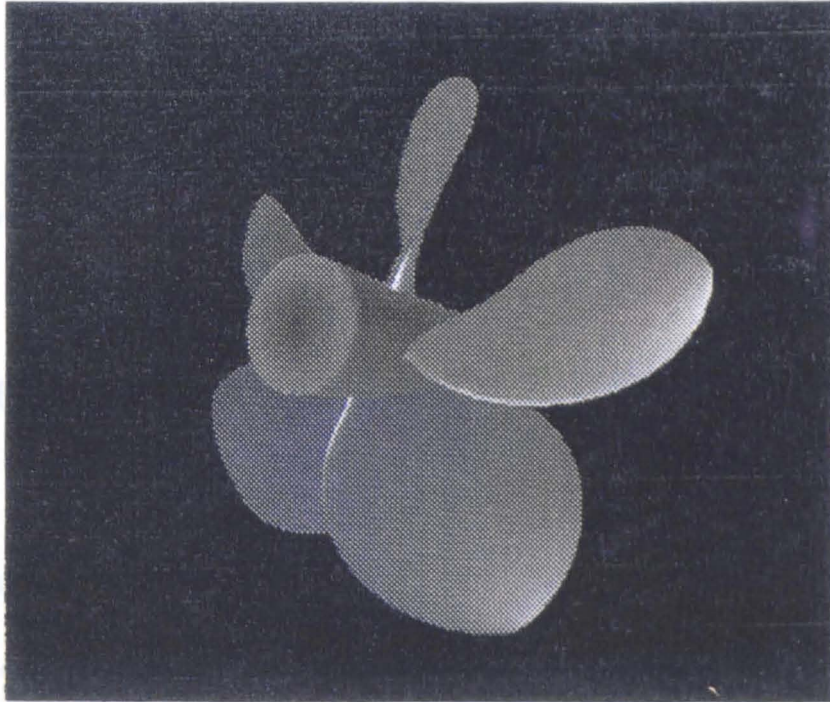


Figure 4.19: The PDE generated propeller with continuity imposed at the tip.

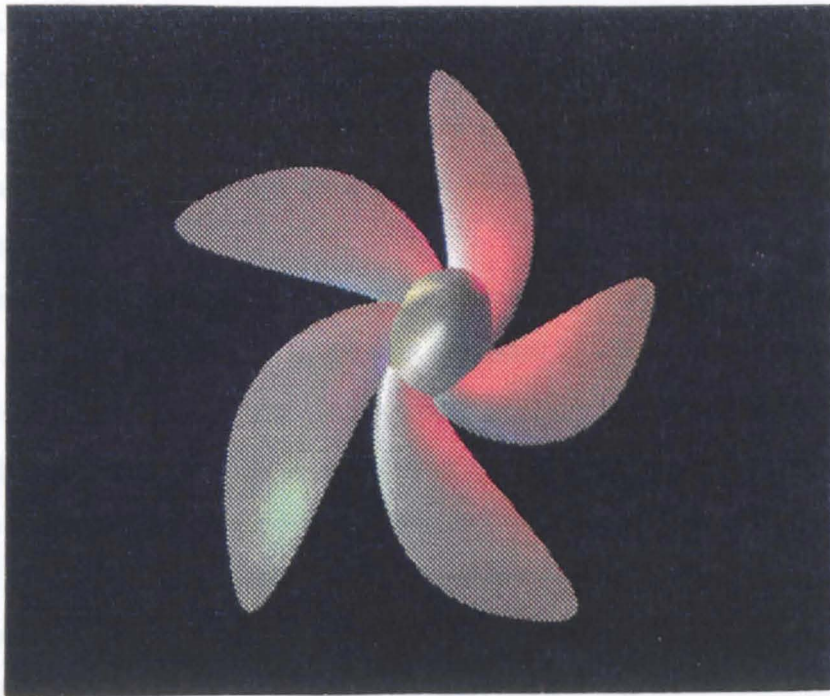


Figure 4.20: An example of a skew propeller generated from the PDE method.

Chapter 5

Panel method implementation

5.1 Introduction

The propellers generated in the previous chapter can now be analysed. In order to optimise the propeller blade geometry, it is important that an accurate prediction of the propeller's performance is determined. The PDE representation of the real propeller can then be used as an initial design from which to improve the propeller's hydrodynamic performance by methods described in Chapter 6. Besides hydrodynamic performance there are also other physical properties that need to be considered, which include strength requirements, vibrational properties and cavitation considerations. In this thesis we ignore strength requirements, etc. and will concentrate mainly on cavitation corrections, and thus, we need to be able to get an accurate picture of the pressure distribution on the blade's surface.

As has been mentioned, the lifting line methods implemented by Lerbs [42], and Eckhardt and Morgen [27] rely heavily on empirical charts to obtain results, and do not give accurate predictions for distributions such as pressure. Lifting surface models do give pressure distributions, but are inaccurate in regions such as at the leading edge, where cavitation may occur. Boundary element methods, or as they are commonly referred to 'panel methods', allow varied complex geometries to be analysed, while still being able to model regions where rapid variations in pressure distributions may occur. These distributions can be accurately modelled by placing a higher concentration of panels in those regions where high pressures occur; for example, near the leading edge of a blade, panels can be concentrated to pick up any leading edge pressure peaks, and near the mid-chord span, the panel resolution can be relatively coarse because the pressure gradients

there are less pronounced.

In this chapter we will illustrate how one such panel method can be adapted to the task of obtaining the performance of the propeller geometry generated in Chapter 4.

5.2 Potential flow theory

Generally, we are unable to solve the full Navier Stokes equations, and in order to model the flow about a body we must make certain assumptions in order to obtain a set of equations which admit a solution, yet which still capture the important physical properties of the flow. By assuming the flow of an ideal fluid we arrive at a potential flow.

We assume that potential flow is a good approximation for a propeller flow provided that it is operating at low Mach numbers, and that separation does not occur. This assumption of no separation can readily be assumed for modern high lift devices for which the range of C_l over which the flow remains attached to the surface is large, thus giving a greater validity for the potential flow solution.

The vorticity in the fluid is defined by

$$\underline{\omega} = \nabla \times \underline{V} \quad (5.1)$$

where \underline{V} is the fluid velocity. If there is zero vorticity in the flow then this is said to be irrotational. Further, if the fluid in which we are working is inviscid and not subject to any body forces, then this flow will remain irrotational.

Taking into account the assumption of incompressible, irrotational flow, the general Navier Stokes equation of motion reduces to the Euler equation of motion:

$$\frac{D\underline{V}}{Dt} = -\frac{1}{\rho}\nabla p \quad (5.2)$$

where all body disturbance forces are assumed to be conservative and are absorbed in the pressure. This can be assumed since the density is uniform.

Equation (5.2) can be written in the alternative form

$$\frac{\partial \underline{V}}{\partial t} - \underline{V} \times \underline{\omega} + \nabla \left(\frac{1}{2}q^2 \right) = -\frac{1}{\rho}\nabla p. \quad (5.3)$$

Now, since an irrotational velocity field may be expressed as the gradient of a scalar potential function, we can write the fluid velocity as

$$\underline{v} = -\nabla \phi \quad (5.4)$$

with the total fluid velocity given by

$$\underline{V} = \underline{V}_\infty + \underline{v}. \quad (5.5)$$

The velocity \underline{V}_∞ is called the onset flow and is defined as the velocity field that would exist if all boundaries were transparent to fluid motion. This is known as the onset of the problem, and is commonly represented as a uniform parallel stream and is thus a constant vector [4].

Now, by substituting equation (5.5) into equation (5.3) we arrive at

$$\underline{\nabla} \left(-\frac{\partial \phi}{\partial t} + 1/2q^2 + p/\rho \right) = 0, \quad (5.6)$$

which for a steady flow gives us Bernoulli's equation

$$p + 1/2\rho q^2 = \text{const}. \quad (5.7)$$

This can be used to determine pressure distributions in cases such as those of an aircraft in steady, uniform flight. However, for a propeller rotating we must make specific alterations to the equations of motion.

The propeller is assumed to be in a uniform stream \underline{V}_∞ , with a steady rotation with angular velocity ω about the y -axis. At the propeller, a rotating frame of reference may be employed, with an angular velocity ω , relative to which the flow about the propeller will be steady. For uniform inflow, the incoming velocity flow field \underline{V}_{in} , with respect to the rotating system will now be given by

$$\underline{V}_{in} = \underline{V}_\infty + \underline{\omega} \times \underline{r} \quad (5.8)$$

where \underline{r} is the distance from the pivot axis (through the centre of the propeller hub) to a point on the blade. The total fluid velocity around the propeller will now be given by

$$\underline{V} = \underline{V}_{in} + \underline{v}. \quad (5.9)$$

Now, the equation of motion of a fluid in the moving frame is identical with that of (5.2) provided that we suppose an additional body force per unit mass

$$- 2\underline{\omega} \times \underline{v} - 1/2\underline{\nabla}(\underline{\omega} \times \underline{r})^2 \quad (5.10)$$

acts upon the fluid. The first term is the deflected or Coriolis force [76], and is perpendicular to both $\underline{\omega}$ and \underline{v} , and the second term is the centrifugal force. The equation of motion (5.6) becomes

$$\underline{\nabla} \left(-\frac{\partial \phi}{\partial t} + 1/2q^2 + p/\rho - 1/2(\underline{\omega} \times \underline{r})^2 \right) = 0. \quad (5.11)$$

This then gives the modified Bernoulli equation for a steady flow relative to the axis

$$p/\rho + 1/2q^2 - 1/2(\underline{\omega} \times \underline{r})^2 = \text{const.} \quad (5.12)$$

The pressure distribution over the surface of the blades can now be obtained by applying (5.12) to give:

$$p_\infty + 1/2\rho V_\infty^2 = p + 1/2\rho q^2 - 1/2\rho(\underline{\omega} \times \underline{r})^2 \quad (5.13)$$

where p_∞ is the pressure of the undisturbed flow.

The pressure distribution is then defined in terms of a coefficient of pressure by

$$C_P = \frac{p - p_\infty}{1/2\rho(V_\infty^2 + r^2\omega^2)} \quad (5.14)$$

or, as a function of the disturbance velocity

$$C_P = 1 - \frac{q^2}{V_\infty^2 + r^2\omega^2}. \quad (5.15)$$

The continuity equation given by

$$\frac{1}{\rho} \frac{D\rho}{Dt} + \nabla \cdot \underline{v} = 0 \quad (5.16)$$

reduces to the equation

$$\nabla \cdot \underline{v} = 0 \quad (5.17)$$

under the assumption of constant density, which when combined with equation (5.4) yields the result that the potential ϕ satisfies Laplace's equation

$$\nabla^2 \phi = 0 \quad (5.18)$$

in the region exterior (or interior) to the boundary surface immersed in the fluid. Usually this region is exterior to the body surface and it will give the physical (potential) flow around the outside of the body (the propeller blade in this instance).

To solve the Laplace equation, boundary conditions must be specified. These we obtain by requiring that on the surface of the body there is zero flow into or out of the body, i.e.

$$\underline{V} \cdot \underline{n} \Big|_{\text{surface}} = 0 \quad (5.19)$$

with the usual exterior problem condition that

$$|\nabla\phi| \rightarrow 0 \quad (5.20)$$

at large distances from the body (specifically as the distance tends to infinity).

The solution of equation (5.18) subject to the boundary conditions (5.19) and (5.20) constitutes a well-posed problem. This can be solved by reducing the problem to an integral equation over the boundary surface by the use of Green's theorem [47].

5.2.1 Green's method of solution

The formal solution of Laplace's equation external to a body surface S in a region R can be given in terms of a Green's function

$$\phi_p = \frac{1}{4\pi} \int_s \frac{\sigma}{r} ds - \frac{1}{4\pi} \int_s \mu \underline{n} \cdot \nabla \left(\frac{1}{r} \right) ds \quad (5.21)$$

where r is the distance from the point P to a point on the boundary surface, and ϕ_p is the potential at that point. Lamb [47] shows that this integral can be thought of as representing the flow external to a body, with the potential at a point P due to an unknown source distribution σ on S represented by the first term of the integral, and the potential due to an unknown doublet distribution μ on S represented by the second integral.

Thus, from equations (5.21), (5.4) and (5.5) the velocity induced at a point outside a body at rest in a uniform flow will be given by

$$\underline{V} = \underline{V}_\infty - \nabla \left(\frac{1}{4\pi} \int_s \frac{\sigma}{r} ds - \frac{1}{4\pi} \int_s \mu \underline{n} \cdot \nabla \left(\frac{1}{r} \right) ds \right). \quad (5.22)$$

5.3 Potential solution using panel methods

In practice the solution of the integral equation (5.22) is obtained by discretising the surface S into many panels. Associated with each of these is an unknown source and/or doublet, which represent the flow as described above. Then, by imposing the boundary condition of no flow normal to the body surface at an appropriate number of points on the panels, we can determine the unknowns σ and μ and hence evaluate the potential, and velocity at any point.

5.3.1 Panel generation

Generally the panels are formed by taking lines of constant spanwise and chordwise stations over the body surface. From the nature of the PDE method, these will automatically be generated as the iso-lines of u and v . However, due to the degree of curvature of the surface, these panels will not usually be planar, and so there is a need to project these panels onto a plane passing through three of the four points. This implies that the panel method implemented is a low-order panel method, as described by Hess [77].¹

To obtain the most appropriate plane on which to project the points, the distance d from each of the four corner points to the plane containing the other three points is found. From this the four points are realigned by moving each one a distance $d/2$ perpendicular to the corresponding common plane, to obtain a new plane which contains all four points. The final plane is that which requires least movement of the fourth point. The four points now correspond to the corners of the panel. This may however mean that slight gaps appear between adjacent panels and 'leakage' may occur [77]. However, Hess [4] says that these are of small significance, since the width of the openings between the panels are small compared to the dimensions of the panels, due to the method of panel formulation.

Once we have formed the planar panels, we need to associate with each of them a location at which the fluid velocity at the surface will be evaluated. This point is known as the control point of the panel. Commonly, the control point is taken to be the centroid of the panel; as will be the case in this thesis. An equally feasible way to locate panels and control points over the surface is by using cosine spacing [3]. This method is useful when concentrating panels in a certain region, since the panels are not uniformly spaced but, as the name suggests, have a spacing which is based on a cosine function. In effect, this is similar to the panel spacing generated by the PDE method for this example, around the airfoil section. This can be seen by noting that the range over which v is taken is from $-\pi/2$ to $\pi/2$. Thus, if v is taken at evenly spaced intervals over this range, and remembering that the parameterisation along the blade section is governed by

$$x = c \sin^2 v \quad (5.23)$$

¹A higher-order panel method would require curved (or parabolic) elements over the surface. The term higher-order does not refer to the accuracy of the solution, but only to the discretisation; in general, higher-order methods can achieve a desired accuracy using a lower number of panels, however the calculation of the induced velocities on a flat plate is easier to evaluate and so low-order panel methods are more commonly used [78].

we see that there will be a higher concentration of panel-generating isolines near $v = -\pi/2$, $v = 0$ and $v = \pi/2$, which correspond to the leading and trailing edge of the section, with a more sparse panel distribution midchord of the section. Thus, the parameterisation used by the PDE isolines proves to be an appropriate choice for the panel method.

Also associated with each panel we define a unit normal to the panel from the cross product of the panel diagonals. The sense in which the cross product is taken is crucial, since the requirement is that the normal to the surface is directed into the fluid flow field to ensure that we obtain the solution external (and not internal) to the body surface.

Hence, if the surface integral (5.22) is discretised into N planar panels as above, and if the corner points of panel i , where $1 \leq i \leq N$, are denoted $\underline{x}_1, \underline{x}_2, \underline{x}_3, \underline{x}_4$ then the centroid and the unit normal will be defined by

$$\underline{c}_i = \frac{1}{4}(\underline{x}_1 + \underline{x}_2 + \underline{x}_3 + \underline{x}_4) \quad (5.24)$$

$$\underline{n}_i = \frac{(\underline{x}_4 - \underline{x}_2) \times (\underline{x}_3 - \underline{x}_1)}{|(\underline{x}_4 - \underline{x}_2) \times (\underline{x}_3 - \underline{x}_1)|} \quad (5.25)$$

5.3.2 Panel source and doublet distribution

The panel method being utilised in this thesis is based on the panel method of J. H. Petrie [59], which has been used for determining the flow fields around wing bodies. However, various adaptations are needed to render it appropriate for the flow about a marine propeller operating in a uniform flow field.

The first panel method calculations of potential flow, derived by Hess and Smith [48], considered the body to be non-lifting. Thus, a distribution of source terms only was associated with the panels. On each panel an unknown source term, of constant strength σ , was placed at the control point q . By assuming the condition of no flow normal to the boundary the unknown source terms σ could be found and thus the potential at a point P could then be determined from

$$\phi_P = \int_S \frac{\sigma(q)}{r(P, q)} ds \quad (5.26)$$

where $r(P, q)$ is the distance between the two points P and q .

The problem of three-dimensional lifting potential flow is a more difficult problem to formulate. Hess [4] demonstrates that lifting portions of the body can be represented by associating a doublet distribution μ with them. This distribution can be arranged in many configurations, and this is one way in which panel methods can differ. Hess [79], for

example, arranges the doublet distribution so that it varies linearly around each section curve of the wing to represent the value of the circulation.

Body surfaces can therefore be divided into two types: those which are lifting sections and those which are non-lifting. The criterion used to distinguish between the two types is the presence of a sharp trailing edge. If one is present, from which issues a zero-thickness trailing vortex (as described in Chapter 3), then the section is considered to be lifting and a Kutta condition is applied to fix a value on the circulation, from which the lift can be calculated (as will be described later). Sections which give no lift, such as the central hub of the propeller, have no sharp edges and do not issue trailing vortices and so they are represented solely by source terms [80].

Hess further illustrates that the doublet distribution μ is equivalent to a sheet of vorticity $\underline{\omega}$ on the surface S , plus a line vortex of strength Γ around the perimeter C of the panel; where

$$\underline{\omega} = -\underline{n} \times \nabla\mu \quad (5.27)$$

$$\Gamma = \mu \text{ (everywhere on } C) \quad (5.28)$$

and \underline{n} is the outward unit normal from the panel.

Physically then, the doublet distributions μ are equivalent to vortex sheets, and can be used to take into account the lift and camber of the surface, whereas the source terms have no direct physical interpretation, but can be used to represent the thickness of the body [59].

The panel method of Petrie is different from others, such as that of Hess [4], in that each of the panels consists of a unique source value σ located at the control point, with a ring vortex around the perimeter of the panel of constant strength μ , plus a vortex sheet $\underline{\omega}$ over the entire surface, as can be seen in figure (5.1). This panel method is termed the SPARV panel method (Source Panel and Ring Vortex).

5.3.3 Calculation of induced velocities

Given the distributions of σ_j and μ_j the value of the velocity (or potential) at a point (5.22) can be determined. By discretising the surface S into N planar panels, we obtain the velocity at the centroid of each panel i , where $1 \leq i \leq N$, to be

$$\underline{V}_i = \underline{V}_\infty - \sum_{j=1}^N \left[\frac{1}{4\pi} \nabla \int_{\text{panel } j} \frac{\sigma_j}{r} ds - \frac{1}{4\pi} \nabla \int_{\text{panel } j} \mu_j \underline{n}_j \cdot \nabla \left(\frac{1}{r} \right) ds \right] \quad (5.29)$$

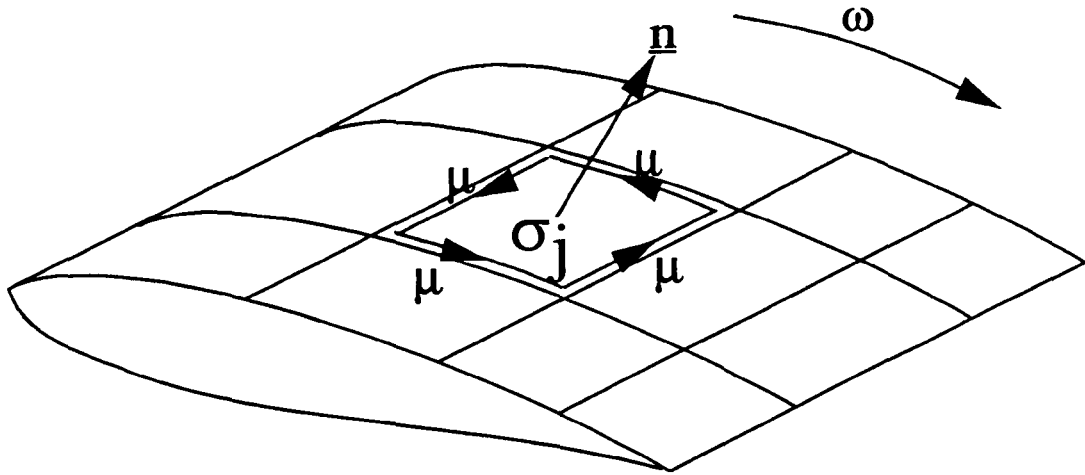


Figure 5.1: Distribution of panels over wing.

where σ_j, μ_j are the unknown distributions we require at each panel.

Now, as we have constant values for the source terms σ_j and ring vortex distributions μ_j , these can be taken outside the integrals.

Thus, we now have N control points at which we must evaluate the influence coefficients for the induced velocities from each of the N panels, given by

$$\underline{V}_{sij} = \nabla \int_j \frac{1}{r} ds \quad (5.30)$$

and

$$\underline{V}_{dij} = -\nabla \int_j \underline{n} \cdot \nabla \left(\frac{1}{r} \right) ds. \quad (5.31)$$

These calculations of the velocity influence at the N control points account for one of the most substantial amounts of computer time in the panel method. The expressions (5.30) and (5.31) can be integrated analytically over each of the panels. This is most conveniently done by using the coordinate system in which the panel itself lies, and thus coordinates of points and vector components must be transformed between the global and 'element' coordinate system, as described by Hess [48]. The analytic integration produces lengthy formulae. A multipole expansion is used to obtain a good approximation if a particular panel is sufficiently far from the control point at which the calculation is done. This expansion is used if the distance between the point and the panel is greater than 2.45 times the maximum dimension of the panel. If the distance is greater than 4 times the maximum dimension of the panel then a point source formula can be used to approximate the influence velocity from the panel. The complete formulae for the different cases are

laid out in Appendix B.

The one task which remains for us to do is to implement some form of Kutta condition into the panel method to obtain a realistic solution.

5.3.4 Kutta condition

In Chapter 3 we noted that for the flow to leave the wing section smoothly, the stagnation point should be located at the trailing edge. For a conventional wing section, there is a unique value of the circulation γ (and hence also lift) which makes the surface velocity finite at the trailing edge. This is the Kutta condition which determines that the streamlines of the flow leave the trailing edge smoothly. Thus, we need a formulation for the Kutta condition which is to be applied at all lifting sections.

The Kutta condition is applied in the SPARV panel method by ensuring that the velocity magnitudes (and hence the pressures) be equal on either side of the surface at the trailing edge. Thus from the conditions that

$$\underline{V}_u \cdot \underline{V}_u - \underline{V}_l \cdot \underline{V}_l = 0 \quad (5.32)$$

where \underline{V}_u , \underline{V}_l are the velocity vectors on the upper and lower surfaces respectively, Petrie [59] arrives at the Kutta condition expressed as

$$\underline{V}_m \times \underline{\gamma} = 0 \quad (5.33)$$

where $\underline{V}_m = \frac{1}{2}(\underline{V}_u + \underline{V}_l)$ is the average velocity at the trailing edge and $\underline{\gamma} = \underline{n} \times (\underline{V}_u - \underline{V}_l)$. Petrie states that this implies that at the trailing edge, the trailing vortex sheet is a streamline of the flow and the bound vorticity is zero. These conditions are satisfied by ensuring that at the trailing edge a set of trailing horseshoe vortices issue, which have associated with each of them the same constant vortex strength μ as on the panel perimeter adjacent to them, as illustrated in figure (5.2).

Each horseshoe vortex is discretised into a finite number of line vortices. Then the velocity at the control point i , due to each of these line vortices, of strength μ can be evaluated using the formulae laid out in Appendix B. The influence velocities from all line vortices are summed for each horseshoe vortex, and added to the contribution from the components \underline{V}_{dij} from the vortex ring on the panel adjacent to the horseshoe vortex.

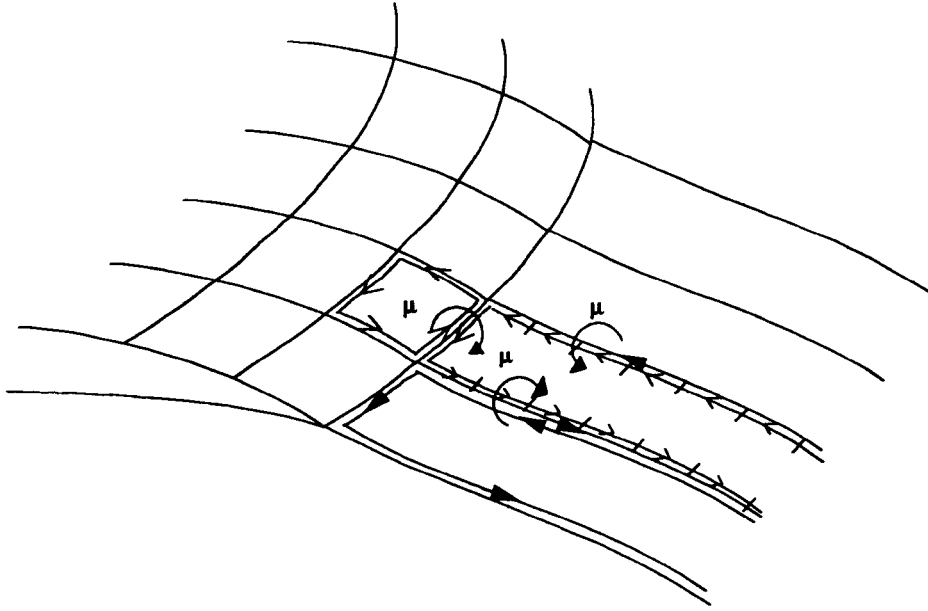


Figure 5.2: Trailing wake geometry.

Therefore, we now have the coefficients from the induced velocities, \underline{V}_{sij} at N control points from the influence of the N source terms, plus the coefficients from the induced velocities \underline{V}_{dij} from the N vortex rings, with an explicit Kutta condition applied on the trailing edge.

5.3.5 Application of boundary conditions

The next stage is to impose the boundary condition of zero normal flow at the control point of each panel. This means that the boundary conditions will only be exactly satisfied at the centroid of each panel; however, once the distributions of sources and doublets are found, the velocity at any point can be obtained from equation (5.29). If we define

$$A_{ij} = \underline{n}_i \cdot \underline{V}_{sij} \quad (5.34)$$

$$B_{ij} = \underline{n}_i \cdot \underline{V}_{dij} \quad (5.35)$$

where A_{ij} and B_{ij} are termed the influence matrices, we obtain the final set of N linearised simultaneous equations

$$\sum_{j=1}^N [A_{ij}\sigma_j + B_{ij}\mu_j] = \underline{n}_i \cdot \underline{V}_\infty \quad (5.36)$$

which contain the $2N$ unknowns σ_j and μ_j , and hence we have a set of simultaneous equations with a non-unique solution.

5.3.6 Solution of simultaneous equations

The main difference between the SPARV panel method and others in the literature [80] is in the rendering of the source and doublet distributions. Many other panel methods assume linearly varying vortex distributions around each wing section, which start at zero at the trailing edge of the wing section, and reach the value of the circulation about the section on the upper side at the trailing edge. Then, to obtain the values of the bound vorticity associated with each section, a Kutta condition is applied at the same number of stations as there are wing sections.

However, Maskew and Woodward [81] suggest that unknown values for each doublet strength on all panels should be assumed, as opposed to an assumed vorticity distribution. They argue that the assumed vorticity distribution does not represent the correct loading, and so the source distribution provides the necessary adjustment by forming source - sink pairs between the upper and lower surfaces. Consequently, the source distribution has a magnitude larger than that required for thickness alone, and so internal cross flows exist which may affect the circulation.

From these experiences they hypothesise that a surface singularity model should be applied so that the mean line of the airfoil is a streamline of the internal flow, so as to minimise the internal crossflows. This constraint requires that both magnitudes of the source and vortex distributions be equal at corresponding points on the upper and lower surfaces. This means that if we have N unknown source terms on the N panels, with $N/2$ panels on both the upper and lower surfaces, we allow for this requirement by enforcing the condition that

$$\sigma_j = \sigma_{j+\frac{N}{2}} \quad \text{for } j = 1 \text{ to } \frac{N}{2} \quad (5.37)$$

and similarly for the vortex strengths

$$\mu_j = \mu_{j+\frac{N}{2}} \quad \text{for } j = 1 \text{ to } \frac{N}{2}. \quad (5.38)$$

Thus equation (5.36) reduces to a set of N simultaneous equations in N unknowns. The solution of this $N \times N$ matrix provides the second most costly procedure of the panel method in terms of computer usage. Commonly this is solved by methods such as lower-upper decomposition [82], due to the matrix of coefficients being completely filled and diagonally dominant. For matrices of coefficients obtained from surfaces having a very high resolution of panels, fast matrix solvers, such as that of Clark [83] have been

developed (specifically for the purpose of obtaining the solutions of influence matrices of panel methods).

5.3.7 The influence of the vortex sheet

Having established the unknown values of the source and doublet terms σ_j and μ_j respectively, we can then substitute these into equation (5.29) to obtain the velocities at the control points of the surface.

However, the assumptions we are using in this method are that the doublet distribution is equivalent to a vortex sheet plus a line vortex around the panel. When we calculated the velocity influence matrix components \underline{V}_{dij} we evaluated the contribution from the line vortex around the panel, but neglected to calculate the influence from the vortex sheet. This was because the velocity component of the vortex sheet acts tangentially to the surface, and so when the boundary conditions were imposed by taking the scalar product with the normal to the surface, there is zero contribution from these terms.

Now that we are calculating the actual velocities at the control points on the surface, we must include the velocity component obtained from the vortex sheet. This is given by Petrie as

$$\underline{V}_i = \frac{1}{2} \underline{\omega} \times \underline{n} \quad (5.39)$$

where \underline{n} is the unit normal at the control point. The numerical evaluation of this velocity component is laid out in Appendix B, as derived by Petrie. The final velocity at a point i can thus be defined as

$$\underline{V}_i = \underline{V}_\infty + \underline{V}_l + \frac{1}{4\pi} \sum_{j=1}^N \sigma_j \underline{V}_{sij} + \mu_j \underline{V}_{dij} \quad (5.40)$$

from which we can obtain the coefficient of pressure C_P from Bernoulli's equation (5.7), which is necessary for the calculation of cavitation numbers, as will be discussed in Chapter 6.

5.4 Propeller model

The SPARV panel method as implemented above would be ideal for the solutions of problems such as determining the flow about an aircraft wing at a fixed location in a uniform stream. Unfortunately, it is not immediately suited to the problem of determining

the flow about a marine propeller operating in a uniform flow, and so we must modify the SPARV model to render it useful, as will be described next.

5.4.1 Number of blades

To evaluate the flow around a complete propeller we consider the body surface to comprise Z blades, each of which is identical and each considered a surface which generates lift. Any particular blade will now produce an effect on all of the others. One of these blades is designated the key blade on which the velocity and pressure distributions are to be evaluated. The others are described as secondary blades and will have the same pressure distributions as the key blade, with the velocity distributions being of a similar form, except for a reorientation determined by the position of each of the blades relative to the key blade.

Some models also provide for the effect of the central hub, which is classed as a non-lifting surface [80]. However, as Kerwin states [84], the presence of the hub as a solid boundary can be conveniently ignored since the inner radii contributes little to overall propeller forces as a result of the low rotational velocity in this region. Thus, since we are primarily looking at the propeller forces and are concerning ourselves in regions closer to the tip (as will be discussed later), the presence of the hub will be completely ignored in this thesis.

The panel method must be able to accommodate any number of blades on the propeller. In equation (5.36) the velocity influence matrix coefficients at all N control points from all panels on the key blade are determined. For a general Z bladed propeller, the influence at a control point on the key blade will be from all N panels on itself, plus all N panels on each of the other $Z - 1$ blades. Hence $Z(N \times N)$ influence velocity matrices \underline{V}_{sij} and \underline{V}_{dij} will be determined. The final velocity influence matrices A and B are then derived by adding the Z matrices together, from which the boundary condition (5.19) can once again be applied.

5.4.2 Steady state rotation

The next modification which needs to be made is to the reference coordinate system, since besides moving uniformly relative to the stream, the propeller also rotates at a constant rate.

Thus, if the propeller is considered to be in a state of steady rotation with angular

velocity ω , about a pivot axis running through the central hub (in this case it will be the y -axis), then there will be a further contribution to the velocity at the panel centroid \underline{c}_i , given by

$$\underline{v}_r = \omega(\underline{N}_0 - \underline{r}_{ci}) \times \underline{N} \quad (5.41)$$

where \underline{N}_0 is the origin of the pivot, \underline{r}_{ci} is the vector from the origin of the pivot (here it is the coordinate origin) to the centroid \underline{c}_i of the panel i , and \underline{N} is the unit vector associated with the pivot axis. This component can be found and is added to the RHS of equation (5.36) to give the inflow velocity \underline{V}_{in} (5.8) before imposing the boundary condition of zero flow normal to the surface. In effect the propeller is at rest in a rotating frame of reference as described in section (5.2).

5.4.3 The trailing wake geometry

In the case where no rotation occurs, straight line vortices can be used to provide a model for the trailing wake (with the option of the vortex rolling up as it gets further from the body [85]). For rotating bodies, such as the marine propeller, the trailing wake geometry is more complicated. Much work has been put into the area of wake modelling for a marine propeller, and is still ongoing [44], [86].

The propeller as it rotates in the water induces three velocity components, radial, tangential and axial. To illustrate these, the propeller blade can be considered as a lifting line operating in a non-viscous fluid, as in figure (5.3). In figure (5.3) u is the induced velocity, u_a the axial velocity, u_t the tangential velocity, β the advance angle, β_i the hydrodynamic pitch angle, and ϕ the pitch of the propeller blade section.

Within the context of propeller design, propellers can then be grouped into three main categories [65], based on the axial component of the induced velocity u_a , by

- $u_a \ll V_\infty$ - for lightly loaded propellers (airscrews)
- $u_a^2 \ll V_\infty^2$ - for moderately loaded propellers (all high-speed propellers, such as marine propellers)
- $u_a \sim V_\infty$ - for heavily loaded propellers (tugs).

In propeller lifting line theory, the propeller blades are each replaced by a vortex line of radially varying strength, with the circulation equal to zero at the hub and tip. This

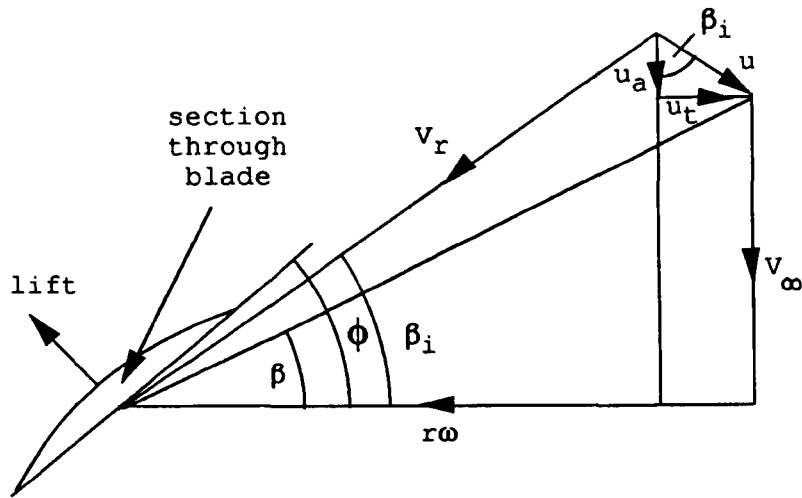


Figure 5.3: Velocity components represented by lifting lines.

radial variation of the circulation of the bound vortices produces the shedding of free vortex sheets from the trailing edge (the trailing wake), the direction of which coincides with the direction of the resulting relative velocity V_r , since no forces can act on the free vortices. Thus, the free vortex sheets form helical surfaces, as the propeller rotates, which are pushed astern with the local axial induced velocity u_a , and rotated around the slipstream axis (y) in the direction of propeller rotation with the local tangential induced velocity u_t .

For lightly loaded propellers, the influence of the induced velocities on the direction of the wake can be neglected, and so the free vortex sheets will form purely helical surfaces of constant pitch P , where the pitch angle corresponds to the advance angle of the propeller blade sections

$$P = 2\pi r \tan \beta. \quad (5.42)$$

For moderately loaded propellers the influence of the induced velocities on the shape of the trailing wake is important. The effects of the induced velocities are such that the trailing wake will have a constant pitch in the axial direction. However, the pitch of the trailing wake in the radial direction can vary and the pitch angle is termed the hydrodynamic pitch angle [65]. The pitch P_i will now be given by

$$P_i = 2\pi r \tan \beta_i \quad (5.43)$$

where the hydrodynamic pitch angle β_i is defined

$$\tan \beta_i = \frac{V_\infty + u_a}{r\omega - u_t}. \quad (5.44)$$

Thus, the model for a lightly loaded propeller's trailing wake is the easiest to generate:² Helical horseshoe vortices, similar to those used in section (5.3), ensue from the trailing edge at an angle equal to the advance angle of the section β .

Creating the geometry for the moderately loaded propeller is more difficult. Since the pitch of the trailing wake depends on the induced velocities (5.44), and the induced velocities are influenced by the trailing wake, an iterative process must be used to calculate the induced velocities. This can be achieved by determining a circulation distribution from a frozen wake geometry. The wake is then realigned with the induced velocities determined from this circulation, and so on until convergence is reached [86].

However, running this iterative process proves far too costly in terms of time and effort for an application such as ours. Kinnas and Coney [39] regard the wake geometry to be frozen when they employ a variational optimisation procedure for the design of ducted propellers. Greeley and Kerwin [44] simplify the wake geometry by producing a model which represents the wake as two regions, the transitional and ultimate wake. In the transitional wake the helices are designed to contract before becoming a fixed geometry in the ultimate wake. However, iterations are still required to determine the pitch in the transitional wake region.

The method employed in this thesis will follow that of Hess and Valarezo [79]. This regards the trailing wake to be helices of fixed geometry, as in the case of lightly loaded propellers, but with a pitch angle β_i which approximates that of the moderately loaded propeller. These values can be read from the data given in the Eckhardt and Morgen design paper. Kerwin [84] compares the method of Greeley and Kerwin with that of Hess and Valarezo, and points out that although the method of Greeley and Kerwin may be closer to physical reality, the second method is computationally more efficient and may well be equally accurate. In this thesis it is computational efficiency which is important in the implementation of the panel method (as is the case with all other considerations in our model). It is not our aim to use the last word in panel method implementation, but to provide a rough estimate of the performance of the propeller from which an optimisation technique can be employed. Since the panel method will be run many times during the optimisation routines, it is therefore better for the panel method to be computationally efficient.

Thus, the trailing wake geometry is formed as helices propagating from the trailing

²Heavily loaded propellers do not have an easily obtainable solution for the trailing wake and are generally ignored. Fortunately all high-speed propellers can be regarded as moderately loaded.

edge at an angle β_i . The length is taken sufficiently far downstream for additional line vortices to have negligible effect on the solution. Then the wake geometry is discretised into line vortices, each having the same doublet strength as the ring vortex on the panel at the trailing edge. Finally, addition of the influence velocity coefficients V_{dij} from these vortices is incorporated into equation (5.36).

The adapted panel method is now ready to be implemented. The complete propeller and trailing wake geometry are illustrated in figure (5.4).

It should finally be noted that this work is thought to be the only application of the SPARV panel method to propeller flows using the assumptions above.

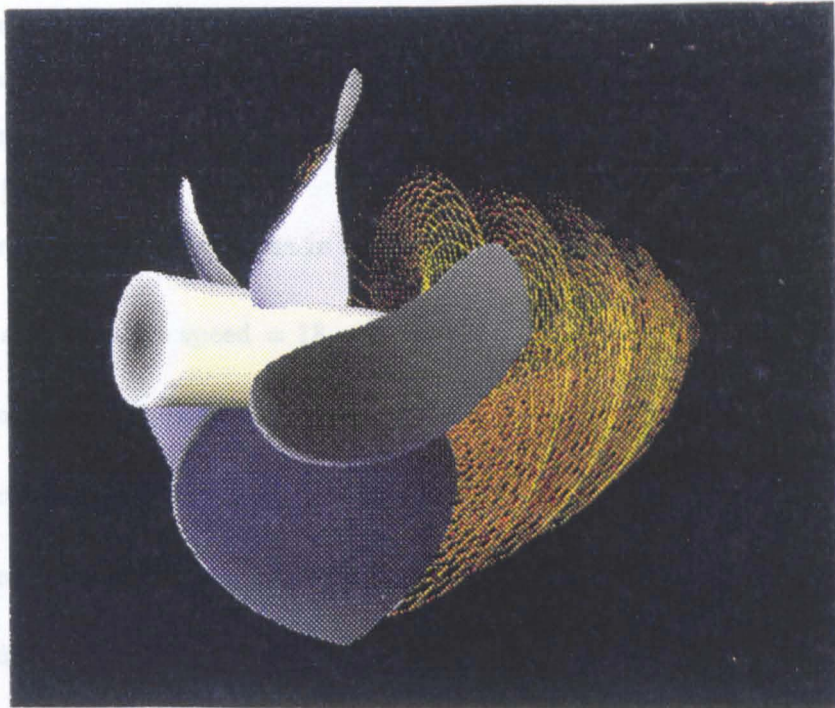


Figure 5.4: The propeller and trailing wake.

5.5 Flow calculation for Eckhardt and Morgen propeller

We are now at a stage to finally evaluate the flow field around the propeller blades. The propeller we are considering is the one generated from the data of Eckhardt and Morgen as in Chapter 4. The original panel geometry is taken from the iso- u and $-v$ lines of the PDE method, which are projected to form new panels, as described in section (5.3.1). It should be noted that most of the panels are approximately planar, and so there is little work to be done in this area. Also note that the panels are concentrated more towards the leading and trailing edges of the sections (see section (5.3.1)).

The propeller will be taken to be rotating with a constant angular frequency ω in a uniform flow $(0, V_\infty, 0)$. This, of course assumes that the propeller is sufficiently far from the ship to which it is attached, which is never really feasible, but for the purposes of the model is adequate. Despite the fact that the influence of the ship trailing wake on the propeller is sufficiently important to warrant interest, up to the present few studies appear to have been published concerning the problem of a propeller operating in a time-dependent, non-uniform flow. However, notable exceptions include the paper of Spiros and Kinnas [52].

The operating conditions given in the paper of Eckhardt and Morgen are as follows.

- $V_\infty = \text{ship advance speed} = 18.m.s^{-1}$
- $D = \text{propeller (optimum) diameter} = 3.81m$
- $n = \text{revs per second} = 5s^{-1}$
- $\omega = \text{angular velocity} = 2\pi n = 31.416rads^{-1}$
- $\lambda = \text{advance coefficient} = V_\infty/nD = 0.945$
- $\rho = \text{density of water} = 1025.kgms^{-1}$

The primary objective of the implementation of the panel method is to produce the pressure distribution over the surface of the propeller. From this we will be able to evaluate the thrust and torque of the generated propeller, and hence its efficiency.

However, due to the geometry used and the particular implementation of this panel method, it is difficult to obtain data with which we can compare the results of our calculations. Kinnas [87] uses a linear extrapolation method to overcome the problem of not having any comparisons, by gradually reducing the thickness on a blade towards the

limiting case of zero thickness, and using his panel method to verify that the circulation obtained gives the same circulation as a vortex lattice lifting surface method (where the geometry is approximated by the mean line surface and is of zero thickness).

Probably the best we can hope for is to obtain similar pressure distributions over the propeller surface to the distributions obtained for similar shaped blades using other panel methods. Secondly, since the thrust, power and efficiency of the propeller generated from the Eckhardt and Morgen design procedure are calculated in their paper, we should hope to be able to evaluate the thrust, power and efficiency from the panel method and get a reasonably close match to this. Hence, we need to determine the equations necessary to evaluate these quantities for the propeller.

5.5.1 Performance of a propeller

To obtain the thrust for the propeller from the panel method the generated lift must firstly be evaluated.

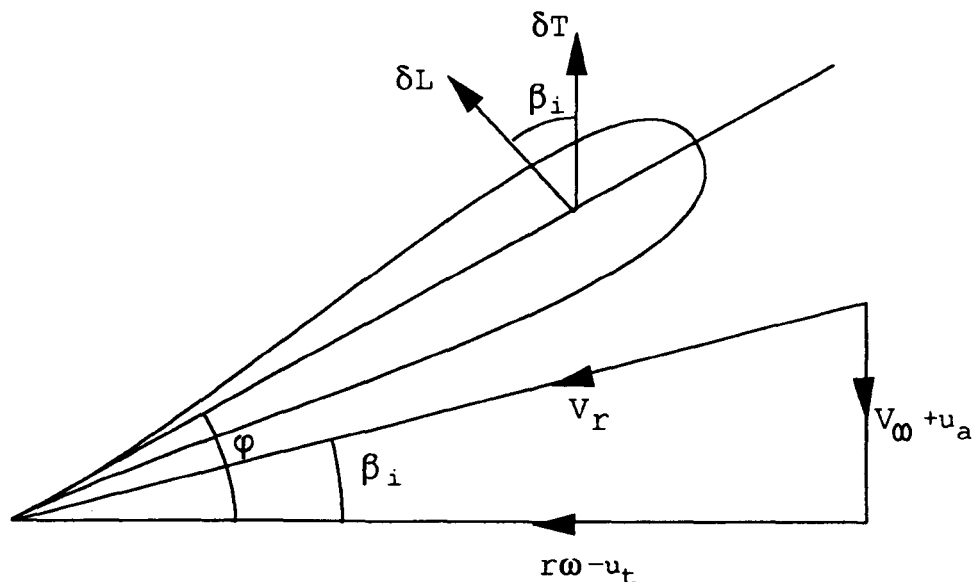


Figure 5.5: Forces on an Airfoil Section

If we consider a blade element as in figure (5.5), located at a span station r , where $r_h \leq r \leq R$, with the relative velocity of the water given by V_r , making an angle of advance β_i , given by

$$\tan \beta_i = \frac{V_\infty + u_a}{r\omega - u_t} \quad (5.45)$$

then the coefficient of lift C_l of the blade section is given by the difference in pressures between the upper and lower surface of the blade,

$$C_l = \int_{x=0}^{x=c} (C_{P_u} - C_{P_l}) d(x/c). \quad (5.46)$$

Viscous flow effects can be allowed for by introducing a drag force which acts in the direction of the resultant relative velocity V_r . In viscous flow, drag flow coefficients

$$C_D = \frac{D}{1/2\rho V_\infty^2 c} \quad (5.47)$$

where D = drag per unit span, are commonly [65] taken to be of the order of

$$C_D = 0.008. \quad (5.48)$$

These lift and drag forces act normal and parallel respectively to the velocity V_r , from which we obtain the total thrust of the propeller

$$T = \int_{r_h}^R Z \cdot \frac{1}{2} \rho V_r^2 c (C_l \cos \beta_i - C_D \sin \beta_i) dr \quad (5.49)$$

with the coefficient of thrust defined by

$$C_T = \frac{T}{\frac{1}{2} \rho V_\infty^2 A_0} \quad (5.50)$$

where

$$A_0 = \frac{1}{4} \pi D^2. \quad (5.51)$$

Similarly the torque will be obtained from

$$Q = \int_{r_h}^R Z \cdot \frac{1}{2} \rho V_r^2 c r (C_l \sin \beta_i + C_D \cos \beta_i) dr \quad (5.52)$$

with the power obtained from

$$P = Q\omega. \quad (5.53)$$

The coefficient of power is then defined by

$$C_P = \frac{P}{\frac{1}{2} \rho V_\infty^3 A_0}. \quad (5.54)$$

Now the efficiency η of the propeller is defined as the ratio of the power output to the power input. Thus,

$$\eta = \frac{TV_\infty}{\omega Q} = \frac{C_T 1/2\rho V_\infty^2 A_0 V_\infty}{C_P 1/2\rho V_\infty^3 A_0} = \frac{C_T}{C_P}. \quad (5.55)$$

Therefore, we are now at a stage to compare our results from the panel method with the data obtained by Eckhardt and Morgen.

5.6 Results

The performance obtained from the panel method and the data given by Eckhardt and Morgen are laid out in Table (5.1). The three columns of results for the panel method refer to different panel resolutions used on the propeller. This is done to verify the numerical convergence of the solution obtained from the panel method. If a degree of agreement between different resolutions is observed, then we can save computer run time in later work by using a coarse mesh when predicting performances in the optimisation procedure. It should also be noted that the trailing wake was kept at a length of 25 metres and was divided into 25 sections as this was considered to be far enough downstream for reliable results. This was determined by observing how far downstream the trailing wake line vortices had a significant effect on the induced velocities at the panels on the blades.

Propeller Characteristics	Method of Solution			
	Eckhardt and Morgen lifting line	Panel Method		
		10 * 20	15 * 30	20 * 40
Thrust	936304	930438	953058	902240
Power	24309820	23815568	24406372	23379921
Torque	773806	758073	776878	744205
C_T	0.4946	0.4915	0.5034	0.4766
C_P	0.7134	0.6989	0.7162	0.6861
C_Q	0.0376	0.0368	0.0378	0.0362
efficiency	69.33	70.32	70.29	69.46

Table 5.1: Comparison between lifting method of Eckhardt and Morgen and panel method

As a first observation it can be seen that the panel method and the lifting line method give similar results. The lifting line method uses corrections to the lifting line approximation to obtain the performance, which include both approximate formulae and adjusting

factors read from graphs and so a detailed picture of the propeller performance will not be possible. However, as an overall picture of the propeller performance, we can regard the Eckhardt and Morgen results as a 'standard' by which to judge our panel method results. It should still be borne in mind, however, that discrepancies between the performances determined by the lifting line method and those of the panel method do not imply that the panel method is inaccurate: in fact probably the contrary, that the lifting line method is less accurate. Comparing the panel resolutions it is seen that the panel

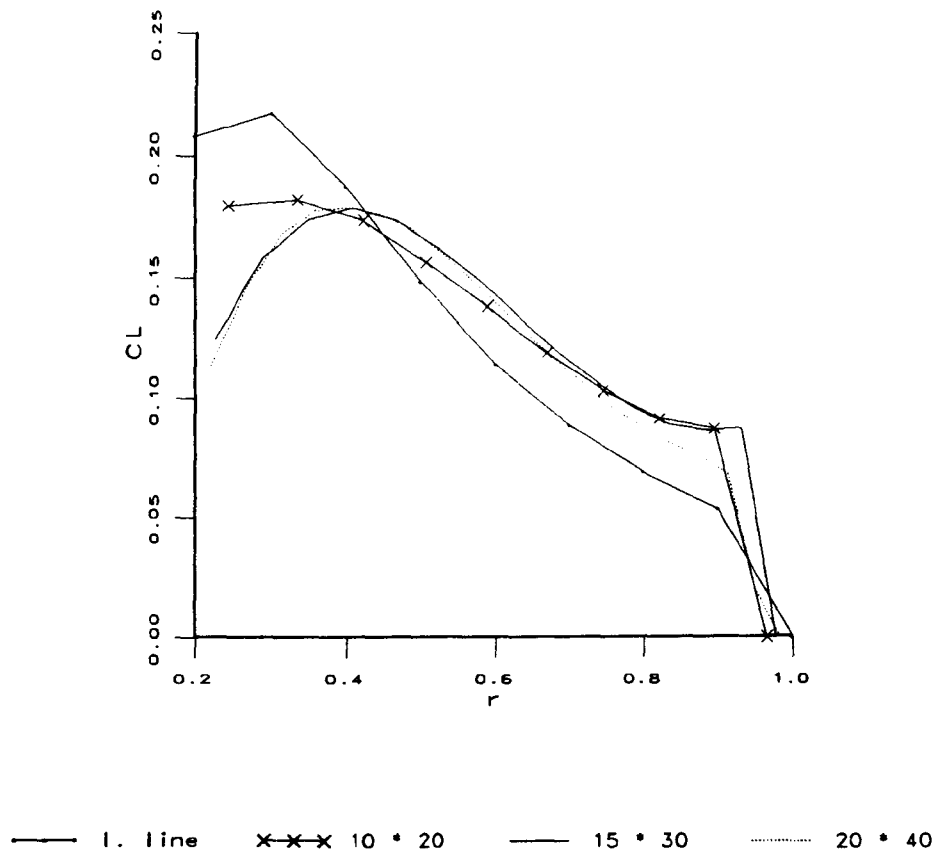


Figure 5.6: Comparison of coefficients of lift across the span of the blades.

method is not entirely grid independent. However, the thrust predictions are all within 4% of that given by the lifting line method and are within 5% of each other. Similarly, the power predictions have a comparable margin of error, with the efficiency being very accurate. If we consider the distributions of coefficient of lift C_l , displayed in figure (5.6), we can see the differences between the coefficients of lift for the different methods. It is observed that the greatest discrepancy between the three resolutions is, indeed, close

to the hub, on which the panelling was neglected. It can thus be concluded that it is probably a good idea to account for the hub geometry to give more accurate predictions. The coarsest mesh appears to give the closest values to those of the lifting line method close to the hub, however, the greater the resolution of the panel method, the closer the graphs appear to converge to a lift distribution, and so there is a possibility that the data from the lifting line method is inaccurate close to the hub. Beyond the radius $r = 0.4$, the three solutions give similar results. The differences observed near the tip where the coefficient of lift becomes zero arise from the fact that the centroids of the panels are at different locations for different resolutions.

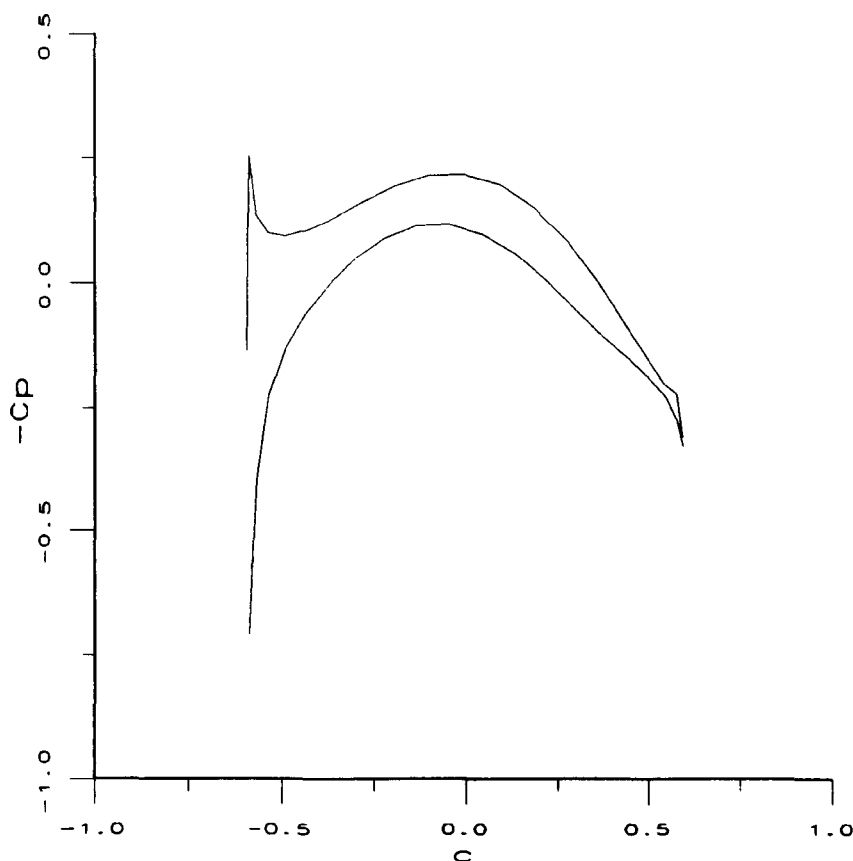


Figure 5.7: Pressure distribution around blade at approximately $x=0.7$.

The pressure and velocity distributions can also be examined on the surface. If the distribution of pressure across the entire surface is required, it is common practise to consider the span station given by $r = 0.7$ [65]. This is since the characteristics of the section at $r = 0.7$ give an overall impression of the characteristics of the blade [65]. Figure (5.7) illustrates the pressure distribution at the blade section closest to this span

station. It can be seen that there is a slight suction peak at the leading edge. This is quite pronounced and so we can assume that the propeller blade section is not operating close to its ideal angle of attack. This leading edge area is the region where much care is required, since a large build up of pressure can occur here, causing cavitation and loss of thrust; however, in the following section it will be demonstrated how changing the local incidence angle away from the design angle increases the thrust losses. It can also be seen that the conditions of equal pressure are satisfied at the trailing edge. Finally note that the maximum pressure (ignoring the suction peak) is situated between 55 and 60% of the chord length. These results all compare well (in a qualitative sense) with those obtained independently by both Hess [79] and Nakatake [88].

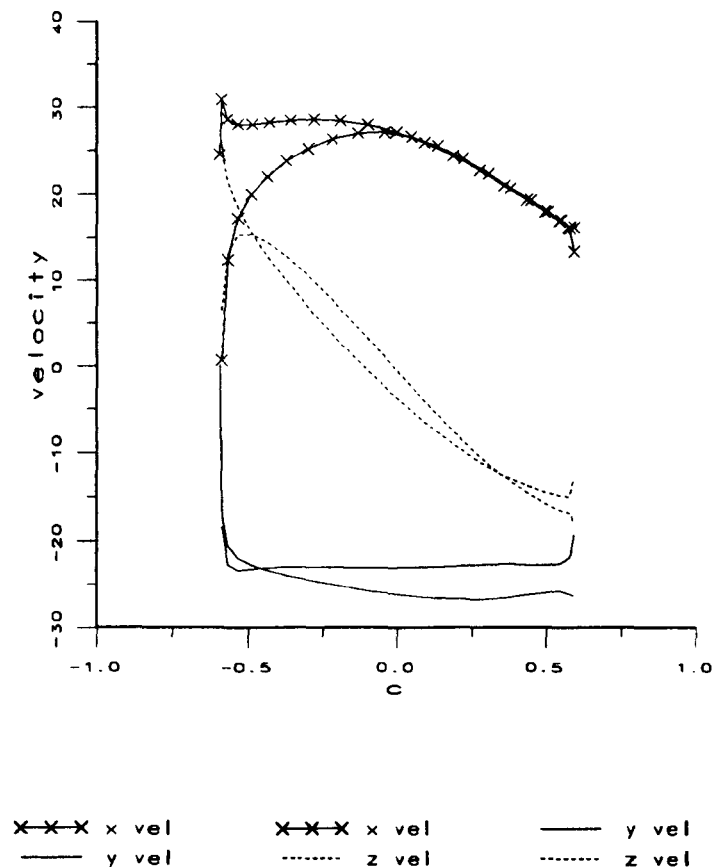


Figure 5.8: Velocity distribution around blade at approximately $r=0.7$.

Figure (5.8) illustrates the velocity close to $r = 0.7$. It can be concluded that the flow around the blade is highly three dimensional, due to the large z -component of the velocity. This illustrates one reason why lifting line methods are inappropriate for the

calculation of velocities and pressures over the surface, since it is inappropriate to consider the flows to be two dimensional.

Finally, figure (5.9) shows the pressure distribution over the complete propeller surface. It can be seen that the leading edge has highly positive pressures on the pressure face, shown by the red band, with negative suction pressure shown on the opposite face at the leading edge, shown by the dark blue shaded strip close to the leading edge of a similar colour to that at the midchord positions of the blade where the highest pressures occur.

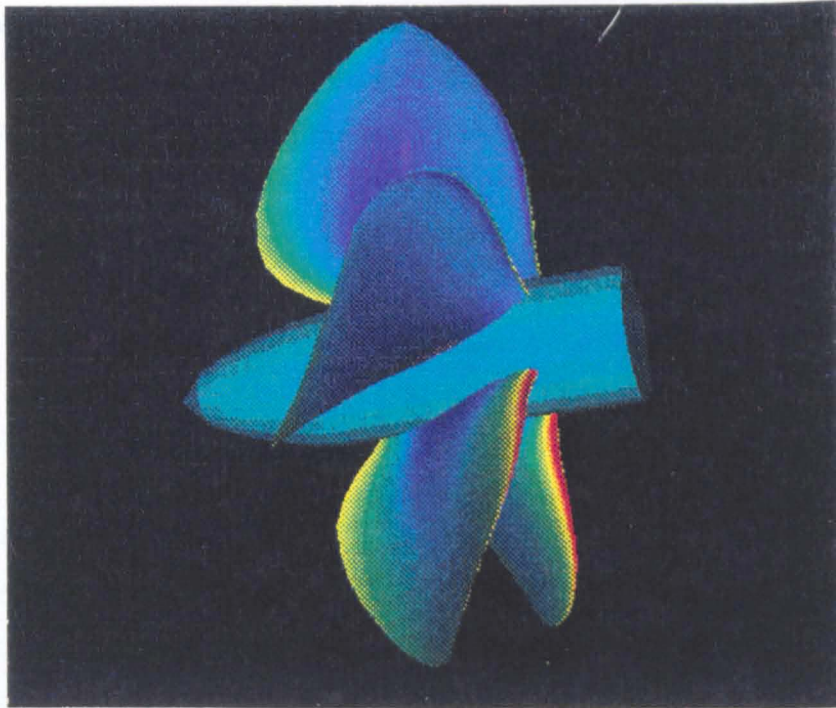


Figure 5.9: The pressure distribution over the surface of the propeller.

Thus, we have obtained similar pressure distributions over the surface and at specific sections to those obtained using other methods. At the same time the graph of C_l against the span station r illustrates that good agreement is obtained between the different resolutions of the panel method and the lifting line method; the major discrepancies occurring close to the hub, which could in all probability be improved by inclusion of the hub geometry. Accuracy is maintained in close proximity to the area of interest ($r = 0.7$). Finally, although we are not implying that the lifting line method gives the actual performance of the propeller, it is reassuring to note that all three panel resolutions give predictions

of within 4% of this value, and are within 5% of each other. Thus, we feel reasonably safe in assuming that the performance predictions obtained by the panel method give us an accurate picture of the propeller, along with the pressures obtained, and hence can be used as a method to improve the design of the propeller.

5.6.1 Loss and gain of performance.

As at the end of Chapter 3, we can use the panel method to determine how the performance will alter with changes in design parameters. As an illustration of one way in which thrust can be lost, we are able to demonstrate the situation where the propeller has the geometry described in Chapter 4, except that the pitch distribution corresponds to that initially given by Eckhardt and Morgen, prior to the implementation of their design procedure. Figure (5.10) illustrates the pitch distributions. The lower curve corresponds

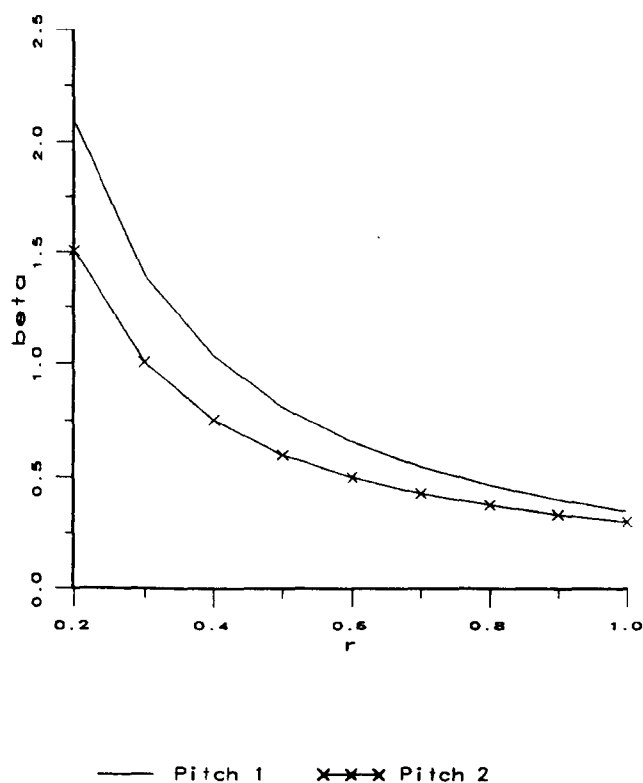


Figure 5.10: Pitch angle curves of Eckhardt and Morgen design procedure.

to their input distribution, while the upper distribution is that determined from their design procedure, and used in our previous calculations. What we can illustrate using the

panel method is the relative merits of their original choice of pitch distribution. It can be seen that the original pitch angle curve has smaller values at corresponding positions and so there is a good chance that this should produce less thrust. If we now use this geometry to generate a propeller blade surface, we can use the panel method to obtain the performance predictions for this propeller. Table (5.2) illustrates the performances we have obtained for these two distributions using the panel method.

Propeller Characteristics	Pitch Curve 1	Pitch Curve 2
Thrust	930438	349738
Power	23815568	11560165
Torque	758073	367971
C_T	0.4915	0.1847
C_P	0.6989	0.3392
C_Q	0.0368	0.0179
efficiency	70.32	54.46

Table 5.2: Output for propeller operating with alternative pitch distribution.

The column entitled 'Pitch Curve 1' corresponds to that obtained using the 10*20 panelling from table (5.1) for the previously utilised pitch distribution. To understand why the performance is lower in the column entitled 'Pitch Curve 2', we need to look at the distribution of lift along the span, and the pressure distribution at $r = 0.7$ which determines the lift. Figure (5.11) illustrates the coefficients of lift along the blade.

It is clear from figure (5.11) that a much lower lift is being generated along the whole length of the blade, and hence the reason for the loss in thrust. To see why there is less lift we must consider the coefficients of pressure. As can be seen from figure (5.12) there is now a steep negative leading edge peak on the pressure surface, along with a crossing of suction and pressure surface peaks close to this. The lift, given by the area between the curves, is therefore much lower. The reason for this change in pressure is that the blade is now operating even further from its ideal angle of attack. Figure (5.13) illustrates the pressure distribution over the complete surface. It is seen that the blades are aligned differently to those of figure (5.9) and it is seen that there are similar pressures on either side of the blades' surface, hence the reduced thrust. Finally, it is observed that

the leading edge pressures are reversed from those of figure (5.9). These features have been verified by Hess [79], by comparison of the pressure plots with a conformal mapping programme which is able to determine features such as these. Hence, we can see that the panel method is a useful tool for distinguishing features such as these.

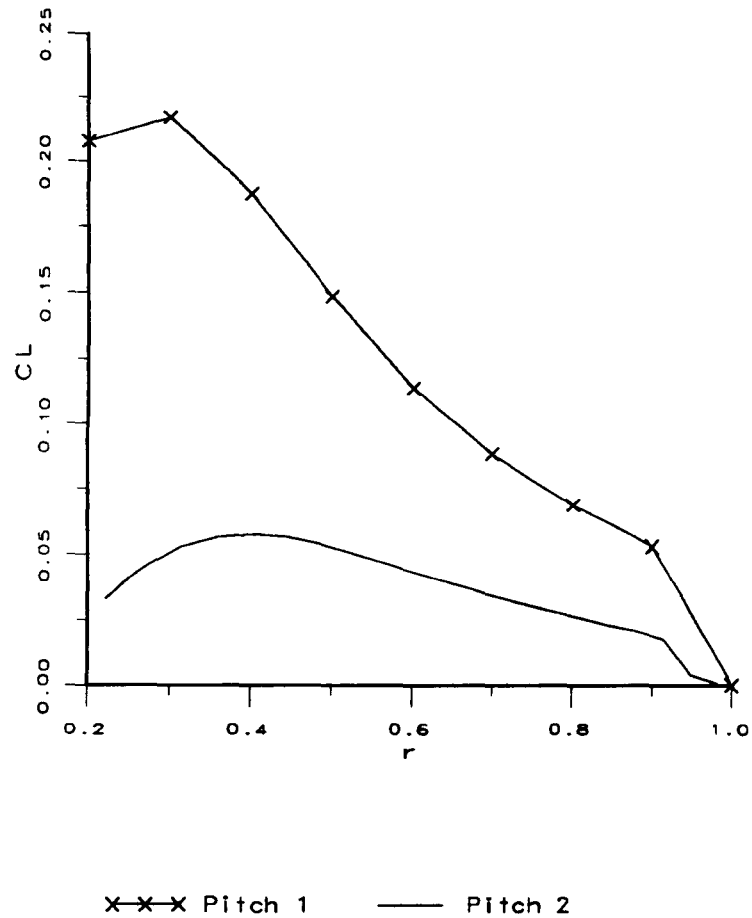


Figure 5.11: Comparison of coefficients of lift across the blade.

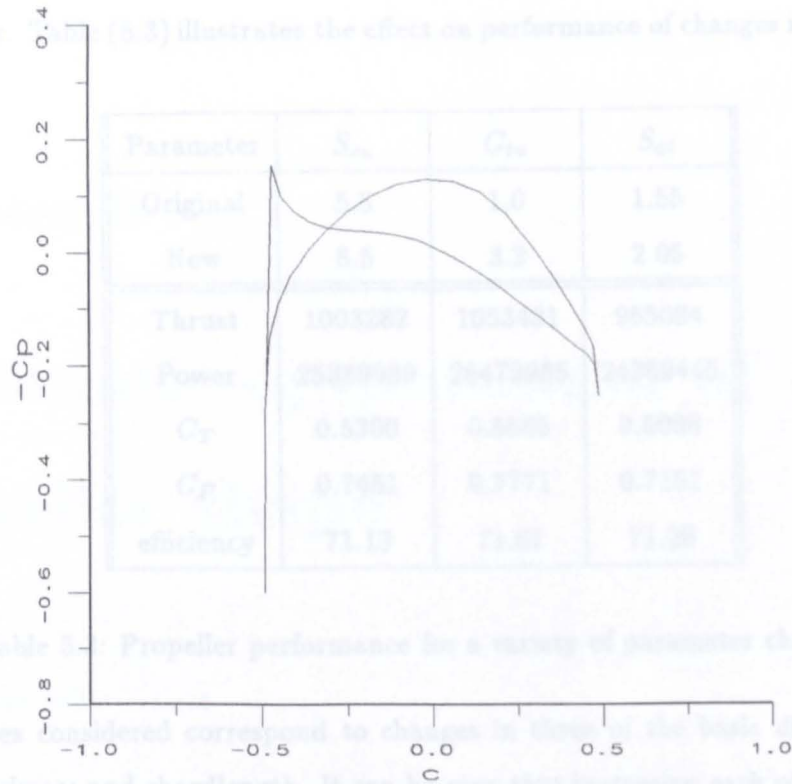


Figure 5.12: Pressure distribution on blade at approximately $r = 0.7$.

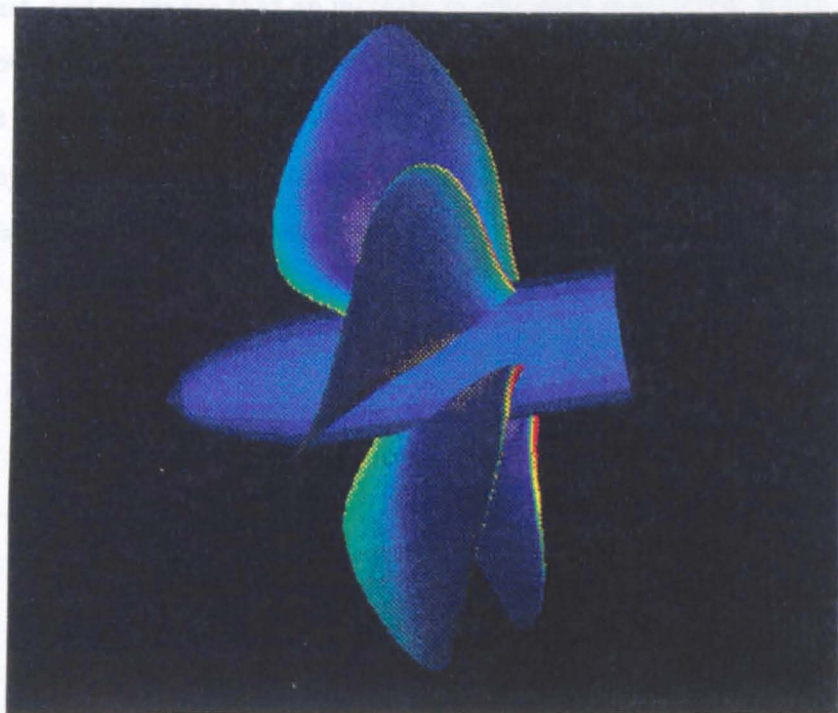


Figure 5.13: The pressure distribution over the surface of the original propeller.

Finally, we can observe how changing various parameters affects the performance of the propeller. Table (5.3) illustrates the effect on performance of changes in the geometry.

Parameter	S_{cu}	C_{tu}	S_{xl}
Original	5.5	1.0	1.55
New	8.5	3.2	2.05
Thrust	1003282	1053431	965084
Power	25389989	26479985	24369445
C_T	0.5300	0.5565	0.5098
C_P	0.7451	0.7771	0.7151
efficiency	71.13	71.61	71.28

Table 5.3: Propeller performance for a variety of parameter changes.

The cases considered correspond to changes in three of the basic distributions; the camber, thickness and chordlength. It can be seen that increasing each of the parameters ensures that a larger thrust is generated, as would be expected for increases in these distributions. At the same time the power output is increasing, but not at a similar rate to the thrust, and so we see that an increase in efficiency is achieved; which is what we are working towards, since this is obviously a good requirement for the improvement in the design. At this stage, however, we have not taken into account any of the requirements for the propeller to be non-cavitating, and so the last area we need to investigate are the constraints needed for the propeller to be non-cavitating.

Chapter 6

Automatic optimisation of propeller shape

6.1 Introduction

Many criteria play an important role in the development of the marine propeller. These, invariably depend on the specific purpose for which the marine propeller is being developed; for instance the requirements for a propeller needed to power a naval submarine will be different from the requirements for the propeller of a large oil tanker. In the case of the submarine, noise excitation is going to be of prime importance as stealth is a crucial factor; tests will have to be made so as to reduce the vibration which builds up in the propeller, since these can, in turn, induce vibrations in the shell of the vessel. For the oil tanker it will be required that the propulsion unit be as efficient as possible to keep fuel costs down, and there will also be the need for manoeuvrability of such a large vessel into and out of port areas.

Inevitably in propeller design there is overlap between the various considerations. For instance, in the design of propulsion units for large, modern luxury liners where speed is not necessarily of the utmost importance, but comfort is, quiet low-vibrating propellers provide an additional degree of comfort for the passengers. Thus, the first problem presented to the designer is the identification of the most important factors affecting the particular functional requirements of the propeller.

6.1.1 Areas of improvement

It is most unlikely that improvement in design can simultaneously be achieved for all aspects of the propeller. The designer must therefore have a full understanding of the situation in which the propeller will be operating in order to identify the features of the operation they wish to improve and also impose sensible constraints. In particular, the main areas of concern involving marine propellers are

1. Efficiency
2. Strength
3. Cavitation

In this thesis, efficiency and cavitation alone will be considered. Strength constraints (which can be estimated from beam theory [89] as a rough guide) will be neglected and left as an area for future work. Thus, this chapter will be primarily concerned with the optimisation of the efficiency of the propeller.

In the absence of practical constraints, the problem would have a solution were it viewed as an abstract mathematical problem. However, many of these solutions would correspond to extreme geometries which either could not be manufactured, would not be strong enough, or when produced as models for basin tests would fail due to excessive cavitation. Realistic constraints must consequently be imposed on the optimisation process to ensure that reasonable geometries are produced. Since cavitation is of particular importance, constraints on the cavitating properties of the propeller should be imposed so that either a non-cavitating propeller design is achieved, or that cavitation is kept to a minimum.

6.2 Cavitation considerations

The particular problem to be considered in this thesis is to improve the design of a propeller so as to achieve a greater efficiency while trying to prevent the onset of cavitation. To achieve this it must first be explained under what conditions cavitation will occur, so that an appropriate set of constraints can be used in the optimisation procedure.

6.2.1 Why reduce cavitation?

Cavitation is the formation and activity of bubbles (or cavities) in a fluid. These bubbles are either suspended in the fluid or trapped in tiny cracks in the surface of the propeller.

In the fluid flow around a propeller, the velocity will vary due to local accelerations, and it is at the points of highest velocity that low or negative pressures will occur and vapour bubbles open up. If the fluid velocity exceeds a certain initial value, the pressure drops below the local vapour pressure and bubbles form. These bubbles then collapse noisily and with great violence causing damage to the surface of the propeller.

If cavitation occurs around a propeller many problems can occur. The first is that a characteristic change in the noise pattern from the propeller is heard. This is particularly troublesome in submarine and warship propellers. The second is the problem of cavitation erosion. This occurs when the intense forces set up by the collapsing bubbles erode the material in the near vicinity. The damage will start as a roughness over the surface and build up to form large holes, with areas around the tip and leading edge particularly prone to such damage due to the high local velocities in these regions. Thus the performance of the propeller is reduced and thrust losses are incurred. Sometimes even after just one voyage, cavitation is so great as to render the propeller effectively inoperative. Thus great care must be paid to delaying cavitation.

6.2.2 Cavitation numbers in propeller design

If the minimum pressure on the surface of a foil section of the propeller blade drops below the critical pressure of the fluid, then cavitation phenomena may become detectable. It is assumed in this thesis that the characteristics of the fluid are such that the critical pressure is equivalent to the vapour pressure p_v . Thus, cavitation can only be avoided if

$$p_{min} > p_v \quad (6.1)$$

which can, alternatively, be written

$$\frac{p_{\infty} - p_v}{q} > \frac{\Delta p_{max}}{q} \quad (6.2)$$

where $\frac{\Delta p_{max}}{q}$ is the value of the minimum pressure coefficient or maximum non dimensional pressure drop, and q is a dynamic pressure, the choice of which depends on whether local or global considerations are important.

The expression on the left hand side of equation (6.2) is termed the cavitation number

$$\sigma = \frac{p_{\infty} - p_v}{q} \quad (6.3)$$

and in propeller design generally comes in two different forms, the propeller cavitation number σ_0 , and the local or blade section cavitation number σ_x . These numbers are used in the evaluation of cavitation characteristics of the propeller. The propeller cavitation number σ_0 is based on the dynamic pressure of the propeller advance speed V_{∞} and is given by

$$\sigma_0 = \frac{p_0 + \rho gh - p_v}{\frac{1}{2}\rho V_{\infty}^2} \quad (6.4)$$

where

- p_0 =atmospheric pressure
- g = acceleration due to gravity
- h = depth of immersion of centreline of propeller.

The local cavitation number σ_x is based on the dynamic pressure of the relative velocity at a blade section and is given as;

$$\sigma_x = \frac{p_0 + \rho g(h - r) - p_v}{\frac{1}{2}\rho(V_{\infty}^2 + (r\omega)^2)} \quad (6.5)$$

where r is the radius of the particular blade section.

6.2.3 Design limitations for non-cavitating propellers

The cavitation numbers having been defined, the next step is to obtain a criterion for the lowest possible local cavitation number at which the blade sections will not cavitate.

Now, according to Kruppe [65], for propellers with optimum diameter, moderate loading and large blade area ratios A_e/A_0 , where

$$A_e/A_0 = \int_{r_h}^R \frac{c(r)}{D} dr, \quad (6.6)$$

a characteristic quantity in propeller design C_{lc}/t_x at $r = 0.7$ will typically be about five. Thus, we take

$$\left(\frac{C_{lc}}{t_x}\right)_{0.7} = 5. \quad (6.7)$$

Furthermore, it is also not very realistic, from the fabrication point of view, to design propellers with

$$\left(\frac{t_x}{c}\right)_{0.7} < 0.02 \quad (6.8)$$

which, using equation (6.7) gives the condition

$$(C_l)_{0.7} \approx 0.1. \quad (6.9)$$

From wing theory, the maximum non-dimensional pressure drop for cambered foil sections can be calculated from

$$\frac{\Delta p_{max}}{q} = (1 + C_1 t_x/c + C_2 C_l)^2 - 1 \quad (6.10)$$

where C_1, C_2 are coefficients which can be obtained from [30] for different wing sections. This results in

$$\left(\frac{\Delta p_{max}}{q}\right)_{0.7} \approx 0.1 \quad (6.11)$$

for the NACA section utilised in Chapter 4.

Now, a general safety margin against cavitation can be achieved by using a quantity S , defined as

$$S = \frac{\sigma_x}{\frac{\Delta p_{max}}{q}} - 1 \quad (6.12)$$

and taking the value $S = 0.2$.

Thus, from equations (6.11) and (6.12) a lower bound σ_{min} on σ_x , at $r = 0.7$, for the design of non-cavitating propellers under uniform inflow conditions can be obtained, since

$$\sigma_{min} = 1.2\left(\frac{\Delta p_{max}}{q}\right) = 0.12. \quad (6.13)$$

For the limitation of cavitation we therefore have a set of criteria which should be adhered to:

1. $\sigma_0 > \frac{\Delta p_{max}}{q}$ over the surface
2. $\sigma_x > \left(\frac{\Delta p_{max}}{q}\right)_{0.7}$ at blade section $r = 0.7$
3. $(\sigma_{0.7})_{min} = 0.12$

and from a geometric point of view the condition

4. $(t/c)_{0.7} \geq 0.02$.

6.3 Verification of Eckhardt and Morgen propeller design

Before we can attempt to improve the design of the propeller generated in Chapter 4, it must first be determined whether the initial propeller design adheres to the above conditions. The propeller design has an optimum diameter, and since it is moderately loaded with a large blade area ratio the derived constraints should be applicable. Thus, for the propeller model we can evaluate the maximum pressure changes over the surface from which can be obtained the local and global cavitation numbers. The results from the panel method for the cavitation considerations are shown in table (6.1).

As can be seen from table (6.1) the design achieved by Eckhardt and Morgen satisfies the requirement for it to be non-cavitating. The local cavitation number σ_x taken at the blade section $r = 0.7$ has a value of 0.125 which is greater than the local cavitation number σ_{min} for the safety margin. Secondly, the value of the local cavitation number $\sigma_{0.7}$ is greater than the maximum pressure coefficient drop at this span station. The global cavitation number σ_0 is greater than the maximum pressure coefficient drop over the surface, and so all cavitation constraints are satisfied.

We can see that the design ratio $(t_x/c) \geq 0.02$ has also been satisfied and hence the validation of the design has been shown.

This ensures that the propeller design can be used as a starting point from which to produce an improved model.

6.4 Improvement of design

The way in which the propeller will be improved is to choose a certain subset of the PDE surface parameters and then within the parameter space of this an improved design will be found. To achieve the improvement, the various parameters are altered until a maximum value of the thrust is found, while the propeller surface is constrained by the bounds of the cavitation considerations of the previous section. From the optimised thrust, the efficiency will be calculated to verify whether a greater performance has been achieved. Hence, an optimisation routine is required which searches around the n -dimensional parameter space of the n PDE parameters. The routine used will now be described.

safety margin against cavitation $[S]$	0.200
acceleration due to gravity $(ms^{-2}) [g]$	9.810
rotational velocity $(rads^{-1}) [\omega]$	31.422
inflow velocity $(ms^{-1}) [V_\infty]$	18.000
depth of centreline of propeller $(m) [h]$	3.658
vapour pressure of water $(Nm^{-2}) [p_v]$	2000.00
atmospheric pressure $(Nm^{-2}) [p_0]$	101300.00

minimum value of local cavitation no. for given safety margin	
$\sigma_{min} = 0.12$	

local cavitation no. $\sigma_{0.7}$	0.125
maximum pressure change at $r = 0.7$	0.098
global cavitation no. σ_0	0.820
maximum pressure change over blade	0.486

minimum design constraint $(t_x/c) > 0.02$ resulting in $C_l \approx 0.1$	

At span station $r = 0.7$	
maximum thickness $(m) [t_x]$	0.038
chordlength $(m) [c]$	1.784
C_l	0.118
(t_x/c)	0.021

Table 6.1: Complete data for the Eckhardt and Morgen propeller

6.4.1 Powell's Quadratically Convergent Method

The method due to Powell [64] is straightforward to implement. It is based on the idea of maximisation of a function of one variable $f(x)$ and has been extended to a function of many variables $f(x_1, \dots, x_n)$. In the problem we are considering the function $f(x_1, \dots, x_n)$ will be taken to be the thrust, obtained from the panel method, with x_1, \dots, x_n being the n parameter subset of the PDE parameter set. The advantage this method has over other methods (such as the Fletcher-Powell method [63]) is that derivatives with respect to the parameters need not be evaluated in the optimisation procedure, which is extremely valuable since the evaluation of derivative terms requires a substantial amount of computer time.

To obtain the maximum of a single valued function it is necessary to use an iterative process. One of the most rapid methods is the Golden Section Search method which we will illustrate.

6.4.2 Golden Section search

In the sequence described in figure (6.1) a maximum is found for the function $f(x)$ by altering the parameter x . This is achieved by firstly considering $f(x)$ to lie within an

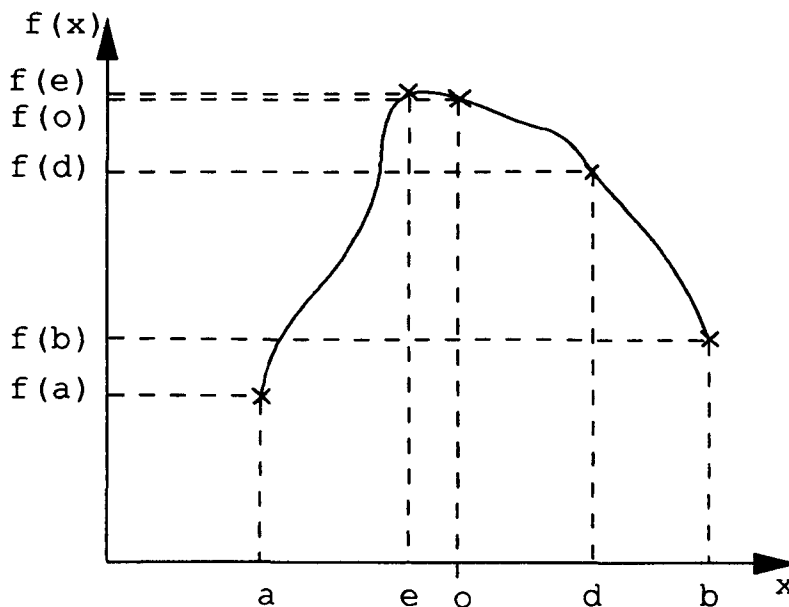


Figure 6.1: The bracketing of a function $f(x)$.

interval (a, b) . Then the function $f(x)$ will have a maximum value if a point c can be found such that $a < c < b$ and also $f(c)$ is greater than both $f(a)$ and $f(b)$.

To obtain a maximum we firstly need to bracket our original estimate, $f(o)$ say. This implies that we must find two values a and b , one either side of o , such that $f(a)$ and $f(b)$ are both less than $f(o)$. For the time being, we will assume that such a bracket can be found. Consider a point o such that $f(o)$ is greater than both $f(a)$ and $f(b)$ where $a < o < b$. Now, somewhere between a and b there lies a maximum (not necessarily $f(o)$). The routine begins by taking the largest of the distances ao and ob , ob say. From this a new point d is obtained which is a distance $W(ob)$ from o , on the same side of o as b . The value $f(d)$ is evaluated, and if it is such that $f(d) > f(b)$ but less than $f(o)$ then the new bracket becomes (a, d) . Again, the largest distance is found out of ao and od , ao say, and a new point e is taken a distance $W(oe)$ from o , on the same side of o as a . This time $f(e)$ may be greater than $f(o)$ and so the new bracket is taken as (a, o) where $f(e)$ is the new maximum. The process is continued until a bracket is obtained which has a sufficiently small tolerance for our purposes. The distance W is taken to be the golden mean or golden section and dates back to Pythagorean times [82]. It has a value of $W = 0.38197$, and gives a better search than a straightforward bisection algorithm.

Now that the maximum of a single valued function can be found, the Powell algorithm for a function of many variables can be given. Firstly, a set of directions \underline{u}_i in which the search is to be carried out for each parameter in the space are defined. These are originally taken as the basis vectors

$$\begin{aligned} \underline{u}_1 &= (1, 0, \dots, 0) \\ \underline{u}_2 &= (0, 1, \dots, 0) \\ &\vdots \\ \underline{u}_n &= (0, 0, \dots, 1) \end{aligned} \quad (6.14)$$

where n is the number of parameters in the parameter space. Then, the following sequence is repeated until the objective function remains a maximum.

1. Obtain the value of the function for the initial parameter values. Store the initial starting position as \underline{P}_0 .
2. For $i = 1, \dots, n$ move \underline{P}_{i-1} to the maximum along the direction \underline{u}_i and call this position \underline{P}_i .
3. For $i = 1, \dots, n - 1$ set $\underline{u}_i \leftarrow \underline{u}_{i+1}$
4. Set $\underline{u}_n \leftarrow \underline{P}_n - \underline{P}_0$

5. Move \underline{P}_n to the maximum along direction \underline{u}_n and call this point \underline{P}_0 .

However, a problem occurs with Powell's convergent method in that when throwing away \underline{u}_1 at each stage in favour of $\underline{P}_n - \underline{P}_0$, the directions \underline{u}_i tend to fold up on each other and a maximum is found over a subspace of the parameter space. Therefore, the algorithm is usually adapted so that instead of removing \underline{u}_1 on each run, the direction which gives the largest increase is now removed. This actually removes any linear dependence amongst the direction vectors and so produces a correct solution over the parameter space. Hence the iteration can now be repeated until the maximum thrust is found.

6.4.3 Penalty functions

In the previous section it was assumed that an initial bracket of the thrust could be determined. However, the Powell method does not take into account constraints on the parameters and so we could be in a situation where either no initial bracket could be found, or alternatively the optimum solution would not be restricted by the cavitation constraints. For instance, if the thrust is to be optimised by changing only one parameter, that being a parameter related to the camber say, then increasing the camber would increase the thrust up to a point where the flow model breaks down and gives indeterminate results due to aspects of the design being unacceptable.

Consequently, one or several penalty functions [90] need to be included so as to take account of the various constraints upon the design. Then, the objective function being maximised is no longer the thrust, say, but a new function given by

$$f(\underline{x}) = f_0(\underline{x}) + p_1 + p_2 + \dots + p_n \quad (6.15)$$

where $f_0(\underline{x})$ is the thrust evaluated by the panel method, p_1, \dots, p_n are the n penalty functions and \underline{x} is the vector of PDE parameters. These penalty functions take the form

$$p_n = -c_n \sinh(h_n) \quad (6.16)$$

where c_n is termed the cost function and h_n is the difference function defined below. This form of penalty function is used since it gives a rapid change in value for p_n for slight changes in h_n , and so it strongly penalises inadmissible regions of parameter space. The cost function c_n is determined so that the penalty function for each constraint is kept to the same order of magnitude. h_n is the difference between the calculated value of a particular quantity and the constraint limit (for example, $h_n = \sigma_{0.7} - 0.12$). If a design

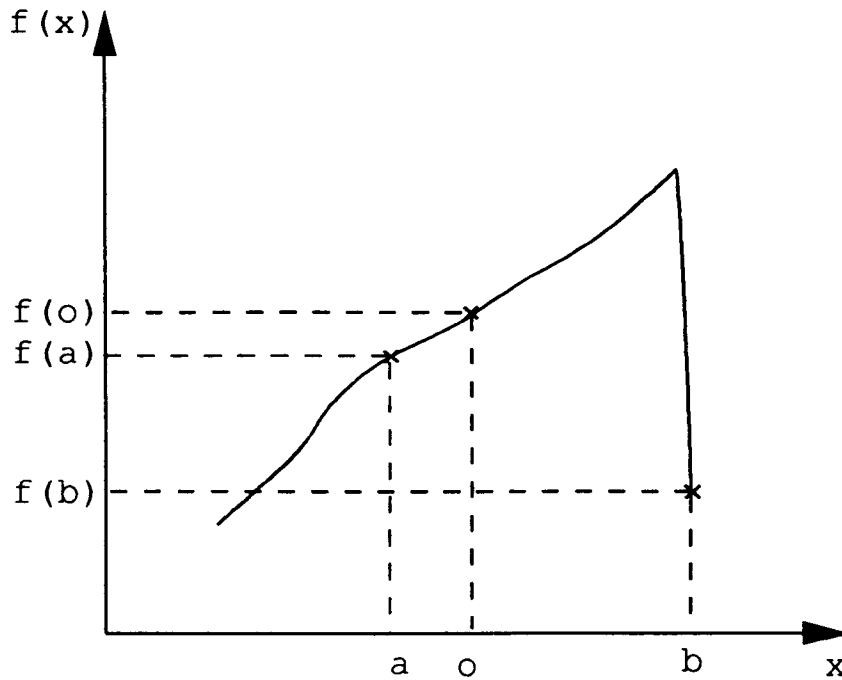


Figure 6.2: A bracket produced by the penalty function p_1 .

alters so that any constraint is broken, then the penalty function corresponding to that constraint becomes highly negative; all penalty functions are set to zero if their constraints are still intact. Hence a bracket may be produced as in figure (6.2).

In this figure $f(x)$ was increasing for increasing x to the point where the constraint was broken (at $x = b$), and so one side of the bracket, b about o is found, since the function has become much smaller than $f(o)$. In the other direction, a value $f(a)$ is immediately found which is smaller than $f(o)$ without breaking any constraints and so a bracket is identified as (a, b) . From this the Powell algorithm can be implemented.

We can now illustrate some results obtained from the optimisation procedure.

6.5 Results

Over the next pages several attempts at improving the efficiency of the propeller are considered. This is initially considered by taking the thrust to be the function to be optimised and observing the effect this has on the performance. Since the panel method is implemented many times during the optimisation routine, the coarsest of resolutions of table (5.1) is used. This resolution is sufficient for determining the cavitating properties of the surface. The initial operating conditions for the propeller in Chapter 5 remain

unchanged, as does the pitch distribution. This remains unchanged since it has no explicit dependence on parameters within the surface generation, and consequently if it were to be optimised then each blade section pitch angle would need to be aligned separately which could generate highly changing pressure distributions at this section. This proves to be unfortunate, since the angle of inclination of the blade sections is one of the main ways of contributing more lift to the propeller.

The cases considered take a variety of subsets of the PDE parameters to be optimised. The examples illustrated in Cases 1-5 have been chosen from many different subsets, since many subsets do not give much improvement due to the chosen parameters. Here, then are the cases considered:

6.5.1 Case 1

In this case it can be seen from figure (6.3) how the geometric distributions are affected by the optimised values of table (6.2). The parameters that are optimised appear in table (6.2) with their initial and final values.

Case 1 optimisation		
parameter	Input	Output
S_{xu}	-3.8	-3.73147
S_{tl}	1.9	1.25088
C_{tu}	1.0	1.52722
S_{xl}	1.55	1.55000
S_{cl}	-5.93	-14.71678

Table 6.2: Parameter values for case 1

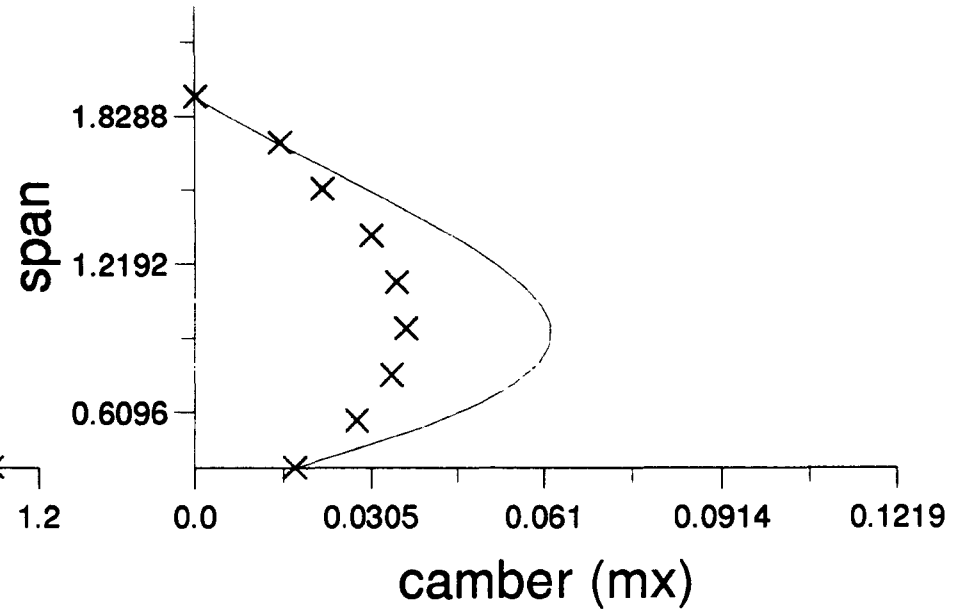
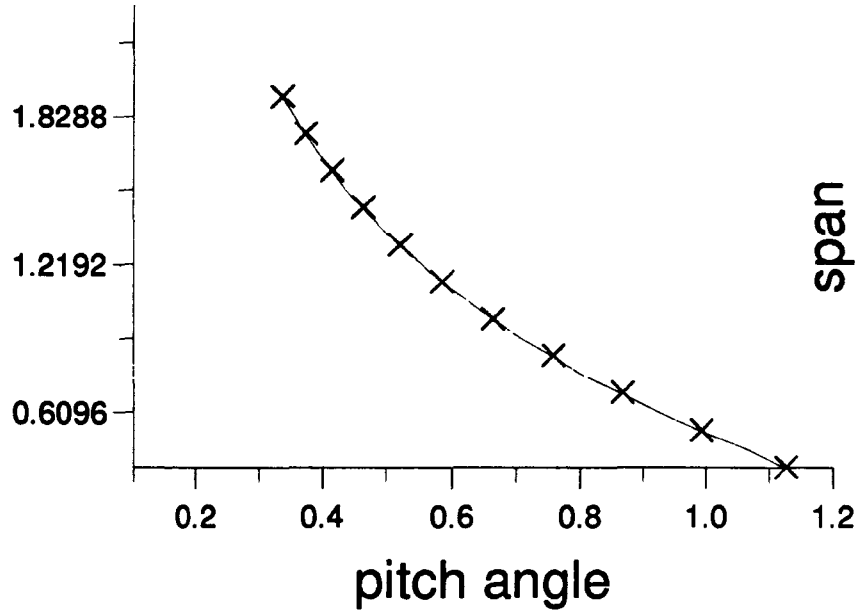
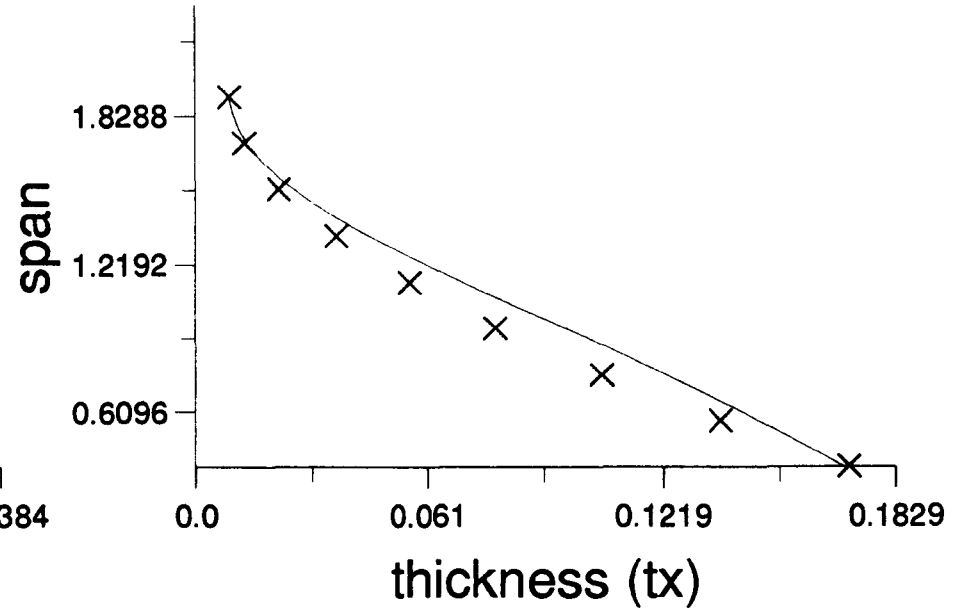
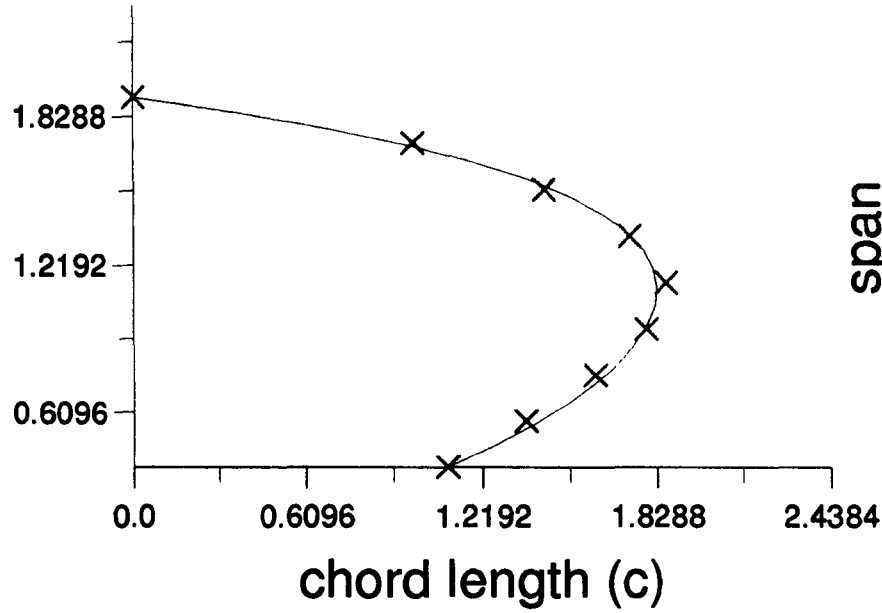
The first parameter S_{xu} should increase the thrust by enlarging the chordlengths close to the tip. However, this parameter remains generally unchanged, firstly due to the geometric constraint $t_x/c \geq 0.02$. Since the original value of $t_x/c = 0.0212$, this implies that the chordlength is unable to increase greatly without a corresponding increase in t_x . However, once S_{tl} and C_{tu} have increased, thickening the blade at all sections, the cavitation constraints prevail and a noticeable change in the chordlength cannot occur. Secondly, we have a noticeable increase in the camber distribution along the blade span, while it can be seen from table (6.3) that the local cavitation number σ_x remains greater

than the maximum pressure coefficient drop at the span station closest to $r = 0.7$, be it ever so slight. Obviously, the greater thrust will be due to the increase in camber, and this is demonstrated in figure (6.3). Figure (6.4) illustrates the lift generated. We can see that there is a pronounced increase close to the root which generates the additional 22% thrust. The coefficients of pressure C_p closest to $r = 0.7$ show that due, mainly, to the increase in camber, the slight suction peak at the leading edge has been substantially removed, as can be seen from figure (6.5) and figure (6.12) where the deep blue band close to the leading edge is marginally smaller than in figure (5.13). Finally we can see that there is indeed an increase in efficiency associated with this set of parameters.

Case 1 optimisation		
	Input	Output
Cavitation output		
σ_0	0.8195	0.8195
$\frac{\Delta p_{max}}{q}$	0.4863	0.5330
$\sigma_{0.7}$	0.1252	0.1250
$\left(\frac{\Delta p_{max}}{q}\right)_{0.7}$	0.0978	0.1251
(t_x/c)	0.0212	0.0290
C_l	0.1185	0.1489
Performance		
Thrust	930438	1131050
Torque	758073	895521
Power	23815568	28133623
Efficiency	70.32	72.37
% increase	2.92	

Table 6.3: Output for optimised propeller

Figure 6.3: Geometric distributions for optimisation case 1



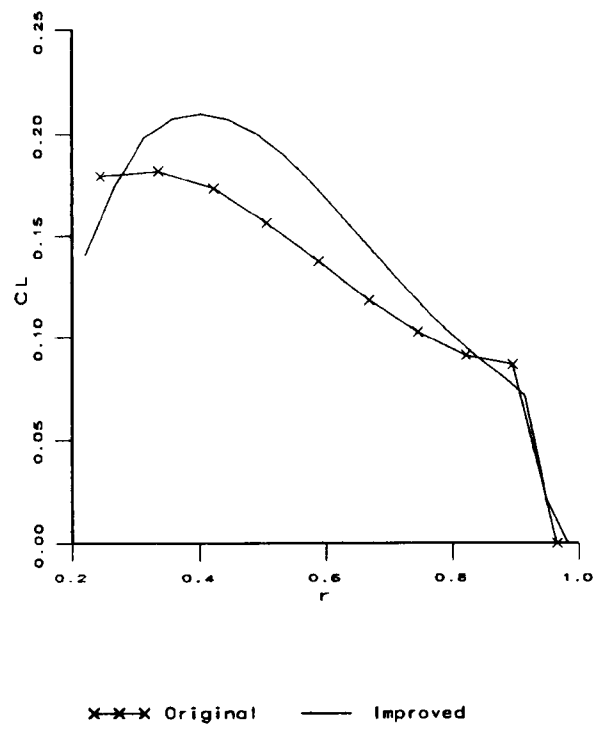


Figure 6.4: Coefficients of lift for case 1.

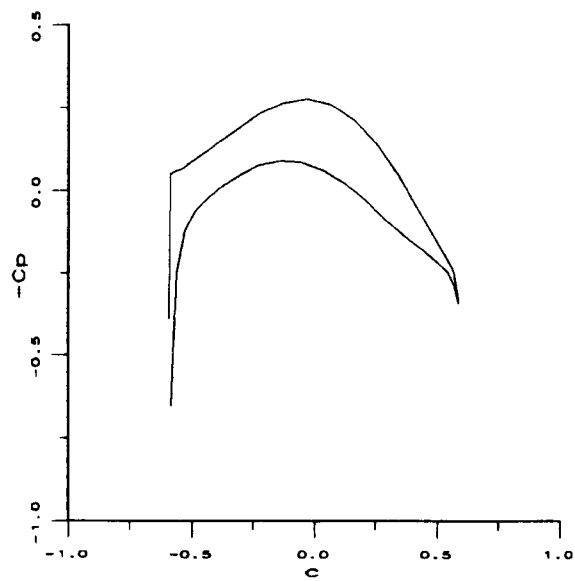


Figure 6.5: Pressure distribution at $r = 0.7$ for case 1.

6.5.2 Case 2

Case 2 optimisation		
parameter	Input	Output
S_{bot}	-1.66	-1.96285
S_{tu}	2.0	9.11432
S_{xu}	-3.8	-4.33569
S_{tl}	1.9	1.75023
S_{cu}	5.5	12.26451
S_{cl}	-5.93	-9.43151

Table 6.4: Parameter values for case 2

Case 2 optimisation		
	Input	Output
Cavitation output		
σ_0	0.8195	0.8195
$\frac{\Delta p_{max}}{q}$	0.4863	0.5944
$\sigma_{0.7}$	0.1252	0.1253
$\left(\frac{\Delta p_{max}}{q}\right)_{0.7}$	0.0978	0.1234
(t_x/c)	0.0212	0.0291
C_l	0.1185	0.1453
Performance		
Thrust	930438	1223090
Torque	758073	969689
Power	23815568	30463671
Efficiency	70.32	72.27
% increase	2.77	

Table 6.5: Output for optimised propeller

The first parameter optimised S_{bot} produces a change in geometry which pushes the surface towards the tip to generate more thrust. The thickness parameters S_{tu} and S_{tl} enable more thrust to be generated by increasing the thickness of the sections. A more

substantial increase in chordlengths closer to the tip occurs, in this case, before the cavitation constraints are disrupted. Again, the camber is increased quite substantially to generate more lift, as can be seen from figure (6.6); the major increase in lift along the blade span appears to be close to the regions where there is the greatest camber. There is a substantially greater increase in the thrust than in the last case, producing a 32% increase in performance, however the power requirements prove to be greater and so we maintain a similar increase in efficiency of 2.77%. Again, viewing the pressure distribution at $r = 0.7$, shows a slight suction peak at the leading edge, however the cavitation requirements are still adhered to.

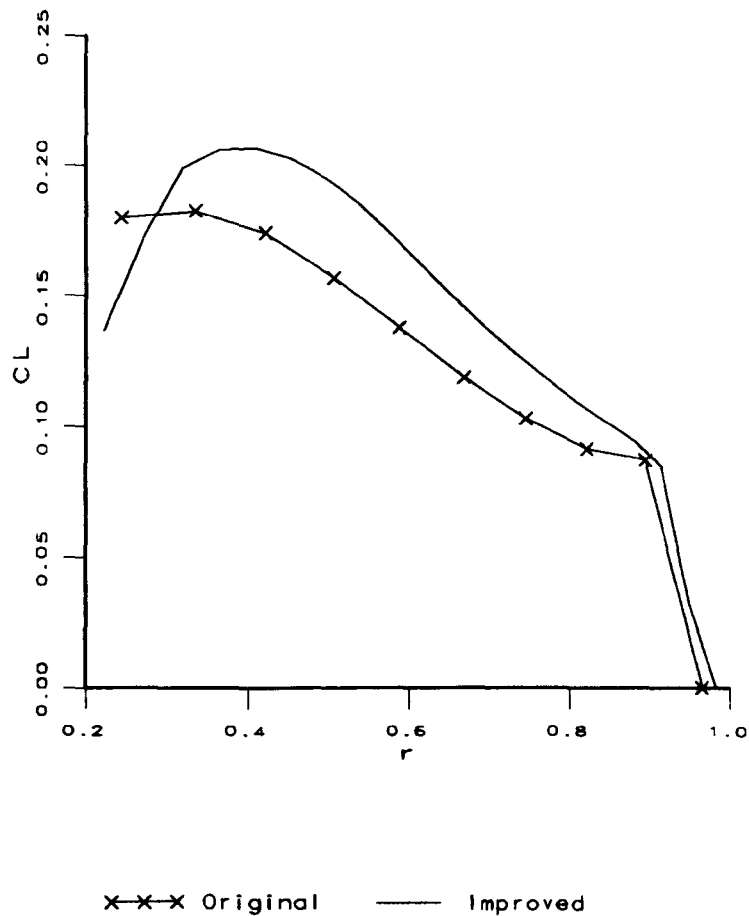
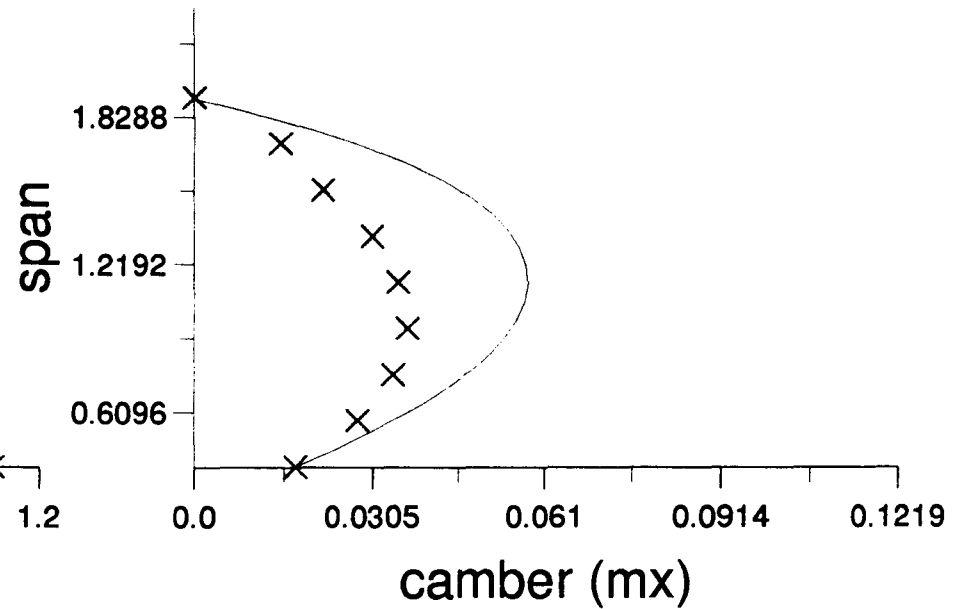
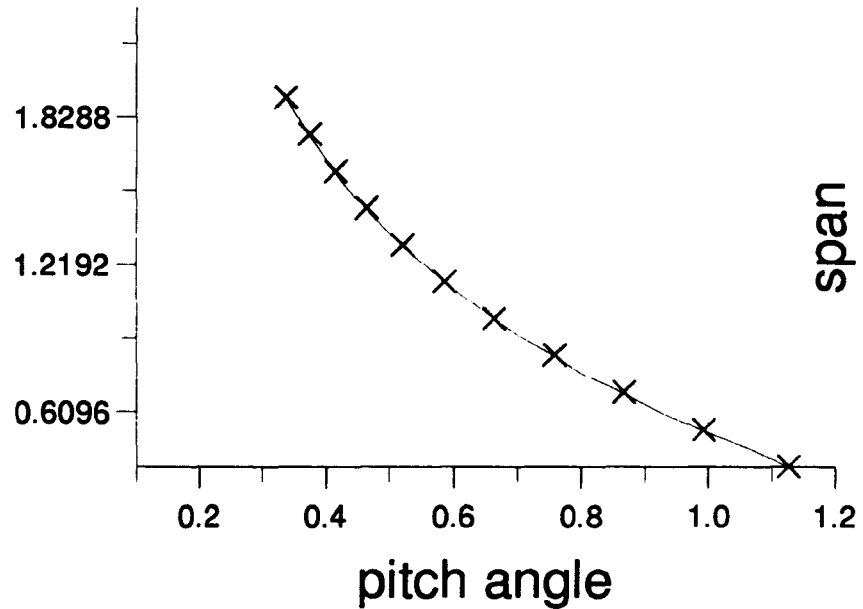
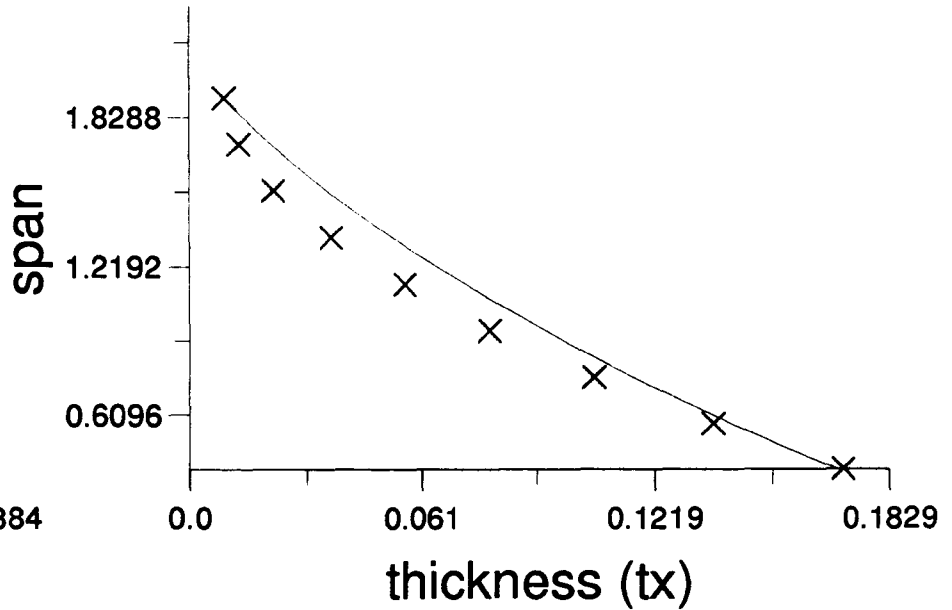
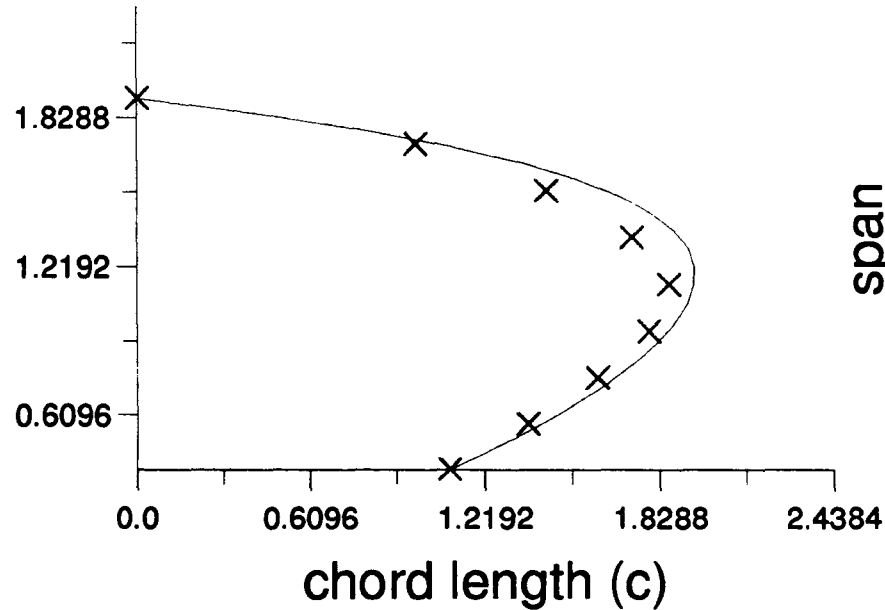


Figure 6.6: Coefficients of lift for case 2.

Figure 6.7: Geometric distributions for optimisation case 2



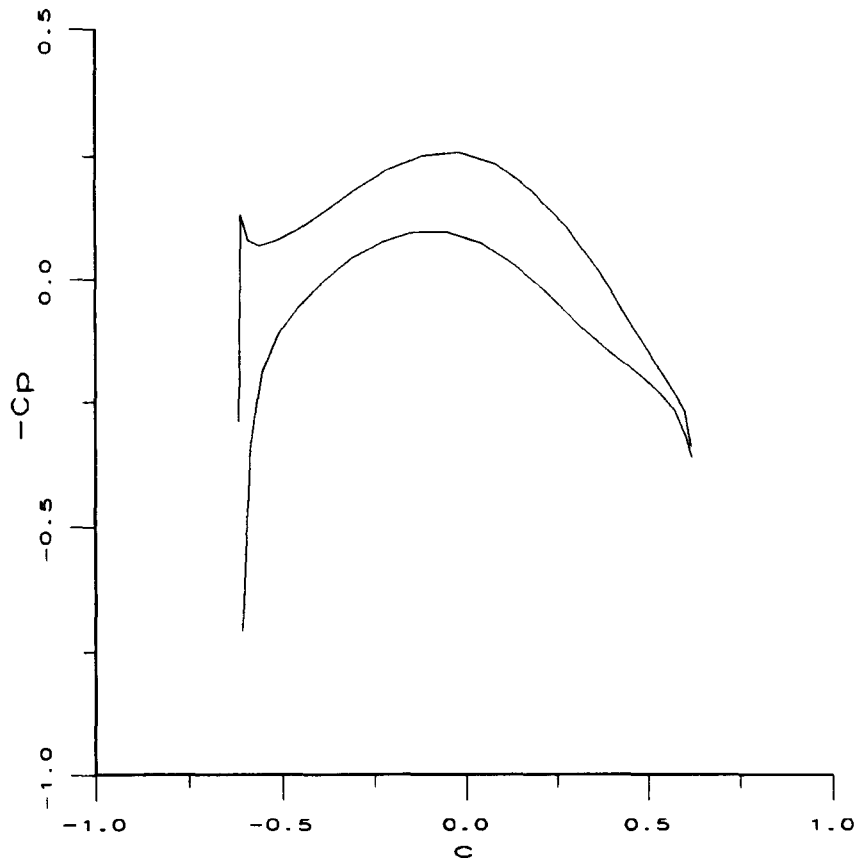


Figure 6.8: Pressure distribution at $r = 0.7$ for case 2.

6.5.3 Case 3

Case 3 optimisation		
parameter	Input	Output
c	3.6	4.62723
S_{tl}	1.9	1.25081
C_{tl}	1.0	2.35175
S_{bot}	-1.6	-1.70843
S_{cl}	-5.93	-15.50117
C_{cl}	0.75	2.30847

Table 6.6: Parameter values for case 3

Case 3 optimisation		
	Input	Output
Cavitation output		
σ_0	0.8195	0.8195
$\frac{\Delta p_{max}}{q}$	0.4863	0.4961
$\sigma_{0.7}$	0.1252	0.1257
$\left(\frac{\Delta p_{max}}{q}\right)_{0.7}$	0.0978	0.1135
(t_x/c)	0.0212	0.0299
C_l	0.1185	0.1184
Performance		
Thrust	930438	1221938
Torque	758073	1008976
Power	23815568	31697904
Efficiency	70.32	69.39
% increase	-1.32	

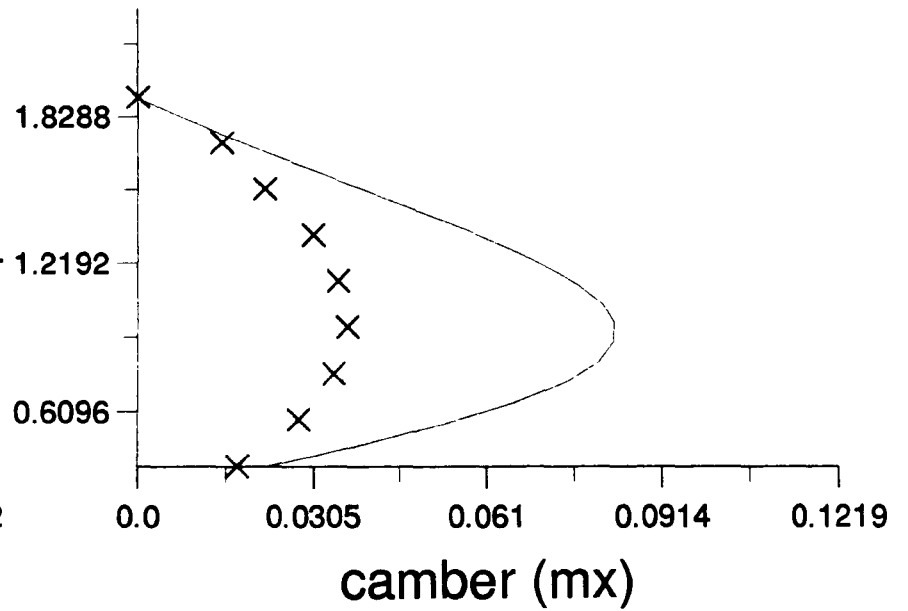
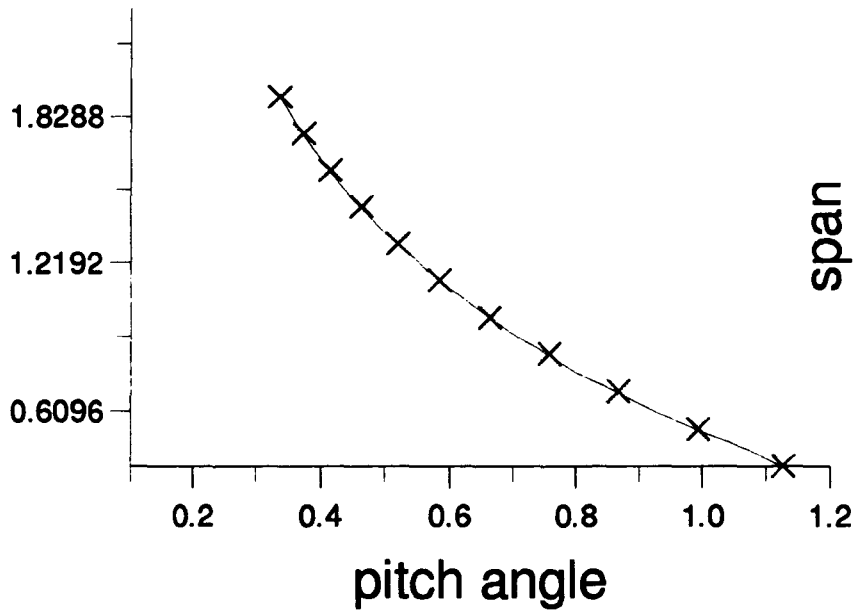
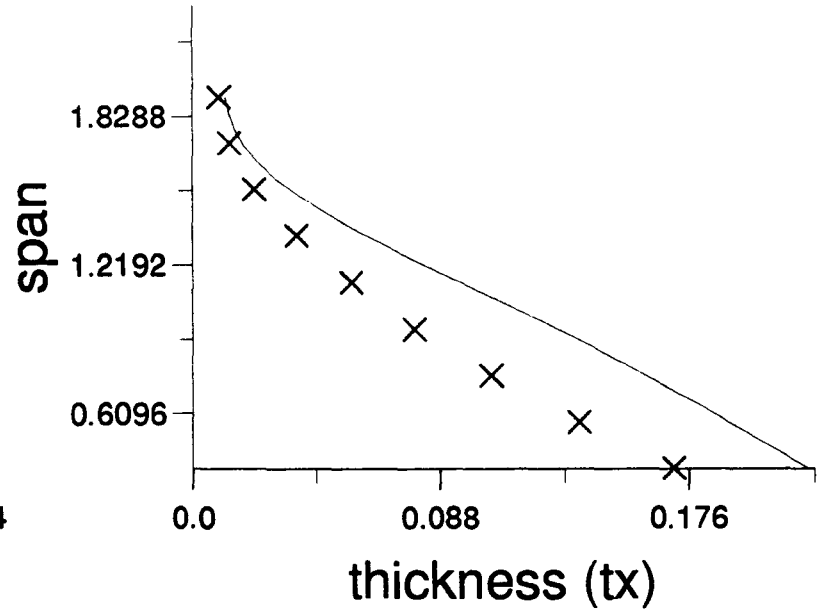
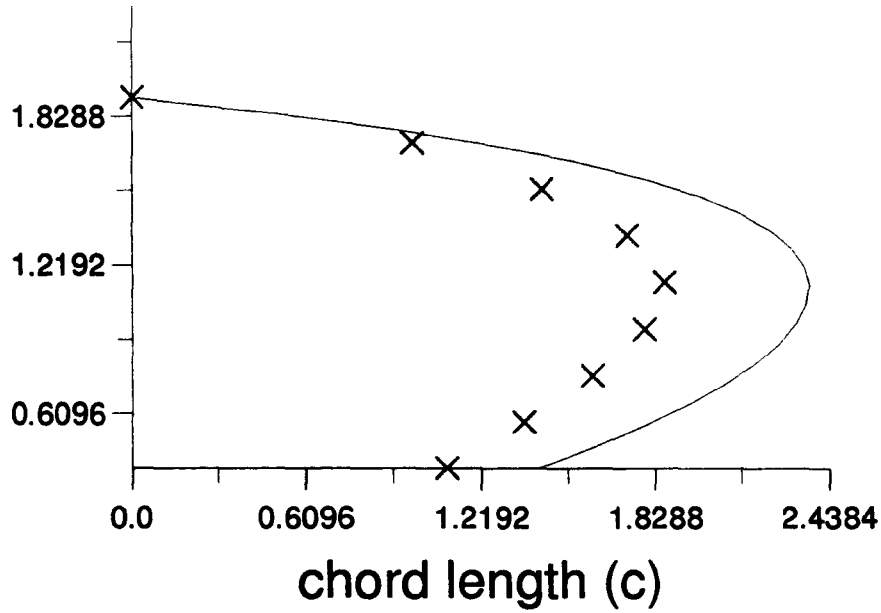
Table 6.7: Output for optimised propeller

In this third example the first parameter is c , the scaling parameter for the size of the blade section at the root of the propeller. Thus, from section 4, there will automatically be a change in all three distributions, chordlength, thickness and camber. It can be seen that a fairly large increase in geometry is acceptable before cavitation occurs. Then, alteration of the thickness and camber derivatives produces a further increase in the thrust generated. However, there is such a substantial increase in the power requirements that an actual decrease in efficiency is noted.

6.6 Discussion

As can be seen from each of the three examples, an increase in the generated thrust is feasible while cavitation restrictions are maintained. The main increase in lift at each section appears to be generated from the increase in camber of the blade.

Figure 6.9: Geometric distributions for optimisation case 3



The chordlength distribution is unable, to a certain degree, to provide much additional thrust, due to the constraint in the design ratio, and primarily due to the restriction on the local cavitation numbers. One point of interest is the degree to which the local cavitation numbers are close to the maximum pressure coefficient drop over the section. This is apparent in both cases 1 and 2 in which the difference is $O(10^{-4})$. This occurs since on maximising the thrust there is a tendency to increase the risk of cavitation. In reality, this shows the importance of building into known constraints a margin of safety.

Case 3 illustrates the potential problem associated with optimising the thrust to gain an increase in efficiency. We are able to generate considerably more thrust using the optimisation, however the power requirements to generate this thrust also increase and, at a rate greater than that of the thrust so that a decrease in efficiency is noted. Therefore, when using the thrust to gain an increase in efficiency it is necessary to impose an extra constraint that the power requirements do not increase for increasing thrust.

We now return to the original Eckhardt and Morgen design and consider an optimisation procedure, but with the additional constraint that the power required does not exceed that used for the original design, as calculated in table (5.1).

6.6.1 Case 4

In this case we consider variations in only 1 parameter C_{tu} . We start with a thickness distribution which generates less thrust than that of the original panel method in Chapter 5. This is achieved by altering the parameter $C_{tu} = -60$, so that the sections closer to the tip are thinner. To be able to include this geometry it is necessary to remove the design ratio constraint that $t_x/c \geq 0.02$. Furthermore, a new constraint will be included which prevents the torque (and hence the power) from getting any higher than that obtained in section (5.6). What we aim to see is whether the thrust will increase with the thickness parameter C_{tu} beyond that originally given while restricting the power.

6.6.2 Results

The results of the optimisation are as illustrated in table (6.8). As is seen the final value of C_{tu} obtained was given as $C_{tu} = 0.9999$, which within the tolerance of the bracketing routine is the same as the original distribution, and so we can conclude that it is not possible to increase the thrust while restricting the power required simply by changing the single parameter C_{tu} . Since each parameter is changed singularly in the optimisation

routine we must find an optimum value for the efficiency via a different route.

Propeller Characteristics	C_{tu}	C_{tu}
Thrust	892913	930438
Power	23004329	23815568
Torque	732251	758073
C_T	0.4717	0.4915
C_P	0.6751	0.6989
C_Q	0.0356	0.0368
efficiency	69.87	70.32

Table 6.8: Performance of altered propeller.

Thus, we see that were we to choose the efficiency as the objective function and optimise over a range of parameters, an improvement in design could be obtained.

6.6.3 Case 5

We consider the optimisation routine as previously defined, however where the objective function is no longer the thrust but efficiency. The input and output values of the optimised parameter set are illustrated in table (6.9).

Case 5 optimisation		
parameter	Input	Output
S_{bot}	-1.66	-2.51069
S_{cl}	-5.93	-31.07331
C_{cu}	2.0	6.76098
S_{tu}	2.0	6.29611
S_{xu}	-3.8	-3.80000

Table 6.9: Parameter values for case 5

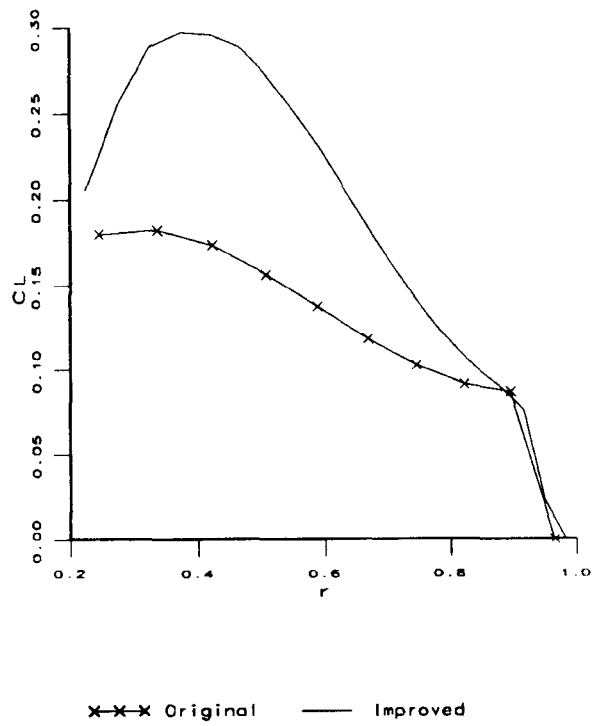


Figure 6.10: Coefficients of lift for case 5.

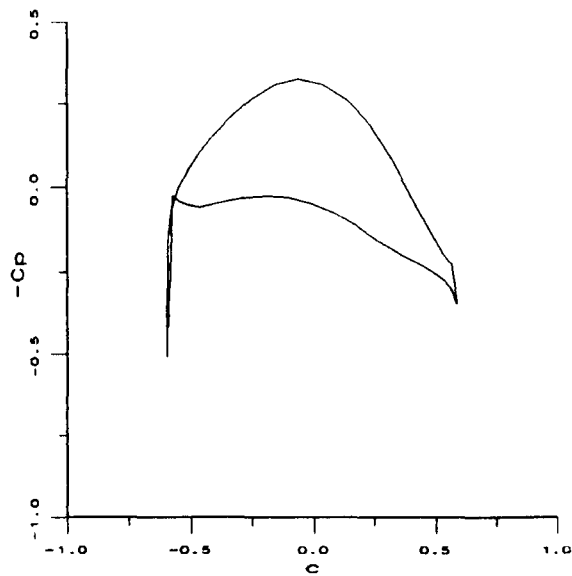
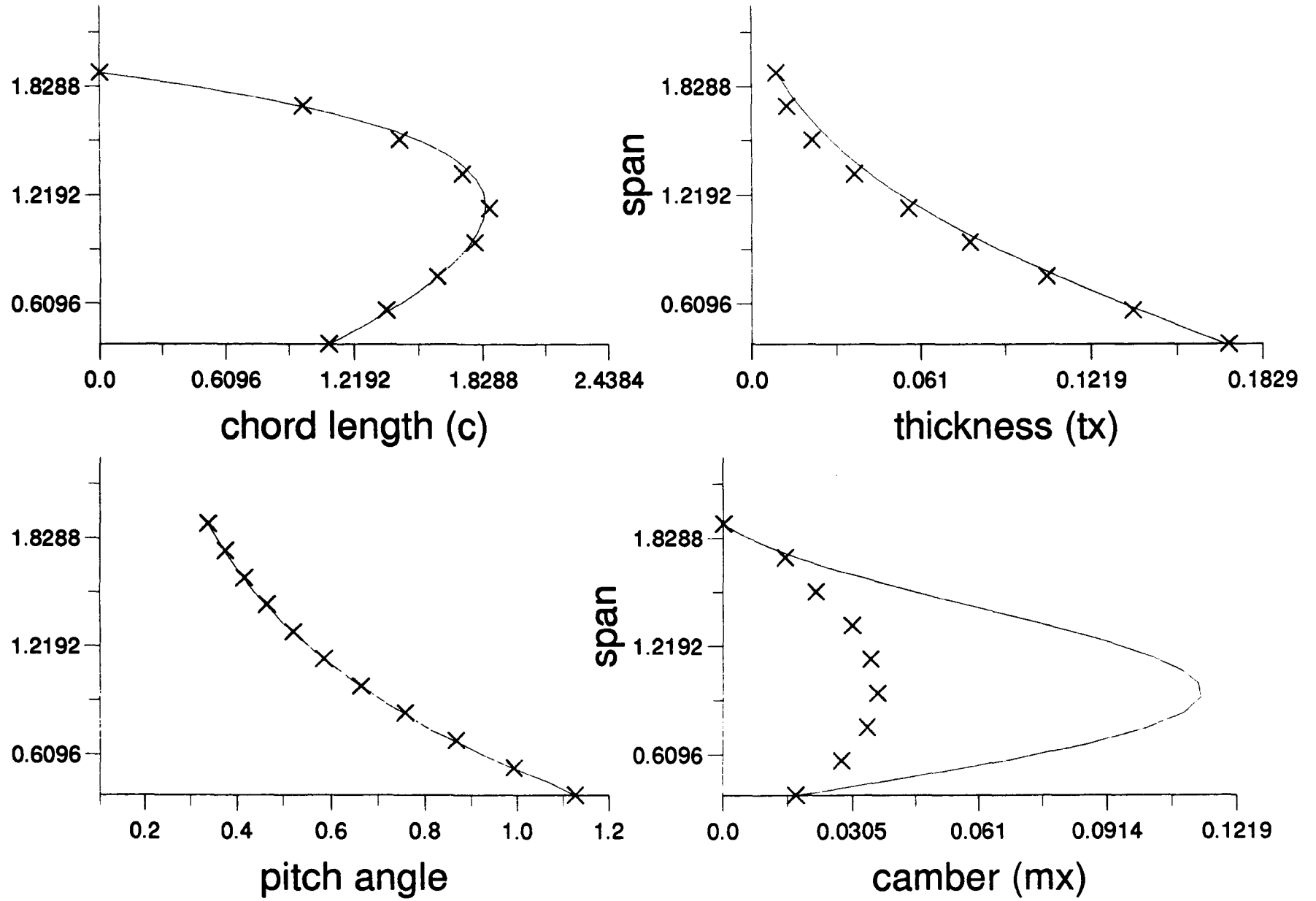


Figure 6.11: Pressure distribution at $r = 0.7$ for case 5.

Figure 6.12: Geometric distributions for optimisation case 5



We see that optimisation of the efficiency is almost completely achieved by an increase in camber. It can be concluded from cases 1, 2 and 5 that the chordlength distribution proves difficult to alter due to the cavitating properties, and that the camber produces the main source of lift while adhering to the non-cavitating conditions. Figure (6.10) illustrates that increasing the camber provides an increased lift distribution along the blade, however, from figure (6.12) we see that a suction peak is starting to form on the blade surface at the leading edge. This is due to the pronounced geometry of the mean line.

Case 5 optimisation		
	Input	Output
Cavitation output		
σ_0	0.8195	0.8195
$\frac{\Delta p_{max}}{q}$	0.4863	0.60744
$\sigma_{0.7}$	0.1252	0.1201
$(\frac{\Delta p_{max}}{q})_{0.7}$	0.0978	0.1201
(t_x/c)	0.0212	0.0211
C_l	0.1185	0.1774
Performance		
Thrust	930438	1441030
Torque	758073	1112840
Power	23815568	34960890
Efficiency	70.32	74.19
% increase	5.50	

Table 6.10: Output for optimised propeller

In this case we can see that using the efficiency as the objective function produces a greater increase in efficiency. Again, it should be noted that the difference between constraints and their evaluated value is $O(10^{-4})$. The optimisations performed showed an improvement in the efficiency of 2% – 6%. Although these are likely to be slight, in economic terms a 6% improvement represents a valuable achievement, since given the likely number of journeys and the period of time a propeller is in sevice, this would produce considerable savings.

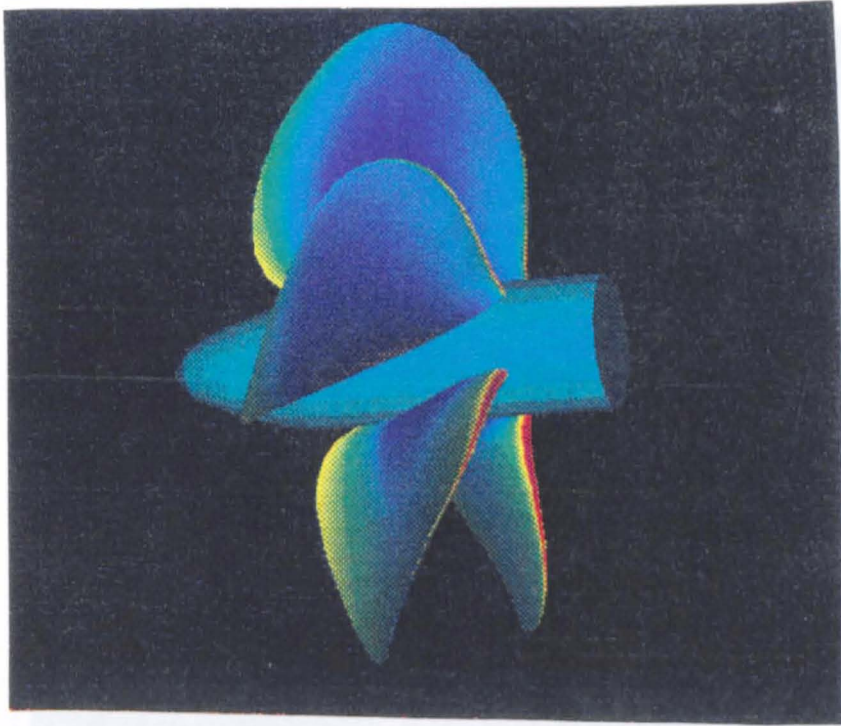


Figure 6.13: Surface pressure distribution for case 1.

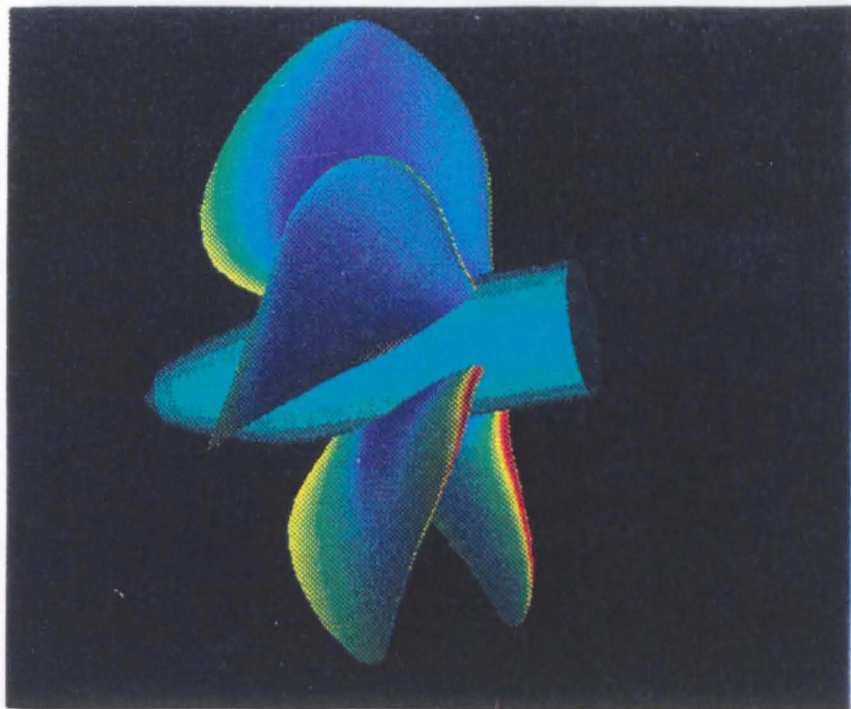


Figure 6.14: Surface pressure distribution for case 2.

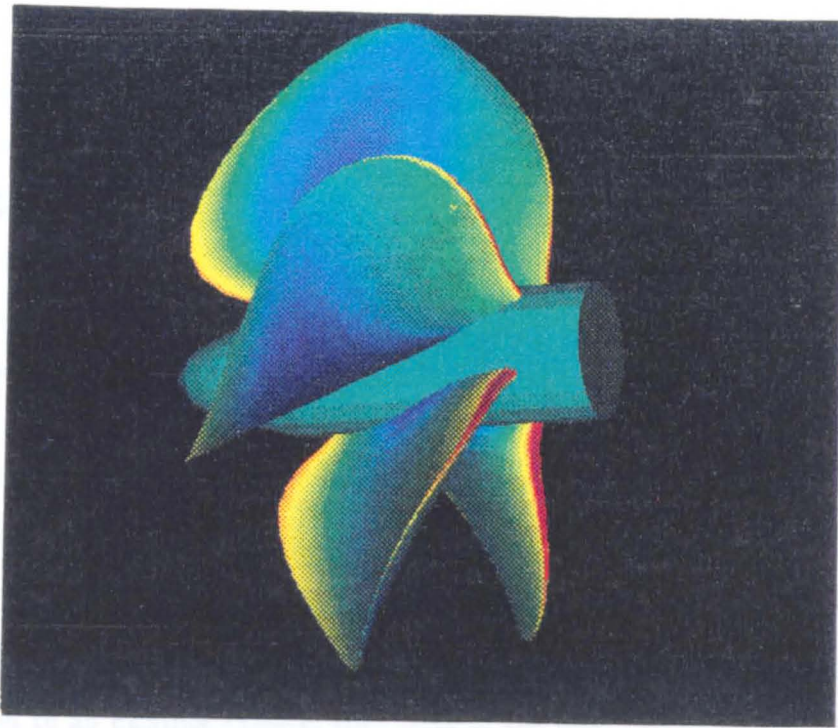


Figure 6.15: Surface pressure distribution for case 3.

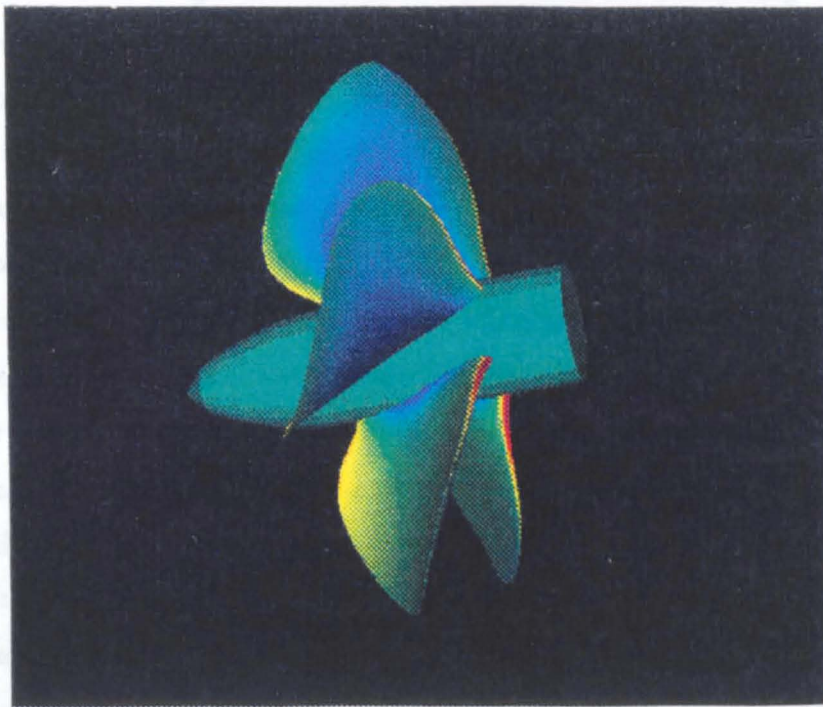


Figure 6.16: Surface pressure distribution for case 5.

Chapter 7

Conclusion

To conclude then, what can we say about the approach adopted using the PDE method compared to existing techniques? One approach conventionally used to generate a surface is given by the B-spline representation. If we wish to generate a surface which is not an approximation to an existing surface, then both of the above methods can be used with degrees of success.

To generate a B-spline surface we need to know the way in which the basis functions are generated. Then, to generate an arbitrary surface, the positioning of all surface control points is required. Although this is straightforward, a large amount of time can be used, especially on large surface patches such as those on ship hulls. In contrast, to generate a PDE surface patch, an understanding of the way in which the boundary conditions control the surface is needed. Once the boundary conditions are derived, the surface can be generated swiftly, be it as an analytic solution for the many closed surfaces, or solved numerically by some finite difference scheme. This was illustrated in Chapter 2 where several surface blends were considered. The initialisation of the problem was made rather more straightforward with the need for the boundaries of the generated surface to coincide with the trimlines on the primary surfaces being blended between, along with the requirements of tangent plane continuity. This enabled a solution to be found almost instantaneously, which when compared with the time required to generate an equally smooth B-spline surface, proves advantageous. The example of the wine glass further illustrates the ease with which the PDE surface can be generated and manipulated. Generating arbitrary surfaces using B-splines requires the positioning of all surface points. However, we have the means by which the two forms can be exchanged, thus providing an ease of data exchange between the two methods and providing compatibility.

Interactively, when a designer is using one of the surface methods to alter the geometry, there are several advantages in using either of the methods. The PDE approach has the main advantage of global manipulation of a given surface. This is more useful in designs of large surfaces, such as those of a yacht, or the simple marine propeller described in Chapter 3. B-spline surfaces have the advantage of highly local control of the surface. This can be achieved by a simple displacement of the B-spline control points to alter the approximating surface. However, applications such as that of the marine propeller surface are not completely suited to these high degrees of local change. Even if the local adjustments may approximate an existing surface to a better degree than the PDE approximation, the fairness of the surface needs to be considered once generated. Thus, if local displacements to the approximating geometry are made, then the designer must have, and be prepared to use, tools to analyse the local properties of the surface in order to judge its fairness. As illustrated in Chapter 4, some work is required to express the boundary conditions in a form which gives us total control of the surface. However, as Bloor and Wilson demonstrate, Fourier analysis of complex boundary curves provides little effort in producing a set of boundary conditions in the form required for an analytic solution. The advantage the PDE generated propeller then has is that due to global alterations and the nature of the surface being found as a solution of an elliptic PDE, we can automatically regard the final surface to be both smooth and fair.

Further simplifications include the interactive design tool available for generating curves in space, using the console and mouse, along with manipulation of positional and tangential boundary conditions on screen in real time. This proves to be just as accessible as design tools used for manipulation of B-spline surfaces by movement and removal of control points.

Therefore, it is reasonable to conclude that if we are prepared to spend some initial time on obtaining the boundary conditions of the surface, manipulation of the PDE generated surface is more appropriate for these hydrodynamic surfaces than conventional spline techniques.

Secondly, the surface geometry is well suited to the implementation of panel methods. This is useful when the hydrodynamic analysis of a surface model is required, as this can reduce the necessity for producing models to be tested in water tanks. The propeller surface generated in Chapter 4 was suited to the panel method due to the fact that the panels needed for the implementation of the panel method were automatically generated

in the PDE method from the iso- u and iso- v lines. Furthermore, the parameterisation was such that in areas of highly varying pressure distributions, the panels were suitably condensed, with a more sparse distribution being displayed at midchord positions of the blade. Also useful to the efficient working of the panel method was the fact that little reorientation of the PDE generated panels was needed to ensure they were planar. This then produced a second saving of time and effort. The generated propeller operating under the conditions given in Chapter 5 proved to give similar performance predictions to those given from existing techniques, along with a pressure distribution which contained all the properties of other predicted distributions. This showed that the panel method could attain the results of other methods, along with the ability of predicting pressures, not entirely feasible on lifting line and surface methods. Caution should however be exercised, since different panel resolutions gave results differing by up to 5%; notable discrepancies arising in regions close to the central hub which was neglected. This could probably be remedied by inclusion of a discretised hub within the workings of the panel method. As has been stated previously though, this thesis concentrated on computing efficiency of the panel method as opposed to trying to implement the most comprehensive of models due to the optimisation procedure.

The ability to determine the hydrodynamic performance of the propeller from its complete surface geometry opened the way for an optimisation scheme to be implemented based on the optimisation of the PDE shape parameters. Essentially this is available to us due to the fact that the PDE generated propeller has a small parameter set to control the surface and the propeller distributions. A B-spline surface could not have used such an effective procedure for optimisation of the actual geometry, but might have had to have relied on some far more complicated scheme based on the manipulation of the control points of the surface (one such method featured in Chapter 1). This is probably one of the most important areas in which the PDE approach is superior to other surface design methods; that is in the functional evaluation of the surface properties, and more importantly in its ability to easily search for an improved design based on the optimisation of the parameter subspace.

This was demonstrated in Chapter 6 in the improvement in both thrust and efficiency of marine propellers. Even though only a small increase in efficiency was produced, this would prove to be beneficial. The size of the increase was limited mainly by the restrictions on cavitation, especially where the chordlength distribution was concerned, and so the

final design should be beneficial, not only from an increase in efficiency, but in that it should be operational longer due to its non-cavitating properties. Again, it is emphasised that safety margins are needed to maintain a sizeable margin between local cavitation numbers and the maximum pressure coefficient changes which are given for the optimum geometry.

Finally, something should be said about the way in which the optimisation is achieved. Even though there are many runs of the panel method in the optimisation procedure, which necessitates many hours computing, the time taken to find some optimum design is used well, since the actual geometry is used within the procedure, as opposed to some other method in which the geometry may be approximated by lifting lines and accurate predictions may not be obtained.

It is worth remarking that an improvement can be made to the PDE blade, by inclusion, and control, of the pitch distribution in the surface model developed in Chapter 4. This would mean that more parameters, which control the angle of inclination of the blade sections to the inflow, could be optimised. This would probably result in greater efficiencies being produced, along with the removal of suction peaks at the leading edge of the blade due to the pitch angle being critical in this respect. Unfortunately, this was not implemented in this thesis and remains as future work.

Thus, to conclude, we can see that the PDE method gives an efficient method of parametrising shape which is of crucial importance if the subsequent functional design and possible optimisation are to be considered and further, once the final surface design has been created, we can rest assured that fairness constraints will also be adhered to.

We have seen just one application to which the PDE method can be put. The application is by no means complete: there are many improvements which could be implemented, for instance the improvement of the panel method, the inclusion of strength testing, and constraints to ensure that the blade remained strong enough in the hydrodynamic optimisation. Of course, to incorporate all of these features would involve many more calculations, and so at some point the user has to decide how many considerations and how complex the model should become. In the end, the aim is to strike a happy medium between the time required and the complexity of the model.

Appendix A

The analytic solution for the 6th order PDE

A.1 Method of solution

Considering each of the dependent surface variables (x, y, z) in turn, we seek the solution of the partial differential equation

$$\left(\frac{\partial^2}{\partial u^2} + a^2 \frac{\partial^2}{\partial v^2} \right)^3 \phi = 0 \quad (\text{A.1})$$

i.e.

$$\phi_{uuuuuu} + 3a^2 \phi_{uuuuuv} + 3a^4 \phi_{uuuvvv} + a^6 \phi_{vvvvvv} = 0 \quad (\text{A.2})$$

where subscript u denotes partial differentiation with respect to u .

Using the method of separation of variables, we can seek a solution of the form

$$\phi = A(u) \cdot V(v) \quad (\text{A.3})$$

and specifically if we let

$$V(v) = e^{imv}. \quad (\text{A.4})$$

Substituting equations (A.3) and (A.4) back into (A.2) implies that

$$A^6 e^{imv} - 3A^4 a^2 m^2 e^{imv} + 3A^2 a^4 m^4 e^{imv} - A a^6 m^6 e^{imv} = 0 \quad (\text{A.5})$$

i.e.

$$A^6 - 3A^4 a^2 m^2 + 3A^2 a^4 m^4 - A a^6 m^6 = 0. \quad (\text{A.6})$$

Now,

$$A(u) = e^{\lambda u} \quad (\text{A.7})$$

is a general solution of the characteristic equation (A.6). The roots of this equation are

$$\lambda = \pm am, \quad (\text{A.8})$$

and thus has two distinct solutions

$$A(u) = A_1 e^{amu} \quad A(u) = A_2 e^{-amu}. \quad (\text{A.9})$$

It is therefore required to look further for four other solutions. These are found to be

$$A(U) = A_3 u e^{amu} \quad A(u) = A_4 u e^{-amu} \quad (\text{A.10})$$

$$A(U) = A_5 u^2 e^{amu} \quad A(u) = A_6 u^2 e^{-amu} \quad (\text{A.11})$$

and the general solution for ϕ may be written as

$$\begin{aligned} \phi = \{ & A_1 e^{amu} + A_2 e^{-amu} + A_3 u e^{amu} + A_4 u e^{-amu} \\ & + A_5 u^2 e^{amu} + A_6 u^2 e^{-amu} \} e^{imv} \end{aligned} \quad (\text{A.12})$$

which may be rewritten in the form of equation (2.31), where a is the smoothing parameter, and m corresponds to the particular Fourier mode.

If z is not dependent on any Fourier modes this implies that

$$\frac{\partial z}{\partial v} = 0 \quad (\text{A.13})$$

and so the equation to be solved is simply

$$\frac{\partial^6 z}{\partial u^6} = 0 \quad (\text{A.14})$$

and so the solution for z will be a quintic polynomial of the form of

$$z(u, v) = z_0 + z_1 u + z_2 u^2 + z_3 u^3 + z_4 u^4 + z_5 u^5 \quad (\text{A.15})$$

Appendix B

The induced velocity at a point due to a source and doublet distribution on a plane quadrilateral

B.1 Source distribution

Following Hess [48], we evaluate the integral of the point source formulae over a panel by specifying the panel to lie in a coordinate plane in some coordinate system. In particular, the panel is taken to lie in the (x, y) plane of this system, as shown in figure (B.1). The positive z -axis of the coordinate system is in the direction of the unit outward normal vector to the element. The four points at the corner of the panel are denoted by subscripts 1, 2, 3, 4 and the maximum dimension of the panel is denoted by t .

Consider now the point $P(x, y, z)$ in the element coordinate system as shown in figure (B.1). For a unit value of source density, the potential at the point $P(x, y, z)$ due to the quadrilateral is given by

$$\phi_p = \frac{1}{4\pi} \int_A \frac{1}{r} dA = \frac{1}{4\pi} \int_A \frac{d\zeta d\eta}{[(x - \zeta)^2 + (y - \eta)^2 + z^2]^{1/2}} \quad (\text{B.1})$$

and

$$\begin{aligned} v_x &= -\frac{\partial\phi}{\partial x} = \frac{1}{4\pi} \int_A \frac{(x - \zeta)}{r^3} d\zeta d\eta \\ v_y &= -\frac{\partial\phi}{\partial y} = \frac{1}{4\pi} \int_A \frac{(y - \eta)}{r^3} d\zeta d\eta \end{aligned}$$

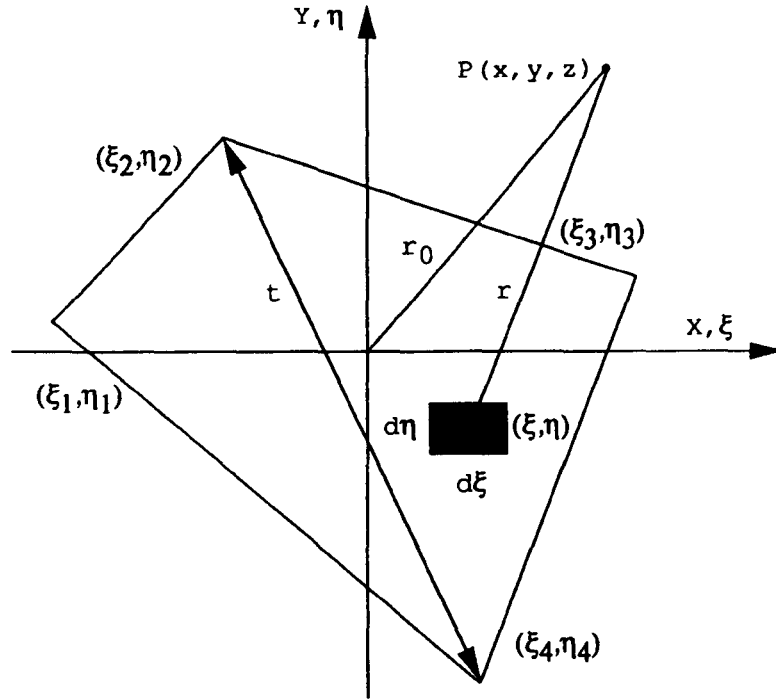


Figure B.1: A planar panel lying in the element coordinate system

$$v_z = -\frac{\partial\phi}{\partial z} = \frac{1}{4\pi} \int_A \frac{z}{r^3} d\zeta d\eta.$$

These integrals can be obtained exactly by analytic means. However, as stated approximations can be used depending on the distance of the point $P(x, y, z)$ from the centroid of the panel. The following formulae are all taken from [48].

If $r/t > 4$ then the quadrilateral may be approximated by a point source at its centroid and the velocity components are given by

$$\begin{aligned} v_x &= \frac{x - x_0}{r^3} I_{00} \\ v_y &= \frac{y - y_0}{r^3} I_{00} \\ v_z &= \frac{z - z_0}{r^3} I_{00} \end{aligned}$$

where (x_0, y_0, z_0) is the centroid of the panel, $r = [(x - x_0)^2 + (y - y_0)^2 + (z - z_0)^2]^{1/2}$ and I_{00} is the area of the panel

$$I_{00} = 1/2(\zeta_3 - \zeta_1)(\eta_2 - \eta_4). \quad (\text{B.2})$$

If $r/t > 2.45$ then a multipole expansion is used and the velocity components are given by

$$v_x = -\frac{\partial\phi}{\partial x} = -I_{00}w_x - 1/2(I_{20}w_{xxx} + 2I_{11}w_{xxy} + I_{02}w_{xyy})$$

$$v_y = -\frac{\partial\phi}{\partial y} = -I_{00}w_y - 1/2(I_{20}w_{xxy} + 2I_{11}w_{xyy} + I_{02}w_{yyy})$$

$$v_z = -\frac{\partial\phi}{\partial z} = -I_{00}w_z - 1/2(I_{20}w_{xxz} + 2I_{11}w_{xyz} + I_{02}w_{yyz})$$

where w and its derivatives are

$$\begin{aligned} w &= r^{-1} & w_{xxx} &= 3x(3p + 10x^2)r^{-7} \\ w_x &= -xr^{-3} & w_{xxy} &= 3ypr^{-7} \\ w_y &= -yr^{-3} & w_{xyy} &= 3xqr^{-7} \\ w_z &= -zr^{-3} & w_{yyy} &= 3y(3q + 10y^2)r^{-7} \\ w_{xx} &= -(p + 2x^2)r^{-5} & w_{xxz} &= 3zpr^{-7} \\ w_{xy} &= 3xyr^{-5} & w_{xyz} &= -15xyzr^{-7} \\ w_{yy} &= -(q + 2y^2)r^{-5} & w_{yyz} &= 3zqr^{-7} \end{aligned}$$

where

$$p = y^2 + z^2 - 4x^2 \quad q = x^2 + z^2 - 4y^2 \quad (\text{B.3})$$

and the moments are given by

$$\begin{aligned} I_{20} &= \frac{1}{12}(\zeta_3 - \zeta_1) \left[\eta_1(\zeta_4 - \zeta_2)(\zeta_1 + \zeta_2 + \zeta_3 + \zeta_4) + (\eta_2 - \eta_4)(\zeta_1^2 + \zeta_1\zeta_3 + \zeta_3^2) \right. \\ &\quad \left. + \zeta_2\eta_2(\zeta_1 + \zeta_2 + \zeta_3) - \zeta_4\eta_4(\zeta_1 + \zeta_3 + \zeta_4) \right] \\ I_{11} &= \frac{1}{24}(\zeta_3 - \zeta_1) \left[2\zeta_4(\eta_1^2 - \eta_4^2) - 2\zeta_2(\eta_1^2 - \eta_2^2) + (\zeta_1 + \zeta_3)(\eta_2 - \eta_4)(2\eta_1 + \eta_2 + \eta_4) \right] \\ I_{02} &= \frac{1}{12}(\zeta_3 - \zeta_1)(\eta_2 - \eta_4) \left[(\eta_1 + \eta_2 + \eta_4)^2 - \eta_1(\eta_2 + \eta_4) - \eta_2\eta_4 \right]. \end{aligned}$$

Finally, if $r/t \leq 2.45$ then exact formulae are used to evaluate the velocity components and are given by

$$\begin{aligned} v_x &= \frac{\eta_2 - \eta_1}{d_{12}} \log \frac{r_1 + r_2 - d_{12}}{r_1 + r_2 + d_{12}} + \frac{\eta_3 - \eta_2}{d_{23}} \log \frac{r_2 + r_3 - d_{23}}{r_2 + r_3 + d_{23}} \\ &\quad + \frac{\eta_4 - \eta_3}{d_{34}} \log \frac{r_3 + r_4 - d_{34}}{r_3 + r_4 + d_{34}} + \frac{\eta_1 - \eta_4}{d_{41}} \log \frac{r_4 + r_1 - d_{41}}{r_4 + r_1 + d_{41}} \\ v_y &= \frac{\zeta_1 - \zeta_2}{d_{12}} \log \frac{r_1 + r_2 - d_{12}}{r_1 + r_2 + d_{12}} + \frac{\zeta_2 - \zeta_3}{d_{23}} \log \frac{r_2 + r_3 - d_{23}}{r_2 + r_3 + d_{23}} \\ &\quad + \frac{\zeta_3 - \zeta_4}{d_{34}} \log \frac{r_3 + r_4 - d_{34}}{r_3 + r_4 + d_{34}} + \frac{\zeta_4 - \zeta_1}{d_{41}} \log \frac{r_4 + r_1 - d_{41}}{r_4 + r_1 + d_{41}} \end{aligned}$$

$$\begin{aligned}
v_z &= \tan^{-1} \left(\frac{m_{12}e_1 - h_1}{zr_1} \right) - \tan^{-1} \left(\frac{m_{12}e_2 - h_2}{zr_2} \right) \\
&+ \tan^{-1} \left(\frac{m_{23}e_2 - h_2}{zr_2} \right) - \tan^{-1} \left(\frac{m_{23}e_3 - h_3}{zr_3} \right) \\
&+ \tan^{-1} \left(\frac{m_{34}e_3 - h_3}{zr_3} \right) - \tan^{-1} \left(\frac{m_{34}e_4 - h_4}{zr_4} \right) \\
&+ \tan^{-1} \left(\frac{m_{41}e_4 - h_4}{zr_4} \right) - \tan^{-1} \left(\frac{m_{41}e_1 - h_1}{zr_1} \right)
\end{aligned}$$

where

$$d_{12} = [(\zeta_2 - \zeta_1)^2 + (\eta_2 - \eta_1)^2]^{1/2}$$

$$d_{23} = [(\zeta_3 - \zeta_2)^2 + (\eta_3 - \eta_2)^2]^{1/2}$$

$$d_{34} = [(\zeta_4 - \zeta_3)^2 + (\eta_4 - \eta_3)^2]^{1/2}$$

$$d_{41} = [(\zeta_1 - \zeta_4)^2 + (\eta_1 - \eta_4)^2]^{1/2},$$

$$m_{12} = \frac{\eta_2 - \eta_1}{\zeta_2 - \zeta_1}, \quad m_{23} = \frac{\eta_3 - \eta_2}{\zeta_3 - \zeta_2}$$

$$m_{34} = \frac{\eta_4 - \eta_3}{\zeta_4 - \zeta_3}, \quad m_{41} = \frac{\eta_1 - \eta_4}{\zeta_1 - \zeta_4}$$

and

$$r_k = [(x - \zeta_k)^2 + (y - \eta_k)^2 + z^2]^{1/2}$$

$$e_k = z^2 + (x - \eta_k)^2$$

$$h_k = (y - \eta_k)(x - \zeta_k)$$

$$k = 1, 2, 3, 4.$$

B.2 The doublet distribution

Consider now a constant doublet distribution of unit strength on the quadrilateral of figure (B.1). If we consider one side of the quadrilateral then the line vortex AB will be as shown in figure (B.2).

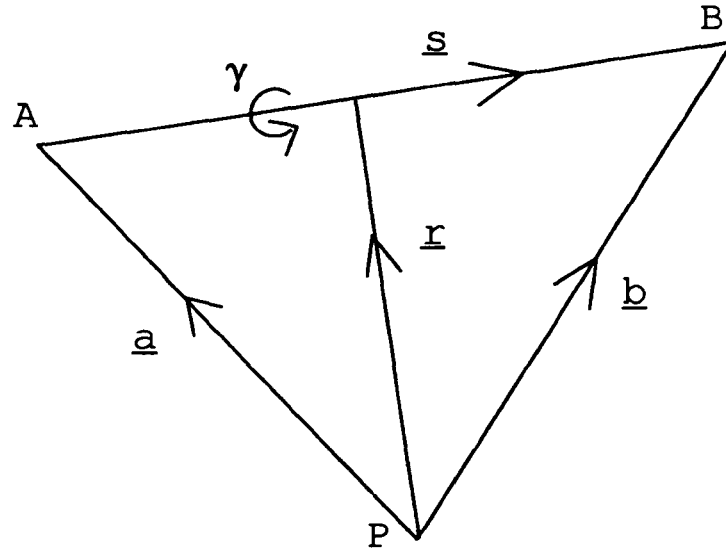


Figure B.2: The contribution from a line vortex

The induced velocity at a point P is given by Petrie [59] as

$$\underline{q}_L = \frac{1}{4\pi} \int_{AB} \frac{\underline{r} \times \gamma}{|\underline{r}|^3} ds \quad (\text{B.4})$$

which Petrie arrives at as

$$\underline{q}_L = \frac{\underline{a} \times \underline{b}}{(\underline{a} \times \underline{b}) \cdot (\underline{a} \times \underline{b})} \left[(|\underline{a}| + |\underline{b}|) \left(1 - \frac{\underline{a} \cdot \underline{b}}{|\underline{a}||\underline{b}|} \right) \right]. \quad (\text{B.5})$$

These velocity components are summed around the perimeter of each panel to give \underline{V}_{dij} . The same formulae are used to determine the influence from the sections of the trailing wake.

B.3 The vortex sheet

Finally, the velocity induced by a vortex sheet of strength $\underline{\gamma}_p$ needs to be obtained. This is only evaluated when the final velocity is required since it acts tangential to the surface and plays no part in the initial evaluation of the influence velocity. The value of $\underline{\gamma}_p$ is obtained numerically by consideration of the vortex rings adjacent to the panel, as in figure (B.3).

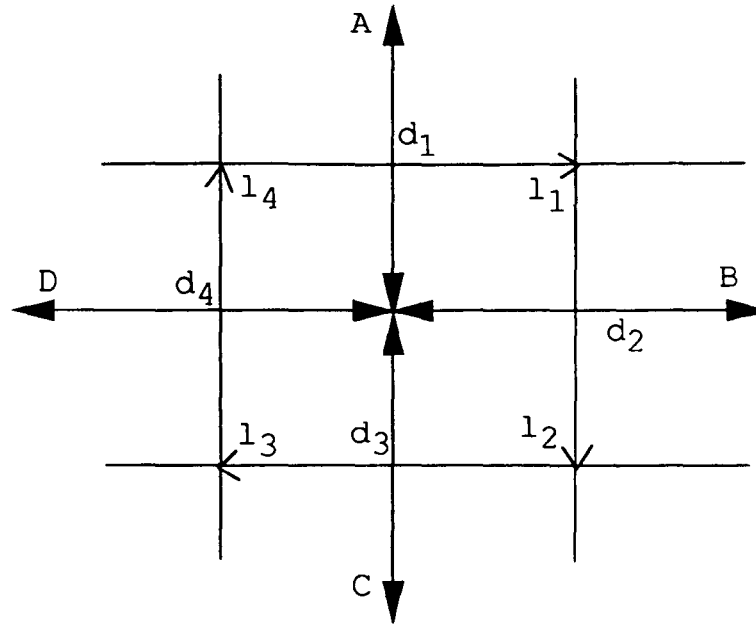


Figure B.3: Evaluation of the vortex sheet velocity component

Petrie [59] obtains the approximation $\underline{\gamma}_p = \underline{\gamma}_{AC} + \underline{\gamma}_{BD}$ where

$$\underline{\gamma}_{AC} \approx \frac{1}{2} \left(\frac{\mu_p - \mu_A}{|d_1 \times l_1|} l_1 + \frac{\mu_p - \mu_C}{|d_3 \times l_3|} l_3 \right)$$

$$\underline{\gamma}_{BD} \approx \frac{1}{2} \left(\frac{\mu_p - \mu_B}{|d_2 \times l_2|} l_2 + \frac{\mu_p - \mu_D}{|d_4 \times l_4|} l_4 \right).$$

Appendix C

The derivation of PDE boundary conditions

C.1 Introduction

In this appendix we deal with the explicit derivation of the boundary conditions required for the solutions of the PDE problems posed throughout the thesis. This appendix is designed as an aid to the reader to further illustrate the initialisation of the posed problems. However, it should be noted that the boundary conditions described here represent a workable choice, since many forms of parameterisation can exist. It should further be noted that all examples considered here are periodic in v ; that is to say that boundary conditions can be applied solely on the $u = 0$ and $u = 1$ isolines. These consist of either the positional and first derivative boundary conditions for the solution to the fourth order partial differential equation (2.3), or the positional, first and second derivatives for the solution to the sixth order partial differential equation given by equation (2.35) with analytic solution described in Appendix A.

C.2 Example 2.3: A surface blend

A surface blend is chosen so that a smooth 'secondary' surface is generated between two primary surfaces. The conditions we require on the blend are that the blend meets each of the surfaces, and that tangent plane continuity is maintained between the blend and the primary surfaces.

In this example we consider the blend between a sphere and a cone. To generate the

surface it is customary to define two trimlines, one lying on each surface. These we give by

$$x(0, v) = R_{top} \cos v \quad (C.1)$$

$$y(0, v) = R_{top} \sin v \quad (C.2)$$

$$z(0, v) = d_1 \quad (C.3)$$

$$(C.4)$$

$$x(1, v) = R_{bot} \cos v \quad (C.5)$$

$$y(1, v) = R_{bot} \sin v \quad (C.6)$$

$$z(1, v) = d_2 \quad (C.7)$$

for $0 \leq u \leq 1, 0 \leq v \leq 2\pi$ as in equations (2.11- 2.16) where $R_{top}, R_{bot}, d_1, d_2$ are as defined in figure (2.2). We therefore have positional boundary conditions applied on $u = 0$ and $u = 1$.

Derivative boundary conditions are chosen so that a smooth surface is generated between primary and secondary surfaces. In section (2.3.1) we illustrated the general form for these conditions.

If we consider equation (2.18) and take

$$\underline{N} = \frac{\underline{X}_\phi \times \underline{X}_v}{|\underline{X}_\phi \times \underline{X}_v|} \quad (C.8)$$

on the surface of the sphere and

$$\underline{N} = \frac{\underline{X}_\zeta \times \underline{X}_v}{|\underline{X}_\zeta \times \underline{X}_v|} \quad (C.9)$$

on the surface of the cone, where ϕ, ζ are as in equations (2.5-10), we can obtain a normal to each surface.

On the sphere

$$\underline{X}_\phi = (R_s \cos \phi \cos v, R_s \cos \phi \sin v, -R_s \sin \phi) \quad (C.10)$$

$$\underline{X}_v = (-R_s \sin \phi \sin v, R_s \sin \phi \cos v, 0) \quad (C.11)$$

from (2.5-2.7) where \underline{X}_ϕ denotes partial differentiation with respect to ϕ , and on the cone

$$\underline{X}_\zeta = (R_c \cos v, R_c \sin v, -h_c) \quad (C.12)$$

$$\underline{X}_v = (-\zeta R_c \sin v, \zeta R_c \cos v, 0) \quad (C.13)$$

from (2.8-2.10), thus giving

$$\underline{N}_{sphere} = (\sin \phi \cos v, \sin \phi \sin v, \cos \phi) \quad (C.14)$$

$$\underline{N}_{cone} = \left(\frac{h_c \cos v}{(h_c^2 + R_c^2)^{1/2}}, \frac{h_c \sin v}{(h_c^2 + R_c^2)^{1/2}}, \frac{R_c}{(h_c^2 + R_c^2)^{1/2}} \right). \quad (C.15)$$

To obtain a vector which is tangent to each surface on both trimlines we take the vector product of \underline{N} with a unit vector along \underline{X}_v to give us the derivative conditions required. Thus

$$\underline{X}_u(0, v) = \begin{vmatrix} \sin \phi \cos v & \sin \phi \sin v & \cos \phi \\ -\sin v & \cos v & 0 \end{vmatrix} \quad (C.16)$$

$$\underline{X}_u(1, v) = \begin{vmatrix} \frac{h_c \cos v}{(h_c^2 + R_c^2)^{1/2}} & \frac{h_c \sin v}{(h_c^2 + R_c^2)^{1/2}} & \frac{R_c}{(h_c^2 + R_c^2)^{1/2}} \\ -\sin v & \cos v & 0 \end{vmatrix}. \quad (C.17)$$

This leads to equations (2.22-2.27)

$$x_u(0, v) = -S_1 \left(\frac{R_s^2 - R_{top}^2}{R_{top}^2} \right)^{1/2} \cos v \quad (C.18)$$

$$y_u(0, v) = -S_1 \left(\frac{R_s^2 - R_{top}^2}{R_{top}^2} \right)^{1/2} \sin v \quad (C.19)$$

$$z_u(0, v) = S_1 \quad (C.20)$$

$$x_u(1, v) = -S_2 \frac{R_c}{h_c} \cos v \quad (C.21)$$

$$y_u(1, v) = -S_2 \frac{R_c}{h_c} \sin v \quad (C.22)$$

$$z_u(1, v) = S_2 \quad (C.23)$$

where

$$S_1 = S_{top} \cdot \frac{R_{top}}{R_s}, \quad S_2 = \frac{S_{bot} \cdot h_c}{(h_c^2 + R_c^2)^{1/2}}. \quad (C.24)$$

The x and y components of the surface are then obtained from equation (2.28) by comparing the boundary conditions with (2.30) and (2.31) to give us (2.32) and (2.33). Since the boundary conditions for z are given by

$$z(0, v) = d_1 \quad z(1, v) = d_2 \quad z_u(0, v) = S_{top} \quad z_u(1, v) = S_{bot}. \quad (C.25)$$

it is possible to fit a cubic polynomial for z .

Thus, from equation (2.29)

$$z(u) = z_0 + z_1 u + z_2 u^2 + z_3 u^3 \quad (C.26)$$

which implies that

$$d_1 = z_0 \quad S_{top} = z_1 \quad (C.27)$$

$$d_2 = z_0 + z_1 + z_2 + z_3 \quad S_{bot} = z_1 + 2z_2 + 3z_3. \quad (C.28)$$

from which we obtain equation (2.34).

The parameters S_{top} and S_{bot} control the speed at which the equally spaced parametric u -lines approach the trimlines. Thus, for large values of S_{top}, S_{bot} the spacing of the u -lines is large, while small values ensure that the boundary conditions influence only a region close to the trimlines. By changing the sign of S_{top} and S_{bot} we effectively reverse the direction in which the iso u -lines propagate as they approach the trimlines. The restrictions we impose on S_{top}, S_{bot} are obtained by maintaining that a self-intersecting surface is not generated. The limit of such an example can be seen in figure (2.6) where any increase in magnitude of the parameters will create a self-intersection. The actual values for S_{top}, S_{bot} are dictated by our initial choice of size of sphere and cone.

Thus, we see in table (2.1) the selected examples which illustrate the choice of parameters.

C.3 The Wine Glass

Moving into the field of free-form design we have more freedom to stipulate our boundary conditions. For the example of a wine glass it can be seen that

$$x(0, v) = R_{top} \cos v \quad x(1, v) = R_{bot} \cos v \quad (C.29)$$

$$y(0, v) = R_{top} \sin v \quad y(1, v) = R_{bot} \sin v \quad (C.30)$$

$$z(0, v) = d \quad z(1, v) = 0 \quad (C.31)$$

for $0 \leq u \leq 1, 0 \leq v \leq 2\pi$, will define the lip of the glass with radius R_{top} , and the base with radius R_{bot} .

To design the glass we want the iso v -lines to propagate radially outwards and downwards from the lip, thus imposing

$$x_u(0, v) = S_t \cos v \quad (C.32)$$

$$y_u(0, v) = S_t \sin v \quad (C.33)$$

$$z_u(0, v) = S_{top} \quad (C.34)$$

gives us two parameters S_t, S_{top} with which to control the surface: S_t controls the rate at which the glass bulges out (or is sucked in for negative S_t) and S_{top} controls the rate of propagation of the iso u -lines towards the base. Thus, for large S_{top} the bulb will be more elongated, whereas for smaller values of S_{top} the bulb will be more compact.

At the bottom of the glass we wish to direct the surface inwards to generate the base and stem. Again, by imposing radially directed derivative vectors with x and y components, then

$$x_u(1, v) = S_b \cos v \quad (\text{C.35})$$

$$y_u(1, v) = S_b \sin v \quad (\text{C.36})$$

and we can control the radial extent of the base, with the parameter S_b while the thickness of the base is controlled by the parameter S_{bot} , thus

$$z_u(1, v) = S_{bot}. \quad (\text{C.37})$$

This can be seen by considering large and small values for S_{bot} . If S_{bot} is small with a large value for S_b we can ensure that the base of the glass pushes inwards towards the stem while remaining in near proximity to the trimline $u = 1$. If S_{bot} is large, the surface moves away from $u = 1$ more rapidly and a 'cone-shaped' base will be formed. S_b should be chosen to generate the thickness of the stem; if S_b is too large, the surface will self-intersect at the stem centre.

We can see from figure (2.8) that there is a limit to the surface variations possible from a fourth order PDE surface. The glass varies in shape slowly along its length. Therefore, in order to increase our control over the surface, it is useful to include second derivative terms, given by

$$x_{uu}(0, v) = C_t \cos v \quad x_{uu}(1, v) = C_b \cos v \quad (\text{C.38})$$

$$y_{uu}(0, v) = C_t \sin v \quad y_{uu}(1, v) = C_b \sin v \quad (\text{C.39})$$

$$z_{uu}(0, v) = C_{top} \quad z_{uu}(1, v) = C_{bot} \sin v \quad (\text{C.40})$$

at the lip and base.

The imposition of a curvature condition at the boundary gives us a greater degree of control over the surface. At the base we impose a large value of C_b to quickly alter the direction of the iso v -lines from a radial first derivative component at the base, to a longitudinal first derivative along the stem to generate a flat base. Similarly, imposing

a large value on C_{top} produces larger values of the curvature in the mid regions of the surface patch, corresponding to the lower position of the bowl. The value of C_t in the radial sense can be used to influence the bulb shape; for extreme values we obtain the effect shown in figure (2.11). C_{bot} is kept small to restrict the thickness of the base of the glass. Hence, by choosing large values for $C_t, C_{top}, C_b, C_{bot}$ we get rapid changes in the surface direction, whereas small values will mean that the surface propagates more with the influence of the first derivative parameters $S_t, S_{top}, S_b, S_{bot}$.

C.4 Boundary conditions for the generic blade

The basic geometry used in section (3.2.1) to describe the blade section at the base was given by

$$x = c \cos v \quad (\text{C.41})$$

$$y = t_x \sin 2v \quad (\text{C.42})$$

over $-\pi/2 \leq v \leq \pi/2$. This ensures that a sharp trailing edge is built into the section, as is discussed in section (3.2.1). The parameter c will control the length of the blade section at the base, and t_x will control the maximum thickness (which is located at the isolines $v = \pm\pi/4$).

To include a degree of twist and camber into the propeller blade, we include a parabolic distribution of the form

$$m_x \left(\cos v - \frac{\cos 2v + 1}{2} \right) \quad (\text{C.43})$$

for the mean line with a rotation β about the origin at the base to twist the blade sections along the span. Thus, if $m_x = 0$ we obtain a symmetric blade section with mean line corresponding to the chordline. By gradually increasing m_x (where m_x is usually considerably smaller than t_x) we include camber into the section which is of a parabolic form.

The parameterisation for x and y will now be of the form

$$x = c \cos v \quad (\text{C.44})$$

$$y = t_x \sin 2v + m_x \left(\cos v - \frac{\cos 2v + 1}{2} \right). \quad (\text{C.45})$$

The twist is included with a simple rotation about the origin using the standard transformation

$$x' = x \cos \beta + y \sin \beta \quad (\text{C.46})$$

$$y' = y \cos \beta - x \sin \beta \quad (\text{C.47})$$

to give the boundary conditions given by equations (3.6) and (3.7).

Thus we have the section at the base of the propeller. To generate the chordlength distribution we control the x distribution at the tip and base with the first derivative terms

$$x_u(0, v) = S_x \cos 2v \quad (\text{C.48})$$

$$x_u(1, v) = E_x \cos 2v. \quad (\text{C.49})$$

These take the above form due to the parameterisation being used. Since v varies over the range $-\pi/2 \leq v \leq \pi/2$ we require the conditions to be periodic. From definition (C.48) above, we see that at $v = -\pi/2$ (the trailing edge) the derivatives will have magnitude S_x along the chordlength at the tip ($u = 0$). Then, as v moves to $v = -\pi/4$ (the midchord section) we have no contribution from the derivative along the chord. At $v = 0$ (the nose) we have a derivative pushing the isolines in the opposite direction to those at the trailing edge, but of equal magnitude. Thus, we have suitable derivatives to describe the blade profile.

The terms

$$y_u(0, v) = S_y \sin 2v \quad (\text{C.50})$$

$$y_u(1, v) = E_y \sin 2v \quad (\text{C.51})$$

act in a similar manner, except that now at $v = -\pi/2$ (the trailing edge) the section curves are not pushed in the y direction. As we traverse the section curve we see that at $v = \pm\pi/4$ the section will be pushed out most, with magnitude S_y at the tip and E_y at the base. Thus the blade is pushed from the mean line to give a measure of the maximum thickness.

The parameters S_{top} and S_{bot} are used in a similar sense to those of the wine glass, in which altering values concentrates the various (thickness/camber) distributions into different regions of the blade. For example, increasing S_{bot} pushes the blade sections rapidly away from the base towards the tip. It should be noted at this stage that the way in which the problem is formulated will decide whether parameters, such as S_{top} , S_{bot} , will be positive or negative.

If we now look at table (3.1) we see the different parameters used for the airscrew and marine propeller.

The span d of the airscrew is much larger than that of the marine propeller. The marine propeller needs wider blades and hence larger c is chosen than for the airscrew. To generate the chordlength distribution it is required that S_x be much larger for the marine propeller than for the airscrew since this controls the chordwise distribution through the span, and that S_{top} be set to zero to give a flat tip. This is in contrast to the airscrew which has $S_{top} = 3.0$ to quickly push the distributions away from the tip into the main part of the blade, thus elongating the blade.

It can thus be seen how we can set up the problem: by generating a suitable section, then determining the blade length, from which a suitable base chordlength can be chosen. Using the parameters S_x, S_{top} etc. we can create a profile of the blade.

C.5 The projected view of the propeller

If we consider the boundary conditions of the last section, we can generate the projected view of the propeller by wrapping the base section onto the hub and using this new section as the base boundary conditions. Then, obtaining the solution to the PDE will generate the actual propeller which has radially curved lines of constant u .

Thus, if we consider a general point on the trimline $u = 1$, its new coordinates will be given by (x', y', z') where $y' = y$. On the trimline $u = 1$ we also have $z = r_h$, since the base section of the blade is located at the hub.

The distance from the centre of the hub to a point on the trimline will be given by OP , say, where

$$OP = (x^2 + z^2)^{1/2}. \quad (\text{C.52})$$

Therefore, the new coordinates of the section projected onto the hub will be given by

$$\frac{x'}{r_h} = \frac{x}{OP} \quad \frac{z'}{r_h} = \frac{z}{OP} \quad (\text{C.53})$$

from similar triangles, from which we obtain equations (3.19) - (3.21)

$$x'(1, v) = \frac{x(1, v) * z(1, v)}{(x(1, v)^2 + z(1, v)^2)^{1/2}} \quad (\text{C.54})$$

$$y'(1, v) = y(1, v) \quad (\text{C.55})$$

$$z'(1, v) = \frac{z(1, v)^2}{(x(1, v)^2 + z(1, v)^2)^{1/2}}. \quad (\text{C.56})$$

The problem associated with the above boundary conditions can then be solved numerically to obtain the desired surface using the finite difference formula of equation

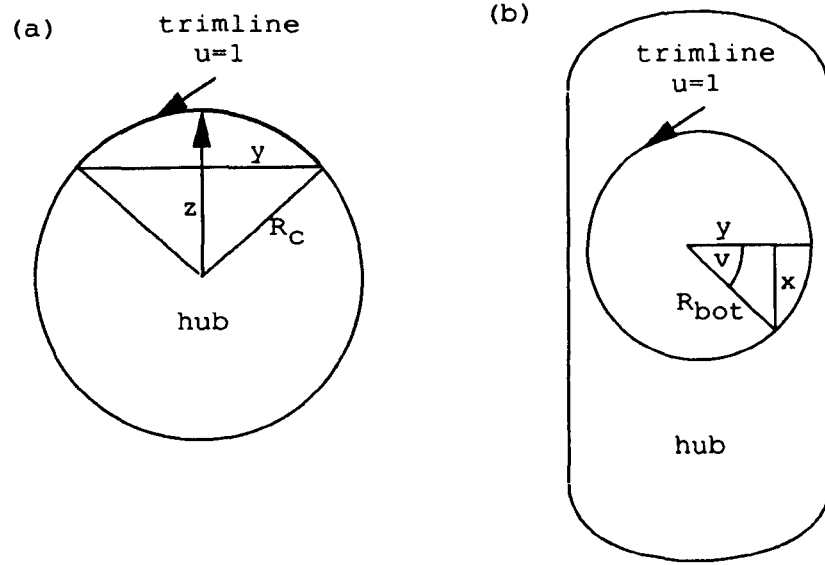


Figure C.1: The trimline on the hub

(3.33) since the boundary conditions are no longer of the form which will give an analytic solution. Figures (3.10) and (3.11) illustrate the solution obtained.

C.6 Fillet design

The fillet design problem is one of blend generation and so to some extent our boundary conditions are decided for us from the requirements of a smooth continuous surface between the blade (defined at the $u = 0$ trimline) and the central hub.

The boundary conditions at $u = 0$ are given by equations (3.19-3.21) and (3.12-3.14) as described in section (3.2.4).

The trimline $u = 1$ is described as a curve lying on the cylinder's surface, whose projection onto the (x, y) plane is a circle, as can be seen from figures (C.1a) and (C.1b). Figure (C.1a) illustrates the view through the cross section of the hub. The z and y coordinates of a point on the trimline are illustrated. In figure (C.1b) we see the hub from above with the trimline $u = 1$ projected onto it.

From figure (C.1b) we can define the x and y components of the trimline by

$$x(1, v) = R_{bot} \cos 2v \quad (C.57)$$

$$y(1, v) = R_{bot} \sin 2v \quad (C.58)$$

where R_{bot} is the radius of the projected circle and $\cos 2v$ is taken since v covers the parameter range $-\pi/2 \leq v \leq \pi/2$ to accord with the parameterisation on the trimline

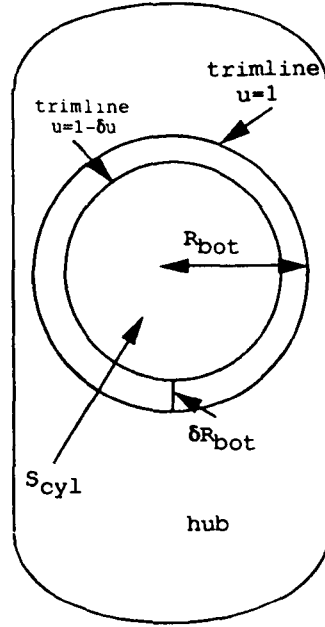


Figure C.2: The isolines on the hub

$u = 0$.

From figure (C.1a) we can see that the radius of the hub is defined by

$$R_c^2 = z^2 + y^2 \quad (\text{C.59})$$

which implies that the z component on the trimline will be given by

$$z(1, v) = (R_c^2 - y^2)^{1/2} = (R_c^2 - R_{bot}^2 \sin^2 2v)^{1/2}. \quad (\text{C.60})$$

To define the derivative conditions (3.46-3.48) we require slightly more work. If we consider figure (C.2) we can see that the u isolines will propagate in a radial direction. If the outer circle on the hub represents the trimline $u = 1$ then moving slightly inwards gives us the next trimline. We can define the parameter S_{cyl} to describe the rate at which the u isolines will propagate through the blend; the larger S_{cyl} the further apart they are spaced.

Therefore, x_u, y_u, z_u are given by S_{cyl} times a unit vector in the radial direction along R_{bot} .

Now

$$\frac{\partial x}{\partial R_{bot}} = \cos 2v \quad (\text{C.61})$$

$$\frac{\partial y}{\partial R_{bot}} = \sin 2v \quad (\text{C.62})$$

$$\frac{\partial z}{\partial R_{bot}} = \frac{-R_{bot} \sin^2 2v}{(R_c^2 - R_{bot}^2 \sin^2 2v)^{1/2}} \quad (\text{C.63})$$

and to obtain a unit vector we divide each of the above quantities by

$$\left(\frac{\partial x^2}{\partial R_{bot}} + \frac{\partial y^2}{\partial R_{bot}} + \frac{\partial z^2}{\partial R_{bot}} \right)^{1/2} \quad (C.64)$$

i.e.

$$\left(\cos^2 2v + \sin^2 2v + \frac{R_{bot}^2 \sin^4 2v}{R_c^2 - R_{bot}^2 \sin^2 2v} \right)^{1/2} \quad (C.65)$$

$$= \left(\frac{R_c^2 - R_{bot}^2 \sin^2 2v + R_{bot}^2 \sin^4 2v}{R_c^2 - R_{bot}^2 \sin^2 2v} \right)^{1/2}. \quad (C.66)$$

Hence

$$x_u(1, v) = S_{cyl} \cos 2v \left(\frac{R_c^2 - R_{bot}^2 \sin^2 2v}{R_c^2 - R_{bot}^2 \sin^2 2v + R_{bot}^2 \sin^4 2v} \right)^{1/2} \quad (C.67)$$

$$= S_{cyl} \cos 2v \left(\frac{R_c^2 - R_{bot}^2 \sin^2 2v - R_{bot}^2 \sin^4 2v + R_{bot}^2 \sin^4 2v}{R_c^2 - R_{bot}^2 \sin^2 2v + R_{bot}^2 \sin^4 2v} \right)^{1/2} \quad (C.68)$$

$$= S_{cyl} \cos 2v \left(1 - \frac{R_{bot}^2 \sin^4 2v}{R_c^2 - R_{bot}^2 \sin^2 2v + R_{bot}^2 \sin^4 2v} \right)^{1/2}. \quad (C.69)$$

Similarly

$$y_u(1, v) = S_{cyl} \sin 2v \left(1 - \frac{R_{bot}^2 \sin^4 2v}{R_c^2 - R_{bot}^2 \sin^2 2v + R_{bot}^2 \sin^4 2v} \right)^{1/2}. \quad (C.70)$$

$$z_u(1, v) = \frac{-S_{cyl} R_{bot} \sin^2 2v}{(R_c^2 - R_{bot}^2 \sin^2 2v)^{1/2}} \left(\frac{R_c^2 - R_{bot}^2 \sin^2 2v}{R_c^2 - R_{bot}^2 \sin^2 2v + R_{bot}^2 \sin^4 2v} \right)^{1/2} \quad (C.71)$$

$$= -S_{cyl} \frac{R_{bot} \sin^2 2v}{(R_c^2 - R_{bot}^2 \sin^2 2v + R_{bot}^2 \sin^4 2v)^{1/2}}. \quad (C.72)$$

Thus, equations (C.69), (C.70) and (C.72) are exactly as in equations (3.46-3.48).

We can therefore control the shape of the fillet by firstly specifying the distance of the base, g from the hub (as in figure 3.13). This should be taken to be smaller than the radius of the hub R_c to produce a realistic geometry. Values of the smoothing parameter a and the gradient magnitude S_{cyl} can be chosen to make the fillet as full as possible (to increase the strength in the fillet). This is why very small values of a are chosen; as can be seen from figures (2.4) and (2.5) for a low value of a a fuller blend surface is generated, whereas when a has larger values (typically a is less than 15) a waistline is created. This is of little use on our fillet for the propeller due to high stress regions.

C.7 The NACA propeller blade

Working through sections (4.3) and (4.4) we can see how we create equations (4.34-4.36) defining the boundary conditions for the shape of the blade section at the base. By taking a similar section at the tip and reducing it to a point we obtain more control over the distributions throughout the blade span.

From these boundary conditions we can then define the parameters of table (4.4) to correspond to the distributions at the base section given by Eckhardt and Morgen. Hence, we now have D, c, m_x, t_x defined. f gives a measure of the skew. ϵ_x, ϵ_y are chosen to give zero chordlength and finite thickness at the tip, as is also required by the data.

The derivative terms need to be defined so that we have control over each of the spanwise distributions along the blade. Equations (4.40-4.43) give us first derivative control for the distributions. For instance, S_{xi}, S_{xu} will highly influence the chordlength, S_{tu}, S_{ti} will influence the normal component of the thickness on the meanline and S_{cu}, S_{ci} control the mean line and camber of the blade.

In a similar fashion we obtain second derivative control from equations (4.44-4.47). These conditions were used as it was found that they produced reliably accurate approximations to the distributions along the blade span, while maintaining the blade section geometry at any span (as is verified in figure (4.14) for the highlighted section of (4.13)). Therefore, we have a model which gives us great control of the propeller geometry.

Determining values of the parameters to fit the geometry is achieved by trial and error by inputting different parameter values.¹ It should be noted that large values of the thickness parameters S_{tu}, C_{tu} are required in table 4.4 to create the thickness distribution of figure (4.18). A large first derivative is required to push the surface out at the tip (since the parameter is scaled from the value of ϵ_y it appears unusually large) while a strong negative value of C_{tu} is required to bring the distribution back into the shape as illustrated in figure (4.18).

We have tried to describe the ways in which the boundary conditions can be set up for the PDE method. These parameterisations are by no means unique. The parameters are controlled largely from understanding the way in which the surface is being generated and from the initial conditions defined, thus giving a wide scope for surface manipulation.

¹This can be achieved using a set of dials at the computer terminal which control the parameters. Moving the dials alters the parameters, and since a graphic display of figures (4.11) and (4.12) can also be shown, it is fast to manipulate the geometry via the parameter set.

Bibliography

- [1] Bloor, M. I. G. and Wilson, M.J. Generating blend surfaces using partial differential equations. *CAD*, 21(3):165–171, 1989.
- [2] Mortenson, M. E. *Geometric modeling*. Wiley-Interscience, New York, 1985.
- [3] Kerwin, J. E. and Lee, C-S. Prediction of steady and unsteady marine propeller performance by numerical lifting-surface theory. *Trans. Society of Naval Architects and Marine Engineers*, 86, 1978.
- [4] Hess, J. L. Calculation of potential flow about arbitrary three-dimensional lifting bodies. Technical Report MDCJ5679-01, McDonell Douglas, Oct 1972.
- [5] Friesch, J. Possibilities of model tests for energy saving devices. In *Marine Jubilee Meeting*, Wageningen, The Netherlands, 1992.
- [6] Young, F. R. *Cavitation*. McGraw-Hill Book Company Limited, Maidenhead, England, 1989.
- [7] Rossignac, A. R. and Requicha, A. A. G. Constant radius blending and solid modelling. *Computers in Mechanical Engineering*, pages 65–73, 1984.
- [8] Elliot, W. S. Computer-aided mechanical engineering: 1958 to 1988. *CAD*, 21(5):274–288, 1989.
- [9] Bézier, P. Style, Mathematics and NC. *CAD*, 22(9):524–526, 1990.
- [10] Woodwark, J. *Computing shape*. Butterworths, London, 1986.
- [11] do Carmo, M. P. *Differential geometry of curves and surfaces*. Prentice-Hall, Inc., New Jersey, 1976.
- [12] Nowacki, H. and Reese, D. Design and fairing of ship surfaces. *Surfaces in CAGD*, pages 121–134, 1983.

- [13] Piegl, L. Key development in Computer-Aided Geometric Design. *CAD*, 21(5):262–274, 1989.
- [14] Bézier, P. *Emploi des machines à commande numerique*. Masson and Cie, Paris, France, 1970.
- [15] Bernstein, S. N. Demonstration du theoreme de Weierstrass fondee sur le calcul des probabilités. *Commun. Soc. Math.*, 13(2):1–2, 1912.
- [16] Weierstrass, K. *Über die analytische Darstellbarkeit Sogenannter willkürlicher Funktionen einer reellen Veränderlichen*. Sitzungsberichte der Akad., Berlin, 1885.
- [17] Faux, I. D. and Pratt, M. J. *Computational geometry for design and manufacture*. Ellis Horwood, Chicester, UK, 1979.
- [18] Barnhill, R. E., Farin, G., Fayard, L. and Hagen, H. Twists, curvatures and surface interrogation. *CAD*, 20(6):341–346, 1988.
- [19] Hockfield, H. and Ahlers, M. Role of Bézier curves and surfaces in the Volkswagen CAD approach from 1967 to today. *CAD*, 22(9):598–607, 1990.
- [20] Gordon, W. and Riesenfeld, R. B-spline curves and surfaces. *Computer Aided Geometric Design*, pages 95–126, 1974.
- [21] Boehm, W. Inserting new knots into B-spline curves. *CAD*, 12(4):199–201, 1980.
- [22] Bloor, M. I. G. and Wilson, M. J. Generating N-sided patches with partial differential equations. *Computer graphics international '89*, pages 129–145, 1989.
- [23] Bloor, M. I. G. and Wilson, M. J. Using partial differential equations to generate free-form surfaces. *CAD*, 22(4):202–212, 1990.
- [24] Brown, J. M. *The design and properties of surfaces generated using partial differential equations*. PhD thesis, Dept of Applied Mathematics, University of Leeds, England, 1992.
- [25] Collatz, L. *The numerical treatment of differential equations*. Springer-Verlag, Berlin, 1960.
- [26] Smith, D. R. and Slater, J. E. The geometry of marine propellers. Technical Report 88/214, Defence Research Establishment Atlantic, Canada, 1988.

- [27] Eckhardt, M. K. and Morgen, W. B. A propeller design method. *Trans. Society of Naval Architects and Marine Engineers*, 63:325–374, 1955.
- [28] Saunders, H. E. In discussion at end of paper of Eckhardt and Morgen.
- [29] Troost, L. Open water test series with modern propeller forms. *Trans. North East Coast institution of Engineers and Shipbuilders*, 67, 1952.
- [30] Abbott, I. H. and von Doenhoff, A. E. *Theory of wing sections*. McGraw-Hill Book Company, Inc., New York, 1949.
- [31] Woodward, C. D. Methods for cross-sectional design of B-spline surfaces. In Requicha, A. A. G, editor, *Eurographics 86*, pages 129–142. Elsevier Science Publishers, 1986.
- [32] Nittel, M. F. Numerically controlled machining of propeller blades. *Marine Technology*, 26, 1989.
- [33] Choi, B. K. and Ju, S. Y. Constant-radius blending in surface modeling. *CAD*, 21(4):213–220, 1989.
- [34] Patience, G. Propeller surface roughness and fuel economy. Technical report, Stone Manganese Marine Limited, 1983.
- [35] Grigson, C. W. B. Propeller roughness, its nature and its effect upon the drag coefficients of blades and ship power. Technical report, R.I.N.A., 1982.
- [36] Struik, D. J. *Lectures on classical differential geometry*. Dover Publications, Inc., New York, 1961.
- [37] Falcão de Campos, J. A. C., van Gent, W. and Holtrop, J. Modelling of propulsors in design, theory and experiment. In *Marine Jubilee Meeting*, Wageningen, The Netherlands, 1992.
- [38] Demy, S. B., Puckette, L. T. et al. A new usable propeller series. *Marine Technology*, 26(3), 1989.
- [39] Kinnas, S. A. and Coney, W. B. The generalized image model - an application to the design of ducted propellers. *to be published*, 1990.
- [40] Betz, A. Schraubenpropeller mit geringstem energieverlust. *K. Ges. Wiss. Göttingern Nachr. Math.-Phys.*, pages 193–217, 1919.

- [41] Prandtl, L. Application of modern hydrodynamics to aeronautics. *Natl. Advis. Comm. Aeronaut. Ann. Rep.*, 7:157–215, 1921.
- [42] Lerbs, H. W. Moderately loaded propellers with a finite number of blades and an arbitrary distribution of circulation. *Trans. Society of Naval Architects and Marine Engineers*, 60:73–123, 1952.
- [43] Morgan, W. B., Silovic, V. and Denny, S. B. Propeller lifting-surface corrections. *Trans. Society of Naval Architects and Marine Engineers*, 76:309–47, 1968.
- [44] Greeley, D. S. and Kerwin, J. E. Numerical methods for propeller design and analysis in steady flow. *Trans. Society of Naval Architects and Marine Engineers*, 90(14):415–453, 1982.
- [45] Szantyr, J. A. and Glover, E. J. The analysis of unsteady propeller cavitation and hull surface pressures for ducted propellers. In *The Royal Institution of Naval Architects*, 1989.
- [46] Lighthill, M. J. A new approach to thin aerofoil theory. *Aerodynamics Quarterly*, pages 193–210, 1951.
- [47] Lamb, H. *Hydrodynamics*. Cambridge University Press, London, 1932.
- [48] Hess, J. L. and Smith, A. M. O. Calculation of potential flow about arbitrary bodies. *Progress in Aeronautical Sciences*, 8:1–138, 1967.
- [49] Kinnas, S. A. and Fine, N. E. Non-linear analysis of the flow around partially or super-cavitating hydrofoils by a potential based panel method. In *IABEM-90 symposium of the international association for boundary element methods*, Rome, 1990.
- [50] Cheng, H. M. and Hadler, J. B. Analysis of NSMB wake surveys on victory ship models. *Marine Technology*, 3(1):1–22, 1966.
- [51] Ligtelijn, J. T., van der Kooij, J. Kuiper, G. and van Gent, W. Research on propeller-hull interaction in the depressurized towing tank. In *Marine Jubilee Meeting*, Wageningen, The Netherlands, 1992.
- [52] Kinnas, S. A. and Hsin, C-Y. A boundary element method for the analysis of the unsteady flow around extreme propeller geometries. *to be published*, 1990.

- [53] Larsson, L., Kim, K. J., Esping, E. and Holm, D. Hydrodynamic optimisation using shipflow. In Caldwell, J. B. and Ward, G., editor, *PRADS 92: Practical design of ships and mobile units*, pages 1.1–1.17, 1992.
- [54] Dekanski, C. W., Bloor, M. I. G., Nowacki, H. and Wilson, M. J. The geometric design of marine propeller blades using the pde method. In Caldwell, J. B. and Ward, G., editor, *PRADS 92: Practical design of ships and mobile units*, pages 1.596–1.610, 1992.
- [55] Houghton, P. and Mullane, U. Geometric modelling and manufacture of marine propeller blades. Technical report, Dept. Mech. Eng., University of Leeds, England, 1992.
- [56] A. E. Turbines. Victoria Way, Yeadon, Bradford.
- [57] Munchmeyer, F. Shape interrogation: A case study. In Farin, G., editor, *Geometric modelling*, pages 291–301. SIAM, 1987.
- [58] Bloor, M. I. G. and Wilson, M. J. Local control of surfaces generated using partial differential equations. *to be published*, 1993.
- [59] Petrie, J. A. H. *Development of an efficient and versatile panel method for aerodynamic problems*. PhD thesis, Department of Applied Mathematical Studies, University of Leeds, England, 1979.
- [60] Greig, D. M. *Optimisation*. Longman, 1980.
- [61] Imam, M. H. Three dimensional shape optimisation. *International Journal for Numerical Methods in Engineering*, 18:661–673, 1982.
- [62] Lowe, T. W. *Functionality in computer aided geometric design*. PhD thesis, Dept. of Applied Mathematics, University of Leeds, England, 1992.
- [63] Fletcher, R. and Powell, M. J. D. A rapidly convergent descent method for minimisation. *Computer Journal*, 6:163–168, 1963.
- [64] Powell, M. J. D. An efficient method for finding the minimum of a function of several variables without calculating derivatives. *The Computer Journal*, 7:155–162, 1964.
- [65] Kruppe, C. F. L. *High speed propellers - Hydrodynamics and design*. The University of Michigan, 1967.

- [66] Bloor, M. I. G. and Wilson, M. J. Blend design as a boundary-value problem. *Geometric modeling: Theory and practise*, pages 221–234, 1989.
- [67] Smith, G. D. *Numerical solutions of partial differential equations*. Oxford University Press, London, 1971.
- [68] Boyce, W. E. and DiPrima, R. C. *Elementary differential equations and boundary value problems*. Wiley-Interscience, New York, 1992.
- [69] Cheng, S. Y. *Blending and fairing using partial differential equations*. PhD thesis, Dept. of Applied Mathematics, University of Leeds, England, 1992.
- [70] Clancy, L. J. *Aerodynamics*. Pitman Publishing, Inc, New York, 1975.
- [71] Umlauf, U. Propellergeometrieentwurf über Formparameter, 1990. Private communication.
- [72] Ortega, J. M. and Poole, W. G. *An introduction to numerical methods for differential equations*. Pitman Publishing, Inc, New York, 1981.
- [73] Kuethe, A. M. and Schetzer, J. D. *Foundations of aerodynamics*. Chapman and Hall, Ltd, London, 1975.
- [74] Theodorsen, T. On the theory of wing sections with particular reference to the lift distribution. Technical Report 383, NACA, 1931.
- [75] Fox, C. *An introduction to the calculus of variations*. Oxford University Press, 1950.
- [76] Batchelor, G. K. *An introduction to fluid dynamics*. Cambridge University Press, 1980.
- [77] Hess, J. L. Panel methods in computational fluid dynamics. *Annual Review of Fluid Mechanics*, 22:255–70, 1990.
- [78] Hess, J. L. The problem of three-dimensional lifting potential flow and its solution by means of surface singularity distribution. *Computer Methods in Applied Mathematics and Engineering*, 4:283–319, 1974.
- [79] Hess, J. L. and Valarezo, W. O. Calculation of steady flow about propellers using a surface panel method. *Journal of Propulsion Power*, 1(6):470–476, 1985.

- [80] Kerwin, J. E. and Kinnas, S. A. A surface panel method for the hydrodynamic analysis of ducted propellers. *Trans. Society of Naval Architects and Marine Engineers*, 95:93–122, 1987.
- [81] Maskew, B. and Woodward, F. A. Symmetrical model for lifting potential flow analysis. *Journal of Aircraft*, 13(9), 1976.
- [82] Press, W. H. et. al. *Numerical recipes: The art of scientific computing*. Cambridge University Press, Cambridge, 1989.
- [83] Clark, R. W. A new iterative matrix solution procedure for three-dimensional panel methods. In *AIAA 23rd Aerospace Sciences Meeting*, 1985.
- [84] Kerwin, J. E. Marine propellers. *Ann. Rev. Fluid Mechanics*, 18:367–403, 1986.
- [85] Maskew, B. *Numerical lifting surface methods for calculating the potential flow about wings and wing-bodies of arbitrary geometry*. PhD thesis, Dept. of Mathematics, Loughborough University, 1972.
- [86] Kerwin, J. E., Coney, W. B. and Hsin, C-Y. Optimum circulation distributions for single and multi-component propulsors. In *American Towing Tank Conference*, 1986.
- [87] Kinnas, S. A. A general theory for the coupling between thickness and loading for wings and propellers. *Journal of Ship Research*, 1990.
- [88] Nakatake, K., Ando, J., Murakami, M. and Kuroi, M. Practical quasi-continuous method to calculate propeller characteristics in uniform inflow. In Caldwell, J. B. and Ward, G., editor, *PRADS 92: Practical design of ships and mobile units*, pages 1.568–1.579, 1992.
- [89] Todd, F. H. *Principles of Naval Architecture*. Trans. Society of Naval Architects and Marine Engineers, 1967.
- [90] Francavilla, A., Ramakrishnan, C. V. and Zienkiewicz, O. C. Optimisation of shape to minimise stress concentration. *Journal of Strain Analysis*, 10(2), 1975.